SCUOLA DI DOTTORATO
UNIVERSITÀ DEGLI STUDI DI MILANO-BICOCCA

Dipartimento di / Department of

SCIENZA DEI MATERIALI

Dottorato di Ricerca in / PhD program in Scienza e Nanotecnologia dei Materiali
Ciclo / Cycle XXXIV

ORGANIC DYE-BASED PHOTOSYSTEMS FOR THE PRODUCTION OF SOLAR FUELS

Cognome / Surname DECAVOLI Nome / Name CRISTINA

Matricola / Registration number 780923

Tutore / Tutor: PROF. ALESSANDRO ABBOTTO

Coordinatore / Coordinator: PROF. MARCO BERNASCONI

ANNO ACCADEMICO / ACADEMIC YEAR 2020/2021

University of Milano–Bicocca

School of Science

Ph.D. program in Materials Science and Nanotechnology

Organic dye-based photosystems for the production of solar fuels

Ph. D. Thesis of

Cristina Decavoli

Supervisor	Dean of the Ph. D. program
Prof. Alessandro Abbotto	Prof. Marco Bernasconi

May 2022

XXXIV Cycle

If you don't make mistakes, you're not
working on hard-enough problems.
And that's a big mistake.

- Frank Wilczek

Table of Content

List of Publications

1. Decavoli, C.; Boldrini, C.L.; Manfredi, N.; Abbotto, A., Dye-sensitized photocatalytic and photoelectrochemical hydrogen production through water splitting. *Rend. Lincei. Sci. Fis. Nat.* **2019**, 30, 469-483.

2. Decavoli, C.; Boldrini, C.L.; Manfredi, N.; Abbotto, A., Molecular Organic Sensitizers for Photoelectrochemical Water Splitting. *Eur. J. Inorg. Chem.* **2020**, 2020, 978-999.

3. Manfredi, N.; Decavoli, C.; Boldrini, C.L.; Coluccini, C.; Abbotto, A., Ferrocene Derivatives Functionalized with Donor/Acceptor (Hetero)Aromatic Substituents: Tuning of Redox Properties. *Energies* **2020**, 13, 3937.

4. Manfredi, N.; Decavoli, C.; Boldrini, C.L.; Dolla, T.H.; Faroldi, F.; Sansone, F.; Montini, T.; Baldini, L.; Fornasiero, P.; Abbotto, A., Multibranched calix[4]arene-based sensitizers for efficient photocatalytic hydrogen production. *Eur. J. Org. Chem.* **2021**, 2021, 284.

5. Decavoli, C.; Boldrini, C.L.; Trifiletti, V.; Luong, S.; Fenwick, O.; Manfredi, N.; Abbotto, A., Dye-catalyst dyads for photoelectrochemical water oxidation based on metal-free sensitizers. *RSC Adv.* **2021**, 11, 5311.

List of Abbreviations

ALD: Atom layer deposition
APCE: Adsorbed photon-to-current efficiency
AQY: Apparent quantum yield
bda: 2,2’-bipyridine-6,6’-dicarboxylate
CA: Chronoamperometry
CB: Conduction band
CE: Counter electrode
cod: 1,5-cyclooctadiene
DDQ: 2,3-dichloro-5,6-dicyano-1,4-benzoquinone
DFT: Density functional theory
DMSO: Dimethyl sulfoxide
DPV: Differential pulse voltammetry
DSPC: Dye-sensitized photocatalysis
DSPEC Dye-sensitized photoelectrochemical cell
D-π-A: Donor-π-spacer-Acceptor structure
Fc: Ferrocene
FE: Faradaic efficiency
FTIR: Fourier-transform infrared
FTO: Florine-doped tin oxide
GC: Gas chromatography
GHG: Greenhouse gases
HEC: Hydrogen evolution catalyst
HOMO: Highest occupied molecular orbital
HRMS: High resolution mass spectroscopy
ICT: Intramolecular charge-transfer
ICT: Intramolecular charge-transfer
IPCE: Incident photon-to-current efficiency
IR: Infrared
ITO: Indium tin oxide
LFE: Light-to-fuel efficiency
LHE: Light-harvesting efficiency

LSV: Linear sweep voltammetry
LUMO: Lowest unoccupied molecular orbital
MOF: Metal organic framework
NMR: Nuclear magnetic resonance
PBS: Phosphate buffer solution
PC: Photocatalysis
PDI Perylene diimide
PEC: Photoelectrochemical cells
pic: 4-picoline
ppy: 4-phenylpyridine
PS I: Photosystem I
PS II: Photosystem II
pyalk: 2-(2’-pyridyl)-2-propanolate
RE: Reference electrode
RGO: Reduced graphene oxide
SC: Semiconductor
SEA: Sacrificial electron acceptor
SED: Sacrificial electron donor
STH: Solar-to-Hydrogen
TCD: Thermal conductivity detector
TEOA: Triethanolamine
TFEC: Total final energy consumption
TOF: Turnover frequency
TON: Turnover number
VB: Valence band
WE: Working electrode
WOC: Water oxidation catalyst
XPS: X-ray photoelectron spectroscopy
β-CD: β-cyclodestrin

Abstract

The pursuit of a clean energy source is a goal that the scientific community should achieve in the next decades. Currently, energy is mainly derived from oil, coal, natural gas, and other non-renewable sources. In recent years, hydrogen has gained much attention in the scientific community as a renewable energy carrier. However, the main goal in the energetic field is to move from the production of grey hydrogen (obtained using fossil sources with the subsequent emission of carbon dioxide) to the evolution of green hydrogen (produced with zero carbon footprint). This thesis investigates two of the most important devices that produce green hydrogen by exploiting the solar-driven water-splitting reaction with dye-sensitized photocatalytic and photoelectrochemical approaches. These devices mimic natural photosynthesis with the ambition of developing an artificial leaf. Thus, Chapter 1 provides the fundamental information to understand the aim of the research performed in this thesis. This chapter presents an overview of the present world energy situation and an introduction to a new hydrogen-driven society. This is followed by the presentation of artificial photosynthesis. Much interest is focused on the importance of solar radiation and on the principal aspects of natural photosynthesis, which artificial photosynthesis imitates.

Chapter 2 introduces the reader to photocatalysis generally, and the working principles and parameters used in the evaluation of the efficiency of the photocatalytic device. Photocatalysis is composed of a semiconductor, which absorbs solar radiation and generates an electron/hole couple. Then, a particular catalyst uses the excited electron to evolve hydrogen, and, in most cases, a sacrificial electron donor restores the semiconductor. In some cases, a dye sensitizes the semiconductor to enlarge its absorption spectrum into the visible region.

An example of dye-sensitized photocatalysis which exploits host-guest interactions with the sacrificial electron donor is described in Chapter 3. We investigated a series of new dyes

characterized by the presence of a calix[4]arene macrocycle which can exploit host-guest interactions with triethanolamine chosen as the sacrificial electron donor. Their performances are compared with a corresponding linear derivative. In this work, the presence of the macrocycle remarkably increases the efficiency of the photocatalytic system even if the compounds present similar optical properties to the linear benchmark. Hence, we hope that the potential of the supramolecular interactions in photocatalytic devices can pave the way for the development of new strategies in this direction.

Chapter 4 introduces the reader to the general aspects of photoelectrochemical cells and the working principles and parameters used in the evaluation of the efficiency of these devices. I focus on simple photoelectrochemical cells characterized by the presence of only one photoactive electrode, in this case, the photoanode. As for photocatalysis, the core of the photoanode is a semiconductor, which a dye can sensitize. The presence of a second molecular element, a water oxidation catalyst, is mandatory to perform the water oxidation in the anodic compartment. Sometimes, a dye and catalyst can be combined in an integrated system called a dyad with the aim of increasing the efficiency of the system. In Chapters 5 and 6, two kinds of non-covalent dyads are investigated, while in Chapters 7 and 8 two covalent ones.

Chapter 5 presents the first example in dye-sensitized photoelectrochemical cells where calix[4]arene macrocycles have been used to exploit host-guest interactions with suitable catalysts. Two new photosensitizers functionalized with a calix[4]arene macrocycle were studied in combination with two water oxidation catalysts. We found that the host-guest interactions with the catalysts could increase or decrease the efficiency of the device, depending on the different designs. Moreover, the higher rigidity of one system with respect to the others could completely limit the performance of the device. The other non-covalent interaction is described in Chapter 6 and exploits π- π interactions between the dye and the catalyst. A push-pull organic photosensitizer is functionalized with a graphene layer to increase the stability of the photoanode and reduce detrimental interactions between the semiconductor and the catalyst. However, only the synthesis of the organic dye is illustrated in this chapter. All further characterizations and the attachment to the reduced graphene layer are in progress.

In Chapter 7, one of the first examples of organic dye-based dyad connected by a covalent bond is presented. A series of eight dyes and eight covalent dyads belonging to two different families, phenothiazine and carbazole, is reported. The dyads are obtained by self-assembly of the dye and catalyst directly on the photoanode. The correct formation of the dyads is confirmed by XPS spectroscopy as well as electrochemistry. Some of these dyads have been investigated in oxygen production using the collector-generator technique. The calculated Faradaic efficiencies show the less stability of the phenothiazine-based dyads as well as the good performances of the carbazole-based ones. The carbazole-based dyads turned out to be the best performing dyads in water oxidation when also compared to the organometallic dye-based systems.

In Chapter 8, I report the projects I followed at Yale University during my Ph D. period abroad. The first project focuses on the optimization of the new way of binding the TiO_2 that the Yale group has recently discovered. I functionalized four different BODIPY dyes in positions 2 and 6 with small and large substituents to study the influence of these substitutions on the binding mode. I found that the presence of only one substituent does not influence the binding mode, while the presence of the second substituent reduces it, until almost preventing if the substituent is large. After this first optimization study, I focus on the synthesis and application in water oxidation of a new iridium-based water oxidation catalyst. This electrocatalyst exhibited good water oxidation capabilities generating high current density on ITO films. It was further used as a dyad for photoelectrochemical application, since one of its ligands is photoactive. However, its performances were not influenced by the solar irradiation, indicating an incorrect charge transfer to the dye.

Finally, in Chapter 9, I report some conclusions and the future perspectives in the DSPC and DSPEC fields.

Chapter 1: Introduction

1.1 Climate is changing

The effects of climate change are exceedingly evident in everyday life. Every year, the winter is warmer than the prior one, spring and autumn are disappearing, the Arctic and Antarctica are melting, seas are rising, biodiversity is getting lost, and all these changes are causing unprecedented risks to vulnerable people and populations. To limit its effects, in September 2015, 193 member States of the United Nations signed the 17 Sustainable Development Goals, a 15-year plan to promote prosperity while protecting the planet. They recognized that ending poverty must go hand-in-hand with strategies that build economic growth and address a range of social needs including education, health, social protection, and job opportunities all while tackling climate change and environmental protection.[1] Two months later, in Paris, COP21 took place, the Paris agreement was defined, and the following year signed by all 196 Parties. In this agreement, all countries agreed to work to limit global temperature rise this century to well below 2 °C, and given the grave risks, to strive for 1.5 °C.[1,2] Any increase beyond that point might enhance the risk of extreme climate events, such as drought, floods, and very high temperatures for a lot of populations.[3] It also provides a roadmap for climate actions that could reduce emissions and build climate resilience. Now the global temperature is rising by 0.2 °C every decade.[4] Greenhouse gases (GHG) emissions, in particular CO_2, NO_x, CH_4, and chlorofluorocarbons, which accumulate in the upper part of our atmosphere, are largely responsible for this rising temperature. Around 99% of total global GHG emissions is due to the energy sources we use to maintain our lifestyles.[5] By 2030 global carbon emissions should decrease by 45% concerning the amount in 2010 and continue a steep decline to zero net emissions by 2050.[6]

Every second, solar radiation reaches the Earth's surface, and it is reflected as infrared (IR) radiation which CO_2 and water vapor in the atmosphere mainly absorb, causing the planet to overheat.[7] Carbon dioxide and water are the major products of the combustion reaction for organic compounds. However, animals and humans also emit CO_2, which plants convert into molecular oxygen and carbohydrates. This perfectly harmonious cycle rules our planet and our existences. The discovery and the extreme abuse of fossil fuels changed this balance. As it is possible to see in Figure 1, the level of carbon dioxide has fluctuated throughout Earth's history, but since the end of World War II, it has never stopped its growth and made it steeper. Nowadays, about 80% of the energy used by humanity comes from oil, coal, gas, and other nonrenewable sources.[8] Every year about 30 Gt of lithosphere carbon, in the form of coal, oil, gas, etc., are transferred as carbon dioxide to the atmosphere to maintain our lifestyles with drastic consequences for the environment and our health.[9] It is reflected in the rise of global CO_2 concentration, which now is about 20 ppm per decade. This is up to 10 times faster than any sustained rise in CO_2 during the past 800,000 years (Figure 1).[3]

Although fossil fuels are no longer sustainable for our Earth, they are not running out, and that is the real problem! Over the past twenty years, accessible reserves of coal and oil have officially increased, making them available for another 200 years.[10,11] This is certainly not a reassuring fact, since it delays the definitive transition to renewable energies even more. Interestingly, fossil fuels are a kind of buried solar radiation. Therefore, defining the Sun as an "alternative" energy source is not entirely correct. Our existence has always been completely dependent on solar energy. The significant difference is that solar energy is continuously generated and delivered in real-time, whereas fossil fuels formed a long time ago and are now consumed at least 100 000 times faster than they were produced. A trend impossible to perpetuate.[12,13]

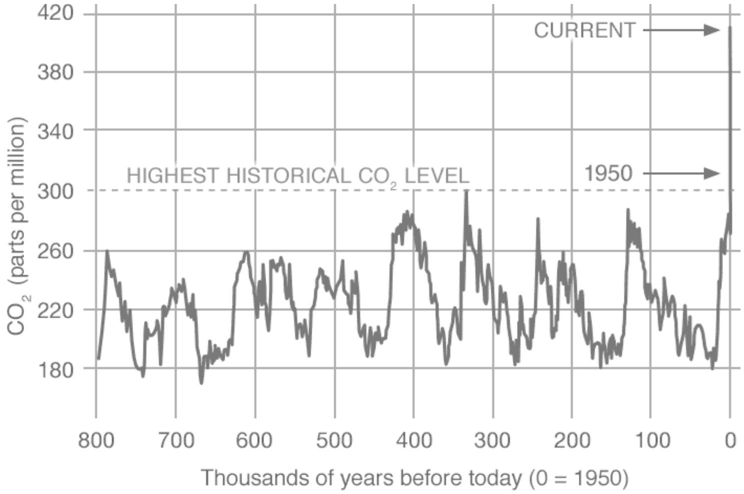

Figure 1: The distribution and variation of the level of carbon dioxide (417 parts per million - ppm) during time (data from www.climate.nasa.gov).

Moreover, the main problem is that energy should be easily concentrated, stored, and transportable. Fossil fuels meet these demands well, while renewable energies mainly meet only one or two of these requirements, such as electricity produced form solar, wind or water that can be easily concentrated and transferred but not stored.[14] In 2020, only 11.2% of world energy demand was satisfied by renewable sources, compared to 8.7% a decade earlier.[15] In the electricity sector the use of modern renewable energy has grown to 27% of the total final energy consumption (TFEC) due to a more increase in the use of solar panels, geothermal energy and wind power.[15] Hydroelectricity remains the most used and developed among the renewable energies, but it does not exhibit any significant increase with respect to the previous year.[16] On the other hand, the use of solar photovoltaics has increased of 22% since 2019.[15] However, in the automotive sector, the renewable sources appear only for a 0.3% of the TFEC. More space is left to the biofuels which reached the 3.1% of the TFEC.[15] As it is possible to see in Figure 2, the transportation field is the most behind in the transition to renewables in almost all the countries.[15]

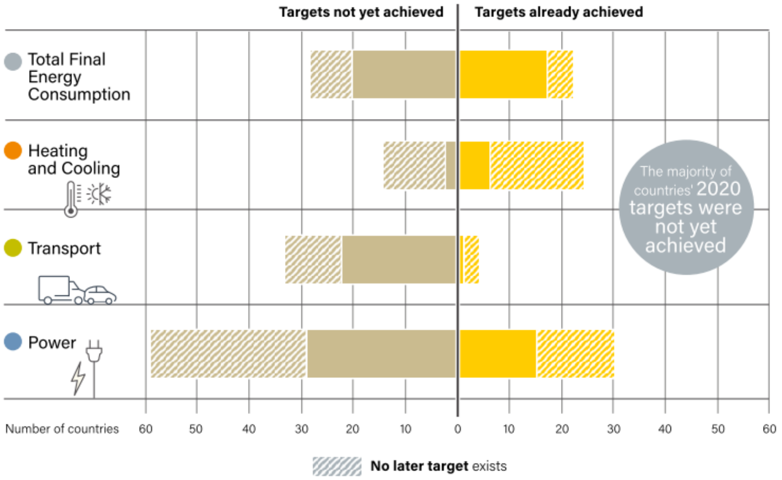

Figure 2: Schematic view of the number of countries that reached or not their 2020 Renewable Energy Targets in the different fields. Image from ref. 15.

In recent years, many car manufacturers have launched new cars that run on electricity or hydrogen, but often these do not come from renewable sources. Although electric cars are now a reality and scientists and industries are putting a lot of efforts into using renewable energy for charging stations, fossil fuels remain a more convenient choice, especially for heavy transport such as planes and boats.[17] In fact, they would need really large and heavy batteries that require many hours of recharging with respect to a car battery which, in the fastest models, recharges in about 30 min.[18] Hydrogen might be the alternative to oil in this field. In fact, filling a tank with hydrogen would take about the same time as using methane. It could be used as a fuel in internal combustion engines or fuel-cell driven cars. Moreover, 9.5 kg of hydrogen contain the same energy of 25 kg of gasoline and its combustion generates only water vapor as a by-product (Eq. 1.1).[19,20]

$$H_2\ (g) + \tfrac{1}{2}O_2\ (g) \rightarrow H_2O\ (l) + 286\ \text{kJ mol}^{-1} \qquad \text{(Eq. 1.1)}$$

1.2 Say "Hy" to the future: Hydrogen storage and production

Although hydrogen has the highest energy density per unit of mass (120 MJ/kg), its specific density is one order of magnitude lower than that of methane.[11] This means that it needs a tank 10 times larger than that of methane. At room temperature, uncompressed hydrogen occupies 11250 L kg^{-1}, pressurizing it into high-pressure (350 atm) steel tanks this is reduced to 56 L kg^{-1}.[20] To store it as gas such as liquefied petroleum gas or methane, it would need special large gas cylinders[21,22] that are a real problem for cars, but not so much for planes, trucks, or buses, which are already powered by hydrogen in many cities.[23] Another way to store hydrogen is to liquefy it but this requires a complex process as it has to be cooled to 20 K and about 30% of its energy is required to condense it.[20] Another drawback is that it must be stored at that low temperature to avoid possible evaporation and leakage. Insulation for liquid hydrogen tanks is usually expensive and delicate. Alternatively, it is possible to chemically store hydrogen in the form of metal hydrides.[24] The advantage of metal hydrides is the less space required compared to compressed hydrogen, and their tanks can also be integrated more easily into the vehicle as they are moldable.[25,26] The downside is their weight. The weight of the metal that the hydrogen binds to determines the weight of the tank. To store only 5 kg of hydrogen, a tank of several hundred kilos is needed.[20] Another possibility is the use of microporous metal organic framework (MOF) compounds. MOFs have a tunable porosity and framework structure, which can accommodate hydrogen molecules through physisorption and favorably desorb the adsorbed H_2 compared with other contemporary materials.[27] MOFs have demonstrated H_2 storage capabilities at cryogenic temperatures (77 K), but storage at acceptable pressures and ambient temperatures is still a challenge.[28] The last possibility is to store hydrogen with carbon nanotubes, which are lighter and their highly porous structure favors interaction between carbon atoms and gases. However, this technology is still in its infancy and much effort is still needed for a future industrial application as many factors regulate the hydrogen storage.[29] Currently, the compression of hydrogen in suitable tanks appears to be the best option for the transport sector due to its ease of carrying, ease of use, acceptable efficiency, and mature technology.[23,30-32]

In addition to the storage problem, there is the problem of finding hydrogen on Earth. Due to its low density, it easily escapes gravitational force.[20] However, hydrogen is one of the most abundant elements on our planet, due to its high ability to bind with other elements. Hydrogen is present in water and every living organism. It is also present in hydrocarbons and most other natural as well as artificial compounds.[20] For this reason, energy is needed to extract pure hydrogen from hydrogen-rich compounds. Hydrogen is only an energy carrier, and its clean or dirty designations depend on what is used to produce it. Currently the production methods are divided into two macro-areas: conventional methods and renewable ones. The former produce “grey hydrogen” and use fossil fuels as raw material, while the latter use energy from renewable sources to split water or biomass to generate "green hydrogen". Grey hydrogen is about 96% of the produced hydrogen, and comes principally from the steam hydrocarbons reforming reaction, which involves the generation of carbon dioxide as a side-product (Eq. 1.2).[33-36] This means that the emissions of carbon dioxide are not eliminated but only moved upstream. Thus, it immediately becomes clear that burning hydrocarbons in isolated areas to generate hydrogen for use as a clean fuel in metropolitan areas is an inefficient solution. The only way to achieve sustainability is to produce hydrogen more cleanly, using renewable sources.

$$C_nH_m + nH_2O \rightleftharpoons nCO + (n+\tfrac{1}{2}m)H_2$$

$$CO + H_2O \rightleftharpoons CO_2 + H_2$$

$$C_nH_m + 2nH_2O \rightleftharpoons nCO_2 + (2n+\tfrac{1}{2}m)H_2 \qquad \text{(Eq. 1.2)}$$

One method uses biofuels in a process similar to steam reforming, but, again, carbon dioxide represents the waste product of the process, and therefore makes this technique unsustainable.[37,38] Other studies have addressed the exploitation of biological processes of some algae to perform different types of bio-photolysis[39] and fermentations[40] by subjecting the algae to different illuminations and in some cases engineered inside bioreactors.[41] The main drawbacks of these biological processes are the high costs associated with low production efficiencies, but also the impossibility of obtaining pure molecular hydrogen, since other gases are often released, requiring a complicated separation of the gas mixture.[30,41,42] The main need to develop a hydrogen-powered society is to seek an alternative and sustainable method of producing it without obtaining secondary products that are harmful to the environment and to the humanity. The most prominent and sustainable solutions focus on water splitting

(Eq. 1.3). Indeed, water is one of the most abundant and inexhaustible materials on Earth.

$$2H_2O \xrightarrow{Energy} 2H_2 + O_2 \ \Delta G = 474 \text{ kJ mol}^{-1} \text{(Eq. 1.3)}$$

This is an endergonic reaction, which means that the energy required to take place will be stored into the chemical bonds of hydrogen and oxygen. This energy will be the same that hydrogen can generate by its combustion. One of the most common methods for splitting water is electrolysis, using an electrolytic cell. In this case, its anode and cathode are immersed in an aqueous solution in two different half-cells, producing oxygen and hydrogen. The energy needed to carry out the process can be generated both from non-renewable sources, such as fossil fuels, and from renewable sources such as solar, wind, or hydroelectric, thus obtaining green hydrogen.[43,44] Another very similar method is thermolysis, which involves the use of heat to decompose water into oxygen and hydrogen. Since more than 2770 K are required to carry out the reaction, several catalytic cycles with inexpensive metals such as copper and tin have been developed, to make the process more feasible at lower temperature (about 820 K) without releasing any GHG into the atmosphere.[34,45,46] Water splitting takes a lot of energy to occur. However, for the first law of thermodynamics, energy cannot be created, but only transferred from one form to another. Therefore, it is mandatory to find an energy source that can provide a continuous flow of energy without sustainability problems for present and future generations.

1.3 Here comes the Sun

Among all the renewable sources, solar radiation is the most promising. Sunlight is abundant, well distributed all over the planet and inexhaustible. The sun has an emission spectrum that can be approximated with a 5800 K blackbody, but as it is possible to see in Figure 3, the solar spectrum that reaches the upper portion of the atmosphere (dark grey) is very different from the one that reaches the Earth's surface (light grey). This effect is merely due to the presence of many particles in our atmosphere. These complex reflections, absorptions, scattering, and re-absorption effects make life on Earth possible. Our atmosphere prevents the highest energy radiation from reaching the surface and keeps the planet warm a comfortable 15 °C average temperature.[13]

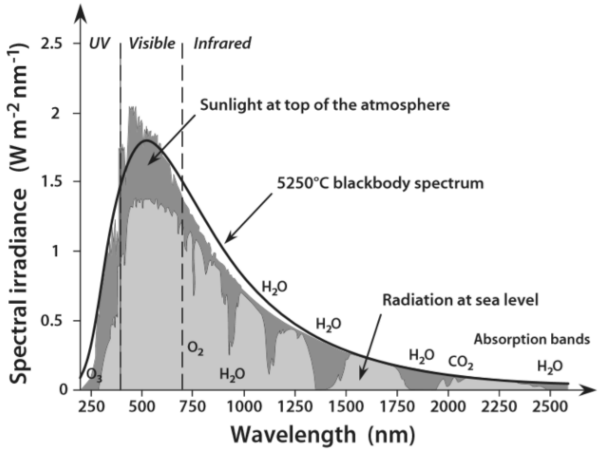

Figure 3: The solar radiation spectrum at the external boundary of the atmosphere (AM0, dark grey) compared to that at sea level (AM1.5, light grey). Imagine from ref 13.

Infrared radiation (IR) makes up about 50% the solar spectrum that reaches the Earth's surface, visible radiation (400-700 nm) is 45%, and ultraviolet radiation is about 5%.[13,47] For now, solar radiation is mainly used just for photovoltaic application, which allows the conversion of sunlight into electricity. Thankfully, the amount of renewable energy in this field is increasing every year, especially for wind and photovoltaics (Figure 4).[48]

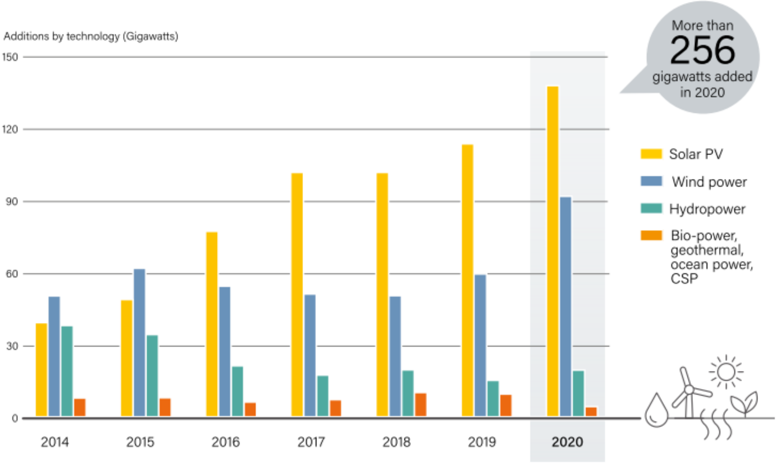

Figure 4: Annual additions of renewable power capacity by technology. Image from ref 15.

Every day, about 90 PW of solar radiation reaches the Earth's surface and feeds all the chemical and physical processes that keep our planet alive. The average primary energy consumption rate in 2018 was around 19 TW, which means that covering 0.16% of the surface of the Earth with solar panels would be enough to meet all of the global annual energy demand.[49,50] Italy would have to cover an area as large as the province of Piacenza to meet all its needs.[14] Perhaps by covering all the roofs of houses and industries throughout Italy, it would be possible. However, the problem is how to store all this energy and use it when needed. The real complications of photovoltaics are the continuous fluctuations and intermittence of solar radiation due to cloudy days and the day-night cycle.

Just a small portion of solar energy is used to sustain fundamental natural processes in the biosphere. Plants and algae capture only 1% of the solar radiation to perform photosynthesis. The amount of energy they consume daily is comparable to the energy stored in all the combined nuclear weapons of the world.[13] They transform hundreds of millions of tons of carbon dioxide into food and living tissue every single day. Plants and bacteria capture and convert light into biological material 100 times greater than the food needed for human sustenance.[51] For millennia, they have always done what the scientific community seeks. With photosynthesis, plants and bacteria split water in oxygen and hydrogen and fix carbon dioxide with the latter to obtain carbohydrates storing the solar energy into chemical bonds (Eq. 1.4).[52]

$$H_2O + CO_2 \xrightarrow{\text{Solar energy}} O_2 + \frac{1}{6}C_6H_{12}O_6 \quad \Delta E^{\circ} = 1.24\ V \quad (Eq.\ 1.4)$$

The energy required to perform water splitting corresponds to photons with a wavelength of about 1000 nm, belonging to the Near IR region. However, irradiation at shorter wavelengths is required to overcome the high activation barrier,[53] and only a small percent of solar photons possesses enough energy to succeed in this effort. Sunlight alone is not enough to drive the water splitting reaction, if it were possible, seas and rivers would no longer exist. Nevertheless, the real limit in the splitting of water for the development of a hydrogen-driven society is not the amount of solar radiation, but the device it needs: a catalyst to drive this reaction with high efficiencies. Nowadays, only 4% of the hydrogen produced is obtained by the splitting of water, using solar radiation as energy.[20] However, this technology suffers from the high cost of materials. These devices are often built with non-abundant elements, so the limiting reagents in the use of solar radiation are not photons, but atoms.[54]

1.4 Towards the artificial leaf

To develop a device, which mimics natural photosynthesis it is mandatory to follow nature. In chloroplasts, two large protein complexes, photosystem II (PS II) and photosystem I (PS I), various redox cofactors, and a hydrogenase enzyme compose this biological machinery (Figure 5).[52]

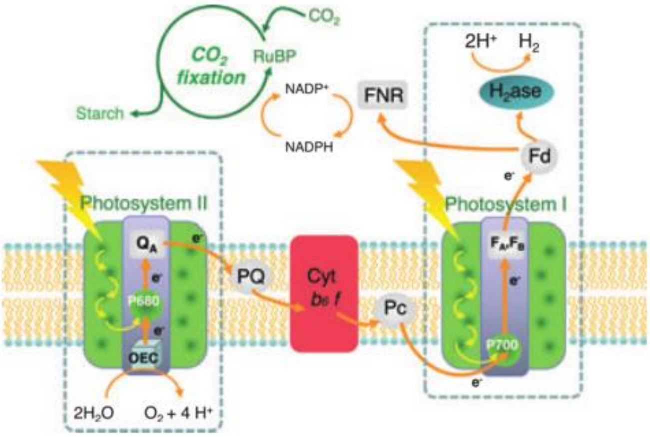

Figure 5: Schematic representation of the photosynthesis chain. Image from ref 55.

Natural photosynthesis can be divided into three stages. The first is the harvest of light and generation of local electron/hole pairs in PS II and PS I. The second is the proton-coupled electron transfer between redox cofactors along the photosynthetic chain by transferring the electron into PS I and leaving the hole in PS II. Finally, the third step is the multi-electronic redox catalysis, which generates molecular oxygen at the PS II thanks to the oxygen-evolving $CaMn_4$ center and molecular hydrogen in the binuclear metal clusters of the hydrogenase.[55] Then, hydrogen is used to fix carbon dioxide in the Calvin cycle. Although the efficiency of this system is low, the principle is incredible. First, antenna systems collect solar radiation and convert it into chemical energy. Second, the electron transfer chain to the PS I avoids the occurrence of charge recombination events. In the end, a second light-harvesting process occurs at PS I, thus providing additional energy to the electrons to perform the Calvin cycle or reduction at the hydrogenase.[55]

The standard potential ΔE° of water splitting or water electrolysis to H_2 and O_2 is 1.23 V at any pH (Eq. 1.3) and the analysis of the potential for the natural photosynthesis reaction (Eq. 1.4) shows that water splitting is the heart of the solar energy storage. Carbon dioxide fixation contributes only 0.01 eV in the storage of energy.[56] Hence, the production of carbohydrates is only a method that nature uses to store the hydrogen produced by the water spitting reaction. Consequently, the key to mimicking photosynthesis lies in obtaining sun-driven water splitting by a direct method. Once scientists become proficient in this, hydrogen could be used to produce synthetic fuels such as methane, methanol, isopropanol, etc., from cheap carbon-rich compounds like carbon dioxide. These new synthetic fuels will gain a zero-carbon footprint on the environment as they derive from atmospheric carbon dioxide, starting a carbon neutral cycle (Figure 6).

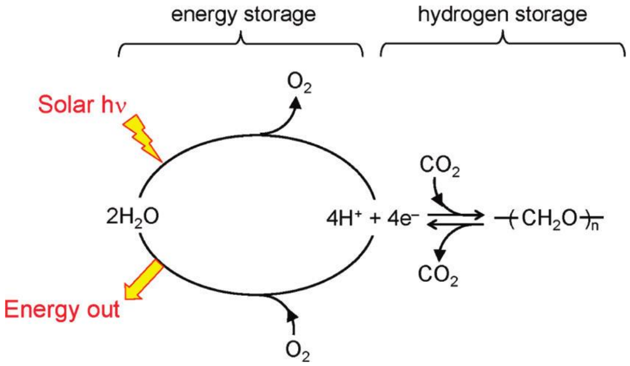

Figure 6: Schematic cycle of the transformation of solar radiation into chemical energy and storage into carbohydrates. Image from ref 56.

To focus on the conversion of solar energy, essentially three new technologies deal with the sun-driven water splitting: photovoltaics associated with an electrolytic cell, photocatalysis (PC), and photoelectrochemical cells (PEC). They are integrated systems made with cheap materials that can obtain hydrogen at a competitive price. This thesis investigates only two of these devices, as they are the most innovative technologies in the field of artificial photosynthesis and focuses on the molecular structures used in these devices.

In the next sections, I will first focus on the main aspects of PC and my research in this field, then I will move to the general aspects of PEC and I will present three chapters showing the development of four different PEC systems ruled by different interactions. The last chapter of this section presents the work I did in collaboration with the Yale University during my abroad period. Finally, I will conclude with a short overview regarding all these techniques and the work done during these three years.

References

1 UN. Paris Agreement. (Secretary-General of the United Nations, Paris, **2015**).

2 Anderson, T. R., Hawkins, E. & Jones, P. D. (**2016**) CO_2, the greenhouse effect and global warming: from the pioneering work of Arrhenius and Callendar to today's Earth System Models. *Endeavour,* **40**, 178-187, doi:10.1016/j.endeavour.2016.07.002.

3 M.R. Allen, O.P. Dube, W. Solecki, F. Aragón-Durand, W. Cramer, S. Humphreys, M. Kainuma, J. Kala, N. Mahowald, Y. Mulugetta, R. Perez, M. Wairiu & Zickfeld, K. in *Global Warming of 1.5 °C. An IPCC Special Report on the impacts of global warming of 1.5 °C above pre-industrial levels and related global greenhouse gas emission pathways, in the context of strengthening the global response to the threat of climate change, sustainable development, and efforts to eradicate poverty* (eds V. Masson-Delmotte, P. Zhai, H.-O. Pörtner, D. Roberts, J. Skea, P.R. Shukla, A. Pirani, W. Moufouma-Okia, C. Péan, R. Pidcock, S. Connors, J.B.R. Matthews, Y. Chen, X. Zhou, M.I. Gomis, E. Lonnoy, T. Maycock, M. Tignor, and T. Waterfield) (Geneva, Switzerland, **2018**).

4 IPCC. Summary for Policymakers. 32 (World Meteorological Organization, Geneva, Switzerland, **2018**).

5 Dincer, I. & Acar, C. (**2015**) A review on clean energy solutions for better sustainability. *Int. J. Energy Res.,* **39**, 585-606, doi:10.1002/er.3329.

6 UN. The Sustainable Development Goals Report. (New York, USA, **2019**).

7 Lacis, A. A., Schmidt, G. A., Rind, D. & Ruedy, R. A. (**2010**) Atmospheric CO_2: Principal Control Knob Governing Earth’s Temperature. *Science,* **330**, 356-359, doi:10.1126/science.1190653.
8 Armaroli, N. & Balzani, V. (**2016**) Solar Electricity and Solar Fuels: Status and Perspectives in the Context of the Energy Transition. *Chem. Eur. J.,* **22**, 32-57, doi:10.1002/chem.201503580.
9 Armaroli, N. & Balzani, V. (**2011**) The legacy of fossil fuels. *Chem. Asian J.,* **6**, 768-784, doi:10.1002/asia.201000797.
10 Armaroli, N. & Balzani, V. (**2007**) The future of energy supply: Challenges and opportunities. *Angew. Chem. Int. Ed.,* **46**, 52-66, doi:10.1002/anie.200602373.
11 Ren, J., Musyoka, N. M., Langmi, H. W., Mathe, M. & Liao, S. (**2017**) Current research trends and perspectives on materials-based hydrogen storage solutions: A critical review. *Int. J. Hydrogen Energy,* **42**, 289-311, doi:10.1016/j.ijhydene.2016.11.195.
12 Dukes, J. S. (**2003**) Burning Buried Sunshine: Human Consumption of Ancient Solar Energy. *Clim. Change,* **61**, 31-44, doi:10.1023/A:1026391317686.
13 Armaroli, N. & Balzani, V. *Energy for a Sustainable World.* (Wiley-VCH Verlag GmbH & Co. KGaA: Weinheim, Germany **2010**)
14 Armaroli, N. & Balzani, V. *Energia per l'astronave Terra.* (Zanichelli: Bologna, Italy **2008**)
15 REN21. Renewables 2021 Global Status Report. (REN21 Secretariat, Paris, **2021**).
16 International Energy Agency, https://www.iea.org/
17 Dominković, D. F., Bačeković, I., Pedersen, A. S. & Krajačić, G. (**2018**) The future of transportation in sustainable energy systems: Opportunities and barriers in a clean energy transition. *Renewable Sustainable Energy Rev.,* **82**, 1823-1838, doi:10.1016/j.rser.2017.06.117.
18 Domínguez-Navarro, J. A., Dufo-López, R., Yusta-Loyo, J. M., Artal-Sevil, J. S. & Bernal-Agustín, J. L. (**2019**) Design of an electric vehicle fast-charging station with integration of renewable energy and storage systems. *Int. J. Electr. Power Energy Syst.,* **105**, 46-58, doi:10.1016/j.ijepes.2018.08.001.
19 Kaur, M. & Pal, K. (**2019**) Review on hydrogen storage materials and methods from an electrochemical viewpoint. *J. Energy Storage,* **23**, 234-249, doi:10.1016/j.est.2019.03.020.
20 Armaroli, N. & Balzani, V. (**2011**) The hydrogen issue. *ChemSusChem,* **4**, 21-36, doi:10.1002/cssc.201000182.
21 Zheng, J., Liu, X., Xu, P., Liu, P., Zhao, Y. & Yang, J. (**2012**) Development of high pressure gaseous hydrogen storage technologies. *Int. J. Hydrogen Energy,* **37**, 1048-1057, doi:10.1016/j.ijhydene.2011.02.125.
22 Liu, Z., You, H.-x., Liu, P.-q., Li, C., Peng, L., Zhao, C. & Dai, X.-t. (**2019**) Novel multi-center concave bottom for hydrogen storage cylinder. *Int. J. Hydrogen Energy,* **44**, 12003-12009, doi:10.1016/j.ijhydene.2019.03.030.
23 Moradi, R. & Groth, K. M. (**2019**) Hydrogen storage and delivery: Review of the state of the art technologies and risk and reliability analysis. *Int. J. Hydrogen Energy,* **44**, 12254-12269, doi:10.1016/j.ijhydene.2019.03.041.
24 Sakintuna, B., Lamari-Darkrim, F. & Hirscher, M. (**2007**) Metal hydride materials for solid hydrogen storage: A review. *Int. J. Hydrogen Energy,* **32**, 1121-1140, doi:10.1016/j.ijhydene.2006.11.022.
25 Lototskyy, M., Tolj, I., Klochko, Y., Davids, M. W., Swanepoel, D. & Linkov, V. (**2020**) Metal hydride hydrogen storage tank for fuel cell utility vehicles. *Int. J. Hydrogen Energy,* **45**, 7958-7967, doi:10.1016/j.ijhydene.2019.04.124.
26 Abe, J. O., Popoola, A. P. I., Ajenifuja, E. & Popoola, O. M. (**2019**) Hydrogen energy, economy and storage: Review and recommendation. *Int. J. Hydrogen Energy,* **44**, 15072-15086, doi:10.1016/j.ijhydene.2019.04.068.

27 Corgnale, C., Hardy, B., Chahine, R., Zacharia, R. & Cossement, D. (**2019**) Hydrogen storage in a two-liter adsorbent prototype tank for fuel cell driven vehicles. *Appl. Energy,* **250**, 333-343, doi:10.1016/j.apenergy.2019.05.055.

28 Gangu, K. K., Maddila, S., Mukkamala, S. B. & Jonnalagadda, S. B. (**2019**) Characteristics of MOF, MWCNT and graphene containing materials for hydrogen storage: A review. *J. Energy Chem.,* **30**, 132-144, doi:10.1016/j.jechem.2018.04.012.

29 Yang, L., Yu, L. L., Wei, H. W., Li, W. Q., Zhou, X. & Tian, W. Q. (**2019**) Hydrogen storage of dual-Ti-doped single-walled carbon nanotubes. *Int. J. Hydrogen Energy,* **44**, 2960-2975, doi:10.1016/j.ijhydene.2018.12.028.

30 Abdalla, A. M., Hossain, S., Nisfindy, O. B., Azad, A. T., Dawood, M. & Azad, A. K. (**2018**) Hydrogen production, storage, transportation and key challenges with applications: A review. *Energy Convers. Manage.,* **165**, 602-627, doi:10.1016/j.enconman.2018.03.088.

31 Niaz, S., Manzoor, T. & Pandith, A. H. (**2015**) Hydrogen storage: Materials, methods and perspectives. *Renewable Sustainable Energy Rev.,* **50**, 457-469, doi:10.1016/j.rser.2015.05.011.

32 Purewal, J., Veenstra, M., Tamburello, D., Ahmed, A., Matzger, A. J., Wong-Foy, A. G., Seth, S., Liu, Y. & Siegel, D. J. (**2019**) Estimation of system-level hydrogen storage for metal-organic frameworks with high volumetric storage density. *Int. J. Hydrogen Energy,* **44**, 15135-15145, doi:10.1016/j.ijhydene.2019.04.082.

33 Sinigaglia, T., Lewiski, F., Santos Martins, M. E. & Mairesse Siluk, J. C. (**2017**) Production, storage, fuel stations of hydrogen and its utilization in automotive applications-a review. *Int. J. Hydrogen Energy,* **42**, 24597-24611, doi:10.1016/j.ijhydene.2017.08.063.

34 Nikolaidis, P. & Poullikkas, A. (**2017**) A comparative overview of hydrogen production processes. *Renewable Sustainable Energy Rev.,* **67**, 597-611, doi:10.1016/j.rser.2016.09.044.

35 Iulianelli, A., Liguori, S., Wilcox, J. & Basile, A. (**2016**) Advances on methane steam reforming to produce hydrogen through membrane reactors technology: A review. *Cat. Rev.,* **58**, 1-35, doi:10.1080/01614940.2015.1099882.

36 Rostrup-Nielsen, J. R. in *Catalysis: Science and Technology Volume 5* (eds John R. Anderson & Michel Boudart) (Springer Berlin Heidelberg: Berlin, Germany, **1984**), 1-117.

37 Profeti, L. P. R., Ticianelli, E. A. & Assaf, E. M. (**2009**) Production of hydrogen via steam reforming of biofuels on Ni/CeO_2-Al_2O_3 catalysts promoted by noble metals. *Int. J. Hydrogen Energy,* **34**, 5049-5060, doi:10.1016/j.ijhydene.2009.03.050.

38 Slinn, M., Kendall, K., Mallon, C. & Andrews, J. (**2008**) Steam reforming of biodiesel by-product to make renewable hydrogen. *Bioresour. Technol.,* **99**, 5851-5858, doi:10.1016/j.biortech.2007.10.003.

39 Morales-Martínez, T. K., Medina-Morales, M. A., Ortíz-Cruz, A. L., Rodríguez-De la Garza, J. A., Moreno-Dávila, M., López-Badillo, C. M. & Ríos-González, L. (**2020**) Consolidated bioprocessing of hydrogen production from agave biomass by Clostridium acetobutylicum and bovine ruminal fluid. *Int. J. Hydrogen Energy,* **45**, 13707-13716, doi:10.1016/j.ijhydene.2019.11.089.

40 Cabrol, L., Marone, A., Tapia-Venegas, E., Steyer, J.-P., Ruiz-Filippi, G. & Trably, E. (**2017**) Microbial ecology of fermentative hydrogen producing bioprocesses: useful insights for driving the ecosystem function. *FEMS Microbiol. Rev.,* **41**, 158-181, doi:10.1093/femsre/fuw043.

41 Show, K.-Y., Yan, Y., Ling, M., Ye, G., Li, T. & Lee, D.-J. (**2018**) Hydrogen production from algal biomass – Advances, challenges and prospects. *Bioresour. Technol.,* **257**, 290-300, doi:10.1016/j.biortech.2018.02.105.

42 Das, D. & Veziroǧlu, T. N. (**2001**) Hydrogen production by biological processes: a survey of literature. *Int. J. Hydrogen Energy,* **26**, 13-28, doi:10.1016/S0360-3199(00)00058-6.

43 Chi, J. & Yu, H. (**2018**) Water electrolysis based on renewable energy for hydrogen production. *Chin. J. Catal.,* **39**, 390-394, doi:10.1016/S1872-2067(17)62949-8.

44 Ju, H., Badwal, S. & Giddey, S. (**2018**) A comprehensive review of carbon and hydrocarbon assisted water electrolysis for hydrogen production. *Appl. Energy,* **231**, 502-533, doi:10.1016/j.apenergy.2018.09.125.

45 E. Funk, J. (**2001**) Thermochemical hydrogen production: past and present. *Int. J. Hydrogen Energy,* **26**, 185-190, doi:10.1016/S0360-3199(00)00062-8.

46 Dincer, I. & Acar, C. (**2015**) Review and evaluation of hydrogen production methods for better sustainability. *Int. J. Hydrogen Energy,* **40**, 11094-11111, doi:10.1016/j.ijhydene.2014.12.035.

47 Kondratyev, K. Y. *Radiation in the Atmosphere.* (Academic Press: New York/London, **1969**)

48 REN21. Renewables 2019 Global Status Report. (REN21 Secretariat, Paris, **2019**).

49 Service, R. F. (**2005**) Is It Time to Shoot for the Sun? *Science,* **309**, 548-551, doi:10.1126/science.309.5734.548.

50 Petroleum, B. BP Statistical Review of World Energy (**2019**).

51 Barber, J. & Andersson, B. (**1994**) Revealing the blueprint of photosynthesis. *Nature,* **370**, 31-34, doi:10.1038/370031a0.

52 Barber, J. & Tran, P. D. (**2013**) From natural to artificial photosynthesis. *J. R. Soc., Interface,* **10**, 20120984, doi:10.1098/rsif.2012.0984.

53 Wang, Y., Suzuki, H., Xie, J., Tomita, O., Martin, D. J., Higashi, M., Kong, D., Abe, R. & Tang, J. (**2018**) Mimicking Natural Photosynthesis: Solar to Renewable H_2 Fuel Synthesis by Z-Scheme Water Splitting Systems. *Chem. Rev.,* **118**, 5201-5241, doi:10.1021/acs.chemrev.7b00286.

54 Smil , V. *Energy at the Crossroads: Global Perspectives and Uncertainties*. (MIT Press: Cambridge, MA, **2003**)

55 Andreiadis, E. S., Chavarot-Kerlidou, M., Fontecave, M. & Artero, V. (**2011**) Artificial Photosynthesis: From Molecular Catalysts for Light-driven Water Splitting to Photoelectrochemical Cells. *Photochem. Photobiol.,* **87**, 946-964, doi:10.1111/j.1751-1097.2011.00966.x.

56 Nocera, D. G. (**2012**) The artificial leaf. *Acc. Chem. Res.,* **45**, 767-776, doi:10.1021/ar2003013.

Chapter 2: Photocatalysis

2.1 General aspects

The heart of heterogeneous PC is the semiconductor (SC). A semiconductor must have defined energy levels to perform both the water oxidation reaction (Eq. 2.1) and the hydrogen evolution reaction (Eq. 2.2).

$$2H_2O \rightarrow 4H^+ + O_2 + 4e^- \qquad \text{(Eq. 2.1)}$$

$$2H^+ + 2e^- \rightarrow H_2 \qquad \text{(Eq. 2.2)}$$

Its conduction band (CB) must be at a more negative potential than the potential of the reduction reaction from protons to hydrogen (0 V vs NHE, pH 0) and its valence band (VB) must be at a more positive potential than the potential of the water oxidation (1.23 V vs NHE, pH 0).[1] Therefore, it must present a bandgap of at least 1.23 eV, but in practice, this value rises to 2.0-2.4 eV, due to kinetic overpotentials and energy losses during the process. Large bandgap SC (more than 3 eV) such as TiO_2 and graphitic carbon nitride g-C_3N_4 may be suitable for driving the overall water-splitting process. However, due to their large bandgaps, they absorb only a modest part of the solar radiation, which belongs to the UV region. Some SC, such as Fe_2O_3 (2.2 eV) and Cu_2O (2.0-2.2 eV), have smaller bandgaps, which allow a broader absorption in the visible region, but their CB and VB are not in the correct position to drive the overall water-splitting process alone (Figure 7). Indeed, the CB of Cu_2O is in the correct position to guide the proton reduction reaction but its VB is at not enough positive potential to favor the oxidation of water. On the other hand, Fe_2O_3 has a VB positive enough to perform the oxidation of water, but a CB which is too positive to drive the reduction of the protons. Consequently, these materials can only be used for one of the half-reactions: photo-driven water oxidation or hydrogen evolution. It is possible to connect these two SC with a redox couple (IO_3^-/I^-, Fe^{2+}/Fe^{3+}, etc.) to obtain a tandem configuration, quite similar to the Z scheme of the PS II and PS I (Figure 8). However, in this case, the energy of two photons is required to generate the electron/hole couple on both SCs, thus the efficiency of the charge separation reaction drops to 50%.[2]

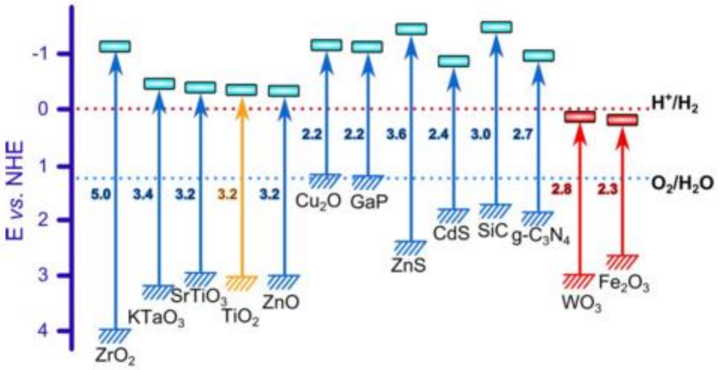

Figure 7: Bandgap energies and band position of several SCs respect to the redox potentials of water splitting relative to the NHE at pH 0. Image from ref 3.

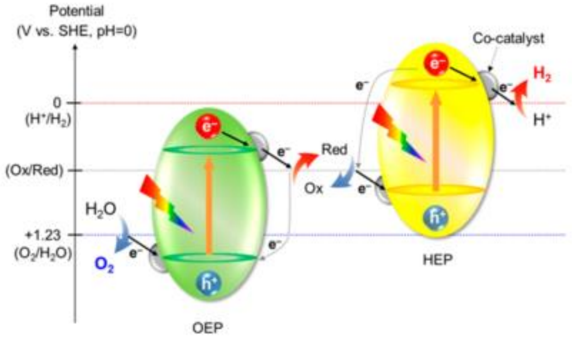

[a]Two dotted curves indicate the back reactions which should be suppressed.

Figure 8: A Z-scheme tandem configuration composed by two SCs connected through a redox couple. Image from ref 2.

A big problem with PC is the charge recombination reactions. The electron and the hole, generated after photoexcitation, must carry out the reduction and oxidation reactions respectively and not neutralize each other. It is indispensable to suppress these undesirable reactions to obtain the maximum photon-to-energy efficiency. To improve charge separation, it is possible to combine one SC with another by creating a pn junction system, which has demonstrated higher activity due to the more intimate contact between the SCs, compared to simply mixing of the two powders.[4,5] Another way to promote charge separation is to combine the SC with an electron acceptor, such as carbon nanotubes, graphene layers, or fullerenes to attract the excited electrons to particular points on the surface, and confine them to its ultrathin layer.[3,6,7] The morphology of photocatalysts also influences the properties, and generally, smaller particle sizes or higher crystallinity yield better performance. For this, it is possible to tune the intrinsic conductivity of SC by doping with other elements or by deleting the surface defects with the application of a thin oxide layer.[1,2] Finally, one last way is to reduce the time in which the charges remain free on the SC and thus speed up the redox reactions. Therefore, it is advisable to add suitable catalysts for both reactions on the SC surface. The main role of these catalysts is to improve charge separation to facilitate the surface chemical reactions. The water oxidation catalyst (WOC) extracts the generated holes and uses them to oxidize water, while the hydrogen evolution catalyst (HEC) extracts the generated electrons and uses them to reduce protons. The WOC and the HEC can be either molecular organometallic compounds bound to the SC surface[8] or small metal nanoparticles, like Au, Pt, or Pd, adsorbed onto the SC.[9,10]

In literature, new approaches are under investigation to substitute traditional metal oxide SC (such as Cu_2O, TiO_2, Fe_2O_3,

WO_3, $BiVO_4$)[11] with carbon nitride-based nanomaterials and MOF structures.[6,12] However, among the traditional metal oxide SCs used in PC, titanium dioxide exhibits the best characteristics for a possible industrial application, due to its non-toxicity, its cost-effectiveness, and its high chemical stability. However, it presents a large bandgap (~3.2 eV) which limits its optical absorption only in the UV region.[3] To overcome this limit, it is possible to decorate the surface with a suitable photosensitizer, to broaden the absorption spectrum into the visible region. When a photosensitizer decorates the SC surface, dye-sensitized PC (DSPC) is defined.[13] As in the case of natural photosynthesis, DSPC is composed of three main elements: a photosensitizer, a SC, and a catalyst. The first absorbs the light and excites an electron generating the electron/hole pair, like the antenna systems. The second transfers the electrons to the catalytic center, like the electron transfer chain, and the last activates the redox reaction, like the manganese clusters and hydrogenases. The advantage of these devices is the possibility of design and optimizing each component one at a time.[2,14] However, this device presents a big problem. Performing pure water splitting evolves a complex gas blend of oxygen and hydrogen, since there is no physical separation between the two-redox cores. Furthermore, the oxidation of water is the real bottleneck (Eq. 2.1), since four holes are required to develop one mole of molecular oxygen. Hence, to avoid these problems, it is possible to study and optimize one half-reaction at a time, using a sacrificial electron donor (SED) or a sacrificial electron acceptor (SEA), which is oxidized instead of water or reduced instead of protons respectively. The redox of SED and SEA is typically a monoelectronic reaction that simplifies the electron transfer and speeds up the other half-reaction. However, to avoid further contamination of the aqueous media with oxidized SED or reduced SEA, benchmark compounds are used for this purpose, like triethanolamine, methyl orange, ethylenediaminetetraacetic acid (EDTA), etc.[15] These compounds are similar to the most well-known emerging organic contaminants present in waters.[16] Thus the development of a device capable of converting organic pollutants into molecular hydrogen while purifying waters, is noteworthy.[17,18] Here, I will limit myself to commenting on some of the main photosensitizers used in this field in combination with different SED showing the parameters and the characteristics that I have considered during my work.

2.2 Working principles and important parameters in DSPC

In DSPC, the general steps involved in the process are the following:

Photoexcitation:

$$Pt/TiO_2/dye \xrightarrow{h\nu} Pt/TiO_2/dye* \quad (1)$$

Oxidative quenching:

$$Pt/TiO_2/dye* \rightarrow Pt/TiO_2(e^-)/dye^+ \quad (2)$$

$$Pt/TiO_2(e^-)/dye^+ + SED \rightarrow Pt/TiO_2(e^-)/dye + SED^+ \quad (3)$$

Reductive quenching:

$$Pt/TiO_2/dye* + SED \rightarrow Pt/TiO_2/dye^{\cdot-} + SED^+ \quad (4)$$

$$Pt/TiO_2/dye^{\cdot-} \rightarrow Pt/TiO_2(e^-)/dye \quad (5)$$

Proton reduction:

$$Pt(e^-)/TiO_2/dye + H^+ \rightarrow Pt/TiO_2/dye + \tfrac{1}{2}H_2 \quad (6)$$

Recombination reactions:

$$Pt/TiO_2/dye* \rightarrow Pt/TiO_2/dye + h\nu \quad (7)$$

$$Pt/TiO_2(e^-)/dye^+ \rightarrow Pt/TiO_2/dye \qquad (8)$$

First, the dye is the responsible for the light harvesting of the system, thus it collects the photon, exciting an electron and becoming dye* (1). Then, two mechanisms are proposed to restore the ground state of the dye. One is oxidative quenching in which the excited electron is transferred to the titanium dioxide (2) and the hole, which remains in the HOMO of dye, catalyzes the oxidation of the SED (3). The other is a reductive quenching in which dye* first oxidizes the SED, becoming a radical anion ($dye^{\cdot -}$, 4), and then transfers the excited electron into the SC (5). In the end, the last step is the reduction of the protons, where the electron trapped in the platinum nanoparticles adsorbed onto the SC generates molecular hydrogen (6). Typically, the oxidative quenching mechanism is predominant, while the reductive quenching is performed only by poorly reducing cationic dyes, such as methylene blue and thionine, and exhibits the lowest hydrogen generation yields.[10,19] In addition to these mechanisms, other detrimental charge recombination reactions can occur limiting the activity of the system. The most common can be the relaxation of the dye to the ground state after excitation (7) and the quenching between the electron injected into the SC and the cationic dye due to a slow hydrogen production or slow dye regeneration (8).[10,13]

The Pt/TiO_2/dye photocatalytic device is typically prepared starting from titanium dioxide nanoparticles where platinum nanoparticles are deposited by impregnation or photodeposition from H_2PtCl_6 under UV irradiation. The Pt/TiO_2 assembly is then suspended in a dye solution for a few hours in the dark to avoid the dye photodegradation. The dye-sensitized nanoparticles are separated after centrifugation, washed with clean solvent, and then dried under nitrogen flow. UV-vis spectroscopy of the solution pre-and post- sensitization is typically used to measure the dye loading. Once the catalytic system is ready, it is suspended in an aqueous buffer solution containing the SED and degassed with inert gases to remove all the oxygen present. The photoreactor is then irradiated with visible light to avoid direct excitation of the TiO_2 electrons. The evolved gas is typically quantified using gas-chromatography (Figure 9).[20]

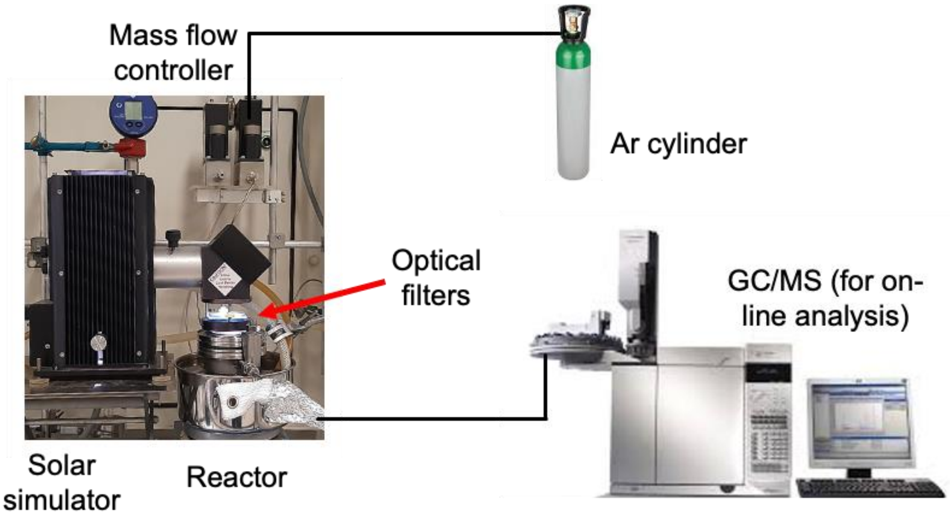

Figure 9: Schematic and pictorial representation of the photocatalytic reactor.

The simplest way to assess the activity of the photosystems is to estimate the amount of hydrogen produced over time. This parameter is typically on the order of µmol, and it is normalized to the mass of the photocatalyst (µmol g^{-1}). Moreover, the hydrogen evolution rate (µmol g^{-1} h^{-1}) is also typically present to evaluate the stability of the photosystem. A key parameter in PC is the turnover number (TON) which is the ratio between the number of electrons generated that produced hydrogen and the number of active sites in the system (Eq. 2.3). The ideal photocatalyst should have an infinite TON. However, since it is difficult, it is sufficient for this number to be higher than one, which means that the number of used electrons is higher than the active catalytic sites.

$$TON = \frac{number\ of\ electrons\ that\ produced\ hydrogen}{numer\ of\ active\ photocatalytic\ sites} \quad \text{(Eq. 2.3)}$$

Since the number of active sites is complicated to measure, in DSPC it can be compared with the amount of dye loaded onto the nanoparticles and the number of the electrons that produced hydrogen is equal to double the amount of evolved hydrogen, hence, the TON equation can be written as follows (Eq. 2.4).

$$TON = \frac{2 \times moles\ of\ evolved\ hydrogen}{moles\ of\ dye\ loaded} \quad \text{(Eq. 2.4)}$$

Because the amount of hydrogen also depends on the time of the experiment, a clearer parameter is the turnover frequency (TOF) that is the rate per active site (Eq. 2.5).

$$TOF = \frac{TON}{time\ of\ the\ experiment} \quad \text{(Eq. 2.5)}$$

However, TON, and thus TOF, depend on all the conditions of the experiment, like temperature, intensity of the irradiation, and wideness of the light spectrum. Therefore, the quantum yield is the most useful parameter for comparing all systems. It evaluates the number of electrons that effectively produced hydrogen with respect to the number of incident photons. Since not all the incident photons are effectively adsorbed, this parameter is called apparent quantum yield (AQY, Eq. 2.6 and Eq. 2.7).

$$AQY = \frac{number\ of\ electrons\ that\ produced\ hydrogen}{numer\ of\ incident\ photons} \quad \text{(Eq. 2.6)}$$

$$AQY = \frac{2 \times moles\ of\ evolved\ hydrogen}{numer\ of\ incident\ photons} \quad \text{(Eq. 2.7)}$$

The number of incident photons can be measured using a silicon photodiode placed in the photoreactor. This value is easier to be recorded with a monochromatic light source, and the typically used wavelength is the λ_{max} of the absorption spectrum of the dye.

For a photosensitizer, it is also important to evaluate the light harvesting efficiency (LHE). The LHE is defined as the fraction of light intensity adsorbed by the photosensitizer at every wavelength (Eq. 2.8).[21]

$$LHE(\lambda) = A(\lambda) = \frac{I_A(\lambda)}{I_0(\lambda)} \qquad \text{(Eq. 2.8)}$$

Where $A(\lambda)$ is the absorptance, $I_A(\lambda)$ is the absorbed light intensity and $I_0(\lambda)$ is the incident light intensity.

In the end, a last important parameter is the light-to-fuel efficiency (LFE) that indicates the efficiency of the conversion of the solar radiation into the chemical bonds of the molecular hydrogen or other solar fuels (Eq. 2.9).

$$LFE = \frac{F_{H_2} \times \Delta H^{\circ}{}_{H_2}}{S \times A_{irr}} \qquad \text{(Eq. 2.9)}$$

Here, F_{H_2} is the flow of hydrogen produced (mol s^{-1}), $\Delta H^{\circ}{}_{H_2}$ is the enthalpy associated with the hydrogen combustion (2.85×10^5 J mol^{-1}), S is the total incident light irradiance (W cm^{-2}) and A_{irr} is the irradiated area (cm^2). LFE is typically below 1%, comparable to the low efficiency of natural photosynthesis (0.1-1%).

All these parameters depend on the experimental conditions, and it is important to first check them before comparing the performances among different studies.

In the next section, I will analyze the most important photosensitizers used in DSPC showing the advantages and the drawbacks of each design.

2.3 Photosensitizers for DSPC

A good photosensitizer should adsorb a large portion of the solar radiation, efficiently convert the photons into hole/electron pairs, allow a faster charge transfer to the catalytic centers while avoiding charge recombination reactions, and bind strongly to the SC surface to increase the stability of the device.[10]

In many examples, the design of the most efficient dyes has multiple anchor groups to prevent dye desorption. Carboxylic acids are the most common anchoring group, especially for titanium dioxide, as they can covalently bind to it by forming an ester linkage with titanium atoms.[10] However, they are also subject to easy hydrolysis in aqueous media where PC functions. Other diffuse anchor groups include phosphonic and hydroxamic acids, which provide long-term stable bonds. However, the synthesis of these groups typically increases the number of synthetic steps and the difficulty of purifying the final compounds. Moreover, although the phosphonic group enhances the stability of the device, it drastically reduces the capability of fast charge transfer due to its tetrahedral geometry and subsequent loss of conjugation.[22]

In addition to the anchoring stability, the position of the energy levels is also important for a photosensitizer. The excited electron should pass from the lowest unoccupied molecular orbital (LUMO) to the CB of the SC and then be transferred to the HEC core. It is thus mandatory that the LUMO stays at higher energies with respect to the CB to allow the charge transfer. On the other side, the hole, which remains in the highest occupied molecular orbital (HOMO) should be neutralized by an electron coming from water or SED oxidation. Hence, the HOMO should remain at lower energies (or more positive potentials) than the redox potential of the SED or the water oxidation reaction.[10,13]

The photosensitizer can have either an organometallic or an organic nature. The former obtains a higher efficiency, but they suffer from high cost due to the presence of expensive metals, greater toxicity due to the metal centers and difficulties in tuning the energy levels. In literature, the main examples of these molecules are ruthenium-based (Figure 10). Two or three bipyridine groups functionalized in different ways coordinate to the ruthenium core. They always present at least one or two carboxylic or phosphonic anchoring groups for binding to the SC since a stronger bond with the surface increases the photocatalytic activity.[23-25] In **GS12**, a terpyridine and a phosphonite ligand complex with the ruthenium center, significantly expanding the light absorption of the molecule (Figure 10). This photosensitizer obtained a TOF of about 1075 h^{-1} under 2-Sun irradiation.[26] Another complex (**MC113**, Figure 10) used thiocyanate ligands which increased the catalytic activity under visible light irradiation.[27] Other attempts using binuclear ruthenium complexes (**Ru2**, Figure 10) have shown high catalytic activity due to both “the antenna effect” driven by a metal-to-metal charge transfer process, and a loose anchoring on the titanium dioxide which established a dynamic absorption equilibrium, resulting in minimized charge recombination.[28] Only a few examples of organometallic dyes based on metal centers other than ruthenium have been investigated (Figure 10). Among these, an asymmetric zinc phthalocyanine (**Zn-*tri*-PcNc**, Figure 10) is characterized by a push-pull structure to generate a more efficient charge separation.[29] This dye showed a wide absorption spectrum through the near-IR region and good results in gas evolution and stability.

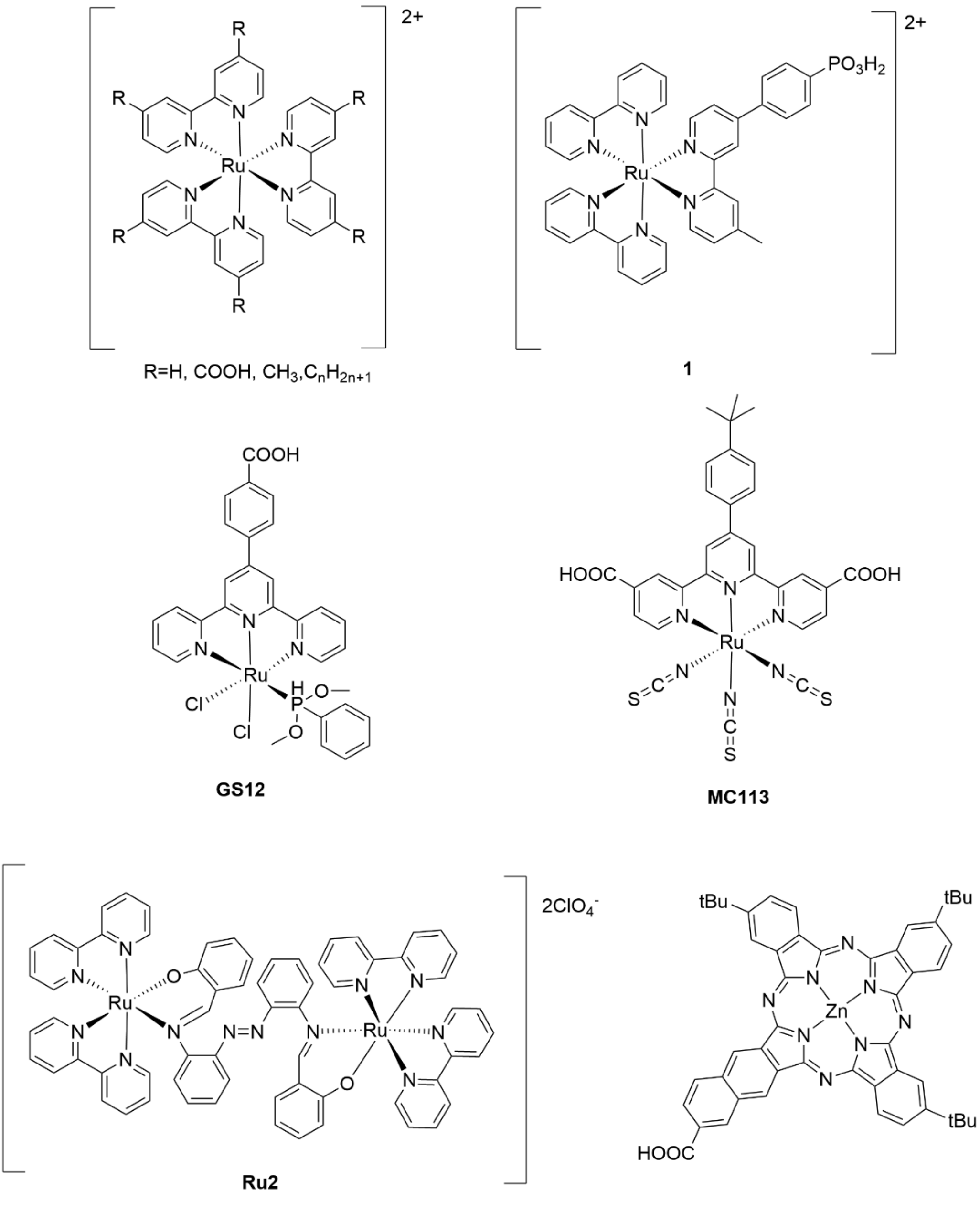

R=H, COOH, CH_3,C_nH_{2n+1}

1

GS12

MC113

Ru2

Zn-*tri*-PcNc

Figure 10: Structure of the main organometallic dyes used in DSPC.

On the other hand, organic dyes are cheaper, and their properties can be adjusted more easily, despite exhibiting lower efficiencies and stability. The use of abundant and not-precious elements pushes the research in this direction. In the literature, there are many examples of organic dye-sensitized systems and the most common design includes the push-pull dyes, typically based on three connected units, donor (D), spacer (π), and acceptor (A). Other types of dyes are polymeric, porphyrin-based, perylene-based, xanthene-based, and coumarin-based. In this thesis, I will not investigate these last categories, but an interested reader can find more information in these articles.[20,30]

The library of push-pull dyes used in this field is very wide (Figure 11). The ordinary design is D-π-A, where D is an electron-rich group, π is the conjugated spacer, and A is the acceptor group, which also provides the anchoring functionality for the TiO_2. These dyes can be easily modified to increase the hydrophilicity of the surface, the light-harvesting capability, and the stability in the device. The introduction of the alkoxyl chains in different positions of triphenylamine-based dyes showed a significant improvement in the hydrogen evolution efficiency due to an enhancement in the hydrophilicity and thus a better interface with the aqueous medium (Figure 11).[31,32] Moreover, the functionalization with bulky, rigid, and hydrophilic substituents characterized by low degrees of freedom and the capability of intramolecular self-assembly, such as in **PTZ-GLU**, clearly improved the wettability of the device (Figure 11). In fact, **PTZ-GLU**-sensitized TiO_2 showed a contact angle with water of just 27°, which is really close to that of the bare TiO_2 (14°).[33] This innovative design resulted in almost doubling the TOF compared with the same phenothiazine-based dye functionalized with a triethylene glycol chain (**PTZ-TEG**) instead. This can be attributed to the more rigid structure given by the glucose. This structure avoided the formation of π-π stacking aggregations and at the same time, allowed a supramolecular organization on the titanium dioxide surface, thanks to the high polar functionalities that can generate strong directional intermolecular interactions with other sugar molecules.

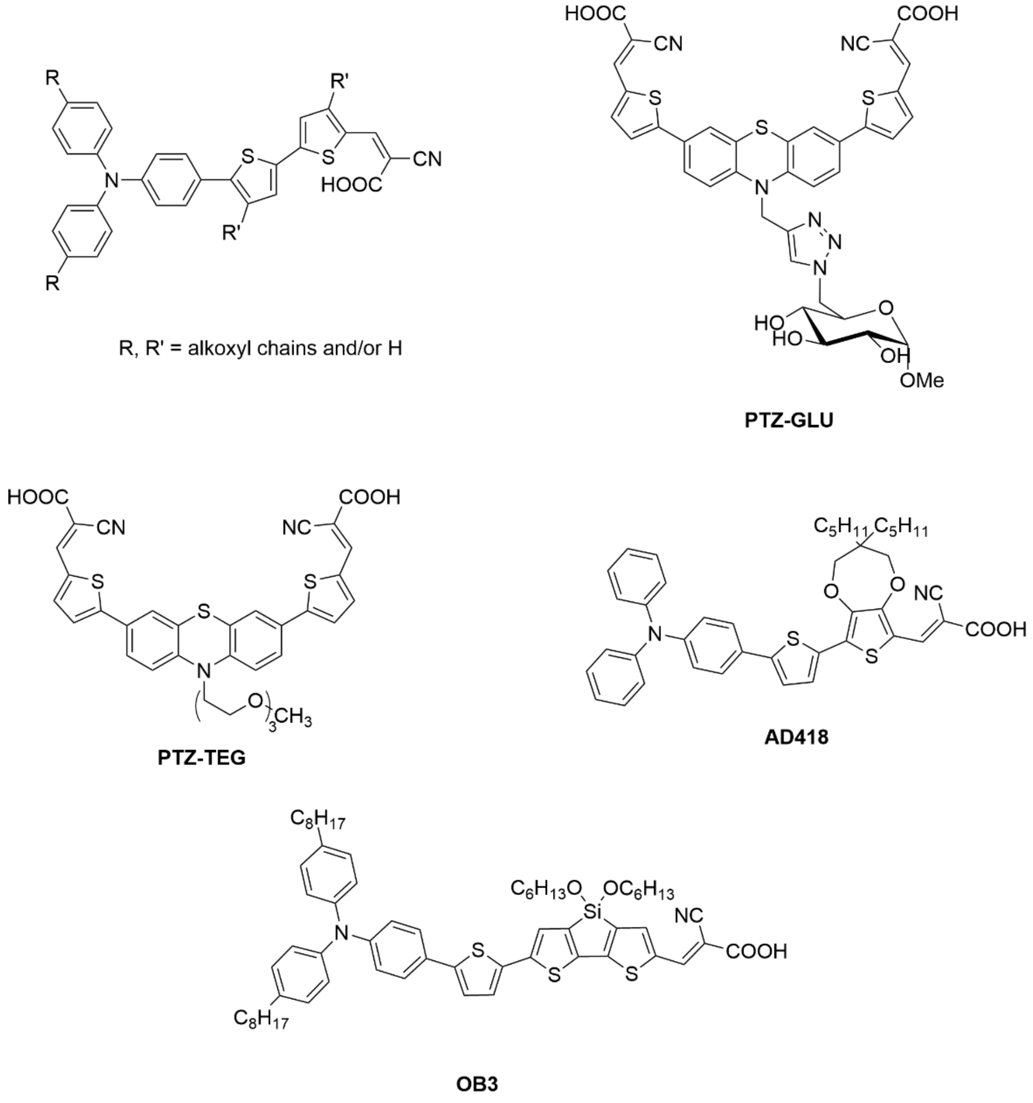

Figure 11: Structure of the main organic push-pull dyes used in DSPC.

Together with the hydrophilicity of the donor moiety, the use of hydrophobic alkyl chains on the π-spacers increases the stability. This hydrophobic barrier protects the carboxylic anchor group from hydrolysis and avoids dye agglomeration thereby limiting detrimental charge recombination reactions.

This effect was evident in **AD418** (Figure 11), which exhibited a TON of 872 after 20 h with incredible stability over time.[32] On the other hand, the alkyl chains both on the donor moiety and on the π-spacer, like **OB3** (Figure 11), reduced the performances of the device due to an excessive steric bulk and poor interaction with the medium.[34]

References

1 Barber, J. & Tran, P. D. (**2013**) From natural to artificial photosynthesis. *J. R. Soc., Interface,* **10**, 20120984, doi:10.1098/rsif.2012.0984.

2 Wang, Y., Suzuki, H., Xie, J., Tomita, O., Martin, D. J., Higashi, M., Kong, D., Abe, R. & Tang, J. (**2018**) Mimicking Natural Photosynthesis: Solar to Renewable H_2 Fuel Synthesis by *Z*-Scheme Water Splitting Systems. *Chem. Rev.,* **118**, 5201-5241, doi:10.1021/acs.chemrev.7b00286.

3 Christoforidis, K. C. & Fornasiero, P. (**2017**) Photocatalytic Hydrogen Production: A Rift into the Future Energy Supply. *ChemCatChem,* **9**, 1523-1544, doi:10.1002/cctc.201601659.

4 Paracchino, A., Laporte, V., Sivula, K., Grätzel, M. & Thimsen, E. (**2011**) Highly active oxide photocathode for photoelectrochemical water reduction. *Nat. Mater.,* **10**, 456-461, doi:10.1038/nmat3017.

5 Chen, S., Qi, Y., Hisatomi, T., Ding, Q., Asai, T., Li, Z., Ma, S. S. K., Zhang, F., Domen, K. & Li, C. (**2015**) Efficient Visible-Light-Driven Z-Scheme Overall Water Splitting Using a $MgTa_2O_{6-x}N_y$ /TaON Heterostructure Photocatalyst for H_2 Evolution. *Angew. Chem. Int. Ed.,* **54**, 8498-8501, doi:10.1002/anie.201502686.

6 Ganguly, P., Harb, M., Cao, Z., Cavallo, L., Breen, A., Dervin, S., Dionysiou, D. D. & Pillai, S. C. (**2019**) 2D Nanomaterials for Photocatalytic Hydrogen Production. *ACS Energy Lett.,* **4**, 1687-1709, doi:10.1021/acsenergylett.9b00940.

7 Du, A., Ng, Y. H., Bell, N. J., Zhu, Z., Amal, R. & Smith, S. C. (**2011**) Hybrid Graphene/Titania Nanocomposite: Interface Charge Transfer, Hole Doping, and Sensitization for Visible Light Response. *J. Phys. Chem. Lett.,* **2**, 894-899, doi:10.1021/jz2002698.

8 Willkomm, J., Orchard, K. L., Reynal, A., Pastor, E., Durrant, J. R. & Reisner, E. (**2016**) Dye-sensitised semiconductors modified with molecular catalysts for light-driven H_2 production. *Chem. Soc. Rev.,* **45**, 9-23, doi:10.1039/C5CS00733J.

9 Fajrina, N. & Tahir, M. (**2019**) A critical review in strategies to improve photocatalytic water splitting towards hydrogen production. *Int. J. Hydrogen Energy,* **44**, 540-577, doi:10.1016/j.ijhydene.2018.10.200.

10 Zani, L., Melchionna, M., Montini, T. & Fornasiero, P. (**2021**) Design of dye-sensitized TiO_2 materials for photocatalytic hydrogen production: light and shadow. *J. Phys.,* **3**, 031001, doi:10.1088/2515-7655/abe04b.

11 Chen, X., Shen, S., Guo, L. & Mao, S. S. (**2010**) Semiconductor-based Photocatalytic Hydrogen Generation. *Chem. Rev.,* **110**, 6503-6570, doi:10.1021/cr1001645.

12 Zhu, Y.-P., Yin, J., Abou-Hamad, E., Liu, X., Chen, W., Yao, T., Mohammed, O. F. & Alshareef, H. N. (**2020**) Highly Stable Phosphonate-Based MOFs with Engineered Bandgaps for Efficient Photocatalytic Hydrogen Production. *Adv. Mater.,* **32**, 1906368, doi:10.1002/adma.201906368.

13 Cecconi, B., Manfredi, N., Montini, T., Fornasiero, P. & Abbotto, A. (**2016**) Dye-Sensitized Solar Hydrogen Production: The Emerging Role

of Metal-Free Organic Sensitizers. *Eur. J. Org. Chem.,* **2016**, 5194-5215, doi:10.1002/ejoc.201600653.

14 Decavoli, C., Boldrini, C. L., Manfredi, N. & Abbotto, A. (**2019**) Dye-sensitized photocatalytic and photoelectrochemical hydrogen production through water splitting. *Rend. Lincei Sci. Fis. Nat.,* **30**, 469-483, doi:10.1007/s12210-019-00824-6.

15 Hampel, B. P., Z.; Sapi, A.; Szamosvolgyi, A.; Baia, L.; Hernadi, K. (**2020**) Application of TiO_2-Cu Composites in Photocatalytic Degradation Different Pollutants and Hydrogen Production. *Catalysts,* **10**, doi:10.3390/catal10010085.

16 Meffe, R. & de Bustamante, I. (**2014**) Emerging organic contaminants in surface water and groundwater: A first overview of the situation in Italy. *Sci. Total Environ.,* **481**, 280-295, doi:10.1016/j.scitotenv.2014.02.053.

17 Compagnoni, M., Ramis, G., Freyria, F. S., Armandi, M., Bonelli, B. & Rossetti, I. (**2017**) Photocatalytic Processes for the Abatement of N-Containing Pollutants from Waste Water. Part 1: Inorganic Pollutants. *J. Nanosci. Nanotechnol.,* **17**, 3632-3653, doi:10.1166/jnn.2017.14006.

18 Reddy, K. R., Jyothi, M. S., Raghu, A. V., Sadhu, V., Naveen, S. & Aminabhavi, T. M. in *Nanophotocatalysis and Environmental Applications: Detoxification and Disinfection* (eds Inamuddin, Abdullah M. Asiri, & Eric Lichtfouse)(Springer International Publishing: Cham, Switzerland, **2020**) 139-169.

19 Reginato, G., Zani, L., Calamante, M., Mordini, A. & Dessì, A. (**2020**) Dye-Sensitized Heterogeneous Photocatalysts for Green Redox Reactions. *Eur. J. Inorg. Chem.,* **2020**, 899-917, doi:10.1002/ejic.201901174.

20 Huang, J. F., Lei, Y., Luo, T. & Liu, J. M. (**2020**) Photocatalytic H_2 Production from Water by Metal-free Dye-sensitized TiO_2 Semiconductors: The Role and Development Process of Organic Sensitizers. *ChemSusChem*, doi:10.1002/cssc.202001646.

21 Guo, M., Xie, K., Lin, J., Yong, Z., Yip, C. T., Zhou, L., Wang, Y. & Huang, H. (**2012**) Design and coupling of multifunctional TiO_2 nanotube photonic crystal to nanocrystalline titania layer as semi-transparent photoanode for dye-sensitized solar cell. *Energy Environ. Sci.,* **5**, 9881-9888, doi:10.1039/C2EE22854H.

22 Zhang, L. & Cole, J. M. (**2015**) Anchoring Groups for Dye-Sensitized Solar Cells. *ACS Appl. Mater. Interfaces,* **7**, 3427-3455, doi:10.1021/am507334m.

23 Borgarello, E., Kiwi, J., Pelizzetti, E., Visca, M. & Grätzel, M. (**1981**) Photochemical cleavage of water by photocatalysis. *Nature,* **289**, 158-160, doi:10.1038/289158a0.

24 Furlong, D. N., Wells, D. & Sasse, W. H. F. (**1986**) Colloidal semiconductors in systems for the sacrificial photolysis of water: sensitization of titanium dioxide by adsorption of ruthenium complexes. *J. Phys. Chem.,* **90**, 1107-1115, doi:10.1021/j100278a029.

25 Saupe, G. B., Mallouk, T. E., Kim, W. & Schmehl, R. H. (**1997**) Visible Light Photolysis of Hydrogen Iodide Using Sensitized Layered Metal Oxide Semiconductors: The Role of Surface Chemical Modification in Controlling Back Electron Transfer Reactions. *J. Phys. Chem. B,* **101**, 2508-2513, doi:10.1021/jp9625319.

26 Swetha, T., Mondal, I., Bhanuprakash, K., Pal, U. & Singh, S. P. (**2015**) First Study on Phosphonite-Coordinated Ruthenium Sensitizers for Efficient Photocatalytic Hydrogen Evolution. *ACS Appl. Mater. Interfaces,* **7**, 19635-19642, doi:10.1021/acsami.5b04020.

27 Koyyada, G., Pilli, N. S., Jung, J. H., Mandari, K. K., Shanigaram, B. & Chandrasekharam, M. (**2018**) Shining light on panchromatic ruthenium sensitizers towards dye-sensitized photocatalytic hydrogen evolution. *Int. J. Hydrogen Energy,* **43**, 6963-6976, doi:10.1016/j.ijhydene.2018.02.117.

28 Zhang, X., Veikko, U., Mao, J., Cai, P. & Peng, T. (**2012**) Visible-Light-Induced Photocatalytic Hydrogen Production over Binuclear

Ru^{II}-Bipyridyl Dye-Sensitized TiO_2 without Noble Metal Loading. *Chem. Eur. J.,* **18**, 12103-12111, doi:10.1002/chem.201200725.

29 Zhang, X., Yu, L., Zhuang, C., Peng, T., Li, R. & Li, X. (**2013**) Highly efficient visible/near-IR-light-driven photocatalytic H_2 production over asymmetric phthalocyanine-sensitized TiO_2. *RSC Adv.,* **3**, 14363-14370, doi:10.1039/C3RA41975D.

30 Warnan, J. & Reisner, E. (**2020**) Synthetic Organic Design for Solar Fuel Systems. *Angew. Chem. Int. Ed.,* **59**, 17344-17354, doi:10.1002/anie.202006013.

31 Lee, S.-H., Park, Y., Wee, K.-R., Son, H.-J., Cho, D. W., Pac, C., Choi, W. & Kang, S. O. (**2010**) Significance of Hydrophilic Characters of Organic Dyes in Visible-Light Hydrogen Generation Based on TiO_2. *Org. Lett.,* **12**, 460-463, doi:10.1021/ol9026182.

32 Han, W.-S., Wee, K.-R., Kim, H.-Y., Pac, C., Nabetani, Y., Yamamoto, D., Shimada, T., Inoue, H., Choi, H., Cho, K. & Kang, S. O. (**2012**) Hydrophilicity Control of Visible-Light Hydrogen Evolution and Dynamics of the Charge-Separated State in Dye/TiO_2/Pt Hybrid Systems. *Chem. Eur. J.,* **18**, 15368-15381, doi:10.1002/chem.201201500.

33 Manfredi, N., Cecconi, B., Calabrese, V., Minotti, A., Peri, F., Ruffo, R., Monai, M., Romero-Ocana, I., Montini, T., Fornasiero, P. & Abbotto, A. (**2016**) Dye-sensitized photocatalytic hydrogen production: distinct activity in a glucose derivative of a phenothiazine dye. *Chem. Commun.,* **52**, 6977-6980, doi:10.1039/c6cc00390g.

34 Bettucci, O., Skaltsas, T., Calamante, M., Dessì, A., Bartolini, M., Sinicropi, A., Filippi, J., Reginato, G., Mordini, A., Fornasiero, P. & Zani, L. (**2019**) Combining Dithienosilole-Based Organic Dyes with a Brookite/Platinum Photocatalyst toward Enhanced Visible-Light-Driven Hydrogen Production. *ACS Appl. Energy Mater.,* **2**, 5600-5612, doi:10.1021/acsaem.9b00782.

Chapter 3: Calix[4]arenes in DSPC

Aim of this section

This section presents an innovative design used for organic dyes in DSPC which employ a calix[4]arene macrocycle in dibranched D-(π-A)$_2$ dyes as the donor moiety. In this case, the calix[4]arene macrocycle acts as a scaffold and holds the two π-A branches on top of it at a fixed distance, avoiding the conjugation between them. These compounds have been optically and electrochemically characterized, and by comparing with a linear reference, we discovered that the macrocycle does not affect the optical properties of the compounds.

However, the calix[4]arene dye exhibits a two-fold higher photocatalytic hydrogen production activity when compared with the linear benchmark. This result cannot be attributed to better optical properties since they present similar molar absorptivity as well as LHE. However, this could indicate the establishment of host-guest interactions between the macrocycle and the SED accelerate the charge transfer. This supramolecular interaction commonly occurs by the upper rim of the macrocycle. In this case, it faces the SC surface and therefore, the length of the branches determines the available physical space for the insertion of the SED. In fact, **Calix-ThTh** has the longest π-spacer in this series and shows the highest photocatalytic activity. On the other hand, any further functionalization on the π-spacers does not improve the activity of the mono-thiophene spacer compounds.

This indicates that factors other than a high conjugation or a large optical absorption can influence the photocatalytic activity in DSPC.

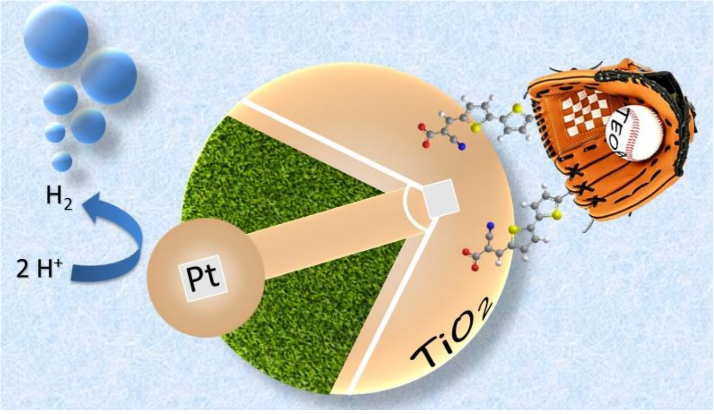

Figure 12: Schematic representation of exploiting host-guest interaction between a sensitizer (baseball mitt) and the SED (baseball ball).

3.1 Introduction

In the last years, among the photosensitizers for DSPC, some interest has been given to the calixarenes-based dyes.[1] Calixarenes are macrocycles composed of methylene-bridged phenol units. Due to their structure, they can host different small molecules and generate labile host-guest complexes which increase the charge transfer in the system.[2] They can also be scaffolds for the construction of molecular or supramolecular complex structures.[3-6] Both of their rims can be functionalized and the addition of alkyl chains longer than ethyl to the lower rim will block the calix[4]arene in the cone structure. In this way, the functionalization added on the upper rim of the cone are oriented in the same direction and kept at a fixed distance imposed by the geometry of the cone.[7] Moreover, the presence of the methylene bridges avoids the conjugation among the different phenyl rings and branches. Hence, their optical properties should not change compared to the single phenyl ring functionalized with the same branch. To the best of my knowledge, in all the examples shown in the literature about DSPC, the calix[4]arene rings are embedded in the structure of a D-π-A dye.[1] Liu et al. presented **Calix-3,** a calix[4]arene scaffold functionalized with four terthiophene-spacers and four acrylic anchor groups (Figure 13).[8] In this case, the calix[4]arene macrocycle embedded in a D-π-A structure replaces the donor moiety. This dye-sensitized system exhibited high performance even after cycling 10-times. The tetra-branched structure promoted greater stability and a more effective injection into the MOF, which was used, in this case, in place of the SC. The performance of this dye was further compared to those of the linear analogous, namely **M-3**.[9] **Calix-3** obtained hydrogen production 10-times higher than when the linear was used at a 4-times loading to match the light-harvesting ability of **Calix-3**. It suggested that, although the two systems exhibited about the same optical properties, the **Calix-3**-sensitized device presented improved charge transfer in the global system. Moreover, **Calix-3** was also used in combination with sol-gel-made TiO_2 nanoparticles, where this micro/mesoporous structure provided a higher surface area, more catalytic active sites, and reflection. This Pt/TiO_2/**Calix-3** system was found to be very stable in long-term cycling and showed a TON of about 17 000 after 50 h of working.

An alternative design was **HO-TPA**, where a calix[4]arene without any alkyl substitution on the hydroxyl groups of the lower rim was used as an anchor group for a triphenylamine-based dye (Figure 13).[10] In this case, the upper rim of the calix[4]arene was functionalized with four bithienyl-spacers topped with four triphenylamine donor moieties. The hydroxyl groups present on the lower rim were exploited as anchoring groups for TiO_2 nanoparticles. As in the other case, the dye-sensitization was prepared by sol-gel synthesis, resulting in a highly stable linkage and a more efficient electron transfer between the dye and TiO_2. This system reached a TON of 6417 in 75 h with recycling 15 times using triethanolamine (TEOA) as SED and maintained a general stable hydrogen production.

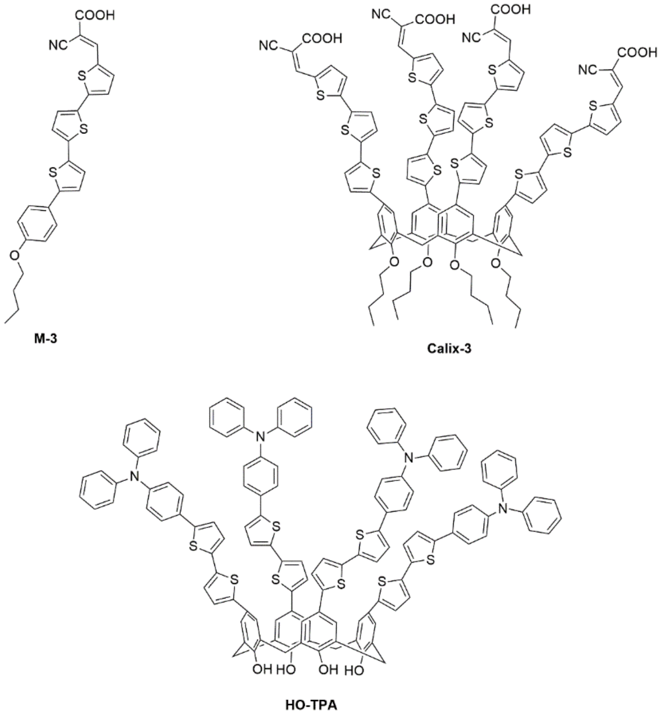

M-3

Calix-3

HO-TPA

Figure 13: Chemical structures of the calix[4]arene-based dyes and the linear **M-3** described in the text.

Based on these works, we investigated a new series of calix[4]arene-based push-pull dyes for photocatalytic hydrogen production. We studied how the electronic and spatial properties of the dyes influenced the performance of the device. We chose Aeroxide TiO_2 nanoparticles on which the Pt catalyst was deposited. Hence, the advantages of the micro/mesoporous structure examined before do not affect our system. We focused on the effects of the sensitization using calix[4]arene-based dyes versus linear ones. The purpose is to discover if the calix[4]arene scaffold could improve the photocatalytic activity due to its more rigid structure and the possibility of exploiting host-guest interaction with a suitable SED.

3.2 Design and synthesis of the dyes

We chose to design different dibranched dyes, D-(π-A)$_2$, where a calix[4]arene macrocycle replaced the donor moiety and acted as a scaffold for the construction of the dyes. Propoxy groups functionalized the entire lower rim and blocked the dyes in the cone conformation, while just two positions of the upper rim were functionalized with two π-A branches. The anchor and acceptor groups were cyanoacrylic acids, while various π-spacers were used to investigate the different optical and electrochemical properties (Figure 14). The peculiar structure of the donor scaffold has been exploited to design a two-dye sensitizer in which the two D-π-A branches were not connected through a π-conjugated linkage.

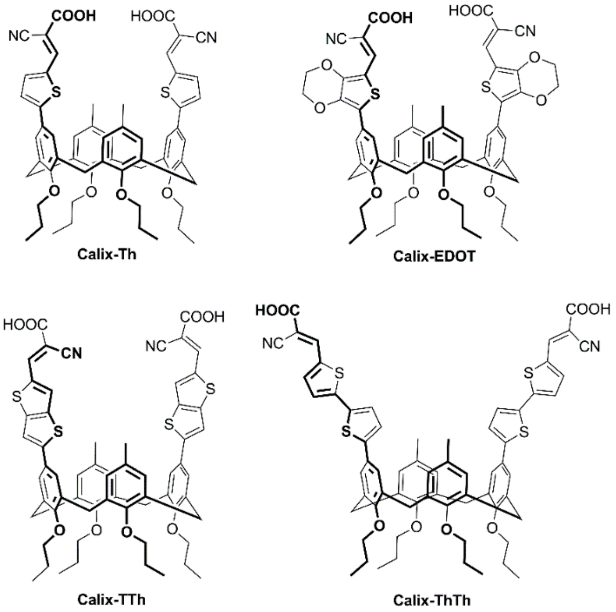

Figure 14: Investigated calix[4]arene-based dyes.

The calix[4]arene dyes have been synthesized following a modified procedure reported in the literature.[11] The synthetic pathway started with a Clemmensen reduction of 5,17-diformyl-

25,27-dipropoxycalix[4]arene[7] (**1**) to obtain the corresponding 5,17-dimethyl-25,27-dipropoxycalix[4]arene (**2**). After the alkylation reaction with iodopropane and subsequent bromination with NBS, the 5,17-dibromo-11,23-dimethyl-25,26,27,28-tetrapropoxycalix[4]arene (**Calix-Br**) has been obtained (Scheme 1). **Calix-Br** was the common intermediate to all the synthesized compounds. It was synthesized by the group of Prof. Baldini at the University of Parma and sent to my research group. From **Calix-Br**, it was possible to obtain the aldehydic precursors for the last Knoevenagel condensation, following three different pathways of Suzuki-Miyaura cross-coupling that added the different π-spacers (Scheme 2).

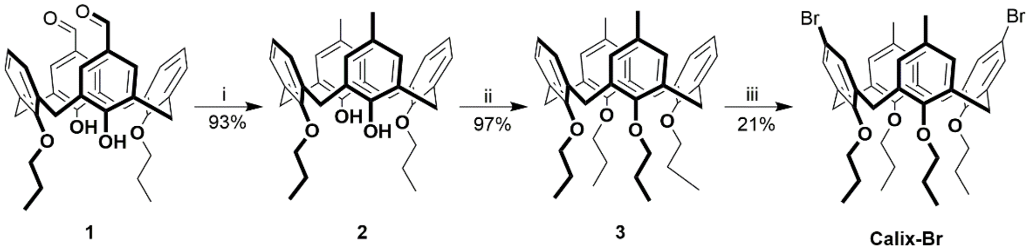

Scheme 1: i) Zn, HCl, EtOH/toluene (1:1), reflux, 2 h; ii) NaH 60%, iodopropane, anhydrous DMF, rt, 12 h; iii) NBS, anhydrous DMF, rt, 12 h.

In the case of **Calix-Th** and **Calix-ThTh**, **Calix-Br** was subjected to a palladium-catalyzed coupling in the presence of (5-formylthiophene-2-yl)boronic acid or 5'-formyl-2,2'-bithiophene-5-boronic acid, respectively. Concerning **Calix-TTh**, **Calix-Br** was first subjected to a Suzuki-Miyaura cross-coupling with thieno[3,2-*b*]thiophene-2-boronic acid pinacol ester[12] and then to a Vilsmeier-Haack formylation in the presence of *N*,*N*-dimethylformamide and phosphorus(V) oxychloride in dry chloroform. In the end, for **Calix-EDOT**, **Calix-Br** was borylated by a Pd-catalyzed Miyaura borylation performed with bis(pinacolato)diboron in anhydrous *N*,*N*-dimethylformamide, and then immediately submitted to a Suzuki-Miyaura coupling with 7-bromo-2,3-dihydrothieno[3,4-*b*][1,4]dioxine-5-carbaldehyde. The cyanoacrylic acceptor group was added after a Knoevenagel condensation with cyanoacetic acid and piperidine to all aldehydic precursors.

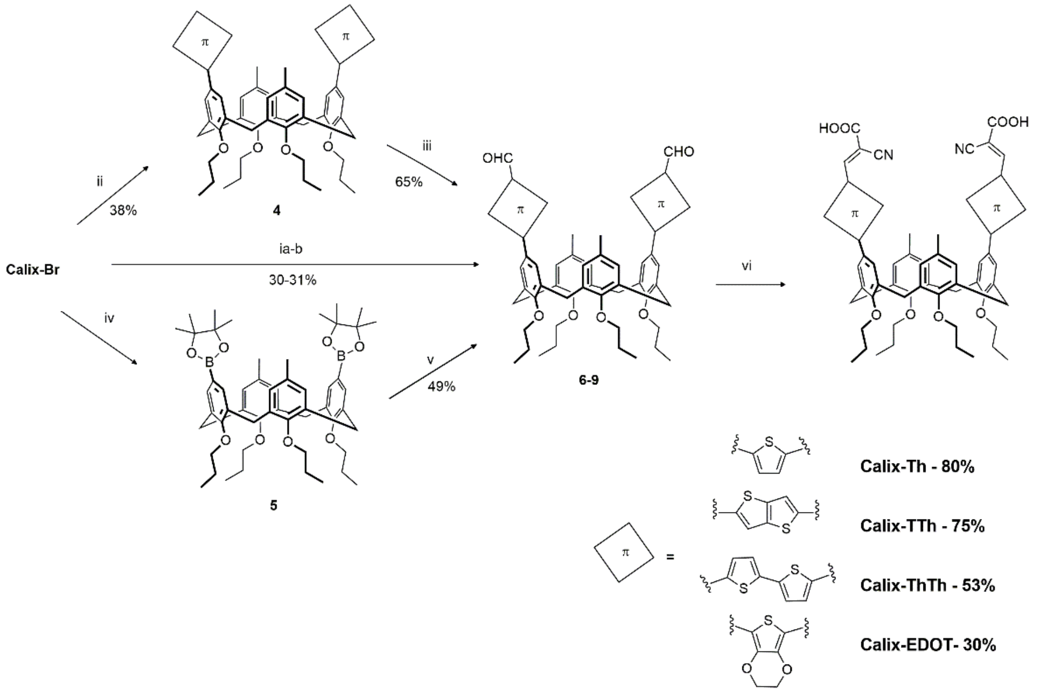

Scheme 2: ia) (5-formyl thiophene-2-yl)boronic acid, Pd(dppf)$Cl_2 \cdot CH_2Cl_2$, K_2CO_3, toluene/MeOH (1:1), microwave, 80 °C, 70 W, 90 min; ib) 5'-formyl-2,2'-bithiophene-5-boronic acid, Pd(dppf)$Cl_2 \cdot CH_2Cl_2$, K_2CO_3, toluene/MeOH (1:1), reflux, 6 h; ii) thieno[3,2-*b*]thiophene-2-boronic acid pinacol ester, Pd(dppf)$Cl_2 \cdot CH_2Cl_2$, K_2CO_3, toluene/MeOH (1:1), microwave, 100 °C, 70 W, 90 min; iii) $POCl_3$, anhydrous DMF, dry $CHCl_3$, 70 °C, 8 h; iv) bis(pinacolato)diboron, Pd(dppf)$Cl_2 \cdot CH_2Cl_2$, anhydrous DMF, rt, 30 min, 200 °C, 2 h; v) 7-bromo-2,3-dihydrothieno[3,4-*b*][1,4]dioxine-5-carbaldehyde, Pd(dppf)$Cl_2 \cdot CH_2Cl_2$, K_2CO_3, toluene/MeOH (1:1), reflux, 6 h; vi) cyanoacetic acid, piperidine, dry $CHCl_3$ or dry CH_3CN/dry toluene (3:1), reflux 5-8 h.

In the end, the linear dye corresponding to the best performing calix[4]arene dye was further synthesized (Scheme 3). The first reaction was a Williamson ether synthesis using 4-bromophenol and 1-bromopropane in refluxed acetone for 12 h to achieve the 1-bromo-4-propoxybenzene (**10**). As in the other cases, the π-spacer was added following a palladium-catalyzed Suzuki-Miyaura protocol, using 5'-formyl-2,2'-bithiophene-5-boronic acid in a mixture of toluene and methanol. Finally, **Linear-ThTh** was obtained after a common Knoevenagel condensation with cyanoacetic acid in chloroform that inserted the cyanoacrylic group.

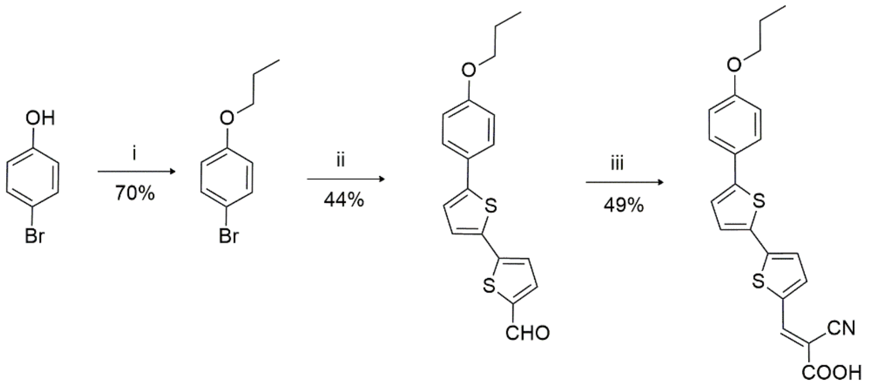

Scheme 3: i) 1-bromopropane, K_2CO_3, acetone, reflux, 12 h; ii) 5'-formyl-2,2'-bithiophene-5-boronic acid, $Pd(dppf)Cl_2 \cdot CH_2Cl_2$, K_2CO_3, toluene: MeOH (1:1), rt, 1 h, reflux, 3 h; iii) cyanoacetic acid, piperidine, dry $CHCl_3$, reflux 5 h.

All the investigated compounds have been characterized by their melting point, FT-IR spectroscopy, and HRMS. Their purity has been controlled via ^1H and ^{13}C NMR spectroscopy.

3.3 Optical and electrochemical properties

The most valuable characterization for a photosensitizer is optical characterization, which show the light-harvesting capability of the compound. This characterization is followed by electrochemistry, which indicates if the dye can allow the correct charge transfer from the WOC to the SC. The main optical and electrochemical parameters are reported in Table 1. The optical characterization of the calix[4]arene-based dyes was performed in 10^{-5} M DMSO solutions. The absorption spectra normalized to the molar extinction coefficient are shown in Figure 15. All the dyes showed an intense absorption band in the visible region attributed to the intramolecular donor-to-acceptor charge-transfer (ICT) transition. As expected, the introduction of a more extended conjugation in the π-spacers led to significant bathochromic effects, thus allowing a more efficient collection of photons. The molar absorptivities range from 40000 (**Calix-Th**) to 46000 M^{-1} cm^{-1} (**Calix-ThTh**), whereas the **Linear-ThTh** reference is around 37400 M^{-1} cm^{-1}. It is interesting to highlight that the molar extinction coefficient of the **Calix-ThTh** was less than the double of **Linear-ThTh** one, even if the former presented two-dye units in its structure. In **Calix-EDOT**, the alkoxy auxochrome groups on the thienyl ring shifted the absorption maximum of more than 30 nm to longer wavelengths than the bare **Calix-Th**.

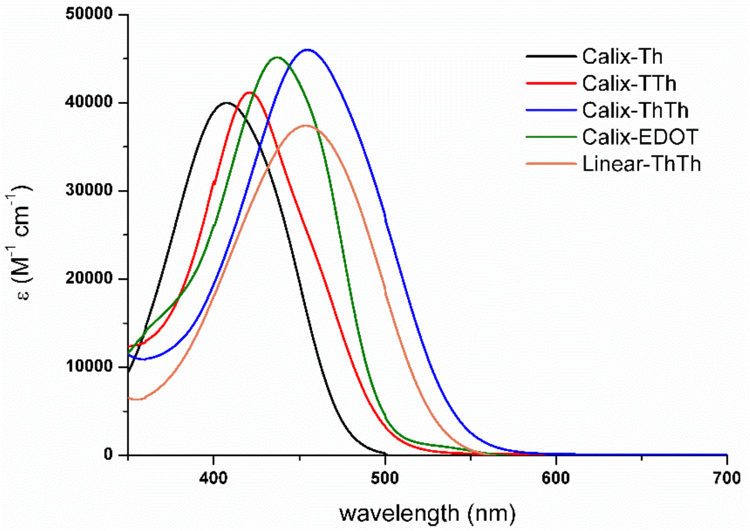

Figure 15: UV-Vis spectra in 10^{-5} DMSO solution of the investigated sensitizers.

Optical bandgaps were calculated by means of the Tauc plots[13] and listed in Table 1 together with the oscillator strengths. This last parameter indicates the probability of the absorption of an electromagnetic radiation and was determined to investigate the light-harvesting capabilities of the different compounds.[14] The absorption quantitative capacity among the calix[4]arene dyes and the linear reference system was very similar. In fact, the oscillator strength of **Calix-ThTh** (f = 11.4 D) was only 10% larger than that of the corresponding linear dye **Linear-ThTh** (f = 10.1 D).

Table 1: Optical and electrochemical parameters of investigated sensitizers in solution.

Dye[a]	λ_{max} (nm)	ε (M^{-1} cm^{-1})	f [b] (D)	E_{gap}^{opt} (eV)	V_{ox} (V vs Fc) ± 10 mV	HOMO[c] (eV) ± 0.05 eV	LUMO[c] (eV) ± 0.05 eV
Linear-ThTh	454	37 400 ± 500	10.1	2.2	0.78	-6.01	-3.81
Calix-Th	405	40 000 ± 500	9.1	2.4	0.96	-6.19	-3.79
Calix-TTh	421	41 200 ± 500	10.5	2.1	0.82	-6.05	-3.95
Calix-ThTh	455	46 000 ± 1400	11.4	2.2	0.71	-5.94	-3.74
Calix-EDOT	437	45 100 ± 350	10.3	2.1	0.81	-6.04	-3.94

[a] In DMSO. [b] Oscillator strength measured in the 300-800 nm range. [c] Fc/Fc$^+$ = -5.23 V vs vacuum.[15]

The LHE of the dye/TiO_2/Pt system on thin films is shown in Figure 16. The width of the LHE changed according to the length of conjugation of the π-spacer. In **Calix-ThTh** and **Linear-ThTh,** the LHE extended up to 600 nm with a peak of 60% at 455 nm, while in all the other cases, it barely reached 550 nm. This result confirmed the similar light-harvesting capability of **Calix-ThTh** and **Linear-ThTh**, highlighting that the presence of the calix[4]arene macrocycle did not influence the optical properties of the compound, also due to the non-conjugation between the two branches.

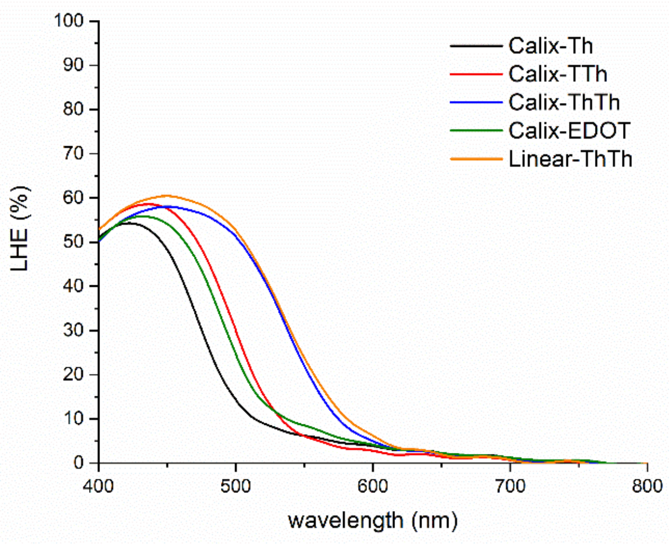

Figure 16: LHE of the investigated compound adsorbed on a 3-μm thick transparent TiO_2+Pt film.

The electrochemical parameters are listed in Table 1 as well. The compounds were electrochemically characterized using cyclic voltammetry (CV) and differential pulse voltammetry (DPV) to evaluate the energetic levels from the oxidation and reduction potentials.[15,16] However, all the compounds presented an irreversible oxidation peak in the cyclic voltammetry profile between +0.7 and +1.2 V vs Fc/Fc^+ complicated the designation of the energy levels (Figure 17), thus DPV was used instead (Figure 18).

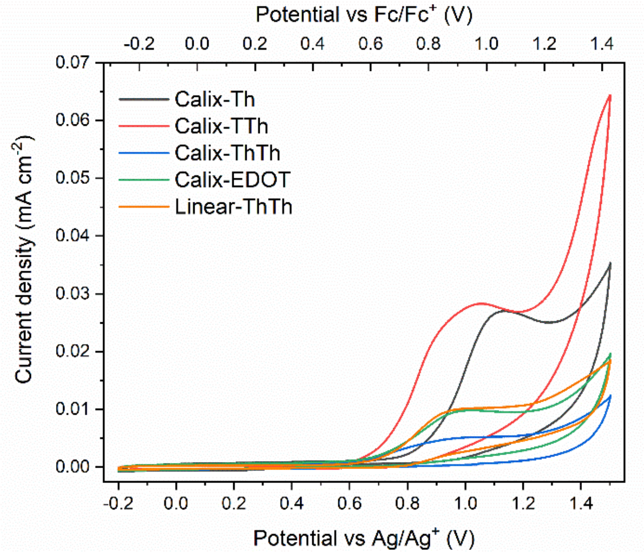

Figure 17: CV of the compounds recorded in CH_3CN $TBABF_4$ 0.1 M solution.

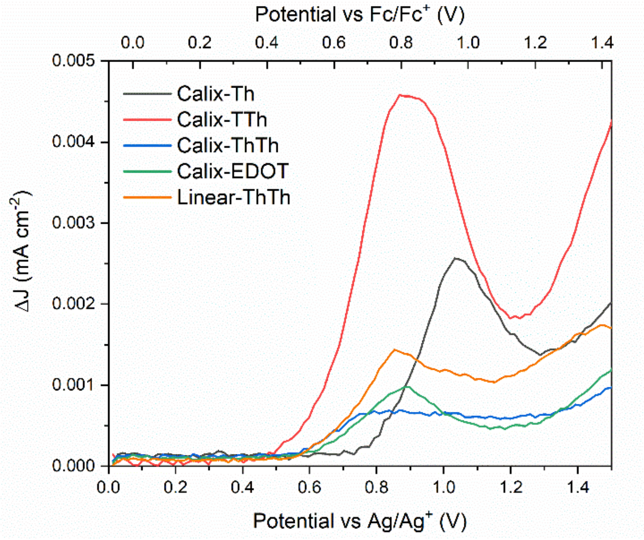

Figure 18: DPV of the compounds recorded in CH_3CN $TBABF_4$ 0.1 M solution.

DPV isolates the different electrochemical processes determining the oxidation potentials and allows for calculating the HOMO energy levels from the current peak. The LUMO levels have been derived from the electrochemical HOMO values and the optical bandgaps. Even though the HOMO energy levels are similar (~-6 eV), the different bandgaps determine the LUMO energies and affect the electron injection capabilities into the Pt/TiO_2 system. In Figure 19, the energy levels of the compounds are schematically compared with the titanium dioxide CB. As it is possible to see, **Calix-TTh** and **Calix-EDOT** presented a LUMO close to the TiO_2 CB. This could indicate a higher probability of back electron transfer reactions.

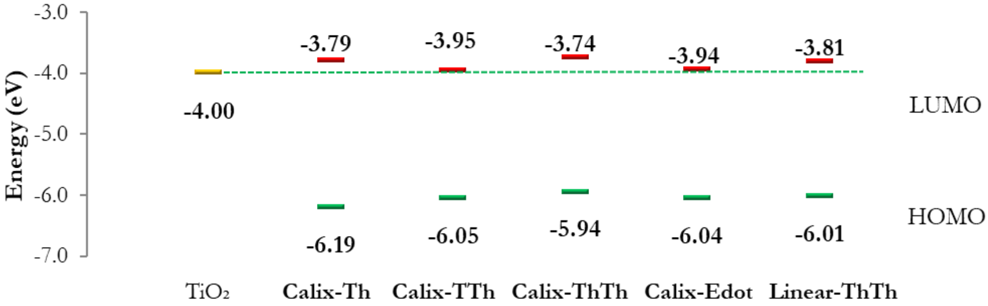

Figure 19: Schematics of calculated energy levels (vs vacuum) of the investigated sensitizers in comparison with TiO_2 CB.

3.4 Photocatalytic hydrogen evolution

The dye-sensitized Pt/TiO_2 photocatalysts were tested for H_2 production under visible light irradiation ($\lambda > 420$ nm) in a TEOA/HCl aqueous buffer solution at pH = 7.0. The experiments have been performed by the groups of Prof. Fornasiero and Prof. Montini at the University of Trieste, adhering to the same conditions previously optimized for dibranched organic dye-based photocatalysts.[17] Measured H_2 productions and H_2 production rate vs irradiation time are presented in Figure 20 and in Figure 21, respectively. TON and LFE after 2 and 15 h of irradiation are listed in Table 2.

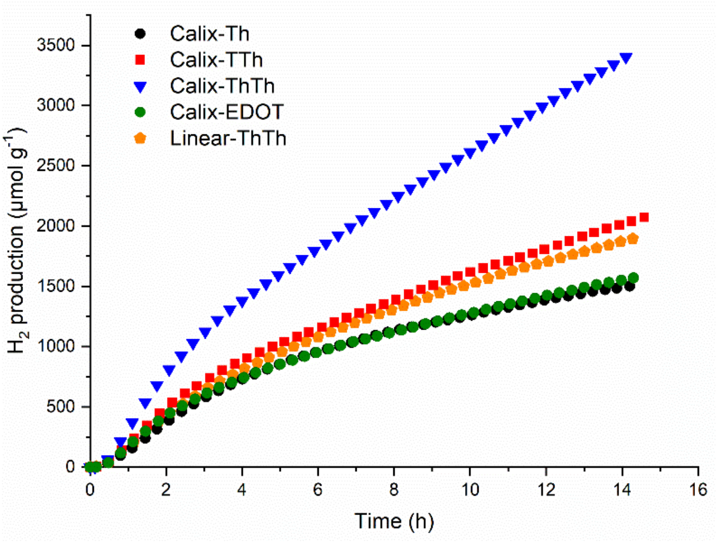

Figure 20: H_2 production measured in TEOA 10% v/v solution at pH 7.0 using the dye/Pt/TiO_2 materials under irradiation with visible light (λ › 420 nm).

All photosystems showed an initial induction period (20 - 30 minutes) before significant H_2 production. This delay is attributed to the activation time of the photocatalysts and/or to a chromatographic effect within the dead volume of the photoreactor. After this time, all the photosystems showed a sharp increase in the H_2 production rate for an initial couple of hours, followed by a progressive decrease, until reaching a plateau after 6 - 8 hours of irradiation (Figure 21). All the photocatalysts showed a similar H_2 production except **Calix-ThTh**, for which the H_2 evolution was significantly higher (Figure 20).

The performances in photocatalytic H_2 production after 2 and 15 hours are summarized in Table 2. The 2-hour set represents the activity of the materials close to the maximum H_2 production rate, while the 15-hour one shows the overall performance of the photosystems after prolonged working conditions. These data highlight the higher performance of the **Calix-ThTh** dye with respect to the other calix[4]arene-based dyes, showing both higher TON and LFE values throughout all experiments. For this sample, it was also possible to measure an AQY of 0.138% under irradiation at 450 nm.

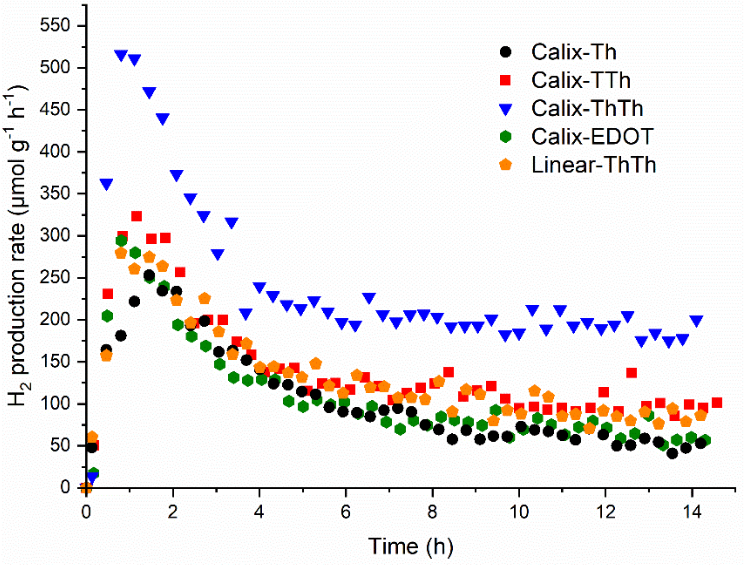

Figure 21: H_2 production rates measured in TEOA 10% v/v solution at pH 7.0 using the dye/Pt/TiO_2 materials under irradiation with visible light (λ › 420 nm).

Table 2: Photocatalytic performance of the dye/Pt/TiO_2 materials in H_2 production from TEOA 10% v/v solution at pH 7.0 under irradiation with visible light (λ › 420 nm).

Dye	After 2 hours			After 15 hours		
	H_2 amount (μmol g^{-1})	TON (μmol(H_2) μmol(dye)$^{-1}$)	LFE (%)	H_2 amount (μmol g^{-1})	TON (μmol(H_2) μmol(dye)$^{-1}$)	LFE (%)
Linear-ThTh	435	43.5	0.061	1870	187.0	0.024
Calix-Th	390	39.0	0.064	1502	150.2	0.015
Calix-TTh	535	53.5	0.071	2008	200.8	0.028
Calix-ThTh	810	81.0	0.103	3401	340.1	0.055
Calix-EDOT	448	44.8	0.053	1550	155.0	0.016

Comparing with the corresponding linear dye **Linear-ThTh**, **Calix-ThTh** shows an about twice-higher peak in the hydrogen production rate. (ca. 525 μmol g^{-1} h^{-1} *vs* ca. 275 μmol g^{-1} h^{-1}). This better behavior is not related to the optical properties of the molecules as they presented about the same molar absorptivity as well as LHE even if **Calix-ThTh** has two donor-acceptor units.

Literature evidence[18-20] suggest that a possible rationale for the improved performance of the calix[4]arene is the possibility of inducing host-guest interactions with protonated TEOA, thus favoring the charge transfer from the SED to the oxidized dye upon photoexcitation of the latter. The interaction of protonated amines with the calix[4]arene is reported to take place through the upper rim of the calix[4]arenes. Hence, the physical space between the macrocycle and the Pt/TiO_2 surface is crucial for hosting the SED. The relative activities of the calix[4]arene dyes followed the trend of the distances between the aromatic cavities and the carboxylic anchoring groups. **Calix-ThTh**, which has the longest π-spacer, showed higher photocatalytic activity than **Calix-TTh**, which in turn is better than the shortest **Calix-Th** and **Calix-EDOT**. The similar LHE behavior between **Calix-ThTh** and **Linear-ThTh** further supported this hypothesis, highlighting the importance of the different structural features on the photocatalytic performance.

Moreover, these calix[4]arene-based compounds showed higher photocatalytic hydrogen production rates as well as AQY, under similar conditions than other dibranched dyes widely present in literature, like the phenothiazine-based ones.[17,21-23] This investigation promotes the beneficial effect of exploiting host-guest interaction with the SED.

In conclusion, a new series of calix[4]arene-based dyes has been investigated in photocatalytic application compared with a linear benchmark. All the new dyes have been optically and electrochemically characterized and their purity has been checked by NMR. The photocatalytic studies highlighted the higher performance of the **Calix-ThTh** with the respect to the linear benchmark even if they both presented about the same optical properties and oscillator strengths, despite the presence of two light-harvesting units in the calix[4]arene dyes. An analysis of the data and similar literature suggests that the increased photocatalytic activity could be related to the addition of host-guest interactions between the calix[4]arene macrocycle and the SED. This new molecular design paves the way to a new strategy for photocatalytic hydrogen production where the calix[4]arene scaffold can offer the potential for host-guest supramolecular effects. More studies to investigate further the supramolecular interactions previously mentioned are currently in progress.

3.5 Experimental section

3.5.1 Electrochemical characterization

Test solutions were prepared by dissolving 2.0 mg of dye in the electrolyte (0.1 M $TBABF_4$ in CH_3CN). DPV and CV were carried out at scan rate of 20 and 50 mV/s, respectively, using a Bio-Logic SP-240 potentiostat in three-electrode electrochemical cell flushed with Ar. The working, counter, and the pseudo-reference electrodes were an FTO glass, a Pt wire, and an Ag/Ag^+ electrode in TBAP 0.1 M CH_3CN, respectively. The Ag/Ag^+ pseudo-reference electrode was calibrated, by adding ferrocene (10^{-4} M) to the test solution after each measurement. Energy levels were calculated using the absolute value of 5.3 V vs. vacuum for the ferrocene reference couple.

3.5.2 Preparation of Pt/TiO_2 nanocomposite

The photocatalysts have been prepared using TiO_2 Aeroxide from Evonik, which replaces the well-known TiO_2 P25 from Degussa. The TiO_2 Aeroxide is a mixture of anatase/rutile 60:40 by weight, with mean crystallite size around 20-25 nm (as determined by powder X-Ray Diffraction), a surface area of 49 m^2 g^{-1}, a total pore volume of 0.258 cm^3 g^{-1} and average pore size of 20 nm (as determined by N_2 physisorption at the liquid nitrogen temperature).

Deposition of Pt nanoparticles on TiO_2 Aeroxide was done through a photodeposition method known in literature.[24-27] 32.7 mg of $Pt(NO_3)_2$ was dissolved in 400 mL of a solution of water/ethanol 1:1 by volume. 2.0 g of TiO_2 Aeroxide was suspended in the Pt solution to reach a final metal loading of 1.0 wt%. After stirring for 1 h in the dark, the suspension was irradiated with a 450 W medium pressure lamp for 4 h. The Pt/TiO_2 nanocomposites were collected by centrifugation, washed 3 times with EtOH and finally dried under vacuum at 50 °C overnight. The photodeposited Pt nanoparticles had a mean size of 1.3 nm (as determined by High Angle Annular Dark Field-Scanning Transmission Electron Microscopy - HAADF-STEM).

3.5.3 Adsorption of dyes on Pt/TiO$_2$

200 mg of Pt/TiO_2 nanocomposite were suspended in 10 mL of EtOH under stirring. 2 μmol of the dyes (the amount required to reach a loading of 10 μmol/g) were dissolved into 0.5 mL of DMSO and the solution added dropwise in the suspension. Adsorption of the dye was performed allowing equilibration of the suspension for 24 h in the dark. The obtained materials were recovered by centrifugation, washed 2 times with 10 mL of EtOH each and dried under vacuum at room temperature overnight. UV-vis spectra of the solutions after dye adsorption showed that the amount of residual dyes is negligible, confirming the quantitative adsorption of the dyes on Pt/TiO_2.

3.5.4 Photocatalytic hydrogen production

The $Dye/Pt/TiO_2$ nanomaterials have been tested for H_2 production following a procedure previously described.[28] Briefly, the reactor is a home-made reactor with a stainless-stell body containing a Teflon beaker (volume of ~ 120 mL). 60 mg of the $Dye/Pt/TiO_2$ was suspended into 60 mL of 10% v/v aqueous solution of TEOA neutralized with HCl to reach a pH = 7.0. The reactor is close with a quartz window (cut-off ~ 200 nm) and is connected to the gas distribution line. Inert gas (generally Ar) is flowed within the reactor using a Mass Flow Controller (Bruker). After purging with Ar (15 mL min^{-1}) for 30 min, the reactor containing the suspension is irradiated with a Solar Simulator (LOT-Oriel) mounting a 150 W Xe lamp and some optical filters, in order to better adjust the light beam to the desired characteristics. In this case, a cut-off filter at λ = 420 nm and a heat adsorbing filter removing all photon with $\lambda < 850$ nm have been employed. Irradiance was ~ 6×10^{-3} W m^{-2} in the UV-A range and ~ 1800 W m^{-2} in the visible range (420 - 850 nm). The concentration of H_2 in gas stream coming from the reactor has been quantified using an Agilent 7890 gas chromatograph equipped with a TCD detector, connected to a Carboxen 1010 column (Supelco, 30 m × 0.53 mm ID, 30 μm film) using Ar as carrier. Notably, the amount of catalyst has been optimized following the indications recently presented by Kisch and Bahnenmann[29] using the **Calix-Th**/Pt/TiO_2 photocatalyst.

In AQY experiments, 10 mg of photocatalyst were suspended in 10 mL of 10% v/v aqueous solution of TEOA/HCl in a 20 mL head-space vial sealed with a gas-tight cap. The vial was sonicated for 10 min and purged with Ar (15 mL min^{-1}) for 30 min. Then, the catalyst was irradiated using a 150 W Xe lamp equipped with a Thorlabs 450 ± 40 nm bandpass filter and H_2 accumulated in the headspace volume of the vial for 15 h. In these conditions, the light power was ~ 10.4 mW cm^{-2}. The concentration of H_2 in the vial after 16 h of irradiation with monochromatic light was quantified using an Agilent 7890 gas chromatograph equipped with a TCD detector, connected to a MolSIEVE 5 Å column (Restek, 30 m × 0.53 mm ID, 30 μm film) using Ar as carrier. 250 μL of He were injected in the vial before the analysis as an internal standard. UV-vis spectra of the aqueous solutions recovered at the end of the photocatalytic runs highlighted that no desorption of the dyes took place during the experiments.

3.5.6 Synthetic procedures

NMR spectra were recorded with a Bruker Advance Neo and a Bruker Advance 400 spectrometers operating at 400 MHz (^1H) and 100 MHz (^{13}C). Coupling constants are given in Hz. Absorption spectra were recorded with a V-570 Jasco spectrophotometer. High resolution mass spectra have been recorded with an Agilent 6230B Time of Flight (TOF) equipped with an electrospray (Dual ESI) source. Flash chromatography was performed with Merck grade 9385 silica gel 230–400 mesh (60 Å). Reactions performed under inert atmosphere were done in oven-dried glassware and a nitrogen atmosphere was generated with Schlenk technique. Conversion was monitored by thin-layer chromatography by using UV light (254 and 365 nm) as a visualizing agent. All reagents were obtained from commercial suppliers at the highest purity grade and used without further purification. Anhydrous solvents were purchased from commercial suppliers and used as received. Extracts were dried with Na_2SO_4 and filtered before removal of the solvent by evaporation. 5,17-diformyl-25,27-dipropoxycalix[4]arene was synthesized according to literature.[7]

5,17-dimethyl-25,27-dipropoxycalix[4]arene (2): To a solution of 5,17-diformyl-25,27-dipropoxycalix[4]arene **1** (3.55 g, 6.29 mmol) in 100 mL of a 1:1 mixture of toluene and ethanol were added zinc (18.12 g, 275 mmol) and, dropwise, HCl 37% (25 mL). The reaction was refluxed for 2 h and checked by TLC (hexane-ethyl acetate, 1:1, v/v). The zinc was then decanted off, the organic phase was washed with water (3 × 150 mL) and the solvent evaporated to dryness. The yellow solid (3.11 g, 5.79 mmol) obtained in 93% yield did not need further purification. m.p. 230 °C. ^{1}H NMR (400 MHz, $CDCl_3$): δ 8.11 (s, 2H), 6.96 (d, *J* = 7.6 Hz, 4H), 6.87 (s, 4H), 6.78 (t, *J* = 7.6 Hz, 2H), 4.32 (d, *J* = 12.8 Hz, 4H), 3.99 (t, *J* = 6.4 Hz, 4H), 3.34 (d, *J* = 12.8 Hz, 4H), 2.22 (s, 6H), 2.09 (sextet, *J* = 6.8 Hz, 4H), 1.32 (t, *J* = 7.2 Hz, 6H). ^{13}C NMR (100 MHz, $CDCl_3$): δ 152.0, 150.9, 133.8, 128.9, 128.8, 128.0, 127.8, 125.2, 78.3, 31.4, 23.5, 20.5, 10.9.

5,17-dimethyl-25,26,27,28-tetrapropoxycalix[4]arene (3): To a solution of 5,17-dimethyl-25,27-dipropoxycalix[4]arene **2** (3.11 g, 5.79 mmol) in anhydrous DMF (130 mL) under nitrogen atmosphere were added NaH 60% (2.23 g, 32.1 mmol) and iodopropane (4.52 mL, 46.3 mmol). The mixture was stirred at room temperature overnight and the reaction checked by TLC (hexane-ethyl acetate, 9:1, v/v). Addition of HCl 1 M (100 mL) resulted in the precipitation of the product that was filtered and purified by trituration in hexane obtaining a white solid (3.48 g, 5.61 mmol) in 97% yield. m.p. 189-190 °C. ^{1}H NMR (400 MHz, $CDCl_3$): δ 6.58 (m, 6H), 6.53 (s, 4H), 4.45 (d, *J* = 13.6 Hz, 4H), 3.86 (t, *J* = 7.6 Hz, 8H), 3.13 (d, *J* = 13.6 Hz, 4H), 2.11 (s, 6H), 1.95 (sextet, *J* = 7.6 Hz, 8H), 0.99-1.05 (m, 12H). ^{13}C NMR (100 MHz, $CDCl_3$): δ 156.4, 154.7, 135.0, 134.9, 130.7, 128.8, 128.0, 121.9, 76.7, 31.0, 23.3, 23.2, 20.8, 10.4, 10.3.

5,17-dibromo-11,23-dimethyl-25,26,27,28-tetrapropoxycalix[4]arene (Calix-Br): To a solution of 5,17-dimethyl-25,26,27,28-tetrapropoxycalix[4]arene **3** (2.53 g, 4.07 mmol) in anhydrous DMF (90 mL) under nitrogen atmosphere was added *N*-bromosuccinimide (1.45 g, 8.14 mmol). The mixture was stirred at room temperature overnight and the reaction checked by TLC (hexane-DCM, 8:2, v/v). Addition of HCl 0.1 M (100 mL) resulted in the precipitation of the product that was filtered and purified by crystallization in DCM-methanol obtaining a white solid (0.69 g, 0.89 mmol) in 21% yield. m.p. 243-245 °C. ^{1}H NMR (400 MHz, $CDCl_3$): δ 6.75 (s, 4H), 6.54 (s, 4H), 4.39 (d, *J* = 13.6 Hz, 4H), 3.80-3.87 (m, 8H), 3.08 (d, *J* = 13.6 Hz, 4H), 2.15 (s, 6H), 1.89-1.95 (m, 8H), 0.96-1.04 (m, 12H). ^{13}C NMR (100 MHz, $CDCl_3$): δ 155.5, 154.5, 137.0, 134.2, 131.4, 130.6, 129.0, 114.7, 76.9, 76.8, 30.9, 23.2, 23.1, 20.8, 10.3, 10.2.

Calix-Th-CHO (6): Calix-Br (122 mg, 0.16 mmol) and $Pd(dppf)Cl_2 \cdot CH_2Cl_2$ (13 mg, 0.016 mmol) were dissolved in dry toluene 2.5 mL and stirred for 15 min under nitrogen atmosphere. Then (5-formyl thiophene-2-yl)boronic acid (59 mg, 0.38 mmol) and methanol (2.5 mL) were added and the solution was stirred for 15 min under nitrogen atmosphere. In the end, K_2CO_3 (220 mg, 1.6 mmol) was added to the solution and the reaction was performed with microwave irradiation (80 °C, 70 W, 90 min) and then quenched by pouring into a saturated solution of NH_4Cl (40 mL) and AcOEt (40 mL). Filtration on Celite and extractions with organic solvent allowed to isolate the crude product, subsequently purified through column chromatography on silica gel (*n*-heptane/AcOEt, 4:1). The desired product was isolated as a light-yellow solid (40 mg, 0.48 mmol) with 30% yield. ^{1}H NMR (400 MHz, $CDCl_3$) δ 9.63 (s, 2H), 7.33 (d, *J* = 4.0 Hz, 2H), 6.78 (s, 4H), 6.73 (d, *J* = 4.0 Hz, 2H), 6.63 (s, 4H), 4.43 (d, *J* = 13.4 Hz, 4H), 3.94 (dd, *J* = 8.9, 7.1 Hz, 4H), 3.76 (t, *J* = 7.0 Hz, 4H), 3.12 (d, *J* = 13.4 Hz, 4H), 2.28 (s, 6H), 1.99 - 1.83 (m, 8H), 1.06 (t, *J* = 7.4 Hz, 6H), 0.93 (t, *J* = 7.5 Hz, 6H).

Calix-Th: Calix-Th-CHO (43 mg, 0.05 mmol), cyanoacetic acid (43 mg, 0.5 mmol), and piperidine (51 mg, 0.6 mmol) were dissolved in 4 mL of a mixture of dry CH_3CN and dry toluene (3:1) and warmed to reflux for 5 h. After having the solvent evaporated, 10 mL of a solution of HCl 10% was added and the mixture was left under magnetic stirring for 2 h at room temperature. The aqueous phase was extracted with CH_2Cl_2 and the organic layers dried. The solvent was evaporated, and the product was obtained as a dark red solid (36 mg, 0.04 mmol, 80%). mp 219-220 °C (d) FT-IR ν/(cm^{-1}): 2961, 2923, 2872, 2216, 1690 (strong), 1573 (strong), 1413 (strong), 1216 (strong), 1070. ^{1}H NMR (400 MHz, DMSO) δ 8.18 (s, 2H), 7.60 (d, *J* = 4.0 Hz, 2H), 6.97 (d, *J* = 4.0 Hz, 2H), 6.81 (s, 4H), 6.71 (s, 4H), 4.33 (d, *J* = 13.2 Hz, 4H), 3.89 - 3.82 (m, 4H), 3.79 (t, *J* = 7.0 Hz, 4H), 3.22 (d, *J* = 13.3 Hz, 4H), 2.13 (s, 6H), 1.96 - 1.80 (m, 8H), 1.03 (t, *J* = 7.4 Hz, 6H), 0.96 (t, *J* = 7.4 Hz, 6H). ^{13}C NMR (101 MHz, DMSO) δ 164.12, 157.80, 154.72, 154.57, 146.60, 141.07, 135.69, 134.80, 133.95, 131.24, 129.38, 126.58, 126.18, 123.53, 116.91, 97.80, 76.94, 76.69, 30.51, 23.39, 23.13, 20.82, 10.82, 10.55. HRMS (Dual-ESI) *m/z*: $[M\text{-}H^+]^-$ calcd for $C_{58}H_{58}N_2O_8S_2$, 973.3562; found 973.3563. Δ(ppm) = 0.10.

Calix-TTh1 (4): Calix-Br (250 mg, 0.32 mmol) and Pd(dppf)$Cl_2 \cdot CH_2Cl_2$ (26 mg, 0.03 mmol) were dissolved in toluene 2.5 mL and stirred for 15 min under nitrogen atmosphere. Then thieno[3,2-b]thiophene-2-boronic acid (141 mg, 0.77 mmol) and methanol (2.5 mL) were added and the solution was stirred for 15 min under nitrogen atmosphere. In the end, K_2CO_3 (442 mg, 3.2 mmol) was added to the solution and the reaction was performed with microwave irradiation (100 °C, 70 W, 90 min) and then quenched by pouring into a saturated solution of NH_4Cl (40 mL) and AcOEt (40 mL). Filtration on Celite and extractions with organic solvent allowed to isolate the crude product, which was dried on sodium sulfate and, then purified through column chromatography on silica gel (*n*-heptane/AcOEt, 95:5). The desired product was isolated as a light-yellow solid (110 mg, 0.12 mmol) with 38% yield. ^{1}H NMR (400 MHz, $CDCl_3$) δ 7.21 (dd, *J* = 2.9, 2.3 Hz, 4H), 7.10 - 7.03 (m, 6H), 6.35 (s, 4H), 4.45 (d, *J* = 13.2 Hz, 4H), 4.00 - 3.89 (m, 4H), 3.79 (t, *J* = 7.3 Hz, 4H), 3.15 (d, *J* = 13.3 Hz, 4H), 2.02 - 1.85 (m, 14H), 1.04 (t, *J* = 7.4 Hz, 6H), 0.97 (t, *J* = 7.5 Hz, 6H).

Calix-TTh-CHO (7): Distilled $POCl_3$ (184 mg, 1.2 mmol) was added dropwise to anhydrous DMF (88 mg, 1.2 mmol) at -5 °C under nitrogen atmosphere; at the end of the addition a white solid formed, that, after 30 min, was dissolved in dry $CHCl_3$ (3 mL). Product **4** (110 mg, 0.12 mmol) was dissolved in 12 mL of dry $CHCl_3$, was added and the mixture warmed at 70 °C for 8 h. The solution was quenched by pouring it into a solution of K_2CO_3 (30 mL) and the mixture was extracted with CH_2Cl_2 (2 × 20 mL), the organic phases were combined, washed with water, and dried. Purification through filtration on silica gel, first with PE/CH_2Cl_2 (9:1) and then with PE/AcOEt 1:1 as eluent, gave the product as a yellow solid in 65% yield (75 mg, 0.08 mmol). ^{1}H NMR (400 MHz, $CDCl_3$) δ 9.67 (s, 2H), 7.36 (s, 2H), 6.88 (s, 4H), 6.78 (s, 2H), 6.54 (s, 4H), 4.45 (d, *J* = 13.3 Hz, 4H), 3.97 (dd, *J* = 9.0, 7.2 Hz, 4H), 3.74 (t, *J* = 7.0 Hz, 4H), 3.13 (d, *J* = 13.4 Hz, 4H), 2.36 (s, 6H), 2.03 - 1.79 (m, 8H), 1.08 (t, *J* = 7.4 Hz, 6H), 0.93 (t, *J* = 7.5 Hz, 6H).

Calix-TTh: **7** (75 mg, 0.08 mmol), cyanoacetic acid (76 mg, 0.89 mmol), and piperidine (91 mg, 1.07 mmol) were dissolved in 12 mL dry $CHCl_3$ and warmed to reflux for 8 h. After having the solvent evaporated, 30 mL of a solution of HCl 10% was added and the mixture was left under magnetic stirring for 2 h at room temperature. The solid that precipitated, was filtered, and washed with water. The product was isolated as a dark orange solid (65 mg, 0.06 mmol) with 75% yield. mp 229-231 °C (d) FT-IR ν/(cm^{-1}): 2962, 2924, 2873, 2218, 1690 (strong), 1572 (strong), 1413 (strong), 1218 (strong), 1070. ^{1}H NMR (400 MHz, $CDCl_3$) δ 8.14 (s, 2H), 7.50 (s, 2H), 7.06 (s, 4H), 6.52 (s, 2H), 6.39 (s, 4H), 4.45 (d, *J* = 13.3 Hz, 4H), 4.06 - 3.95 (m, 4H), 3.68 (t, *J* = 6.7 Hz, 4H), 3.13 (d, *J* = 13.5 Hz, 4H), 2.49 (s, 6H), 1.94-1.82 (m, 8H), 1.12 (t, *J* = 7.4 Hz, 6H), 0.90 (t, *J* = 7.5 Hz, 6H). HRMS (Dual-ESI) *m/z*: $[M-H^+]^-$ calcd for $C_{62}H_{58}N_2O_8S_4$, 1085.3003; found 1085.2982, Δ(ppm) = 1.93. ^{13}C NMR spectrum was not recorded due to low solubility of the compound.

Calix-ThTh-CHO (8): Calix-Br (121 mg, 0.16 mmol), dissolved in toluene (5 mL), 5'-formyl-2,2'-bithiophene-5-boronic acid (91 mg, 0.38 mmol), Pd(dppf)Cl_2 (13 mg, 0.016 mmol), K_2CO_3 (220 mg, 1.6 mmol) were added to a flask under nitrogen atmosphere, and then methanol (5 mL) was added. The reaction mixture was stirred at room temperature for about 10 min and then refluxed for 6 hours. After completion of the reaction as monitored by TLC, the mixture was quenched by pouring into a saturated solution of NH_4Cl (30 mL) and CH_2Cl_2 (30 mL). Filtration on Celite and extractions with organic solvent allowed to isolate the crude product, then purified through column chromatography on silica gel (*n*-heptane/AcOEt, 3:2). The desired product was isolated as a light-yellow solid (53 mg, 0.05 mmol) with 31% yield. ^1H NMR (400 MHz, $CDCl_3$) δ 9.76 (s, 2H), 7.50 (d, *J* = 4.0 Hz, 2H), 6.97 (d, *J* = 4.0 Hz, 2H), 6.91 (d, *J* = 3.8 Hz, 2H), 6.74 (s, 4H), 6.65 (s, 4H), 6.60 (d, *J* = 3.8 Hz, 2H), 4.44 (d, *J* = 13.3 Hz, 4H), 3.92 (dd, *J* = 8.5, 7.2 Hz, 4H), 3.79 (t, *J* = 7.2 Hz, 4H), 3.13 (d, *J* = 13.4 Hz, 4H), 2.25 (s, 6H), 2.02 - 1.84 (m, 8H), 1.05 (t, *J* = 7.4 Hz, 6H), 0.96 (t, *J* = 7.5 Hz, 6H).

Calix-ThTh: 8 (53 mg, 0.05 mmol), cyanoacetic acid (54 mg, 0.64 mmol), and piperidine (0.8 mL, 11.3 mmol) were dissolved in 8 mL of a mixture of dry toluene and dry acetonitrile (1:3) and warmed to reflux for 5 h. After having the solvent evaporated, a solution of HCl 10% was added and the mixture was left under magnetic stirring for 1 h at room temperature. The solid that precipitated, was filtered, and washed with water. The desired product was isolated as a red solid (30 mg, 0.03 mmol) with 53% yield. mp 243-244 °C (d) FT-IR $\nu/(cm^{-1})$: 2959, 2923, 2872, 2212, 1703 (weak), 1579 (strong), 1436 (strong), 1211 (strong), 791 (strong). ^1H NMR (400 MHz, DMSO) δ 8.30 (s, 2H), 7.75 (d, *J* = 3.9 Hz, 2H), 7.25 (d, *J* = 4.0 Hz, 2H), 7.21 (d, *J* = 3.8 Hz, 2H), 6.88 (d, *J* = 3.6 Hz, 2H), 6.81 (s, 4H), 6.69 (s, 4H), 4.34 (d, *J* = 13.0 Hz, 4H), 3.88 - 3.73 (m, 8H), 3.20 (d, *J* = 13.3 Hz, 4H), 2.12 (s, 6H), 1.88 (dt, *J* = 14.0, 7.1 Hz, 8H), 1.02 (t, *J* = 7.4 Hz, 6H), 0.96 (t, *J* = 7.4 Hz, 6H). HRMS (Dual-ESI) *m/z*: $[M-H^+]^-$ calcd for $C_{66}H_{62}N_2O_8S_4$, 1137.3316; found 1137.3311, Δ(ppm) = 0.44. ^{13}C NMR spectrum was not recorded due to low solubility of the compound.

Calix-boronic acid pinacol ester (5): Calix-Br (500 mg, 0.64 mmol) was dissolved in anhydrous DMF 10 mL and stirred for 15 min under nitrogen atmosphere. Then bis(pinacolato)diboron (490 mg, 1.93 mmol) and $Pd(dppf)Cl_2 \cdot CH_2Cl_2$ (52 mg, 0.06 mmol) were dissolved in others 10 mL of anhydrous DMF and added to the solution, and it was stirred for 15 min under nitrogen atmosphere. In the end, AcOK (377 mg, 3.84 mmol) was added to the solution and the reaction was heated at reflux for 2 h. It was quenched by pouring into a saturated solution of NH_4Cl (40 mL) and Et_2O (40 mL). Filtration on Celite and extractions with organic solvent allowed to isolate the crude product which was dried on sodium sulfate. After filtration, the crude product was a sticky liquid that was used for the following cross-coupling step without any further purification.

Calix-EDOT-CHO (9): 7-bromo-2,3-dihydrothieno[3,4-b][1,4]dioxine-5-carbaldehyde (90 mg, 0.36 mmol) was dissolved in toluene (5 mL) and stirred for 15 min under nitrogen atmosphere. Then **5** (131 mg, 0.15 mmol) and Pd(dppf)$Cl_2 \cdot CH_2Cl_2$ (13 mg, 0.015 mmol) were added as suspension in methanol (5 mL). In the end, K_2CO_3 (207 mg, 1.5 mmol) was added to the solution and the reaction was heated to reflux for 6 h and then quenched by pouring into mixture of a saturated solution of NH_4Cl (50 mL) and AcOEt (40 mL). Filtration on Celite and extractions with organic solvent allowed to isolate the crude product, then dried, filtered, and purified through column chromatography on silica gel (first CH_2Cl_2/PE 9:1, then CH_2Cl_2 and in the end AcOEt). The desired product was isolated as a yellow solid (71 mg, 0.074 mmol) with 49% yield. ^1H NMR (400 MHz, $CDCl_3$) δ 9.72 (s, 2H), 6.88 (s, 4H), 6.73 (s, 4H), 4.38 (d, *J* = 13.3 Hz, 4H), 4.20 (dd, *J* = 9.6, 5.2 Hz, 8H), 3.93 (dd, *J* = 9.1, 7.1 Hz, 4H), 3.66 (t, *J* = 6.8 Hz, 4H), 3.07 (d, *J* = 13.3 Hz, 4H), 2.34 (s, 6H), 2.00 - 1.81 (m, 8H), 1.05 (t, *J* = 7.4 Hz, 6H), 0.88 (t, *J* = 7.5 Hz, 6H).

Calix-EDOT: 9 (71 mg, 0.07 mmol), cyanoacetic acid (59 mg, 0.7 mmol), and piperidine (71 mg, 0.84 mmol) were dissolved in in 8 mL of a mixture of dry CH_3CN and dry toluene (3:1) and warmed to reflux for 6 h. After having the solvent evaporated, 10 mL of a solution of HCl 10% was added and the mixture was left under magnetic stirring for 3 h at room temperature. The solid that precipitated, was filtered, and washed with water. The product was isolated as a dark red solid (24 mg, 0.02 mmol) with 30% yield. mp 221-223 °C (d) FT-IR ν/(cm^{-1}): 2961, 2926, 2874, 2209, 1697 (strong), 1572 (strong), 1445 (strong), 1221 (strong), 1104 (weak), 1071. ^1H NMR (400 MHz, DMSO) δ 7.93 (s, 2H), 6.90 (s, 4H), 6.72 (s, 4H), 4.32 (t, *J* = 9.7 Hz, 12H), 3.95 - 3.83 (m, 4H), 3.68 (t, *J* = 6.6 Hz, 4H), 3.15 (d, *J* = 13.3 Hz, 4H), 2.28 (s, 6H), 2.01 - 1.86 (m, 8H), 1.08 (t, *J* = 7.4 Hz, 6H), 0.91 (t, *J* = 7.5 Hz, 6H). HRMS (Dual-ESI) *m/z*: $[M-H^+]^-$ calcd for $C_{62}H_{62}N_2O_{12}S_2$, 1089.3671; found 1089.3670, Δ = 0.09. $[M-H^+-CO_2]^-$= calcd for $C_{61}H_{62}N_2O_{10}S_2$, 1045.3773; found 1045.3762, Δ(ppm) = 0.86. $[M-H^+-2CO_2]^-$= calcd for $C_{60}H_{62}N_2O_8S_2$, 1001.3875; found 1001.3856, Δ(ppm) = 1.89. ^{13}C NMR spectrum was not recorded due to low solubility of the compound.

1-bromo-4-propoxybenzene (10): A solution of 1-bromopropane (860 mg, 6.93 mmol) in acetone (2 mL) was added dropwise to a stirred mixture of 4-bromophenol (1.01 g, 5.78 mmol) and potassium carbonate (4.0 g, 28.9 mmol) in acetone (40 mL). The stirred mixture was heated under reflux for 12 h. The potassium carbonate was filtered off and the filter was washed with acetone, water was added to the filtrate and the product was extracted into diethyl ether (twice). The combined ethereal extracts were washed with water, 10% sodium hydroxide solution (twice), water and dried over Na_2SO_4. The solvent was removed in vacuum to yield a light-yellow liquid (800 mg, 3.25 mmol, 70%). ^1H NMR (400 MHz, $CDCl_3$) δ 7.33 (d, *J* = 9.1 Hz, 2H), 6.75 (d, *J* = 9.1 Hz, 2H), 3.85 (t, *J* = 6.6 Hz, 2H), 1.87 – 1.65 (m, 2H), 1.00 (t, *J* = 7.4 Hz, 3H).

5'-(4-propoxyphenyl)-[2,2'-bithiophene]-5-carbaldehyde (11): 10 (150 mg, 0.70 mmol), dissolved in toluene (5 mL), 5'-formyl-2,2'-bithiophene-5-boronic acid (338 mg, 1.40 mmol), Pd(dppf)Cl_2 (285 mg, 0.35 mmol), K_2CO_3 (2.0 g, 14.0 mmol) were added to a flask under nitrogen atmosphere, and then methanol (5 mL) was added. The reaction mixture was degassed with N_2 at room temperature for about 60 min and then refluxed for 3 hours. After completion of the reaction as monitored by TLC, the mixture was quenched by pouring into a saturated solution of NH_4Cl (30 mL) and CH_2Cl_2 (30 mL). Filtration on Celite and extractions with organic solvent allowed to isolate the crude product, then purified through column chromatography on silica gel (*n*-heptane/AcOEt - 4:1). The desired product was isolated as a light-yellow solid (100 mg, 0.31 mmol) with 44% yield. ^1H NMR (400 MHz, $CDCl_3$) δ 9.86 (s, 1H), 7.67 (d, *J* = 3.8 Hz, 1H), 7.53 (d, *J* = 8.7 Hz, 2H), 7.31 (d, *J* = 3.8 Hz, 1H), 7.23 (d, *J* = 3.5 Hz, 1H), 7.15 (d, *J* = 3.7 Hz, 1H), 6.92 (d, *J* = 8.7 Hz, 2H), 3.96 (t, *J* = 6.6 Hz, 2H), 1.83 (dd, *J* = 14.1, 6.8 Hz, 2H), 1.05 (t, *J* = 7.4 Hz, 3H).

2-cyano-3-(5'-(4-propoxyphenyl)-[2,2'-bithiophen]-5-yl)acrylic acid (Linear ThTh): 11 (100 mg, 0.31 mmol), cyanoacetic acid (130 mg, 1.52 mmol), and piperidine (0.18 mL, 1.8 mmol) were dissolved in 10 mL of dry $CHCl_3$ and warmed to reflux for 5 h. After having the solvent evaporated, a solution of HCl 10% was added and the mixture was left under magnetic stirring for 1 h at room temperature. The brown solid that precipitated, was filtered, and washed with water. Then, it was washed with $CHCl_3$ and filtered again. The desired product was isolated as a red solid (60 mg, 0.15 mmol) with 49% yield. mp 168-169 °C (d) FT-IR ν/(cm^{-1}): 3072, 2963, 2937, 2871, 2214, 1665 (strong), 1567 (strong), 1411 (strong), 1210 (strong), 797 (strong). ^1H NMR (400 MHz, DMSO) δ 8.48 (s, 1H), 7.98 (d, *J* = 4.1 Hz, 1H), 7.65 (d, *J* = 8.7 Hz, 2H), 7.61 (d, *J* = 3.9 Hz, 1H), 7.58 (d, *J* = 4.0 Hz, 1H), 7.48 (d, *J* = 3.9 Hz, 1H), 7.00 (d, *J* = 8.8 Hz, 2H), 3.98 (t, *J* = 6.5 Hz, 2H), 1.75 (dd, *J* = 14.0, 6.9 Hz, 2H), 0.99 (t, *J* = 7.4 Hz, 3H). ^{13}C NMR (101 MHz, DMSO) δ 164.10, 159.48, 146.64, 146.20, 146.05, 141.93, 134.16, 133.38, 128.79, 127.42, 125.76, 125.12, 124.62, 117.16, 115.61, 98.60, 69.59, 22.46, 10.83. HRMS (Dual-ESI) *m/z*: $[M-H^+]^-$ calcd for $C_{21}H_{17}NO_3S_2$, 394.0577; found 394.0571, Δ(ppm) = 1.52. $[M-H^+-CO_2]^-$= calcd for $C_{20}H_{17}NO_1S_2$, 350.0679; found 350.0682, Δ(ppm) = 0.86.

References

1 Boldrini, C. L., Manfredi, N., Montini, T., Baldini, L., Abbotto, A. & Fornasiero, P. (**2021**) Calix[4]arene-based molecular photosensitizers for sustainable hydrogen production and other solar applications. *Curr. Opin. Green Sustain. Chem.,* **32**, 100534, doi:https://doi.org/10.1016/j.cogsc.2021.100534.

2 Gutsche, C. D. & Chemistry, R. S. o. *Calixarenes: An Introduction.* (RSC Publishing: Cambridge, United Kingdom, **2008**)

3 Pognon, G., Wytko, J. A., Harvey, P. D. & Weiss, J. (**2009**) Evidence for Dual Pathway in Through-Space Singlet Energy Transfers in Flexible Cofacial Bisporphyrin Dyads. *Chem. Eur. J.,* **15**, 524-535, doi:10.1002/chem.200800299.

4 Tosi, I., Segado Centellas, M., Campioli, E., Iagatti, A., Lapini, A., Sissa, C., Baldini, L., Cappelli, C., Di Donato, M., Sansone, F., Santoro, F. & Terenziani, F. (**2016**) Excitation Dynamics in Hetero-bichromophoric Calixarene Systems. *ChemPhysChem,* **17**, 1686-1706, doi:10.1002/cphc.201501065.

5 Helttunen, K. & Shahgaldian, P. (**2010**) Self-assembly of amphiphilic calixarenes and resorcinarenes in water. *New J. Chem.,* **34**, 2704-2714, doi:10.1039/C0NJ00123F.

6 Pasquale, S., Sattin, S., Escudero-Adán, E. C., Martínez-Belmonte, M. & de Mendoza, J. (**2012**) Giant regular polyhedra from calixarene carboxylates and uranyl. *Nat. Commun.,* **3**, 785, doi:10.1038/ncomms1793.

7 Gutsche, C. D., Levine, J. A. & Sujeeth, P. K. (**1985**) Calixarenes. 17. Functionalized calixarenes: the Claisen rearrangement route. *J. Org. Chem.,* **50**, 5802-5806, doi:10.1021/jo00350a072.

8 Huang, J.-F., Liu, J.-M., Xiao, L.-M., Zhong, Y.-H., Liu, L., Qin, S., Guo, J. & Su, C.-Y. (**2019**) Facile synthesis of porous hybrid materials based on Calix-3 dye and TiO_2 for high photocatalytic water splitting performance with excellent stability. *J. Mater. Chem. A,* **7**, 2993-2999, doi:10.1039/C8TA10633A.

9 Chen, Y.-F., Tan, L.-L., Liu, J.-M., Qin, S., Xie, Z.-Q., Huang, J.-F., Xu, Y.-W., Xiao, L.-M. & Su, C.-Y. (**2017**) Calix[4]arene based dye-sensitized Pt@UiO-66-NH_2 metal-organic framework for efficient visible-light photocatalytic hydrogen production. *Appl. Cat. B,* **206**, 426-433, doi: 10.1016/j.apcatb.2017.01.040.

10 Chen, Y.-F., Huang, J.-F., Shen, M.-H., Liu, J.-M., Huang, L.-B., Zhong, Y.-H., Qin, S., Guo, J. & Su, C.-Y. (**2019**) A porous hybrid material based on calixarene dye and TiO2 demonstrating high and stable photocatalytic performance. *J. Mater. Chem. A,* **7**, 19852-19861, doi:10.1039/C9TA06038C.

11 Tan, L.-L., Liu, J.-M., Li, S.-Y., Xiao, L.-M., Kuang, D.-B. & Su, C.-Y. (**2015**) Dye-Sensitized Solar Cells with Improved Performance using Cone-Calix[4]Arene Based Dyes. *ChemSusChem,* **8**, 280-287, doi:10.1002/cssc.201402401.

12 Alesi, S., Di Maria, F., Melucci, M., Macquarrie, D. J., Luque, R. & Barbarella, G. (**2008**) Microwave-assisted synthesis of oligothiophene semiconductors in aqueous media using silica and chitosan supported Pd catalysts. *Green Chem.,* **10**, 517-523, doi:10.1039/B718776A.

13 Tauc, J. (**1968**) Optical properties and electronic structure of amorphous Ge and Si. *Mater. Res. Bull.,* **3**, 37-46, doi:10.1016/0025-5408(68)90023-8.

14 Atkins, P., de Paula, J., Keeler, J. *Atkins' physical chemistry.* (Oxford University Press: Oxford, United Kingdom, **2018**)

15 Bard, A. J. & Faulkner, L. R. *Electrochemical Methods: Fundamentals and Applications.* 2nd edn, (Wiley: New York, USA, **2002**)

16 Sawyer, D. T., Roberts, J. L., Jr. & Sobkowiak, A. *Electrochemistry for chemists.* 2nd edn, (Wiley: New York, USA, **1995**)

17 Manfredi, N., Cecconi, B., Calabrese, V., Minotti, A., Peri, F., Ruffo, R., Monai, M., Romero-Ocana, I., Montini, T., Fornasiero, P. & Abbotto, A. (**2016**) Dye-sensitized photocatalytic hydrogen

production: distinct activity in a glucose derivative of a phenothiazine dye. *Chem. Commun.,* **52**, 6977-6980, doi:10.1039/c6cc00390g.

18 Arnaud-Neu, F., Böhmer, V., Dozol, J.-F., Grüttner, C., Jakobi, R. A., Kraft, D., Mauprivez, O., Rouquette, H., Schwing-Weill, M.-J., Simon, N. & Vogt, W. (**1996**) Calixarenes with diphenylphosphoryl acetamide functions at the upper rim. A new class of highly efficient extractants for lanthanides and actinides. *J. Chem. Soc., Perkin Trans. 2,* 1175-1182, doi:10.1039/P29960001175.

19 Arduini, A., Pochini, A. & Secchi, A. (**2000**) Rigid Calix[4]arene as a Building Block for the Synthesis of New Quaternary Ammonium Cation Receptors. *Eur. J. Org. Chem.,* **2000**, 2325-2334, doi:10.1002/1099-0690(200006)2000:12‹2325::AID-EJOC2325›3.0.CO;2-E.

20 McGovern, R. E., Snarr, B. D., Lyons, J. A., McFarlane, J., Whiting, A. L., Paci, I., Hof, F. & Crowley, P. B. (**2015**) Structural study of a small molecule receptor bound to dimethyllysine in lysozyme. *Chem. Sci.,* **6**, 442-449, doi:10.1039/C4SC02383H.

21 Cecconi, B., Manfredi, N., Ruffo, R., Montini, T., Romero-Ocana, I., Fornasiero, P. & Abbotto, A. (**2015**) Tuning Thiophene-Based Phenothiazines for Stable Photocatalytic Hydrogen Production. *ChemSusChem,* **8**, 4216-4228, doi:10.1002/cssc.201501040.

22 Cecconi, B., Manfredi, N., Montini, T., Fornasiero, P. & Abbotto, A. (**2016**) Dye-Sensitized Solar Hydrogen Production: The Emerging Role of Metal-Free Organic Sensitizers. *Eur. J. Org. Chem.,* **2016**, 5194-5215, doi:10.1002/ejoc.201600653.

23 Manfredi, N., Monai, M., Montini, T., Peri, F., De Angelis, F., Fornasiero, P. & Abbotto, A. (**2017**) Dye-Sensitized Photocatalytic Hydrogen Generation: Efficiency Enhancement by Organic Photosensitizer–Coadsorbent Intermolecular Interaction. *ACS Energy Lett.,* **3**, 85-91, doi:10.1021/acsenergylett.7b00896.

24 Bae, E., Choi, W., Park, J., Shin, H. S., Kim, S. B. & Lee, J. S. (**2004**) Effects of Surface Anchoring Groups (Carboxylate vs Phosphonate) in Ruthenium-Complex-Sensitized TiO_2 on Visible Light Reactivity in Aqueous Suspensions. *J. Phys. Chem. B,* **108**, 14093-14101, doi:10.1021/jp047777p.

25 Lee, S.-H., Park, Y., Wee, K.-R., Son, H.-J., Cho, D. W., Pac, C., Choi, W. & Kang, S. O. (**2010**) Significance of Hydrophilic Characters of Organic Dyes in Visible-Light Hydrogen Generation Based on TiO_2. *Org. Lett.,* **12**, 460-463, doi:10.1021/ol9026182.

26 Montini, T., Gombac, V., Sordelli, L., Delgado, J. J., Chen, X., Adami, G. & Fornasiero, P. (**2011**) Nanostructured Cu/TiO_2 Photocatalysts for H2 Production from Ethanol and Glycerol Aqueous Solutions. *ChemCatChem,* **3**, 574-577, doi:10.1002/cctc.201000289.

27 Romero Ocaña, I., Beltram, A., Delgado Jaén, J. J., Adami, G., Montini, T. & Fornasiero, P. (**2015**) Photocatalytic H_2 production by ethanol photodehydrogenation: Effect of anatase/brookite nanocomposites composition. *Inorg. Chim. Acta,* **431**, 197-205, doi:10.1016/j.ica.2015.01.033.

28 Manfredi, N., Monai, M., Montini, T., Salamone, M., Ruffo, R., Fornasiero, P. & Abbotto, A. (**2017**) Enhanced photocatalytic hydrogen generation using carbazole-based sensitizers. *Sustain. Energy Fuels,* **1**, 694-698, doi:10.1039/c7se00075h.

29 Kisch, H. & Bahnemann, D. (**2015**) Best Practice in Photocatalysis: Comparing Rates or Apparent Quantum Yields? *J. Phys. Chem. Lett.,* **6**, 1907-1910, doi:10.1021/acs.jpclett.5b00521.

Chapter 4: Photoelectrochemical Cells

4.1 General aspects

PEC is the other device able to mimic the first step of natural photosynthesis which is the solar-driven water splitting. Unlike PC, a PEC is a device capable of converting solar radiation into energy carriers through electrochemical processes, and in addition to chemical energy, it can produce electricity simultaneously.[1] The first example reported in the literature of photogenerated water splitting is a pioneering PEC made by Honda and Fujishima in 1972.[2] It was composed of a titanium dioxide-based photoactive anode and a platinum black cathode. Even if this device achieved a low efficiency, it laid the basis for future developments and studies in this direction. In a PEC, anode and cathode are connected through an external circuit and immersed in two different half-cells filled with an aqueous medium. To collect the solar radiation, anode and cathode are made by *n*- or *p*-type SC respectively and in this case, they are called photoelectrodes.[3] Depending on the photoactive electrode(s), a PEC can be set up in three different ways: a photoanode and a passive cathode, a photocathode and a passive anode, or both a photoanode and a photocathode (Figure 22). The last set-up, called tandem PEC, is the most attractive since it allows for collection of a wider solar spectrum, and it is the closest to natural photosynthesis since the device can absorb two photons and thus excite two electrons at one time. A tandem PEC could reach a theoretical solar-to-hydrogen conversion efficiency of 15%.[4]

Some examples of PECs made by pure SCs can absorb visible light, generate the electron/hole couple, and have the CB or the VB at the right potential to drive the water oxidation or the proton reduction (Figure 7). The most used SCs in these types of PECs are metal oxides and oxynitrides for the photoanode, like WO_3, Fe_2O_3, TaON, $LaTiO_2N$ and *p*-type chalcogenides and metal oxides for the photocathode, like CdTe, $CuIn_{1-x}Ga_xSe_2$, *p*-Cu_2O.[4-14] However, their efficiency is still below the threshold for commercial application. Some examples of PEC using a mixture of indium phosphate or gallium arsenide overcame that threshold, but they suffer from high instability and the use of precious non-abundant metals.[15-17]

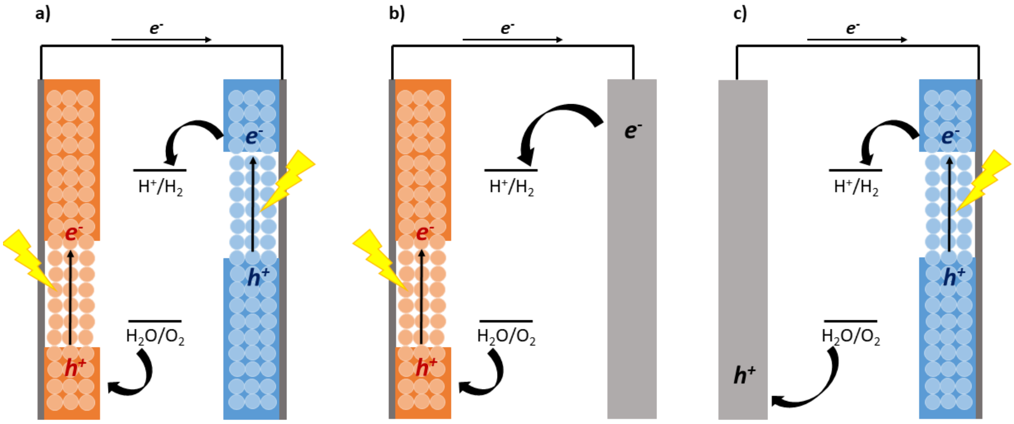

Figure 22: Examples of PEC structures. a) tandem PEC with a photoanode and a photocathode; b) PEC with a photoanode and a passive platinum cathode; c) PEC with a photocathode and a passive platinum anode.

An innovative approach for these systems can be a hybrid design in which the SCs with large band gaps are sensitized with dyes and coupled with a WOC and/or an HEC. Dyes and catalysts are required to increase the light-harvesting of the device and to accelerate the water-splitting reactions, respectively. In this way, dye-sensitized PEC (DSPEC) are defined.[1] The non-toxic nature of TiO_2, along with its low cost, chemical stability, abundance, ease of dye-sensitization, and the positions of its energy levels make it the most popular SC for a DSPEC anode, even if it presents a high charge recombination rate.[18] The most common *p*-SC used for DSPEC cathodes is NiO.[19] NiO is a mixed-valence SC consisting of Ni^{2+} and Ni^{3+} states. It has a quite wide bandgap (about 3.6-4 eV), thus it cannot compete with the dye for the light absorption. It has good thermal and chemical stability, and it is easily synthesized in the form of nanoparticles at reasonably low temperatures.[20-22] It is a good electron-donor for many sensitizers since the potential of its VB is 0.47 V vs NHE at pH 7. However, it has very low charge mobility, which favors recombination phenomena, lowering the cell performance.[22] To overcome these drawbacks, other better-performing SC are under investigation, like copper-based oxides with a delafoxitic structure as $CuGaO_2$[15-17], $CuAlO_2$[23,24] and $CuCrO_2$[25], that present a wider band-gap and better charge mobility.

The sensitization of the surface plays a central role because the dye is the strategic light-harvesting component of the photodevice. This sensitizer should be stable over long term irradiation, adsorb a large portion of the visible spectrum, and guarantee a fast charge transfer to the SC while avoiding charge recombination reactions that might reduce its efficiency.[1] The sensitizers absorb light and move to an excited state, generating an electron/hole couple. In the anode, the excited electrons are transferred to the *n*-SC CB and then into the *p*-SC VB in the cathode through the external circuit, while in the cathode the excited electrons are used by the HEC to evolve hydrogen. In the end, the WOC and the *p*-SC VB regenerate the oxidized dyes (Figure 23).

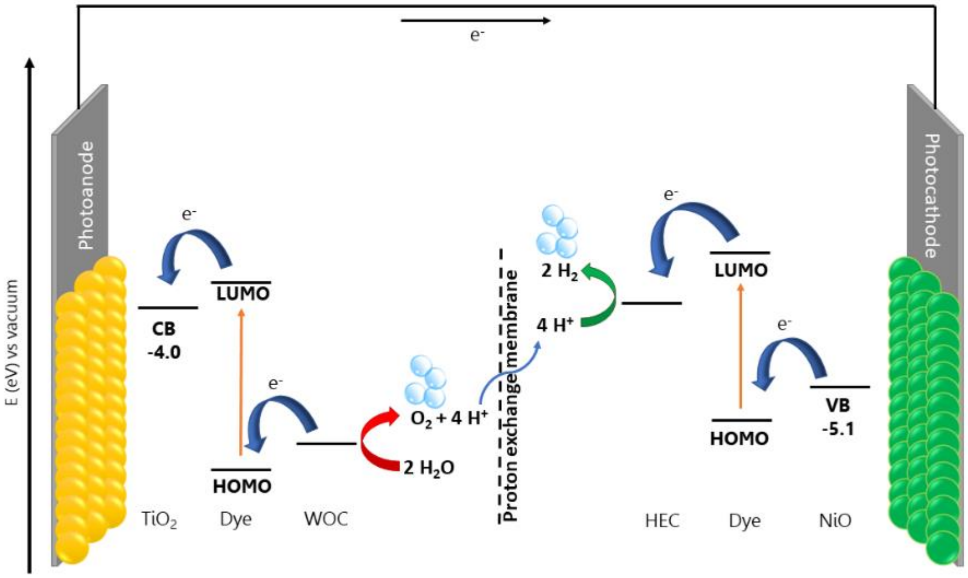

Figure 23: Scheme of the energy levels in a tandem DSPEC. Image from Ref 26.

A DSPEC is the closest device to the Z-scheme of natural photosynthesis. The photosensitizers absorb the photons and the excited electrons like the P680 and P700 dyes present in the PS II and PS I, respectively. The SC and the external circuit act as the proton-coupled electron transfer chain, and finally, the WOC and the HEC substitute the oxygen-evolving $CaMn_4$ center and the binuclear metal clusters of the hydrogenase to evolve the gases. Water oxidation is a four-electron, multi-atomic, thermodynamic energy demanding, and kinetically hampered process with a high activation barrier. Therefore, the catalytic site needs time (on the order of milliseconds) to accumulate four holes to oxidize water, while the charge recombination reactions occur on a submillisecond time scale. Because of the fast kinetics of charge recombination, which compete with the slow water oxidation, the quantum yield of the process is typically about 1-2%.[4,22]

4.2 Working principles and important parameters in DSPEC

In a tandem DSPEC, the general steps involved are the following:

Photoexcitation:

$$WOC/dye1/TiO_2||NiO/dye2/HEC \xrightarrow{2h\nu} WOC/dye1^*/TiO_2||NiO/dye2^*/HEC \qquad (1)$$

Charge separation and regeneration of the dye:

$$WOC/dye1^*/TiO_2||NiO/dye2^*/HEC \rightarrow$$
$$WOC(h^+)/dye/TiO_2(e^-)||NiO(h^+)/dye/HEC(e^-) \qquad (2)$$

Water oxidation:

$$4 \times WOC(h^+)/dye/TiO_2(e^-)||NiO(h^+)/dye/HEC(e^-) + 2H_2O \rightarrow$$
$$WOC/dye/TiO_2(e^-)||NiO(h^+)/dye/HEC(e^-) + O_2 + 4H^+ \qquad (3)$$

Proton reduction:

$$2 \times WOC/dye/TiO_2(e^-)||NiO(h^+)/dye/HEC(e^-) + 2H^+ \rightarrow$$
$$WOC/dye/TiO_2(e^-)||NiO(h^+)/dye/HEC + H_2 \qquad (4)$$

Regeneration of the photosystems:

$$WOC/dye/TiO_2(e^-)||NiO(h^+)/dye/HEC \rightarrow WOC/dye/TiO_2||NiO/dye/HEC \qquad (5)$$

Recombination reactions:

$$WOC/dye(h^+)/TiO_2(e^-)||NiO(h^+)/dye(e^-)/HEC \rightarrow$$
$$WOC/dye/TiO_2||NiO/dye/HEC \qquad (6)$$

$$WOC(h^+)/dye/TiO_2(e^-)||NiO(h^+)/dye/HEC(e^-) \rightarrow$$
$$WOC/dye/TiO_2||NiO/dye/HEC \qquad (7)$$

As in PC, the dyes are responsible for the light-harvesting of the system thus they collect the photons, exciting an electron and becoming dye* (1). Subsequently, at the photoanode, the electron is transferred to the CB of the TiO_2, and the hole to the WOC. In the same moment, at the photocathode, the electron of the second dye goes to the HEC and the hole to the NiO (2). In this step, the ground state of the dyes is regenerated. Once the WOC collects four holes, it can reduce two molecules of water to evolve a molecule of oxygen (3). In the meantime, at the cathode, the HEC uses the electrons received from the LUMO of dye2 to reduce protons and evolve molecular hydrogen (4). In the end, the electrons transferred from the LUMO of dye1 to the CB of TiO_2 are transferred to the oxidized NiO through the external circuit to restore the photosystem (5). It is not well known if the regeneration of the dye always happens before the redox reactions. The accumulation of holes and electrons in the WOC and HEC, respectively, is the main contribution to the water spilling driving force. Undesired charge recombination reactions often occur, especially between the TiO_2 and the oxidized dye or NiO and the reduced dye (6) or between the catalysts and the SC (7).[27]

The photoelectrodes are typically fluorine-doped tin oxide (FTO) or indium tin oxide (ITO) glass covered with a thin layer of the SC paste through screen-printing, spin coating, or doctor blading. In some cases, the SC nanoparticles can be prepared hydrothermally and then suspended in a cellulose/surfactant mixture. The films are then annealed at 400/500 °C to eliminate all the organic compounds and form a porous and conductive film.[21] Next, the films are sensitized in the dark by soaking in a dye and/or catalyst solution (depending on whether also the catalyst is anchored to the SC surface). Finally, the films are removed from the solution bath, washed with clean solvent, and dried under nitrogen flow. UV-vis spectroscopy is then used to evaluate the optical behavior of the photoelectrode and the dye and/or catalyst loading. High molar extinction coefficients are required to afford efficient light-harvesting even in the presence of low dye loadings. The compounds and the films are electrochemically characterized using cyclic voltammetry (CV) and differential pulse voltammetry (DPV) to evaluate the energetic levels from the oxidation and reduction potentials.[28,29] The difference between the two potentials is the bandgap. In some cases, the bandgap is calculated using a Tauc plot[30] if one of the two potentials cannot be recorded. In the end, a last characterization of the film is the X-ray photoelectron spectroscopy (XPS) measurements, especially when the catalyst is connected to the surface.[31] XPS is a surface-sensitive technique that uses binding energy to identify the elements present in a film. It identifies the atoms present on the surface and helps elucidate which bonds exist.

A DSPEC is evaluated through photoelectrochemical measurements with a three-electrode setup in an aqueous electrolyte degassed with inert gas (Figure 24). To optimize the device, the photoanode and photocathode are typically studied separately using a simple platinum wire as the counter electrode (CE). However, this set-up requires a supply of electricity (bias) to increase the electron injection into the SC and simulate the VB of *p*-SC or CB of *n*-SC. The working electrode (WE) is the investigated photoelectrode, while the reference electrode (RE) is typically an Ag/AgCl electrode. The anodic and cathodic half-cells are separated by a Nafion® film which acts as the proton exchange membrane in order to block the transit of protons from the cathode to the anode and allow only the inverse transit. The DSPEC is then irradiated with visible light to avoid the direct excitation of the TiO_2 electrons. The lamp should simulate the AM1.5 solar spectrum and should be calibrated to an intensity of 1000 W m^{-2} for measurements at one-sun intensity.[4]

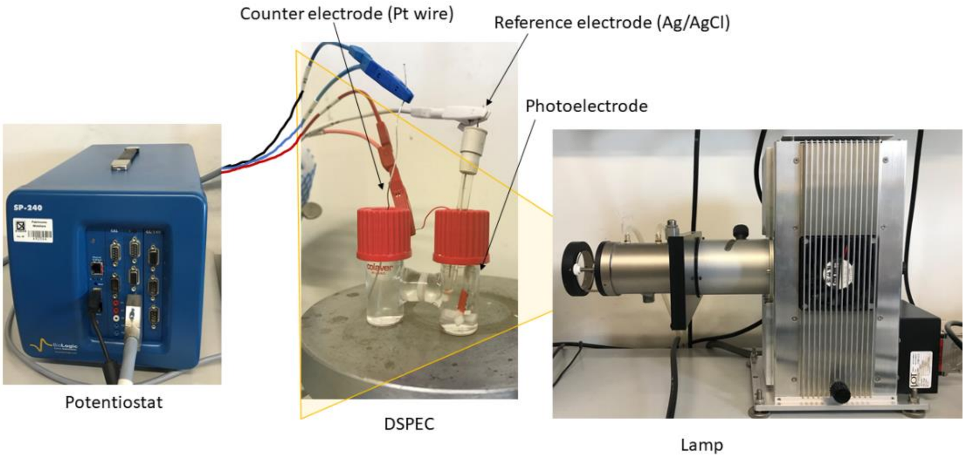

Figure 24: Schematic and pictorial representation of a three-electrode setup of a DSPEC coupled with a potentiostat and a lamp.

The first photoelectrochemical experiment is the linear sweep voltammetry (LSV), where the current density at the photoelectrode is recorded while the potential applied between the working and the reference electrode extends over a fixed range, usually normalized for the active surface area.[28,29] LSV experiments are performed both under light and in the dark to evaluate the photoactivity of the system. The current generated at every potential is expected to be almost zero when the system is in the dark, while it should show a clear signal when it is under illumination. In the LSV plot, it is possible to evaluate the potential where the difference in the generated current between dark and light is the highest (Figure 25).

This potential is then used as applied bias in the chronoamperometry (CA) measurements.[28,29] As for LSV, the current generated by the photoelectrode is recorded both under dark and light conditions. A CA measurement typically starts in the dark to record the “dark current”. After about 5 min, the device is irradiated with 1 Sun illumination and registers a spike of current. After a few seconds, the signal decreases and stabilizes to a steady value. By switching off the light, it is possible to record the amplitude of the photocurrent by the difference between the stabilized current under light and the new current in the dark. In the end, the stability of the DSPEC is evaluated through long-time measurements.

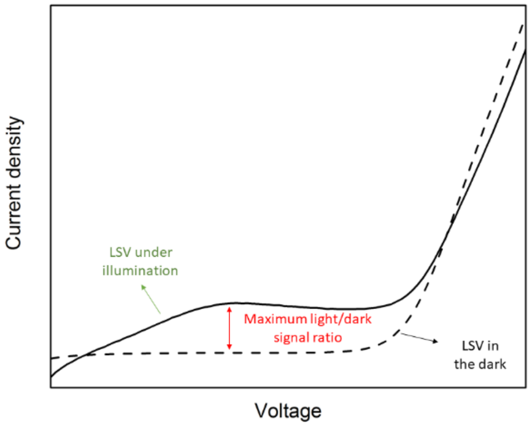

Figure 25: Graphical representation of a LSV plot.

A measurement in DSPEC aims to record the generated amounts of O_2 and H_2, which should be collected, with a stoichiometry of 1:2. This ratio should be always checked to avoid over- or underestimation due to the permeation of gases from the outside or losses from the inside, respectively. Hydrogen is typically detected by means of a thermal conductivity detector (TCD) with a gas chromatography (GC). This instrument senses changes in the thermal conductivity of the column effluent and compares it to a reference flow of carrier gas (Ar to detect H_2 or He to detect O_2).[32] Another way to measure the evolved oxygen is using a Clark electrode, which measures the gas concentration in the cell electrolyte. However, the detection of oxygen is still challenging due to the easy external contamination thus, it is more straightforward to calculate the Faradaic efficiency (FE) of the device. The FE evaluates the charge transfer in an electrochemical device. The FE is stated as the ratio between four times the moles of generated oxygen and the moles of all the electrons generated (Eq. 4.1). However, the latter can be easily evaluated as the current generated by the photoanode, while the former is difficult due to all the problems previously mentioned.

$$FE = \frac{4 \times mol\ O_2}{mol\ e^-} = \frac{n^\circ\ charges\ which\ produced\ O_2}{n^\circ\ e^-\ produced\ by\ the\ anode} \quad \text{(Eq. 4.1)}$$

The research groups of Mallouk and Meyer developed the collector-generator technique that helps overcome this problem.[33,34] This technique transforms a very-difficult-to-evaluate variable (affected, among other things, by leakage and air contamination) into a simple electric signal. The set-up is composed by two working electrodes in proximity (~400 µm). One is the photoanode, and under illumination, it oxidizes water to oxygen and records a positive current over time. The integration of that current corresponds to the total amount of electrons produced by the photoanode. The other working electrode is a simple FTO electrode kept at a reductive potential (~-0.6 V *vs* NHE) to reduce all the oxygen produced by the photoanode. Reducing the oxygen, it records a negative current, whose integration matches with the number of charges that actually produced oxygen. By the ratio between these two values and referring to the FE of the device (i.e., measured using two FTO films, one at an oxidizing potential and one at a reductive potential), it is possible to obtain the FE of the photosystem (Eq. 4.2).

$$FE(\%) = \frac{Integrated\ Area_C}{Integrated\ Area_G} \times 100 \times \frac{1}{FE_{coll}} \quad \text{(Eq. 4.2)}$$

The experiment starts with a few minutes in the dark, where the collector reduces all the oxygen present in the electrolyte medium between the two working electrodes, recording a current (Figure 26, 1). Once a plateau in the collector current is reached, all the oxygen present has been eliminated (2). In this way, the problem of external oxygen contamination is minimized. Then, the light turns on and as a result, the generator starts registering a sharp increase in current (3). At the same time, the collector begins to reduce the oxygen (produced by the generator) with only slight increase in current due to the time the oxygen takes to diffuse (4). When the light turns off, the current recorded by the generator drastically drops down (5). However, the collector still registers a current for the presence of oxygen (6), and only once all oxygen is reduced, the current returns to the plateau value (7). At this point, the experiment is concluded, and the curves can be integrated.

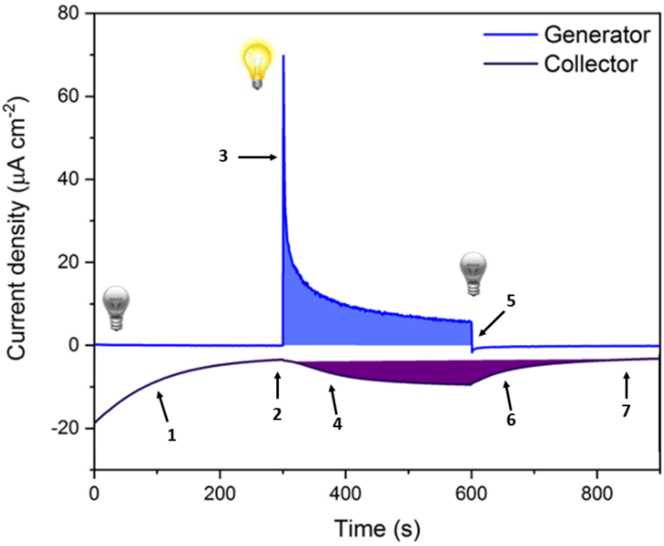

Figure 26: Example of an ideal collector-generation graph. In light blue, the current recorded by the generator and the relative integrated area. In purple, the current recorded by the collector and the relative integrated area.

An additional parameter to determine the efficiency of a DSPEC is the external quantum efficiency, commonly referred to as Incident Photon-to-Current conversion Efficiency (IPCE). IPCE(λ) is defined as the number of collected electrons under short circuit conditions per number of incident photons at a given excitation wavelength λ and provides the ability of a cell to generate current as a function of the wavelength of the incident monochromatic light.[28,29] IPCE is calculated by measuring the photocurrent at a given potential as a function of the monochromatic photon flux (Eq. 4.3).

$$IPCE(\lambda) = \frac{J_{sc}(\lambda)/_{e}}{P_{in}(\lambda)/_{h\nu}} = \frac{hc}{\lambda e} \times \frac{J_{sc}(\lambda)}{P_{in}(\lambda)} = \frac{1240}{\lambda} \times \frac{J_{sc}(\lambda)}{P_{in}(\lambda)} \quad \text{(Eq. 4.3)}$$

Where $J_{sc}(\lambda)$ and $P_{in}(\lambda)$ are the amperometric photocurrent and the power of the incident light at every wavelength, respectively. The LHE (Eq. 2.8) is usually measured to calculate the adsorbed photon-to-current efficiency (APCE) following the Eq. 4.4.

$$IPCE(\lambda) = LHE(\lambda) \times APCE\ (\lambda) \quad \text{(Eq. 4.4)}$$

Finally, in some cases, the solar-to-hydrogen efficiency (STH) is reported. This value is the efficiency of the photosystem in terms of incoming solar energy power converted into output power related to the produced hydrogen (Eq. 4.5).

$$STH\ (\%) = \frac{steady\ current\ (mA) \times FE\ (\%) \times potential\ (V)}{total\ incident\ light\ (mW)} \quad \text{(Eq. 4.5)}$$

DSPECs are still in their infancy, especially those that use a molecular approach for dyes and catalysts. However, in less than 15 years, the global interest and the number of publications in the field have quickly grown. Dyes and catalysts are the two independent components that can be engineered at the molecular level in a DSPEC. In the following paragraphs, I will present a brief overview of the most remarkable photosensitizers and WOCs for photoanode optimization. I leave the more curious readers the freedom to check out these articles on cathode optimization.[21,26,35]

4.3 Photosensitizers for photoanode in DSPEC

Photosensitizers for DSPEC photoanode should have approximately the same characteristics as the ones for DSPC, already mentioned in paragraph 1.5.2. Therefore, it is common to find the same photosensitizers in different papers covering different applications like DSSC, DSPC, and/or DSPEC. Ideally, the dye must absorb a significant fraction of the visible spectrum, convert all photons absorbed into electron-hole pairs, bind strongly to the surface of the photoelectrode, and have an appropriate redox potential to drive the catalytic water oxidation with the WOC.[4,5,36] The dye can be either chemisorbed on the surface of the SC or covalently linked to it. To obtain a stable bond with the SC oxide, the photosensitizer must present a particular anchoring site such as a carboxylic, a phosphonic, or a hydroxamic functionality, whose differences have been already discussed in paragraph 1.5.2. It is important that the energy levels of the dye match with the energy levels of the systems. Its LUMO should be at higher energy than the CB of the SC while its oxidation potential should be more positive than the redox potential of the WOC to allow the regeneration of the dye.[22,37] Moreover, the dye must be photo(electro)chemically stable and present a long-lived excited state to perform the charge transfer, and be competitive with the recombination process.[1,26] With respect to DSSC and DSPC, just a few examples of dyes have been investigated for a long time and at the beginning, they mostly presented an organometallic nature. The first example was a trisbipirydine ruthenium complex (**Ru1**, Figure 27) characterized by two phosphonic anchor groups for the SC and a malonic acid group for binding hydrated iridium oxide nanoparticles that acted as WOC.[38] In this case, the dye stabilized the WOC keeping it away from the surface to limit the charge recombination reactions between the WOC and the SC. However, this set-up exhibited a low internal quantum yield that was attributed to a faster kinetics of the back electron transfer between the SC and the dye with respect to the electron transfer from the WOC to the photo-oxidized dye. Other papers showed trisbipirydine ruthenium complexes (**Ru2**, Figure 27) which were employed due to their strong absorbance between 400 and 500 nm, their sufficiently long-lived excited state lifetime, and an oxidation potential of the Ru^{II}/Ru^{III} couple which is positive enough to drive the oxidation of the water (+1.26 V vs NHE). However, ruthenium is a rare and expensive element, and this is a notable impediment to large-scale production.[39-43] Now, more interest is turned to organometallic dyes made with abundant metals like zinc porphyrins or phthalocyanines.[44,45] They present remarkable activities, however they have complex synthetic paths characterized by difficult purification of the compounds and low yields.

In recent years, there has been a growing interest in organic dyes due to the advantages they present over their organometallic cousins. They exhibit a lower cost, easy tunability, are composed of abundant, and there is a possibility to shift their absorption maximum towards longer wavelengths just by adding conjugated double bonds. Moreover, they typically present higher molar extinction coefficients with respect to the organometallic ones.[5,46] However, they also tend to aggregate more on the surface favoring the non-radiative relaxation processes, and therefore decreasing the excited-state injection efficiency.[47-49] One category of organic dyes includes the metal-free porphyrins, characterized by a strong Soret band absorption into the blue part of the visible spectrum and weaker Q bands at longer wavelengths. Thus, they exhibit an efficient overlap with visible solar radiation.[26] However, porphyrin-sensitized photoanodes suffer from low photocurrents compared to the ruthenium counterparts due to low injection rate and slow electron self-exchange between oxidized porphyrins. In any case, their capability of exploiting red photons to perform water splitting increased the interest in this category of dyes.[41,50] In the literature, some examples of perylene-based dyes are also present. They exhibit a strong absorption in the visible region, and they have found a place in many industrial applications due to their robust nature, low cost, and chemical and thermal stability. A particular interest is aimed at the perylene diimide (PDI, Figure 27) derivatives. In these compounds, the nitrogen atom can be easily modified to insert anchor groups or to increase the steric hindrance of the molecules since these compounds suffer from strong π-π stacking aggregation. These functionalizations are also important to obtain a long-lived charge separation state to avoid the back electron transfer from the SC.[51,52] In the end, a last important category includes the push-pull dyes characterized by a D-π-A structure. In the photoanode case, the acceptor group is the closest part to the SC and brings the anchor functionality. It should help the charge separation that takes place after the solar-driven excitation, injecting the electrons into the SC. At the same time, the donor group facilitates the electron transfer to A, stabilizing the generated hole. Hence, D should be the most peripheral part and interact with the aqueous medium. Regarding this type of dye, many papers report triphenylamine-based photosensitizers with different π-spacers.[53,54] Among these, **PS1** presents good optical properties and a stable phosphonic anchor group (Figure 27). However, the photoanode exhibits low FE due to a high oxidative decomposition of the dye.[55] The same group discovered that an Al_2O_3 layer deposited by atomic layer deposition (ALD) before catalyst loading protects the dye from degradation and reduces charge recombination. Hence, they obtained around 100% in FE using a less light-harvesting triphenylamine-based dye.[54] Other studies used dibranched dyes characterized by one donor group from which two π-spacers and two acceptor groups branch off. The presence of more anchor groups enhanced the stability of the dyes reducing the desorption from the electrode.[56] Moreover, they highlighted the responsibility of the 3D structure of the dye. They presented three different dyes changing the heteroaromatic donor moiety, using phenothiazine, carbazole, and phenoxazine. They discovered that the phenothiazine-based **PTZ-Th** showed a higher oxygen production with respect to the carbazole-based one. This higher performance could partially arise from better optical properties as well as a higher IPCE compared to the other investigated dyes despite its lower loading due to the bent geometry. This 3D structure could reduce the formation of aggregates on the film and all the relative non-radiative relaxation processes.

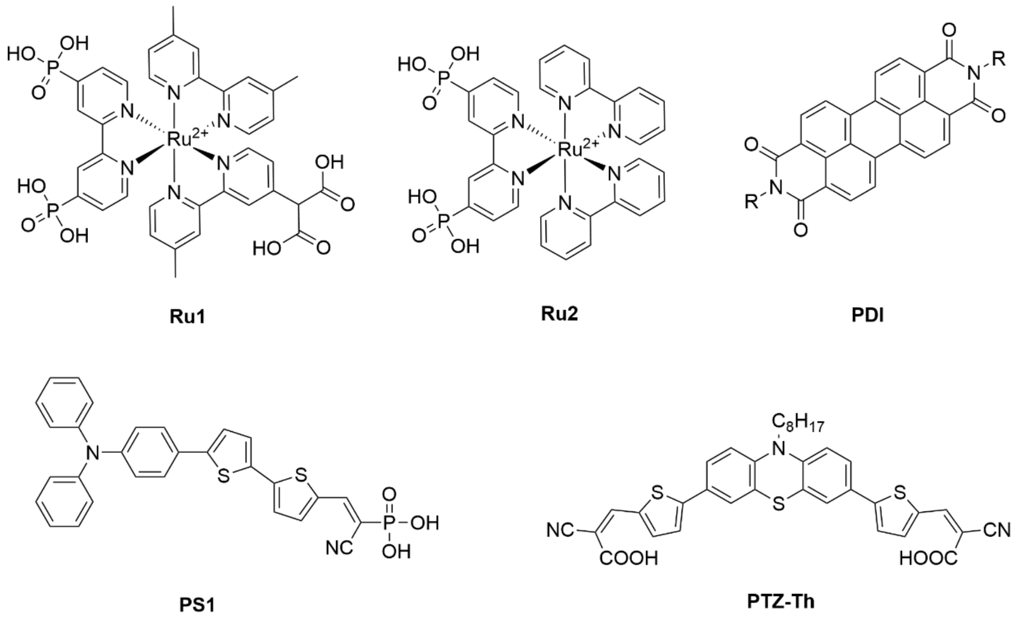
Ru1 **Ru2** **PDI**

PS1 **PTZ-Th**

Figure 27: Structures of the main photosensitizers used in DSPEC.

Together, these results highlight that organic dyes may be able to achieve the appropriate kinetic stability in DSPEC for water oxidation. If they are designed in such a way as to promote rapid regeneration of the oxidized photosensitizer, the reactions of recombination and degradation could be reduced. It is therefore necessary to develop systems that allow efficient holes transfer from the photosensitizer to the WOC.[36]

4.4 Water oxidation catalysts for DSPEC

The first request for a compound to be a WOC is to lower the water oxidation energy barrier to speed up the charge transfer. It must have a redox potential less positive with respect to the oxidation potential of the dye to ensure the regeneration of the oxidized photosensitizer. In most cases, the WOCs are metal oxide nanoparticles, like iridium oxide or cobalt oxide.[38,51,57] However, these kinds of WOCs suffers from slow electron transfer kinetics between the oxidized PS and the WOC, causing fast kinetics of back electron transfer which reduce the efficiency of the device. To overcome these problems, it is possible to add a thin layer of TiO_2 over the dye-sensitized SC and/or keep a basic environment near the electrode, since the free protons generated by the water oxidation combine with the electrons in the SC causing a drastic drop in the efficiency. Finally, an idea is to use low overpotential metal oxide, like alloys of $NiFeO_x$ or $CoFeO_x$, to speed up the kinetics of the charge transfer between oxidized dye and WOC.[4] The other possibility for WOCs is to use molecular metal complexes. The advantage of using molecular catalysts is the modulation of the electronic properties by varying the substituents on the ligands. Moreover, the investigation of the water oxidation mechanism, the active sites and the charge recombination reactions are more difficult in the metal oxides-based WOCs.[58] However, most molecular WOC are made of expensive and rare transition metals, like iridium or ruthenium. Some exceptions use earth-abundant elements, like calcium-manganese oxides[59,60] or iron complexes,[61,62]and present a TOF higher than 0.5 s^{-1} (the approximate rate achievable by the photon flux at 1 sun illumination), but their stability is very low that is not sufficient for long-lived devices.[36]

The different configurations of a DSPEC depend on the WOC, since the photosensitizer, except for a few rare cases,[63,64] is always bound to the electrode surface. In the simplest case, the WOC is solubilized or suspended in the aqueous electrolyte medium and just the diffusion, typically helped with a constant stirring of the aqueous medium, allows it to reach the SC surface and to perform the electron transfer. In the most common cases, the WOC is bound onto the electrode surface together with the photosensitizer. However, its adsorption competes with the adsorption of the dye and thus reduces the light-harvesting of the system. In the end, the most innovative strategy is to connect the WOC with the adsorbed dye using either supramolecular interactions or a covalent bond between the two entities. This last configuration allows reducing the charge recombination reactions between the WOC and the SC because the WOC is maintained away from the electrode surface by the interaction with the dye.

The first WOC that was presented in the literature is the "blue dimer", an oxo-bridged ruthenium dimer (Figure 28).[65] The system showed O_2 formation for the first 15 minutes at a rate of 330-μL h^{-1}, and then dramatically decreased. However, to be comparable with the PS II, the TOF of the WOC should be closer to 100 s^{-1}. Despite the expensive cost of these WOCs, the first systems able to achieve a speed comparable to the PS II were two ruthenium complexes $[Ru(bda)(X)_2]$ (bda = 2,2'-bipyridine-6,6'-dicarboxylate; X = 4-picoline or isoquinoline) developed by Sun and coworkers (Figure 28).[66-68] The bda equatorial ligand can chelate the ruthenium center in four positions, and it is essential to reach the seven-ligand coordination, an indispensable structure for the water oxidation.[66] In fact, the reaction kinetics need two parallel ruthenium complexes connected by two molecules of water as a bridge (Figure 29). The isoquinoline as axial ligand highly increases the TOF due to the strong π-π stacking between the isoquinoline rings which block the ruthenium dimer in the right position to perform the water oxidation.[67] However, these WOCs are always solubilized in the electrolyte medium. This configuration drastically reduces the efficiency of the photosystem since the diffusion of the WOC near the electrode rules the charge transfer, and it can also cause some charge recombination reactions between the WOC and the SC.[69]

The most common configuration regards a WOC immobilized on the SC. The first example was a [Ru(bda)(pic)$_2$] (pic = 4-picoline) immobilized onto a **RuP**-sensitized SC surface through a Nafion® film.[70] They found that a basic pretreatment of the film until pH 9.8 highly reduced the current decay rate obtaining a TOF for the complete catalytic system of 27 h^{-1}. For the first time a molecular WOC was used in combination with a dye-sensitized photoanode! Another approach is the functionalization of the WOC by adding a suitable anchor group onto one or more ligands. In most cases, the functionalization is onto an axial ligand by adding an alkyl chain characterized by the proper anchor group at one extremity (Figure 28).[40-42,55,71,72] The longer is the chain, the higher is the flexibility of the WOC. This notable feature increases the opportunity for two WOC to meet and form the two water molecules bridge.[73] Moreover, longer alkyl chains reduce the back electron transfer because of its insulating behavior and because it allows the WOC to fluctuate away from the SC surface.[73] Brudvig and coworkers presented a more rigid anchor group, that increased the stability of the photoanode for more than 20 h (**Ir1**, Figure 28).[50] However, the efficiency of the device was low, mainly due to the rigid structure of the WOC, which discouraged the combination with another iridium center to perform the water oxidation.

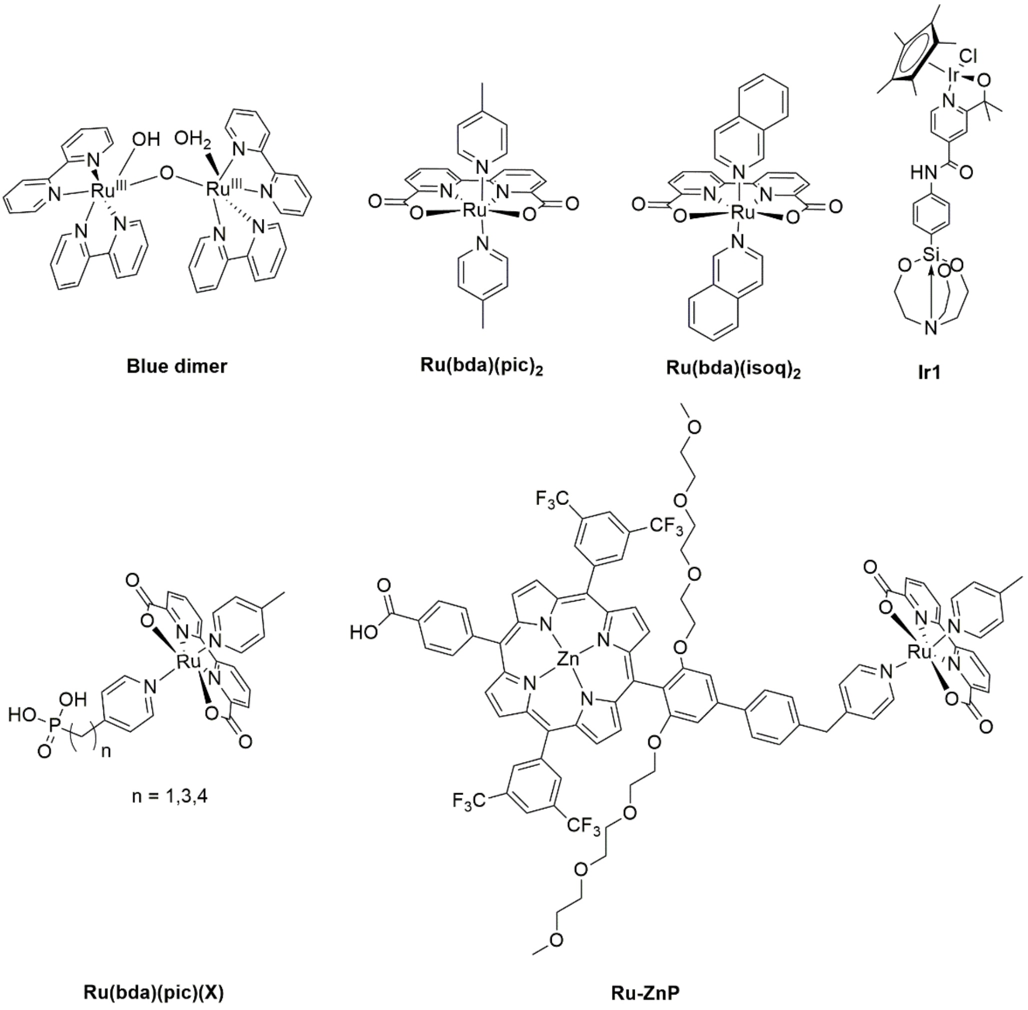
Blue dimer **Ru(bda)(pic)$_2$** **Ru(bda)(isoq)$_2$** **Ir1**

Ru(bda)(pic)(X) n = 1,3,4 **Ru-ZnP**

Figure 28: Structures of the main WOC used in DSPEC.

Finally, the most interesting configuration regards the combination of dye and catalyst in one single system, called dyad. In this case, the WOC can be covalently bound to the dye or dissolved in the medium exploiting supramolecular interactions with it that attract the WOC near the dye reducing the contacts with the SC. Among the supramolecular approaches, the most present are the host-guest,[52] the hydrophobic/hydrophilic,[74] the π-π stacking,[75,76] or the ion-mediated interactions.[77-81] On the other hand, some examples of ruthenium dimer dyads made through a bidentate ligand were published in the literature, paving the way to these new covalent designs.[80,82,83] Famous among covalent dyads is the ruthenium-based WOC–zinc porphyrin sensitizer (**Ru-ZnP**, Figure 28).[84] The benchmark [Ru(bda)(pic)$_2$] was modified by adding a zinc porphyrin to one of its axial ligands and blocking the conjugation between the dye and the catalyst with a methylene bridge to avoid back electron transfer reactions. Moreover, the long alkoxyl chains present in the structure of the porphyrin-based dye generated a protective layer from the approaching protons to the SC, which achieved an IPCE of 18% at 424 nm. The use of a covalent bond is the most promising strategy. By immobilizing the WOC away from the surface of the SC, it is possible to reduce charge recombination with the SC and develop a device that can work in flow and does not create pollution in the water.

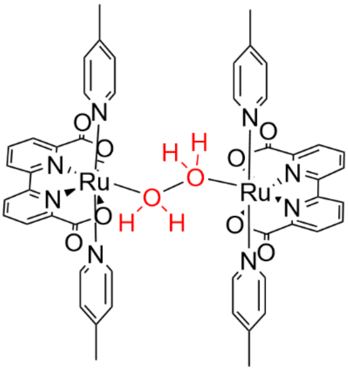

Figure 29: Schematic representation of the oxo-bridge between two ruthenium WOC while performing water oxidation.

References

1 Vlachopoulos, N. & Hagfeldt, A. (**2019**) Photoelectrochemical Cells Based on Dye Sensitization for Electricity and Fuel Production. *Chimia,* **73**, 894-905, doi:10.2533/chimia.2019.894.

2 Fujishima, A. & Honda, K. (**1972**) Electrochemical Photolysis of Water at a Semiconductor Electrode. *Nature,* **238**, 37, doi:10.1038/238037a0.

3 Niu, F., Wang, D., Li, F., Liu, Y., Shen, S. & Meyer, T. J. (**2019**) Hybrid Photoelectrochemical Water Splitting Systems: From Interface Design to System Assembly. *Adv. Energy Mater.,* **10**, 1900399, doi:10.1002/aenm.201900399.

4 Collomb, M.-N., Morales, D. V., Astudillo, C. N., Dautreppe, B. & Fortage, J. (**2020**) Hybrid photoanodes for water oxidation combining a molecular photosensitizer with a metal oxide oxygen-evolving catalyst. *Sustain. Energy Fuels,* **4**, 31-49, doi:10.1039/C9SE00597H.

5 Swierk, J. R. & Mallouk, T. E. (**2013**) Design and development of photoanodes for water-splitting dye-sensitized photoelectrochemical cells. *Chem. Soc. Rev.,* **42**, 2357-2387, doi:10.1039/C2cs35246j.

6 Asahi, R., Morikawa, T., Ohwaki, T., Aoki, K. & Taga, Y. (**2001**) Visible-Light Photocatalysis in Nitrogen-Doped Titanium Oxides. *Science,* **293**, 269-271, doi:10.1126/science.1061051.

7 Kasahara, A., Nukumizu, K., Hitoki, G., Takata, T., Kondo, J. N., Hara, M., Kobayashi, H. & Domen, K. (**2002**) Photoreactions on LaTiO$_2$N under Visible Light Irradiation. *J. Phys. Chem. A,* **106**, 6750-6753, doi:10.1021/jp025961+.

8 Kasahara, A., Nukumizu, K., Takata, T., Kondo, J. N., Hara, M., Kobayashi, H. & Domen, K. (**2003**) LaTiO$_2$N as a Visible-Light (≤600 nm)-Driven Photocatalyst (2). *J. Phys. Chem. B,* **107**, 791-797, doi:10.1021/jp026767q.

9 Li, F., Li, J., Gao, L., Hu, Y., Long, X., Wei, S., Wang, C., Jin, J. & Ma, J. (**2018**) Construction of an efficient hole migration pathway on hematite for efficient photoelectrochemical water oxidation. *J. Mater. Chem. A,* **6**, 23478-23485, doi:10.1039/C8TA07832G.

10 Ohashi, K., Uosaki, K. & Bockris, J. O. M. (**1977**) Cathodes For Photodriven Hydrogen Generators: ZnTe and CdTe. *Int. J. Energy Res.,* **1**, 25-30, doi:10.1002/er.4440010104.

11 Paracchino, A., Laporte, V., Sivula, K., Grätzel, M. & Thimsen, E. (**2011**) Highly active oxide photocathode for photoelectrochemical water reduction. *Nat. Mater.,* **10**, 456-461, doi:10.1038/nmat3017.

12 Sherman, B. D., McMillan, N. K., Willinger, D. & Leem, G. (**2021**) Sustainable hydrogen production from water using tandem dye-sensitized photoelectrochemical cells. *Nano Converg.,* **8**, 7, doi:10.1186/s40580-021-00257-8.

13 Siripala, W., Ivanovskaya, A., Jaramillo, T. F., Baeck, S.-H. & McFarland, E. W. (**2003**) A Cu$_2$O/TiO$_2$ heterojunction thin film cathode for photoelectrocatalysis. *Sol. Energy Mater. Sol. Cells,* **77**, 229-237, doi:10.1016/S0927-0248(02)00343-4.

14 Yokoyama, D., Minegishi, T., Maeda, K., Katayama, M., Kubota, J., Yamada, A., Konagai, M. & Domen, K. (**2010**) Photoelectrochemical water splitting using a Cu(In,Ga)Se$_2$ thin film. *Electrochem. Commun.,* **12**, 851-853, doi:10.1016/j.elecom.2010.04.004.

15 Yu, M., Natu, G., Ji, Z. & Wu, Y. (**2012**) *p*-Type Dye-Sensitized Solar Cells Based on Delafossite CuGaO$_2$ Nanoplates with Saturation Photovoltages Exceeding 460 mV. *J. Phys. Chem. Lett.,* **3**, 1074-1078, doi:10.1021/jz3003603.

16 Renaud, A., Chavillon, B., Le Pleux, L., Pellegrin, Y., Blart, E., Boujtita, M., Pauporté, T., Cario, L., Jobic, S. & Odobel, F. (**2012**) CuGaO$_2$: a promising alternative for NiO in *p*-type dye solar cells. *J. Mater. Chem.,* **22**, 14353-14356, doi:10.1039/C2JM31908J.

17 Xu, Z., Xiong, D., Wang, H., Zhang, W., Zeng, X., Ming, L., Chen, W., Xu, X., Cui, J., Wang, M., Powar, S., Bach, U. & Cheng, Y.-B. (**2014**) Remarkable photocurrent of *p*-type dye-sensitized solar cell

achieved by size controlled $CuGaO_2$ nanoplates. *J. Mater. Chem. A,* **2**, 2968-2976, doi:10.1039/C3TA14072E.

18 Ni, M., Leung, M. K. H., Leung, D. Y. C. & Sumathy, K. (**2007**) A review and recent developments in photocatalytic water-splitting using TiO_2 for hydrogen production. *Renew. Sustain. Energy Rev.,* **11**, 401-425, doi:10.1016/j.rser.2005.01.009.

19 Dini, D., Halpin, Y., Vos, J. G. & Gibson, E. A. (**2015**) The influence of the preparation method of NiO_x photocathodes on the efficiency of *p*-type dye-sensitized solar cells. *Coord. Chem. Rev.,* **304-305**, 179-201, doi:10.1016/j.ccr.2015.03.020.

20 Odobel, F., Le Pleux, L., Pellegrin, Y. & Blart, E. (**2010**) New Photovoltaic Devices Based on the Sensitization of *p*-type Semiconductors: Challenges and Opportunities. *Acc. Chem. Res.,* **43**, 1063-1071, doi:10.1021/ar900275b.

21 Gibson, E. A. (**2017**) Dye-sensitized photocathodes for H_2 evolution. *Chem. Soc. Rev.,* **46**, 6194-6209, doi:10.1039/C7CS00322F.

22 Xu, P., McCool, N. S. & Mallouk, T. E. (**2017**) Water splitting dye-sensitized solar cells. *Nano Today,* **14**, 42-58, doi:10.1016/j.nantod.2017.04.009.

23 Nattestad, A., Zhang, X., Bach, U. & Cheng, Y. (**2011**) Dye-sensitized $CuAlO_2$ photocathodes for tandem solar cell applications. *J. Photonics Energy,* **1**, 1-10, 10, doi:10.1117/1.3528236.

24 Koriche, N., Bouguelia, A., Aider, A. & Trari, M. (**2005**) Photocatalytic hydrogen evolution over delafossite $CuAlO_2$. *Int. J. Hydrogen Energy,* **30**, 693-699, doi:10.1016/j.ijhydene.2004.06.011.

25 Powar, S., Xiong, D., Daeneke, T., Ma, M. T., Gupta, A., Lee, G., Makuta, S., Tachibana, Y., Chen, W., Spiccia, L., Cheng, Y.-B., Götz, G., Bäuerle, P. & Bach, U. (**2014**) Improved Photovoltages for p-Type Dye-Sensitized Solar Cells Using $CuCrO_2$ Nanoparticles. *J. Phys. Chem. C,* **118**, 16375-16379, doi:10.1021/jp409363u.

26 Decavoli, C., Boldrini, C. L., Manfredi, N. & Abbotto, A. (**2020**) Molecular Organic Sensitizers for Photoelectrochemical Water Splitting. *Eur. J. Inorg. Chem.,* **2020**, 978-999, doi:10.1002/ejic.202000026.

27 Tian, H., Boschloo, G. & Hagfeldt, A. *Molecular Devices for Solar Energy Conversion and Storage.* (Springer: Singapore, Singapore **2018**)

28 Bard, A. J. & Faulkner, L. R. *Electrochemical Methods: Fundamentals and Applications.* 2nd edn, (Wiley: New York, USA, **2002**)

29 Sawyer, D. T., Roberts, J. L., Jr. & Sobkowiak, A. *Electrochemistry for chemists.* 2nd edn, (Wiley: New York, USA, **1995**)

30 Tauc, J. (**1968**) Optical properties and electronic structure of amorphous Ge and Si. *Mater. Res. Bull.,* **3**, 37-46, doi:10.1016/0025-5408(68)90023-8.

31 Moulder, J. F., Stickle, W. F., Sobol, P. E. & Bomben, K. D. *Handbook of X-ray Photoelectron Spectroscopy.* (Perkin-Elmer Corporation: Minnesota, USA, **1992**)

32 Chen, Z., Dinh, H., Miller, E., Deutsch, T., Domen, K., Emery, K., Forman, A., Gaillard, N., Garland, R., Heske, C., Jaramillo, T., Kleiman-Shwarsctein, A., Takanabe, K. & Turner, J. *Photoelectrochemical Water Splitting: Standards, Experimental Methods, and Protocols.* (Springer: New York, USA, **2013**)

33 Lee, S. H., Zhao, Y., Hernandez-Pagan, E. A., Blasdel, L., Youngblood, W. J. & Mallouk, T. E. (**2012**) Electron transfer kinetics in water splitting dye-sensitized solar cells based on core-shell oxide electrodes. *Faraday Discuss.,* **155**, 165-176, doi:10.1039/C1FD00083G.

34 Sherman, B. D., Sheridan, M. V., Dares, C. J. & Meyer, T. J. (**2016**) Two Electrode Collector-Generator Method for the Detection of Electrochemically or Photoelectrochemically Produced O_2. *Anal. Chem.,* **88**, 7076-7082, doi:10.1021/acs.analchem.6b00738.

35 Queyriaux, N., Kaeffer, N., Morozan, A., Chavarot-Kerlidou, M. & Artero, V. (**2015**) Molecular cathode and photocathode materials for hydrogen evolution in photoelectrochemical devices. *J. Photochem.*

Photobiol. C: Photochem. Rev., **25**, 90-105, doi:10.1016/j.jphotochemrev.2015.08.001.

36 Kirner, J. T. & Finke, R. G. (**2017**) Water-oxidation photoanodes using organic light-harvesting materials: a review. *J. Mater. Chem. A,* **5**, 19560-19592, doi:10.1039/C7TA05709A.

37 Yu, Z., Li, F. & Sun, L. (**2015**) Recent advances in dye-sensitized photoelectrochemical cells for solar hydrogen production based on molecular components. *Energy Environ. Sci.,* **8**, 760-775, doi:10.1039/c4ee03565h.

38 Youngblood, W. J., Lee, S. H., Kobayashi, Y., Hernandez-Pagan, E. A., Hoertz, P. G., Moore, T. A., Moore, A. L., Gust, D. & Mallouk, T. E. (**2009**) Photoassisted overall water splitting in a visible light-absorbing dye-sensitized photoelectrochemical cell. *J. Am. Chem. Soc.,* **131**, 926-927, doi:10.1021/ja809108y.

39 Ding, X., Gao, Y., Ye, L., Zhang, L. & Sun, L. (**2015**) Assembling Supramolecular Dye-Sensitized Photoelectrochemical Cells for Water Splitting. *ChemSusChem,* **8**, 3992-3995, doi:10.1002/cssc.201500313.

40 Gao, Y., Ding, X., Liu, J., Wang, L., Lu, Z., Li, L. & Sun, L. (**2013**) Visible light driven water splitting in a molecular device with unprecedentedly high photocurrent density. *J. Am. Chem. Soc.,* **135**, 4219-4222, doi:10.1021/ja400402d.

41 Swierk, J. R., Mendez-Hernandez, D. D., McCool, N. S., Liddell, P., Terazono, Y., Pahk, I., Tomlin, J. J., Oster, N. V., Moore, T. A., Moore, A. L., Gust, D. & Mallouk, T. E. (**2015**) Metal-free organic sensitizers for use in water-splitting dye-sensitized photoelectrochemical cells. *Proc. Natl. Acad. Sci. USA,* **112**, 1681-1686, doi:10.1073/pnas.1414901112.

42 Yamamoto, M., Nishizawa, Y., Chabera, P., Li, F., Pascher, T., Sundstrom, V., Sun, L. & Imahori, H. (**2016**) Visible light-driven water oxidation with a subporphyrin sensitizer and a water oxidation catalyst. *Chem. Commun.,* **52**, 13702-13705, doi:10.1039/C6CC07877J.

43 Wang, L., Shaffer, D. W., Manbeck, G. F., Polyansky, D. E. & Concepcion, J. J. (**2019**) High-Redox-Potential Chromophores for Visible-Light-Driven Water Oxidation at Low pH. *ACS Catal.*, 580-585, doi:10.1021/acscatal.9b04034.

44 Moore, G. F., Blakemore, J. D., Milot, R. L., Hull, J. F., Song, H.-e., Cai, L., Schmuttenmaer, C. A., Crabtree, R. H. & Brudvig, G. W. (**2011**) A visible light water-splitting cell with a photoanode formed by codeposition of a high-potential porphyrin and an iridium water-oxidation catalyst. *Energy Environ. Sci.,* **4**, 2389, doi:10.1039/c1ee01037a.

45 Yıldız, B., Güzel, E., Akyüz, D., Arslan, B. S., Koca, A. & Şener, M. K. (**2019**) Unsymmetrically pyrazole-3-carboxylic acid substituted phthalocyanine-based photoanodes for use in water splitting photoelectrochemical and dye-sensitized solar cells. *Sol. Energy,* **191**, 654-662, doi:10.1016/j.solener.2019.09.043.

46 Ding, X., Zhang, L., Wang, Y., Liu, A. & Gao, Y. (**2018**) Design of photoanode-based dye-sensitized photoelectrochemical cells assembling with transition metal complexes for visible light-induced water splitting. *Coord. Chem. Rev.,* **357**, 130-143, doi:10.1016/j.ccr.2017.10.020.

47 Giribabu, L., Kanaparthi, R. K. & Velkannan, V. (**2012**) Molecular engineering of sensitizers for dye-sensitized solar cell applications. *Chem. Rec.,* **12**, 306-328, doi:10.1002/tcr.201100044.

48 Hagfeldt, A., Boschloo, G., Sun, L., Kloo, L. & Pettersson, H. (**2010**) Dye-Sensitized Solar Cells. *Chem. Rev.,* **110**, 6595-6663, doi:10.1021/cr900356p.

49 Mishra, A., Fischer, M. K. R. & Bäuerle, P. (**2009**) Metal-Free Organic Dyes for Dye-Sensitized Solar Cells: From Structure: Property Relationships to Design Rules. *Angew. Chem. Int. Ed.,* **48**, 2474-2499, doi:10.1002/anie.200804709.

50 Materna, K. L., Jiang, J., Regan, K. P., Schmuttenmaer, C. A., Crabtree, R. H. & Brudvig, G. W. (**2017**) Optimization of Photoanodes for Photocatalytic Water Oxidation by Combining a Heterogenized

Iridium Water-Oxidation Catalyst with a High-Potential Porphyrin Photosensitizer. *ChemSusChem,* **10**, 4526-4534, doi:10.1002/cssc.201701693.

51 Kirner, J. T., Stracke, J. J., Gregg, B. A. & Finke, R. G. (**2014**) Visible-light-assisted photoelectrochemical water oxidation by thin films of a phosphonate-functionalized perylene diimide plus CoO_x cocatalyst. *ACS Appl. Mater. Interfaces,* **6**, 13367-13377, doi:10.1021/am405598w.

52 Lindquist, R. J., Phelan, B. T., Reynal, A., Margulies, E. A., Shoer, L. E., Durrant, J. R. & Wasielewski, M. R. (**2016**) Strongly oxidizing perylene-3,4-dicarboximides for use in water oxidation photoelectrochemical cells. *J. Mater. Chem. A,* **4**, 2880-2893, doi:10.1039/c5ta05790f.

53 Sheridan, M. V., Sherman, B. D., Coppo, R. L., Wang, D., Marquard, S. L., Wee, K.-R., Murakami Iha, N. Y. & Meyer, T. J. (**2016**) Evaluation of Chromophore and Assembly Design in Light-Driven Water Splitting with a Molecular Water Oxidation Catalyst. *ACS Energy Lett.,* **1**, 231-236, doi:10.1021/acsenergylett.6b00142.

54 Wang, D., Eberhart, M. S., Sheridan, M. V., Hu, K., Sherman, B. D., Nayak, A., Wang, Y., Marquard, S. L., Dares, C. J. & Meyer, T. J. (**2018**) Stabilized photoanodes for water oxidation by integration of organic dyes, water oxidation catalysts, and electron-transfer mediators. *Proc. Natl. Acad. Sci. USA,* **115**, 8523-8528, doi:10.1073/pnas.1802903115.

55 Wee, K.-R., Sherman, B. D., Brennaman, M. K., Sheridan, M. V., Nayak, A., Alibabaei, L. & Meyer, T. J. (**2016**) An aqueous, organic dye derivatized SnO2/TiO2 core/shell photoanode. *J. Mater. Chem. A,* **4**, 2969-2975, doi:10.1039/c5ta06678f.

56 Manfredi, N., Boldrini, C. L. & Abbotto, A. (**2018**) Organic Sensitizers for Photoanode Water Splitting in Dye-Sensitized Photoelectrochemical Cells. *ChemElectroChem,* **5**, 2395-2402, doi:10.1002/celc.201800592.

57 Kirner, J. T. & Finke, R. G. (**2017**) Sensitization of Nanocrystalline Metal Oxides with a Phosphonate-Functionalized Perylene Diimide for Photoelectrochemical Water Oxidation with a CoO_x Catalyst. *ACS Appl. Mater. Interfaces,* **9**, 27625-27637, doi:10.1021/acsami.7b05874.

58 Zhang, B. & Sun, L. (**2019**) Ru-bda: Unique Molecular Water-Oxidation Catalysts with Distortion Induced Open Site and Negatively Charged Ligands. *J. Am. Chem. Soc.,* **141**, 5565-5580, doi:10.1021/jacs.8b12862.

59 Kanady, J. S., Tsui, E. Y., Day, M. W. & Agapie, T. (**2011**) A Synthetic Model of the Mn_3Ca Subsite of the Oxygen-Evolving Complex in Photosystem II. *Science,* **333**, 733-736, doi:10.1126/science.1206036.

60 Mukherjee, S., Stull, J. A., Yano, J., Stamatatos, T. C., Pringouri, K., Stich, T. A., Abboud, K. A., Britt, R. D., Yachandra, V. K. & Christou, G. (**2012**) Synthetic model of the asymmetric $[Mn_3CaO_4]$ cubane core of the oxygen-evolving complex of photosystem II. *Proc. Natl. Acad. Sci. USA,* **109**, 2257-2262, doi:10.1073/pnas.1115290109.

61 Das, B., Lee, B.-L., Karlsson, E. A., Akermark, T., Shatskiy, A., Demeshko, S., Liao, R.-Z., Laine, T. M., Haukka, M., Zeglio, E., Abdel-Magied, A. F., Siegbahn, P. E. M., Meyer, F., Karkas, M. D., Johnston, E. V., Nordlander, E. & Akermark, B. (**2016**) Water oxidation catalyzed by molecular di- and nonanuclear Fe complexes: importance of a proper ligand framework. *Dalton Trans.,* **45**, 13289-13293, doi:10.1039/C6DT01554A.

62 Kärkäs, M. D., Laine, T. M., Johnston, E. V. & Åkermark, B. in *Applied Photosynthesis - New Progress* (ed Mohammad Mahdi Najafpour)(InTech: Rijeka, Croatia, **2016**) Ch. 10.

63 Li, F., Jiang, Y., Zhang, B., Huang, F., Gao, Y. & Sun, L. (**2012**) Towards a solar fuel device: light-driven water oxidation catalyzed by a supramolecular assembly. *Angew. Chem. Int. Ed.,* **51**, 2417-2420, doi:10.1002/anie.201108051.

64 Gao, Y., Duan, L., Yu, Z., Ding, X. & Sun, L. (**2014**) Artificial photosynthesis: photosensitizer/catalyst supramolecular assemblies for light driven water oxidation. *Faraday Discuss.,* **176**, 225-232, doi:10.1039/c4fd00127c.

65 Gersten, S. W., Samuels, G. J. & Meyer, T. J. (**1982**) Catalytic oxidation of water by an oxo-bridged ruthenium dimer. *J. Am. Chem. Soc.,* **104**, 4029-4030, doi:10.1021/ja00378a053.

66 Duan, L., Fischer, A., Xu, Y. & Sun, L. (**2009**) Isolated seven-coordinate Ru(IV) dimer complex with $[HOHOH]^-$ bridging ligand as an intermediate for catalytic water oxidation. *J. Am. Chem. Soc.,* **131**, 10397-10399, doi:10.1021/ja9034686.

67 Duan, L., Bozoglian, F., Mandal, S., Stewart, B., Privalov, T., Llobet, A. & Sun, L. (**2012**) A molecular ruthenium catalyst with water-oxidation activity comparable to that of photosystem II. *Nat. Chem.,* **4**, 418-423, doi:10.1038/nchem.1301.

68 Wang, L., Duan, L., Wang, Y., Ahlquist, M. S. G. & Sun, L. (**2014**) Highly efficient and robust molecular water oxidation catalysts based on ruthenium complexes. *Chem. Commun.,* **50**, 12947-12950, doi:10.1039/C4CC05069J.

69 Kamire, R. J., Materna, K. L., Hoffeditz, W. L., Phelan, B. T., Thomsen, J. M., Farha, O. K., Hupp, J. T., Brudvig, G. W. & Wasielewski, M. R. (**2017**) Photodriven Oxidation of Surface-Bound Iridium-Based Molecular Water-Oxidation Catalysts on Perylene-3,4-dicarboximide-Sensitized TiO_2 Electrodes Protected by an Al_2O_3 Layer. *J. Phys. Chem. C,* **121**, 3752-3764, doi:10.1021/acs.jpcc.6b11672.

70 Li, L., Duan, L., Xu, Y., Gorlov, M., Hagfeldt, A. & Sun, L. (**2010**) A photoelectrochemical device for visible light driven water splitting by a molecular ruthenium catalyst assembled on dye-sensitized nanostructured TiO_2. *Chem. Commun.,* **46**, 7307-7309, doi:10.1039/c0cc01828g.

71 Eberhart, M. S., Wang, D., Sampaio, R. N., Marquard, S. L., Shan, B., Brennaman, M. K., Meyer, G. J., Dares, C. & Meyer, T. J. (**2017**) Water Photo-oxidation Initiated by Surface-Bound Organic Chromophores. *J. Am. Chem. Soc.,* **139**, 16248-16255, doi:10.1021/jacs.7b08317.

72 Suryani, O., Higashino, Y., Mulyana, J. Y., Kaneko, M., Hoshi, T., Shigaki, K. & Kubo, Y. (**2017**) A near-infrared organic photosensitizer for use in dye-sensitized photoelectrochemical water splitting. *Chem. Commun.,* **53**, 6784-6787, doi:10.1039/c7cc02730c.

73 Gao, Y., Zhang, L., Ding, X. & Sun, L. (**2014**) Artificial photosynthesis--functional devices for light driven water splitting with photoactive anodes based on molecular catalysts. *Phys. Chem. Chem. Phys.,* **16**, 12008-12013, doi:10.1039/c3cp55204g.

74 Wang, D., Wang, L., Brady, M. D., Dares, C. J., Meyer, G. J., Meyer, T. J. & Concepcion, J. J. (**2019**) Self-Assembled Chromophore-Catalyst Bilayer for Water Oxidation in a Dye-Sensitized Photoelectrosynthesis Cell. *J. Phys. Chem. C*, doi:10.1021/acs.jpcc.9b07125.

75 Bonchio, M., Syrgiannis, Z., Burian, M., Marino, N., Pizzolato, E., Dirian, K., Rigodanza, F., Volpato, G. A., La Ganga, G., Demitri, N., Berardi, S., Amenitsch, H., Guldi, D. M., Caramori, S., Bignozzi, C. A., Sartorel, A. & Prato, M. (**2019**) Hierarchical organization of perylene bisimides and polyoxometalates for photo-assisted water oxidation. *Nat. Chem.,* **11**, 146-153, doi:10.1038/s41557-018-0172-y.

76 Li, F., Zhang, B., Li, X., Jiang, Y., Chen, L., Li, Y. & Sun, L. (**2011**) Highly efficient oxidation of water by a molecular catalyst immobilized on carbon nanotubes. *Angew. Chem. Int. Ed.,* **50**, 12276-12279, doi:10.1002/anie.201105044.

77 Bettis, S. E., Hanson, K., Wang, L., Gish, M. K., Concepcion, J. J., Fang, Z., Meyer, T. J. & Papanikolas, J. M. (**2014**) Photophysical Characterization of a Chromophore/Water Oxidation Catalyst Containing a Layer-by-Layer Assembly on Nanocrystalline TiO2 Using Ultrafast Spectroscopy. *J. Phys. Chem. A,* **118**, 10301-10308, doi:10.1021/jp411139j.

78 Ding, X., Gao, Y., Zhang, L., Yu, Z., Liu, J. & Sun, L. (**2014**) Visible Light-Driven Water Splitting in Photoelectrochemical Cells with Supramolecular Catalysts on Photoanodes. *ACS Catal.,* **4**, 2347-2350, doi:10.1021/cs500518k.

79 Wang, D., Sheridan, M. V., Shan, B., Farnum, B. H., Marquard, S. L., Sherman, B. D., Eberhart, M. S., Nayak, A., Dares, C. J., Das, A. K., Bullock, R. M. & Meyer, T. J. (**2017**) Layer-by-Layer Molecular Assemblies for Dye-Sensitized Photoelectrosynthesis Cells Prepared by Atomic Layer Deposition. *J. Am. Chem. Soc.,* **139**, 14518-14525, doi:10.1021/jacs.7b07216.

80 Brennaman, M. K., Gish, M. K., Alibabaei, L., Norris, M. R., Binstead, R. A., Nayak, A., Lapides, A. M., Song, W., Brown, R. J., Concepcion, J. J., Templeton, J. L., Papanikolas, J. M. & Meyer, T. J. (**2018**) Pathways Following Electron Injection: Medium Effects and Cross-Surface Electron Transfer in a Ruthenium-Based, Chromophore-Catalyst Assembly on TiO_2. *J. Phys. Chem. C,* **122**, 13017-13026, doi:10.1021/acs.jpcc.8b04837.

81 Wang, D., Sampaio, R. N., Troian-Gautier, L., Marquard, S. L., Farnum, B. H., Sherman, B. D., Sheridan, M. V., Dares, C. J., Meyer, G. J. & Meyer, T. J. (**2019**) Molecular Photoelectrode for Water Oxidation Inspired by Photosystem II. *J. Am. Chem. Soc.,* **141**, 7926-7933, doi:10.1021/jacs.9b02548.

82 Ashford, D. L., Song, W., Concepcion, J. J., Glasson, C. R. K., Brennaman, M. K., Norris, M. R., Fang, Z., Templeton, J. L. & Meyer, T. J. (**2012**) Photoinduced Electron Transfer in a Chromophore-Catalyst Assembly Anchored to TiO_2. *J. Am. Chem. Soc.,* **134**, 19189-19198, doi:10.1021/ja3084362.

83 Sherman, B. D., Xie, Y., Sheridan, M. V., Wang, D., Shaffer, D. W., Meyer, T. J. & Concepcion, J. J. (**2017**) Light-Driven Water Splitting by a Covalently Linked Ruthenium-Based Chromophore-Catalyst Assembly. *ACS Energy Lett.,* **2**, 124-128, doi:10.1021/acsenergylett.6b00661.

84 Yamamoto, M., Wang, L., Li, F., Fukushima, T., Tanaka, K., Sun, L. & Imahori, H. (**2016**) Visible light-driven water oxidation using a covalently-linked molecular catalyst-sensitizer dyad assembled on a TiO_2 electrode. *Chem. Sci.,* **7**, 1430-1439, doi:10.1039/c5sc03669k.

Chapter 5: Host-Guest interaction in DSPEC

Aim of this section

This section presents an innovative design for organic dyes in DSPEC where the donor moiety of a dibranched D-(π-A)$_2$ dye is functionalized with a calix[4]arene macrocycle to exploit host-guest interactions with a properly functionalized WOC. This is the first time where the host-guest properties of a calix[4]arene macrocycle are used in DSPEC applications.

We considered three different dyes and two WOCs. Two dyes had a macrocycle connected to one or two molecules of a phenothiazine-based photosensitizer, while the last one is a simple phenothiazine-based photosensitizer. We studied the influence of the calix[4]arene in the photoelectrochemical experiments. The best interaction developed between **Calix-PTZ** and **[Ru(bda)(pic)$_2$]** obtained the highest photocurrent that remained stable over time for the entire course of the experiment. On the other hand, when **[Ru(bda)(ppy)$_2$]** was used, **PTZ-Th** exhibited a photocurrent two times higher than with the other WOC, but with a sharp decrease with time. The high stability of **Calix-PTZ** proved a positive interaction with the two WOCs, but more favored in the case of **[Ru(bda)(pic)$_2$]**. These results agree with the electrochemical investigation, where the formation of more reactive species, especially in the case of **[Ru(bda)(pic)$_2$]** with **Calix-PTZ** or **PTZ-Th**, was evident.

Despite the best optical properties, the most rigid structure of **Calix-PTZ$_2$** highly reduced the possibility of interaction between the two ruthenium centers mandatory for the formation of the oxo-bridge, and this is made clear by the low photogenerated currents in every situation. This behavior was further investigated with molecular dynamics, and we found that the calix[4]arene macrocycle of **Calix-PTZ** can easily rotate around its bonds, while the one of **Calix-PTZ$_2$** is constrained between the two phenothiazine dyes, thus reducing its mobility in the system.

The oxygen evolution of these systems is still under investigation at the Mibsolar center of the University Milano-Bicocca.

5.1 Introduction

In some examples, DSPECs exploited supramolecular interactions between dye and WOC to overcome the problem of the slow diffusion of the catalyst in the electrolyte. With this arrangement, the WOC could have a great interaction with the water molecules; organize with the other WOC molecules to perform the oxo-bridge and be attracted to the electrode surface through host-guest interactions with the dye to favor the charge transfer. Moreover, this design highly reduces the difficulties in the synthesis of the molecular compounds, avoiding the formation of high-weight molecules, which can present problems of solubility and purification. With a simple modification, typically performed in one of the last steps of the synthesis with a sort of click chemistry reaction, it is possible to functionalize properly the dye and the catalyst to favor the interaction between them. The most remarkable example of this kind of interaction for DSPEC is by Sun and coworkers.[1] In that work, they functionalized a trisbipyridine ruthenium complex with a β-cyclodestrin (β-CD). On the other hand, the axial ligands of the benchmark [Ru(bda)(pic)$_2$] catalyst have been modified with two 4-phenylpyridine (ppy) (Figure 30). β-CD can easily host phenyl rings. The stabilization of the complex is achieved through van der Waals forces, hydrogen bonding, a decrease of strain energy, and the release of high-energy water molecules from the cavities.[2] CV, CA, and IPCE demonstrated the formation of the complex and the capacity of water oxidation for the supramolecular arrangement. They got further confirmation by testing the photosystem without one or both functionalization and obtaining low currents. These results highlighted the importance of developing and exploiting particular interactions between the WOC and the dye easily obtained by simple modifications of the molecular structures. These simple preparation methods, ease of tunability, and the high catalytic activity of the system are remarkable and may be of value in many solar fuel device applications.

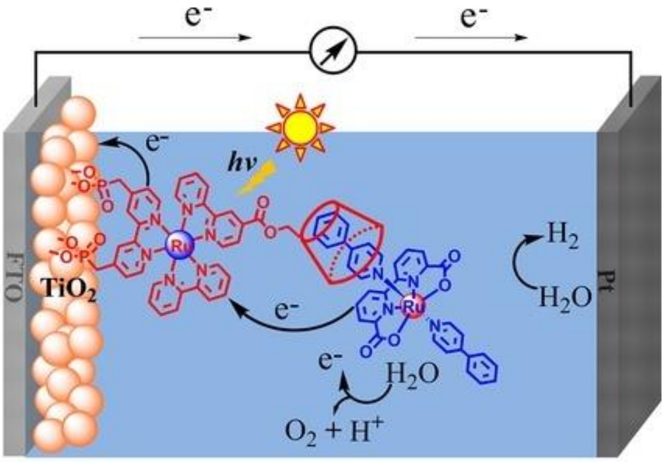

Figure 30: Schematic representation of the host-guest configuration presented by Sun et al.[1]

Few other papers present the use of supramolecular interactions between β-CD-sensitized electrodes and electrocatalysts for water or ammonia oxidation.[3] These works highlight how these interactions highly favor the catalytic process. Moreover, this configuration allows the regeneration of the electrodes by reabsorption of fresh catalyst guests.

Calixarenes are other common molecules that exploit host-guest interactions with some small molecules. They have been used in DSPEC application[4,5] as simple photosensitizers, but no one has ever studied their supramolecular properties in this field.

My group has recently reported the use of dibranched donor-(π-acceptor)$_2$ heteroaromatic sensitizers bearing different donor groups with different geometries in DSPEC, demonstrating the influence of spatial arrangements on photoelectrosynthetic properties.[6] In this work, we combined the superior host-guest properties of the *p-tert*-butylcalix[4]arene with an easy-to-synthesize metal-free organic sensitizer to investigate its interactions with different WOCs. The *p-tert*-butylcalix[4]arene derivative has bulky alkyl chains, which increase the solubility of the systems and is expected to reduce dye aggregation. Moreover, the introduction of propyl or longer alkyl chains into the lower rim blocks these systems in the cone conformation.[7] We chose to investigate two different configurations of the photosensitizer. In one case, the lower rim of a calix[4]arene macrocycle is connected to just one molecule of phenothiazine-based dibranched dye (**Calix-PTZ**); in the other, it is connected to two molecules of it (**Calix-PTZ$_2$**). The calix[4]arene structure is used to pre-organize several chromophores in one single molecule, obtaining high molar extinction coefficients and several anchor groups.[8] These photosensitizers have been studied in combination with two different WOCs, one of these bearing a 4-picoline as an axial ligand **[Ru(bda)(pic)$_2$]**, and the other a 4-phenylpyridine as an axial ligand **[Ru(bda)(ppy)$_2$]**. The results have been compared with a benchmark phenothiazine-based dye (**PTZ-Th**) functionalized with an octyl chain which cannot exploit any supramolecular interaction with the WOC (Figure 31).

5.2 Design and synthesis

The push-pull structure of the photosensitizer is a phenothiazine donor moiety from which two branches depart, bearing thienyl rings as π-spacers and cyanoacrylic acids as acceptor and anchor groups. The donor moiety is then functionalized with a *p-tert*-butylcalix[4]arene in **Calix-PTZ** and **Calix-PTZ$_2$**, while with an octyl chain in the case of **PTZ-Th**. The sensitizer **PTZ-Th** and the ruthenium catalysts **[Ru(bda)(pic)$_2$]** and **[Ru(bda)(ppy)$_2$]** were synthesized according to the literature.[9-11]

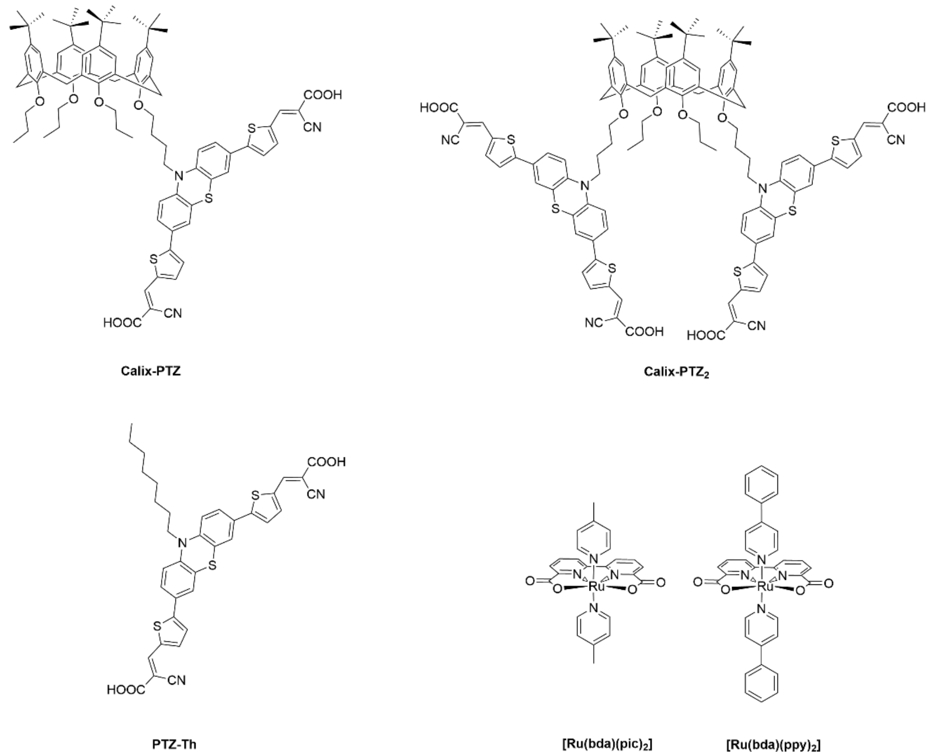

Calix-PTZ

Calix-PTZ$_2$

PTZ-Th

[Ru(bda)(pic)$_2$]

[Ru(bda)(ppy)$_2$]

Figure 31: Chemical structures of the investigated compounds.

The synthetic procedure for the preparation of the calix[4]arene intermediates **2**, **4** is depicted in Scheme 4, and the synthesis of the photoactive compounds **Calix-PTZ** and **Calix-PTZ$_2$** is depicted in Scheme 5.

Precursors 5,11,17,23-tetra-tert-butyl-25,26,27-tripropoxycalix[4]arene **1** and 5,11,17,23-tetra-tert-butyl-25,27-dipropoxycalix[4]arene **3** were synthesized according to literature procedures by the research group of Prof. Baldini at the University of Parma.[12] The alkylation reactions to give intermediates **2**, **4** are performed under an inert atmosphere in DMF using 1,4-diiodobutane in presence of NaH as base. The reactions gave the products in good yield after neutralization with 0.1 N HCl and column chromatography. The so obtained intermediates were used in the synthesis of the calix-dye molecules depicted in Scheme 5.

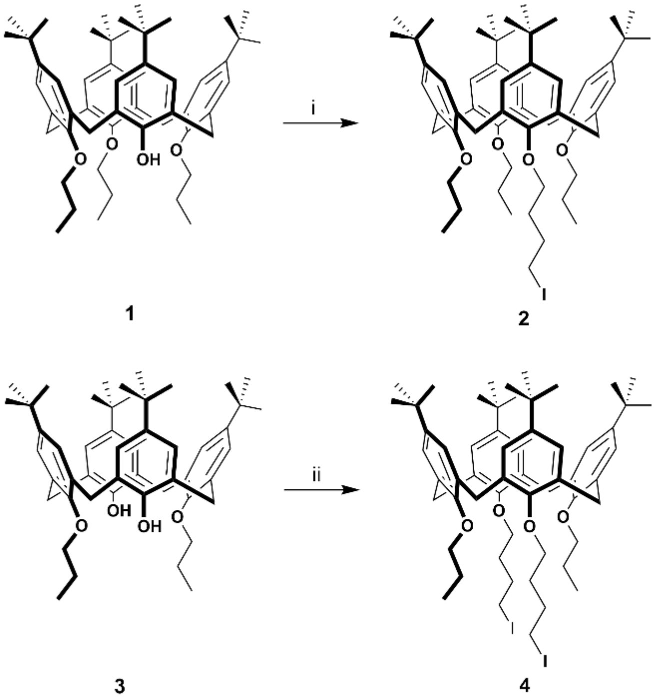

1 2 3 4

Scheme 4. Synthesis of calix[4]arene intermediates. Reagents and conditions. ii) 1,4-diiodobutane, NaH, anhydrous DMF, rt, 3 h.

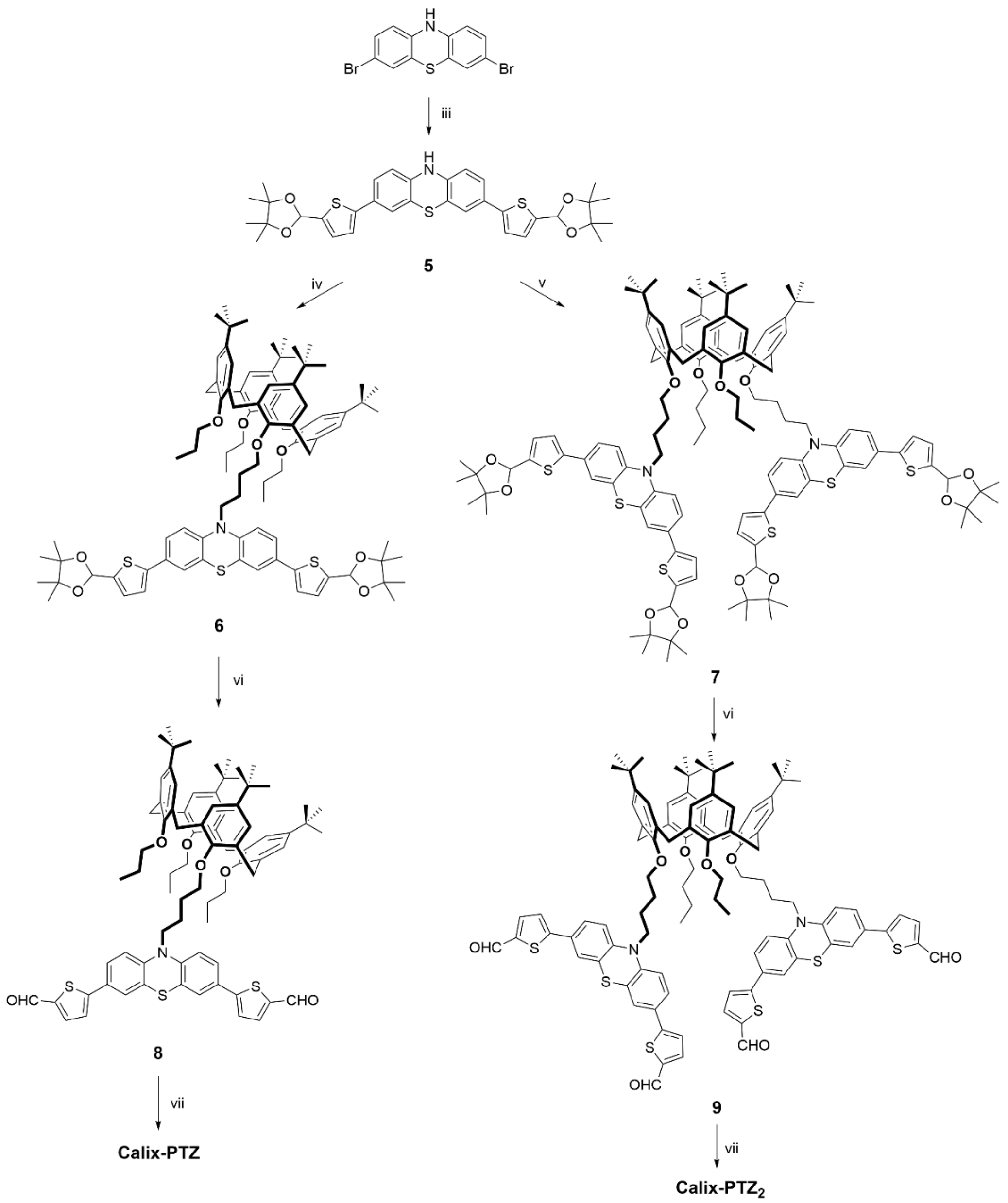

Scheme 5: Synthesis of **Calix-PTZ** and **Calix-PTZ$_2$**. Reagents and conditions. iii) 4,4,5,5-Tetramethyl-2-[5-(4,4,5,5-tetramethyl-1,3-dioxolan-2-yl)-thiophen-2-yl]-1,3,2-dioxaborolane, Pd(dppf)Cl_2, K_2CO_3, DME/MeOH 1:1 (v/v), microwave 75 W, 90 min, 90 °C; iv) **2**, NaH 60%, DMF, rt, 1 day; v) **4**, NaH 60%, anhydrous DMF, rt, 3 days; vi) THF/10% HCl_{aq} 1:2 (v/v), 50 °C, 2 h; vii) cyanoacetic acid, piperidine, $CHCl_3$, reflux, 8 h.

The synthesis started with a palladium-catalyzed Suzuki-Miyaura cross-coupling reaction between the 3,7-dibromo-10*H*-phenothiazine[13] and the 5-formylthienyl-2-boronic acid protected as pinacol ester[14] in ethylene glycol dimethyl ether and methanol under microwave irradiation. After a proper work-up and column chromatography, compound **5** was obtained with reasonable yield. The so obtained intermediate was reacted with the proper iodobutylcalix[4]arene compound, namely 1,3,4-bis-(propoxy)-2-bis-(butoxy-4-iodide)-tetrakis-*p-tert*-butylcalix[4]arene (**2**) for **Calix-PTZ** and 1,3-bis-(propoxy)-2,4-bis-(butoxy-4-iodide)-tetrakis-*p-tert*-butylcalix[4]arene (**4**) for **Calix-PTZ$_2$**. The reaction was performed under inert atmosphere in DMF in presence of sodium hydride as base for one or three days. The following reaction was the deprotection of the aldehydic functionalities performed in 10% HCl_{aq}/THF (1:2, v/v) at 50 °C for 2 h. Finally, the desired products were obtained in good yield after Knoevenagel condensation with cyanoacetic acid and piperidine in chloroform at reflux.

The photoanodes were prepared by screen-printing a 1-µm- or 3-µm-thick transparent TiO_2 layer over an FTO-coated glass. These samples were then treated with ozone for 20 minutes and soaked in a dye $2 \cdot 10^{-4}$ M DMSO/EtOH (1:15) solution overnight.

5.3 Optical and electrochemical properties

The new product, **Calix-PTZ** and **Calix-PTZ$_2$** have been optically and electrochemically characterized both in solution and adsorbed on a 1-µm TiO_2 film. The UV-Vis spectra of the sensitizers compared with the reference dye **PTZ-Th** are depicted in Figure 32 and Figure 33, respectively. The main relevant parameters are collected in Table 3.

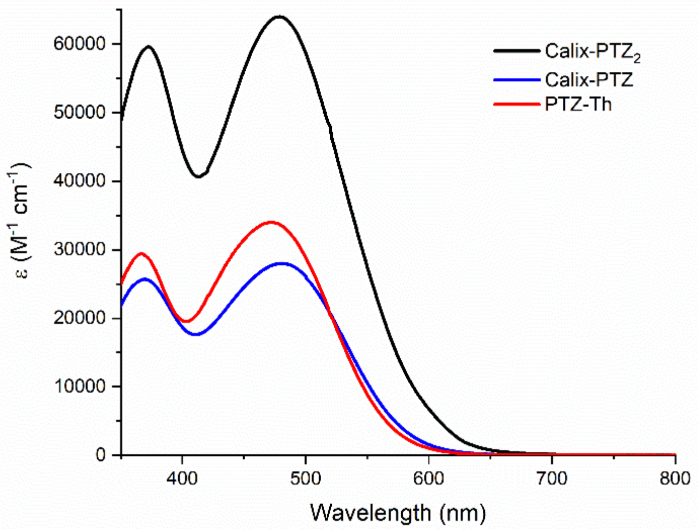

Figure 32: UV-Vis spectra in 10^{-5} DMSO solution of the investigated sensitizers.

As illustrated in Figure 32, the optical response of the dye-calix systems, **Calix-PTZ** and **Calix-PTZ$_2$**, is similar to the reference dye. Indeed, the absorption spectra of the three sensitizers are similar because the photoactive behavior of the molecule is mainly dominated by the push-pull **PTZ-Th** dye. The three dyes exhibited the same two bands structure, ascribed to the local π-π* absorption in the 350 – 400 nm range and to the ICT transition in the 400-600 nm range. The molar absorptivity is similar in **Calix-PTZ** and **PTZ-Th**, while it is almost twice in **Calix-PTZ$_2$**, in agreement with previous analogous systems reported in the literature.[8] The absorption spectra on 1-μm TiO_2 films presented a shape similar to the ones in solution (Figure 33). The absorption maxima are blue-shifted of about 30 nm, in agreement with the formation of an ester bond between the carboxylic acid and the titanium dioxide that reduces the electron-withdrawing strength of the acceptor groups.

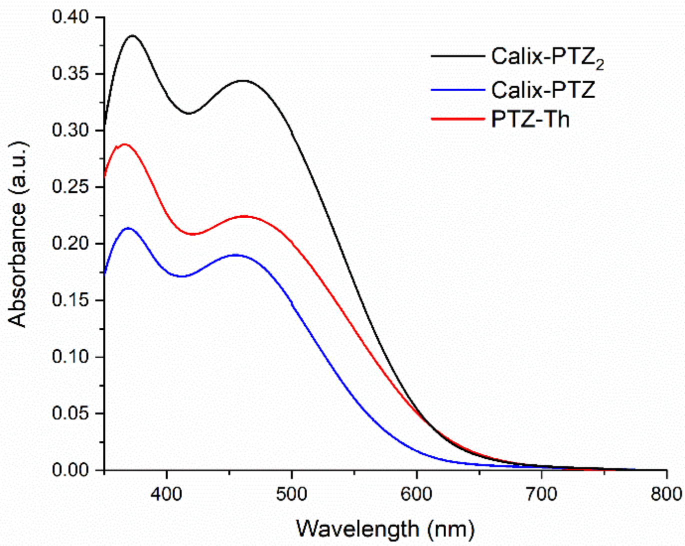

Figure 33: UV-Vis spectra on 1-µm TiO_2 films of the investigated sensitizers.

The optical bandgaps have been calculated by means of the Tauc plots[15] and listed in Table 3. It was not possible to estimate the amount of sensitizer adsorbed on the films due to the high stability of these systems even in a basic environment.

Table 3: Optical parameters of investigated sensitizers in solution and on 1-µm transparent TiO_2 film.

Sample	λ_{max}[b,c,d] (nm)	λ_{onset} [b,c,d] (nm)	ε[b] (M^{-1} cm^{-1})	E_{gap}^{opt} [b,c,d] (eV)
PTZ-Th	470 (463)	592 (657)	34000 ± 1000[a]	1.90 (1.70)
Calix-PTZ	481 (457)	594 (618)	28000 ± 1000	1.89 (1.84)
Calix-PTZ$_2$	478 (462)	624 (628)	64000 ± 1000	1.83 (1.74)

[a] Value from ref. 6. [b] Dye solution 10^{-5} M in DMSO. [c] 1-µm transparent TiO_2 photoanode. [d] Values in brackets have been recorded as films.

The electrochemical parameters are listed in Table 4. The oxidation potentials were determined using CV and DPV in solution and adsorbed onto TiO_2. In solution, all the compounds presented irreversible oxidation peaks in the CV profile, thus DPV was used (Figure 34). The potential of the first oxidation peak for each curve was considered the oxidation potential of the dye. DPV allowed discovery of a first oxidation peak that was hidden in the CV profile of **Calix-PTZ**. These oxidation potentials are positive enough to drive water oxidation and to inject excited electrons in the CB of the TiO_2 (-4 eV) from their LUMO.[16]

Table 4: Electrochemical parameters of investigated sensitizers in solution and on 3.5-µm transparent TiO_2 film.

Sample	V_{ox}[b,c] (V vs NHE) ± 10 mV		HOMO[b,c,d] (eV) ± 0.05 eV		$E_{gap}{}^{opt}$ [b,c] (eV)		LUMO [b,c,d] (eV) ± 0.05 eV	
	soln	film	soln	film	Soln	film	soln	Film
PTZ-Th	0.88	0.84	-5.38[a]	-5.48	1.90	1.70	-3.33	-3.78
Calix-PTZ	1.06	0.93	-5.66	-5.53	1.89	1.84	-3.77	-3.69
Calix-PTZ$_2$	1.02	0.93	-5.62	-5.53	1.83	1.74	-3.79	-3.79

[a] Value from Ref. 6. [b} 10^{-4} M dye solution in $TBABF_4$ 0.1 M DMF. [c] 3.5-µm transparent TiO_2 photoanode in 0.5 M KNO_3 PBS pH 6.5. [d] Vacuum potential = -4.6 – NHE.[17]

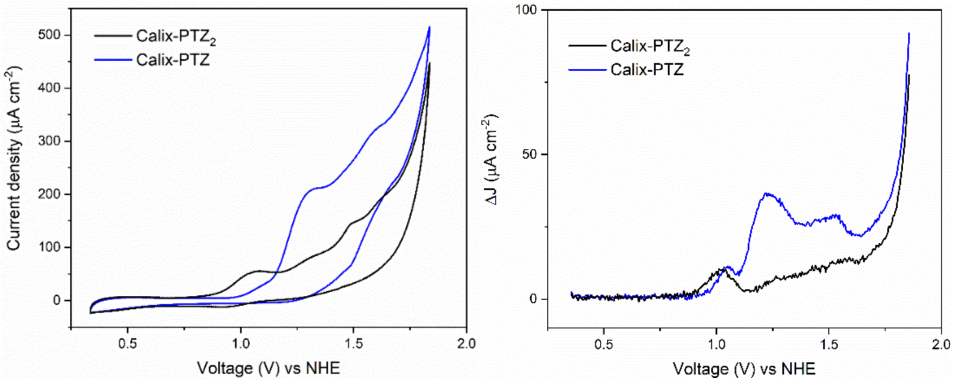

Figure 34: CV (left) and DPV (right) of the compounds recorded in $TBABF_4$ 0.1 M DMF solution.

CV measurements of the dye-sensitized photoanodes were performed using a three-electrode electrochemical cell in a phosphate buffer solution (PBS) at pH = 6.5 (Figure 35a). The photoanode acted as WE, Pt wire as CE, and Ag/AgCl (KCl 3 M) as RE. Each measurement showed an irreversible oxidative peak between +0.9 and +1.1 V *vs* NHE. **Calix-PTZ$_2$** showed its onset at the highest oxidizing potential followed by **Calix-PTZ** and then by **PTZ-Th** (Figure 35a). **PTZ-Th** presented the highest current density. The current density produced by **Calix-PTZ$_2$** is higher than **Calix-PTZ**. This behaviour might be ascribed to a better packing on the electrode surface of **Calix-PTZ$_2$** due to the presence of a more rigid structure. On the other hand, the presence of a free-to-rotate calix[4]arene macrocycle in **Calix-PTZ** highly increases the steric hindrance of the molecule, thus reducing the packing on the electrode.

The electrochemical characterization of the photoanodes was also performed with the two investigated WOCs dissolved in the electrolyte medium (Figure 35b-d). In this case, the WOC was dissolved in CF_3CH_2OH and then added into the PBS solution in the electrochemical cell (1×10^{-3} M). In all CV profiles, the current density increased with respect to the measurement without the WOC, especially at +1.2 V *vs* NHE which corresponds to the beginning of the catalytic wave for water oxidation.[18] The CV profile of all dyes with **[Ru(bda)(pic)$_2$]** widely change. In all profiles, it was possible to find the oxidation and reduction peaks of **[Ru(bda)(pic)$_2$]**. However, in **Calix-PTZ**, these peaks were shifted at +0.81 V and +0.44 V vs NHE, as compared to the +0.71 V and +0.63 V *vs* NHE of the other two cases. Moreover, the oxidation peak at +0.81 V *vs* NHE indicated the presence of the Ru^{III}/Ru^{IV} couple, that is mandatory to perform water oxidation.[18]

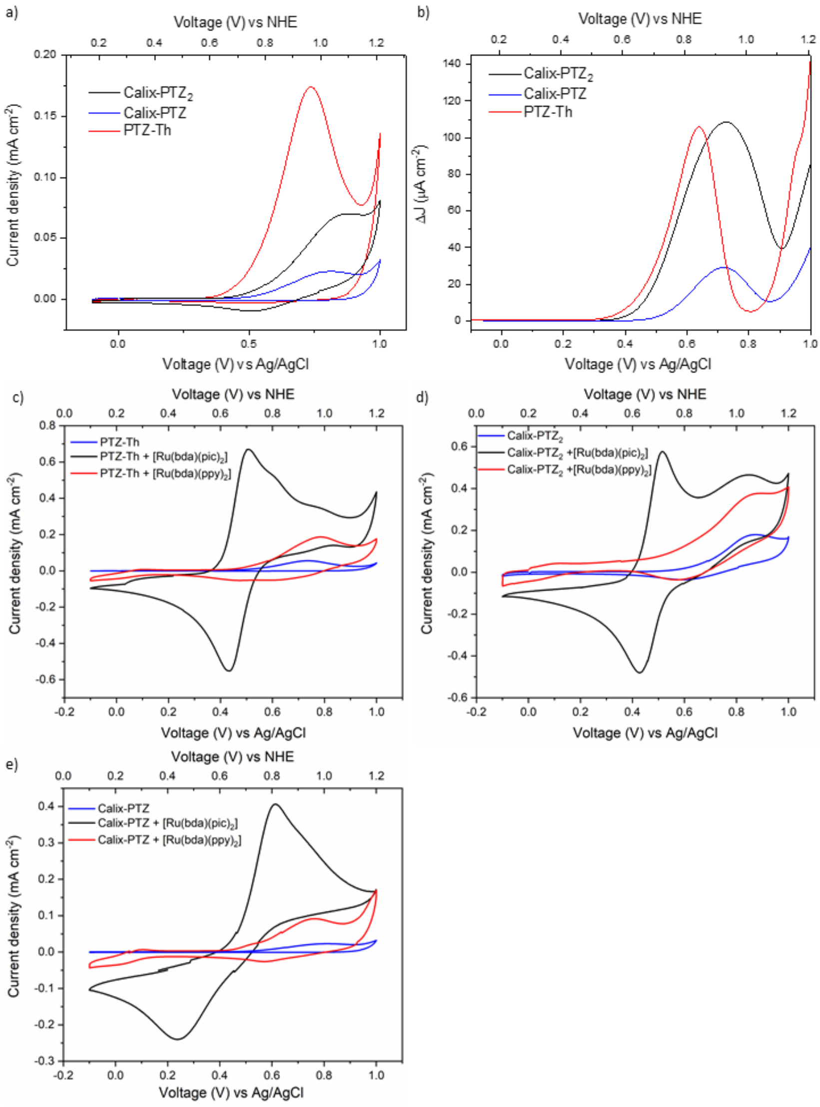

Figure 35: a) CV of the dye-sensitized photoanodes; b) DPV of the dye-sensitized photoanode; c) CV of the **PTZ-Th**-sensitized photoanode in presence or in absence of **[Ru(bda)(pic)$_2$]**, or **[Ru(bda)(ppy)$_2$]**. d) CV of the **Calix-PTZ$_2$**-sensitized photoanode in presence or in absence of **[Ru(bda)(pic)$_2$]**, or **[Ru(bda)(ppy)$_2$]**. e) CV of the **Calix-PTZ**-sensitized photoanode in presence or in absence of **[Ru(bda)(pic)$_2$]**, or **[Ru(bda)(ppy)$_2$]**. Conditions: the spectra without the catalysts were recorded in PBS electrolyte solution at pH 6.5., while the spectra with the WOC in PBS electrolyte solution +5% CF_3CH_2OH (v/v) at pH 6.5. CE = Pt wire, RE = Ag/AgCl KCl 3 M, scan rate 50 mV s^{-1}.

In **Calix-PTZ**, the peak at ~+0.70 V *vs* NHE has totally disappered, suggesting the complete formation of a more reactive species. In **PTZ-Th**, the peak at +0.81 V *vs* NHE was present as a shoulder to the main oxidation peak at +0.71 V *vs* NHE, indicating a partial formation of the Ru^{IV} species. In **Calix-PTZ$_2$**, no particular changes in the position of the peaks were evident.

On the other hand, with **[Ru(bda)(ppy)$_2$]**, every CV profile presented a reduction bump at ~+0.79 V *vs* NHE. **PTZ-Th** and **Calix-PTZ** presented an oxidation peak at ~+0.95 V *vs* NHE, while **Calix-PTZ$_2$** at ~+1.04 V *vs* NHE. In the latter case, it agrees with the oxidation peak of the dye, while in the former case this peak might be attributed to catalysis since it was slightly shifted from the oxidation peaks at +0.94 V and +0.98 V *vs* NHE of the bare **PTZ-Th** and **Calix-PTZ**, respectively. Moreover, all CV profiles presented a sort of bump at negative currents that was not present in the bare dye profiles.

In all cases, the onsets of the catalytic current resulted less positive than the oxidation potential of the dye on film, thus indicating that the photocatalytic water oxidation in these systems is thermodynamically favored.[1]

5.4 Photoelectrochemistry

The photosystems were studied in DSPEC with the same set-up used for the electrochemical investigations. LSV measurements were performed both under illumination and in the dark in presence of the two WOC (Figure 36). In both cases, the current density of **Calix-PTZ$_2$** under illumination was almost comparable to the current that is generated in the dark. With **[Ru(bda)(pic)$_2$]** the current densities generated by **Calix-PTZ** and **PTZ-Th** were almost similar at oxidative potentials higher than +0.3 V *vs* NHE (~ 20 vs 25 μA cm^{-2}).

On the other hand, with **[Ru(bda)(ppy)$_2$]**, **PTZ-Th** exhibited a current density twice as high as **Calix-PTZ** (~ 25 vs 51 $\mu A\ cm^{-2}$ at every potential). The complete inactivity in the dark for each sample confirmed the photoactivity of all the photoanodes. A bias of +0.4 V vs NHE was adopted to maximize the photocurrents in the following CA experiments.

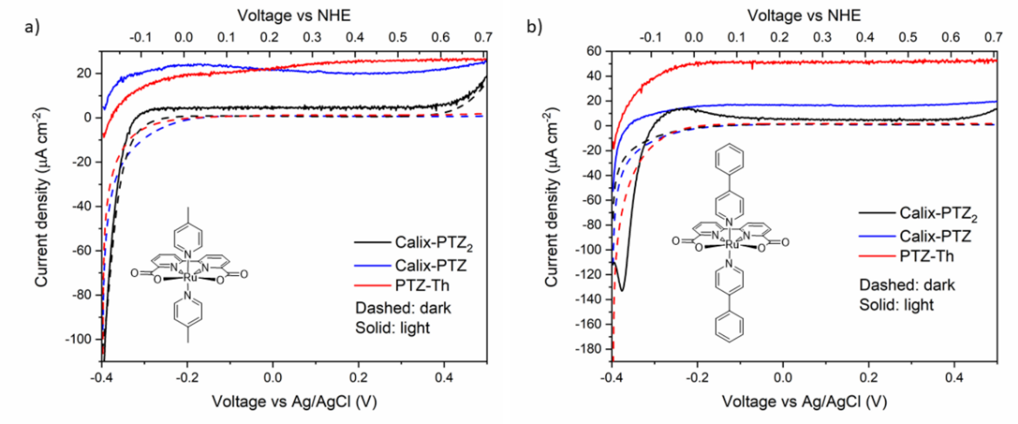

Figure 36: LSV measurements of the WE with **[Ru(bda)(pic)$_2$]** (a), or with **[Ru(bda)(ppy)$_2$]** (b) in PBS electrolyte solution and 0.5 M KNO_3 +5% CF_3CH_2OH (v/v) at pH 6.5 under illumination (200 W Xe lamp; $420<\lambda<800$ nm). CE = Pt wire, RE = Ag/AgCl (KCl 3 M), scan rate 50 mV s^{-1}.

In CA experiments, the photoanode was irradiated with white light illumination (200 W Xe lamp, $420<\lambda<800$ nm)(Figure 37). The DSPEC set-up was the same as for LSV. The measurements were performed with 5 min of one-minute-chopped illumination followed by 5 min of white light irradiation. For each cycle, a photocurrent spike was observed. This is consistent with the initial fast charge separation due to the efficient electron injection from the excited dye to the CB of TiO_2 followed by extensive hole-electron recombination.[1] The surface recombination is probably a result of the slow catalytic kinetics of the catalyst, which is unable to consume completely the photogenerated holes.[1,19] In Figure 37, it is possible to see two opposite trends for **Calix-PTZ** and **PTZ-Th**. With **[Ru(bda)(pic)$_2$]** the current density generated by **Calix-PTZ** was double with respect to **PTZ-Th** (~ 39 vs 14 μA cm^{-2}), while with **[Ru(bda)(ppy)$_2$]**, **PTZ-Th** presented 1.5-times higher current density than **Calix-PTZ** after 10 min (~ 41 vs 27 μA cm^{-2}).

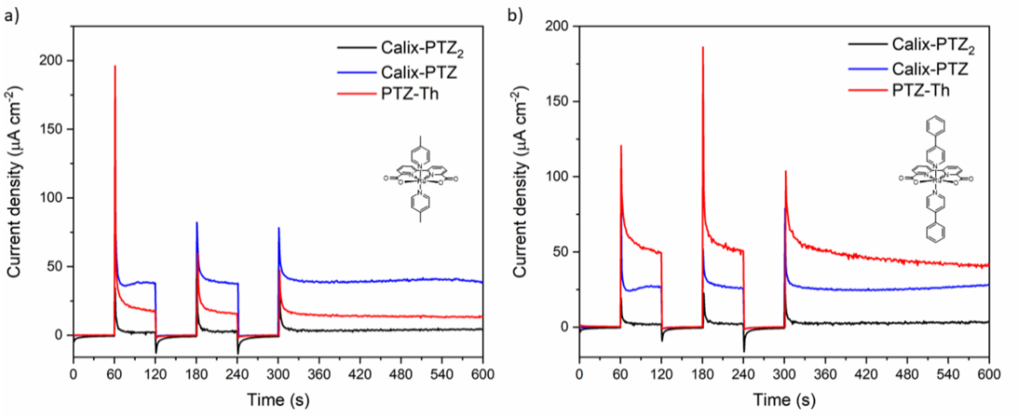

Figure 37: CA measurements of the WE with **[Ru(bda)(pic)$_2$]** (a), or with **[Ru(bda)(ppy)$_2$]** (b) in PBS electrolyte solution and 0.5 M KNO_3 +5% CF_3CH_2OH (v/v) at pH 6.5 under illumination (200 W Xe lamp; $420<\lambda<800$ nm). CE = Pt wire, RE = Ag/AgCl KCl 3 M, scan rate 50 mV s^{-1}, with an applied bias of +0.2 V vs Ag/AgCl.

Regarding the stability of the photocurrents, the **PTZ-Th** one showed a decrease after 10-min measurement in both cases, passing from 17 μA cm^{-2} after the first min of illumination to 14 μA cm^{-2} at the end of the experiment with **[Ru(bda)(pic)$_2$]** and from 50 μA cm^{-2} to 41 μA cm^{-2} with **[Ru(bda)(ppy)$_2$]**. **Calix-PTZ**, instead, showed excellent stability with time and no absolute decrease in the photocurrent even after a 10-min measurement.

The singular photoelectrochemical trends could be attributed to a unique interaction between the dye and the different WOCs. The *p*-*tert*-butylcalix[4]arene could easily host small guest molecules. However, the four *tert*-butyl groups on its upper rim reduces the available physical space and interacts with the cyclic aromatic groups through a CH_{host}-π_{guest} interaction.[20,21] Thus, every phenyl ring should remain blocked due to this interaction at the top of the calix[4]arene cavity. However, small functional groups on the aromatic cycle could easily enter the macrocycle and favor a better orientation of the phenyl ring in order to exploit the CH_{host}-π_{guest} interaction.[20-22] For these reasons, *p-tert*-butylcalix[4]arene could have a different interaction with the two investigated WOCs, **[Ru(bda)(pic)$_2$]** and **[Ru(bda)(ppy)$_2$]**. Since the photocurrents generated by **Calix-PTZ** were different in the two cases, we postulated that this interaction might take place with the axial ligand of the WOC. With **[Ru(bda)(pic)$_2$]**, the methyl group of the 4-picoline might enter the macrocycle and the interaction should happen between the pyridyl ring and the CH_3 of the macrocycle. With **[Ru(bda)(ppy)$_2$]**, the phenyl ring of the 4-phenylpyridine interacting with the CH_3 of the macrocycle, might not enter the macrocycle, thus the interaction between the pyridyl ring and the *tert*-butyl group should not take place. The lower photoelectrochemical activity of **Calix-PTZ** with **[Ru(bda)(ppy)$_2$]** could be attributed to the confinement of the WOC at a longer distance from the dye portion (~ 27 vs 39 μA cm^{-2} with **[Ru(bda)(pic)$_2$]**).

On the other hand, a 3-fold increase in the **PTZ-Th** photocurrent when **[Ru(bda)(ppy)$_2$]** was used indicated that the presence of an additional phenyl ring on the WOC ligands allowed a better alignment in the energy levels of that system and a better charge transfer. Moreover, the presence of a more extended π-structure in the WOC can favor the formation of a more stable oxo-bridge between two ruthenium centers.[10,23] Further studies are in progress to better investigate this trend and evaluate the oxygen produced by the different photosystems.

Next, we investigated the photocurrents of **Calix-PTZ$_2$**, pointing our attention to the differences in the design with respect to **Calix-PTZ**. These low photocurrents may indicate an almost-impossible charge transfer between dye and WOC. We hypothesized that the presence of four anchor groups at a fixed distance imposed by the macrocycle remarkably increased the rigidity of the photosensitizer when anchored onto the SC. This conformation might block the calix[4]arene macrocycle completely and avoid its rotation around the alkyl chain. This could prevent the WOC from approaching the dye and performing charge transfer, as in the case of **Calix-PTZ**. Moreover, this inflexible conformation should reduce the possibility of two ruthenium complexes being close to each other and building the oxo-bridge with two molecules of water. Some detailed computational studies have been performed by the group of Prof. Cosentino and Prof. Greco in the department of environmental science at the University of Milano-Bicocca and are reported in the next paragraph.

5.5 Molecular Dynamics simulations

To investigate the higher performance of **Calix-PTZ** with respect to **Calix-PTZ$_2$**, we modeled the TiO_2-co-adsorbed dye by Molecular Dynamics simulations in aqueous solution. We anchored the dyes on a [101] anatase TiO_2 slab of ca 9.2 × 7.9 × 1.1 nm dimensions. We investigated the calix[4]arene orientation compared to the surface in the two different dye-sensitized systems. We defined a plane passing from the methylene bridges of the calix[4]arene and during the simulations, we calculated the Θ angle between the plane previously defined and the TiO_2 surface. The most sampled Θ angle in **Calix-PTZ** is around 60°; while in **Calix-PTZ$_2$** it is around 90° (Figure 38). Then, to investigate the different charge transfers in the two systems, we calculated the distance between the LUMO and the SC surface and the distance between the HOMO and the hypothetical ruthenium catalyst bound into the calix[4]arene.

First, we calculated the HOMO and the LUMO of a dye model, in which we retained only the carboxy-phenothiazine core, replacing the neglected substituent by a methyl group. The electronic isosurfaces showed that the HOMO is mainly distributed on the phenothiazine ring, while the LUMO on the thienyl rings and on the acrylic groups (Figure 39).

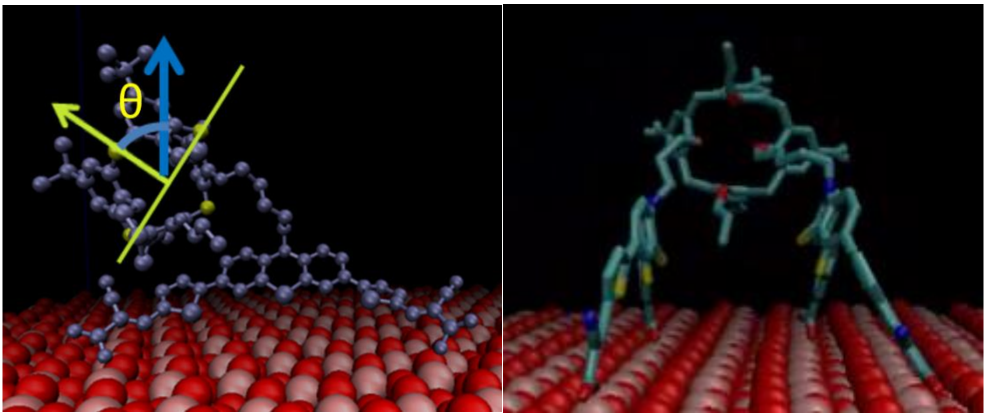

Figure 38: **Calix-PTZ** (left) and **Calix-PTZ$_2$** (right) structures after modeling with Molecular Dynamics on a [101] anatase TiO_2 slab.

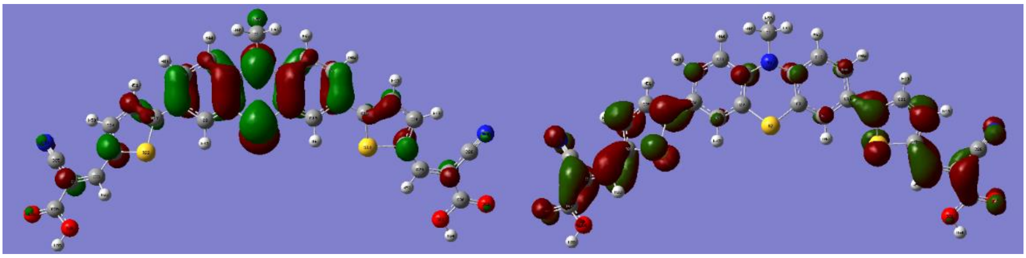

Figure 39: Distribution of HOMO (left) and LUMO (right) on the phenothiazine portion, calculated by density functional theory (DFT).

During the Molecular Dynamics simulations, we monitored: i) the distance between atoms of the phenothiazine rings, representative of the HOMO, and the center of mass of the *t*-

butyl substituents on the calix[4]arene macrocycle, representative of the hypothetical position of the catalyst; ii) the distance between the geometric center of the thienyl rings, representative of the LUMO, and the TiO_2 surface.

We found insignificant differences in the distance HOMO - center of mass of the *t*-butyl between **Calix-PTZ** and **Calix-PTZ$_2$** (Figure 40a). However, we found that the LUMO of **Calix-PTZ** is closer to the TiO_2 than the one of **Calix-PTZ$_2$** (Figure 40b), thus it might favor charge transfer from the dye to the TiO_2 and justify the higher performances of **Calix-PTZ** in the photoelectrochemical studies.

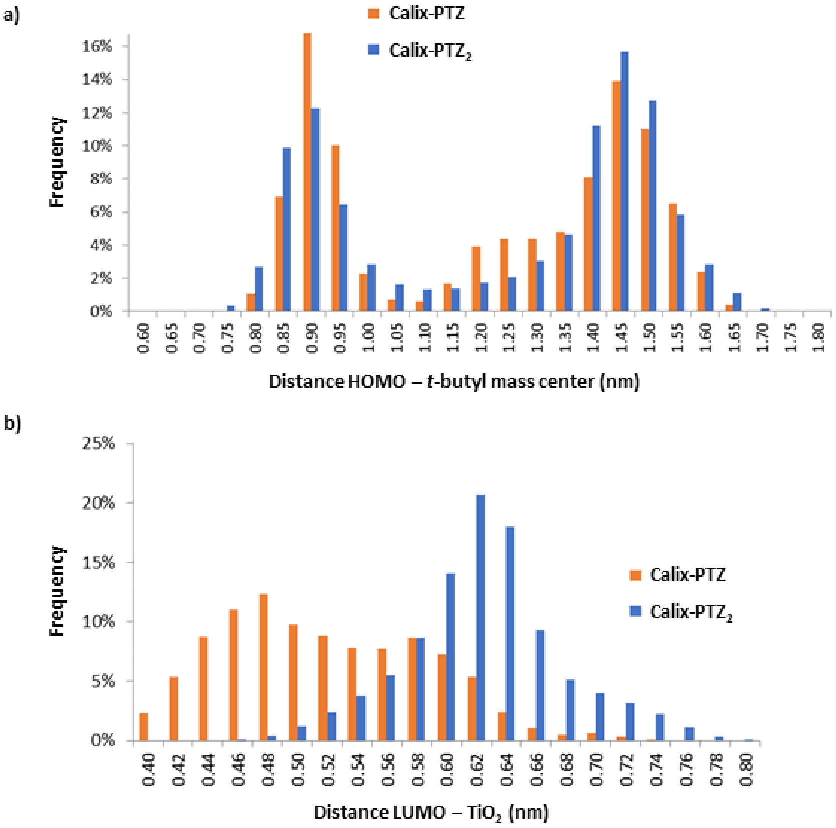

Figure 40: Distribution of the distance between HOMO and the *t*-butyl mass center (a), and between LUMO and TiO_2 (b) for **Calix-PTZ** and **Calix-PTZ$_2$**.

In conclusion, for the first time in the literature, calix[4]arene-based photosensitizers were employed in photoanodes of DSPEC to exploit their supramolecular capabilities with properly functionalized WOC.[24] We presented two new calix[4]arene-based dyes that have been used in combination with two WOC. All the dyes were characterized also in the presence of the WOC. We found that they possess the correct energy levels for performing water oxidation in combination with the WOC. The photosystems have been tested only in CA experiments where **Calix-PTZ** exhibited the best photocurrent in combination with **$[Ru(bda)(pic)_2]$**, while in the presence of **$[Ru(bda)(ppy)_2]$** its performance decreases. It might be attributed to the establishment of host-guest interactions between the calix[4]arene and the axial ligands of the WOC, that in the former case increased the photocurrents, and thus the charge transfer, while in the latter, reduced it due to a non-beneficial geometry of the system. The geometry also affects the performances of **Calix-PTZ$_2$**, which was the worst of all systems, despite it presenting the best optical properties. The extreme rigidity of its system might have blocked the possibility of two ruthenium centers to be in proximity to each other, which is mandatory to perform water oxidation. Moreover, Molecular Dynamics calculations highlighted the higher distance of the LUMO of **Calix-PTZ$_2$** from the SC with respect to the other investigated dyes. These results could be considered a further explanation of the bad photoelectrochemical performance of **Calix-PTZ$_2$**.

5.6 Experimental section

5.6.1 Spectroscopic and electrochemical investigation of dyes

The following materials were purchased from commercial suppliers: FTO-coated glass plates (2.2 mm thick; sheet resistance ~7 ohm per square;

Solaronix); Dyesol 18NR-T transparent TiO_2 blend of active 20 nm anatase particles. UV-O_3 treatment was performed using Novascan PSD Pro Series - Digital UV Ozone System. The thickness of the layers was measured by means of a VEECO Dektak 8 Stylus Profiler. Cyclic Voltammetry (CV) was carried out at a scan rate of 50 mV s^{-1}, using a Bio-logic SP-240 potentiostat in a three-electrode electrochemical cell under Ar. The working, counter, and the pseudo-reference electrodes were a glassy carbon pin (surface area = 0.02 cm^2), an Ag/Ag^+ TBAP in CH_3CN (0.1 M tetrabutylammonium perchlorate and 0.01 M $AgNO_3$ in acetonitrile) and a Pt wire for the dyes in solution or a sensitized 3.5 μm thick TiO_2 film, a Pt wire and an Ag/AgCl electrode (3 M KCl) for the measurements on film. The working electrodes discs were well polished with alumina 0.1 μm suspension. The preparation and sensitization of the 3.5 μm thick TiO_2 film is described below. The Pt wire was sonicated for 15 min in deionized water, washed with 2-propanol, and cycled for 50 times in 0.5 M H_2SO_4 before use. The Ag/Ag^+ pseudo-reference electrode was calibrated, by adding ferrocene (10^{-3} M, Fc) to the test solution after each measurement.[25] The Ag/AgCl (KCl 3 M) pseudo-reference electrode was calibrated, by adding potassium hexacyanoferrate(II) trihydrate (10^{-3} M) to the test solution after each measurement.[26] Electrochemistry in solution was performed in $TBABF_4$ 0.1 M DMF, while the one on film in 0.01 M aqueous buffer phosphate and 0.5 M KNO_3 at pH 6.5. 5% CF_3CH_2OH (v/v) was added to solubilize the WOC in the experiments with the WOC (1×10^{-3} M - final concentration). The potentials were recorded respect to Fc/Fc^+ and $[Fe(CN)_6]^{3-}/[Fe(CN)_6]^{2-}$ and converted to NHE adding +0.72 V or +0.408 V respectively.[25,26]

5.6.2 Preparation of photoanodes.

The photoanodes have been prepared adapting from a procedure reported in the literature.[27] In order to exclude metal contamination all the containers were in glass or Teflon and were treated with EtOH and 10% HCl prior to use. Plastic spatulas and tweezers have been used. FTO glass plates were cleaned in a detergent solution for 15 min using an ultrasonic bath, rinsed with pure water and EtOH. After treatment in a UV-O_3 system for 18 min, a transparent active layer of 0.8 cm^2 was screen-printed using Dyesol 18NR-T active transparent TiO_2 paste. The coated films were thermally treated at 125 °C for 6 min, 325 °C for 10 min, 450 °C for 15 min, and 500 °C for 15 min. The heating ramp rate was 5 - 10 °C min^{-1}.

These films were then treated in a UV-O_3 system for 20 min at room temperature, then soaked into a 2×10^{-4} M solution in EtOH/DMSO (15:1) of the photosensitizer overnight at room temperature in the dark. The stained substrates were rinsed with EtOH and dried with a stream of dry nitrogen. The UV-Vis spectra were recorded in comparison with a bare 1 µm transparent TiO_2 film, while CV and LSV with a bare 3.5 µm transparent TiO_2 film.

5.6.3 Photoelectrochemical measurements

Photoelectrochemical measurements of DS-PEC were carried out with black metal mask on top of the photoanode of 0.50 cm^2 surface area under a 200 W Xenon lamp (using a LOT-Oriel xenon white light source, equipped with a 420 nm cut-off filter to minimize TiO_2 contribution and an IR filter to avoid cell warming). The LSV (scan rate 20 mV s^{-1}) and CA measurements on the DS-PEC were performed using a Biologic SP-240 potentiostat in a three-electrode purposely designed photoelectrochemical cell filled with pH 6.5 PBS (Sigma Aldrich, product number P4417), KNO_3 0.5 M under Ar, and the data collected with EC-Lab.

5.6.4 Molecular Dynamics simulations.

Starting from the crystallographic structure of anatase [101],[28] a TiO_2 slab (dimensions: 9.2 × 7.9 × 1.1 nm) was built with Maestro 2021 suite.[29] The slab was inserted in a simulation box large enough to contain the two dyes (final dimensions 9.2 × 7.9 × 6.0 nm). The structures of the two dyes were built in Maestro and optimized with *all atom* force field OPLS-2005[30] before approaching them to the surface. The systems were solvated with water molecules described by SPC model. Carboxylic groups of the dyes were considered in their anionic form to guarantee the anchoring to the surface. Neutralization of the total charge of the systems was reached by adding Na^+ ions. For titanium dioxide, a force field described only by non-bonded electrostatic and van der Waals interactions was used.[31] The all-atom force field OPLS-2005 was used for the photosensitizers.[30] Molecular Dynamics simulations were performed with Gromacs (release 2019.1).[32] Periodic Boundary Conditions were applied in the three dimensions. For non-bonded interactions a 1.2 nm cut-off was used, beyond which long-range electrostatics interactions were treated by Particle Mesh Ewald algorithm.[33] Systems were minimized with steepest descent algorithm. Initial velocities were generated from a Maxwell distribution at 300 K with a random seed. Molecular Dynamics simulations were performed at constant temperature ($T = 300$ K) and pressure ($P = 1$ bar) with a 2fs timestep. TiO_2 surface, dyes and aqueous solutions were coupled to V-rescale thermostats[34] every 0.1 ps and to Parrinello-Rahman barostat[35] every 2 ps. Bonds involving hydrogen atoms were constrained with LINCS algorithm.[36] For each system two 50 ns simulations were run and analysed every 100 ps.

5.6.5 Quanto-mechanical calculations.

Ground state geometry optimization of the dye was performed by a DFT calculation in vacuo, with PBE0 functional[37] and 6-31G* basis set by using the Gaussian 16 program (revision A.03).[38] HOMO and LUMO were visualized with GaussView (version 6.1).[39]

5.6.6 Synthetic strategies

NMR spectra were recorded with a Bruker Advance-Neo spectrometer operating at 400 MHz (^{1}H) and 100 MHz (^{13}C). Coupling constants are given in Hz. Absorption spectra were recorded with a V-570 Jasco spectrophotometer. ATR FT-IR spectra were recorded with a PerkinElmer Spectrum 100. High resolution mass spectra have been recorded with an Agilent 6230B Time of Flight (TOF) equipped with an electrospray (dual ESI) source. Compounds were purified using flash chromatography with Merck grade 9385 silica gel 230–400 mesh (60 Å). The glassware for water-free reactions was dried in a 130 °C oven for 4 h before use and then attached to the vacuum pump. Inert atmosphere was generated by Schlenk technique using nitrogen flow. Conversion was monitored by thin-layer chromatography (Silica gel on TLC Al foils with fluorescent indicator 254 nm) by using UV light (254 and 365 nm) as a visualizing agent. All reagents were obtained from commercial suppliers at the highest purity grade and used without further purification. Anhydrous solvents were purchased from Acros Organics and used without further purification. Organic phases obtained after extraction were dried with Na_2SO_4 and filtered before removal of the solvent by evaporation. The **PTZ-Th**,[9] 4,4,5,5-tetramethyl-2-(5-(4,4,5,5-tetramethyl-1,3-dioxolan-2-yl)thiophen-2-yl)-1,3,2-dioxaborolane,[14] 5,11,17,23-tetra-tert-butyl-25,26,27-tripropoxycalix[4]arene (**1**),[40] 5,11,17,23-tetra-*tert*-butyl-25,27-dipropoxycalix[4]arene (**3**),[12] **[Ru(bda)(pic)$_2$]**,[10] and **[Ru(bda)(ppy)$_2$]**[11] have been synthesized according to literature procedures.

1,2,3-tris-(propoxy)-4-(butoxy-4-iodide)-tetrakis-p-tert-butylcalix[4]arene (2). A mixture of 5,11,17,23-tetra-tert-butyl-25,26,27-tripropoxycalix[4]arene **1** (1.38 g, 1.78 mmol), NaH 60% (0.085 g, 3.56 mmol) and 1,4-diiodobutane (1.64 mL, 12.46 mmol) in dry DMF (170 mL) was stirred at room temperature for 5 hrs. A solution of 0.1 N HCl (150 mL) was then slowly added, the mixture was extracted twice with ethyl acetate (180 mL) and the organic phase was concentrated in vacuo until the formation of a precipitate occurred. Methanol was added and the precipitate was collected by Buchner filtration and further purified by column chromatography (silica gel, cyclohexane-toluene 9:1, v/v) followed by recrystallization from diethyl ether-ethanol obtaining white needle-like crystals. Yield: 79% (1.35 g, 1.41 mmol). 1H NMR (400 MHz, CDCl3): δ (ppm) 6.81-6.78 (m, 8H); 4.43 (d, J = 12.6 Hz, 2H); 4.39 (d, J = 12.6 Hz, 2H); 3.90 (t, J = 7.2 Hz, 2H); 3.83 (t, J = 7.0 Hz, 6H); 3.30 (t, J = 7.1 Hz, 2H); 3.14 (d, J = 12.6 Hz, 2H); 3.13 (d, J = 12.6 Hz, 2H); 2.16-2.12 (m, 2H); 2.07-2.01 (m, 8H); 1.11 (s, 9H); 1.10 (s, 9H); 1.09 (s, 18H); 1.04-1.00 (m, 9H). 13C NMR (100 MHz, CDCl3): δ (ppm) 153.7; 153.6; 153.5; 144.5; 144.2; 133.9; 133.8; 133.6; 125.0; 124.9; 124.8; 77.2; 76.9; 73.8; 33.8; 31.5; 31.3; 31.1; 30.6; 23.4; 23.3; 10.4; 10.3; 6.4.

1,3-bis-(propoxy)-2,4-bis-(butoxy-4-iodide)-tetrakis-*p*-*tert*-butylcalix[4]arene (4). A mixture of 5,11,17,23-tetra-*tert*-butyl-25,27-dipropoxycalix[4]arene **3** (1.52 g, 2.08 mmol), NaH 60% (0.33 g, 8.34 mmol) and 1,4-diiodobutane (4.1 mL, 31.09 mmol) in dry DMF (250 mL) was stirred at room temperature for 3 hrs. A solution of 0.1 N HCl (200 mL) was then slowly added, the mixture was extracted twice with ethyl acetate (180 mL) and the organic phase was concentrated *in vacuo* until the formation of a precipitate occurred. After cooling the flask at 0 °C the precipitate was collected by Buchner filtration and further purified by column chromatography (silica gel, cyclohexane-toluene 85:15, v/v) yielding the pure product as an oily residue that becomes a solid foam under high vacuum. Yield: 56% (1.28 g, 1.17 mmol). m.p.=181-182°C ^{1}H NMR (400 MHz, $CDCl_3$): δ (ppm) 6.81 (s, 4H); 6.79 (s, 4H); 4.40 (d, *J* = 12.4 Hz, 4H); 3.89 (t, *J* = 6.8 Hz, 4H); 3.85 (t, *J* = 7.2 Hz, 4H); 3.31 (t, *J* = 6.9 Hz, 4H); 3.15 (d, *J* = 12.4 Hz, 4H); 2.11-2.16 (m, 4H); 2.00-2.08 (m, 8H); 1.10 (s, 18H); 1.09 (s, 18H); 1.03 (t, *J* = 7.4 Hz, 6H). ^{13}C NMR (100 MHz, $CDCl_3$): δ (ppm) 153.5; 153.4; 144.5; 144.3; 133.8; 133.7; 125.0; 124.9; 77.0; 73.8; 33.8; 31.5; 31.3; 31.1; 30.5; 23.5; 10.5; 6.5.

3,7-bis(5-(4,4,5,5-tetramethyl-1,3,2-dioxaborolan-2-yl)thiophen-2-yl)-10*H*-phenothiazine (5). 3,7-dibromo-10*H*-phenothiazine (760 mg, 2.11 mmol) and $Pd(dppf)Cl_2 \cdot CH_2Cl_2$ (172 mg, 0.21 mmol) were dissolved in dimethoxyethane (12.5 mL) and stirred for 15 minutes under nitrogen atmosphere. Then 4,4,5,5-tetramethyl-2-(5-(4,4,5,5-tetramethyl-1,3-dioxolan-2-yl)thiophen-2-yl)-1,3,2-dioxaborolane (1.50 g, 4.44 mmol) and K_2CO_3 (2.90 g, 21.1 mmol) were added as suspension in methanol (12.5 mL). The reaction was performed with microwave irradiation (100 °C, 70 W, 60 minutes) and then quenched by pouring into a saturated solution of NH_4Cl (50 mL). Filtration on Celite and extractions were performed with CH_2Cl_2 (3 × 50 mL). The solution dried and the solvent evaporated. A mixture of PE/AcOEt (3:1) was used as eluent for purification through column chromatography on silica gel. The desired product was isolated as a dark yellow solid (1.10 g, 1.80 mmol) with an 84% of yield. ^{1}H NMR (Benzene-d_6, 400 MHz): δ (ppm) = 7.21 (d, *J* = 1.0 Hz, 2H), 7.09 (dd, *J* = 7.2, 1.7 Hz, 2H), 6.99 (d, *J* = 3.5 Hz, 2H), 6.75 (d, *J* = 3.5 Hz, 2H), 6.24 (s, 2H), 5.76 (d, *J* = 8.2 Hz, 2H), 4.87 (s, 1H), 1.20 (s, 12H), 1.09 (s, 12H).

Compound 6. NaH 60% (25 mg, 0.64 mmol) was added as a solid to a solution of **5** (200 mg, 0.32 mmol) in anhydrous DMF (25 mL) kept at 0 °C under N_2 atmosphere. The reaction mixture was allowed to warm up to room temperature and, after 1 h, compound **2** (340 mg, 0.35 mmol) was added in a DMF solution (5 mL). The day after, the reaction mixture was poured in an ice bath and a yellow solid precipitated. It was filtered on Büchner and washed with water. The crude product was purified using PE/Et_2O eluent (1:1), affording the product as a yellow solid (450 mg, 0.31 mmol, 97%) ^{1}H NMR (400 MHz, $CDCl_3$) δ 7.39 - 7.33 (m, 4H), 7.08 (dd, J = 3.7, 0.5 Hz, 2H), 7.04 (d, J = 3.7 Hz, 2H), 6.89 - 6.81 (m, 6H), 6.73 (dd, J = 7.6, 2.4 Hz, 4H), 6.17 (d, J = 0.3 Hz, 2H), 4.40 (t, J = 12.5 Hz, 4H), 3.99 - 3.92 (m, 4H), 3.89 - 3.73 (m, 6H), 3.12 (dd, J = 12.5, 6.2 Hz, 4H), 2.25 - 2.15 (m, 2H), 2.11 - 1.90 (m, 8H), 1.36 (s, 12H), 1.32 (s, 12H), 1.13 (s, 18H), 1.05 (s, 18H), 1.02 - 0.96 (m, 9H).

Compound 8. NaH 60% (91 mg, 2.27 mmol) was added as a solid to a solution of **5** (253 mg, 0.41 mmol) in anhydrous DMF (10 mL) kept at 0 °C under N_2 atmosphere. The reaction mixture was allowed to warm up to room temperature and, after 1 h, compound **4** (212 mg, 0.19 mmol) was added in a DMF solution (5 mL). After 3 days, the reaction mixture was poured in an ice bath and extracted with AcOEt (3 × 25 mL) and washed with water (3 × 20 mL). The organic phase was dried, and the solvent evaporated. The crude product was purified using PE/Et_2O eluent (1:1), affording the product as a yellow solid (323 mg, 0.16 mmol, 82%). ^{1}H NMR (400 MHz, $CDCl_3$) δ 7.38 - 7.32 (m, 8H), 7.09 (dd, J = 3.7, 0.5 Hz, 4H), 7.03 (d, J = 3.7 Hz, 4H), 6.86 (s, 4H), 6.82 (d, J = 9.2 Hz, 4H), 6.76 (s, 4H), 6.20 (d, J = 0.3 Hz, 4H), 4.41 (d, J = 12.4 Hz, 4H), 4.05 - 3.90 (m, 8H), 3.84 - 3.75 (m, 4H), 3.14 (d, J = 12.6 Hz, 4H), 2.27 - 2.14 (m, 4H), 2.06 - 1.92 (m, 8H), 1.39 (s, 24H), 1.35 (s, 24H), 1.16 (s, 18H), 1.08 (s, 18H), 1.00 (t, J = 7.5 Hz, 6H).

General procedure A for the cleavage of the protective group for the aldehydic functionality. Pinacol ester precursor was dissolved in 10% HCl_{aq}/THF (1:2). The mixture was heated at 50 °C for 4 h. The volume was reduced to 1/3, K_2CO_3 saturated aqueous solution (30 mL) and CH_2Cl_2 (50 mL) were added. The mixture was separated and the organic phase dried. After the evaporation of the solvent evaporated.

Compound 7. Compound **7** was synthesized according to general procedure A using as reagent compound **6** (450 mg, 0.31 mmol), 30 mL 10% HCl_{aq}/THF (1:2). The desired product was isolated after purification through column chromatograph PE/Et_2O (1:1) as an orange solid (230, 0.19 mmol, 60%). ^{1}H NMR (400 MHz, $CDCl_3$) δ 9.87 (s, 2H), 7.71 (d, J = 4.0 Hz, 2H), 7.46 (dd, J = 8.5, 2.2 Hz, 2H), 7.42 (d, J = 2.2 Hz, 2H), 7.29 (d, J = 3.9 Hz, 2H), 6.91 (d, *J* = 8.6 Hz, 2H), 6.81 (d, *J* = 2.6 Hz, 4H), 6.75 (d, *J* = 2.5 Hz, 2H), 6.72 (d, *J* = 2.5 Hz, 2H) 4.39 (t, *J* = 12.7 Hz, 4H), 4.05 - 3.89 (m, 4H), 3.87 - 3.73 (m, 6H), 3.11 (t, *J* = 11.5 Hz, 4H), 2.27 - 2.15 (m, 2H), 2.12 - 1.88 (m, 8H), 1.11 (d, *J* = 1.0 Hz, 18H), 1.05 (s, 18H), 0.99 (dt, *J* = 14.1, 7.1 Hz, 9H).

Compound 9. Compound **9** was synthesized according to general procedure A using as reagent compound **8** (328 mg, 0.16 mmol), 30 mL 10% HCl_{aq}/THF (1:2). The desired product was isolated as an orange solid without any further purification (206 mg, 0.12 mmol, 75%). ^1H NMR (400 MHz, $CDCl_3$) δ 9.86 (s, 4H, α), 7.69 (d, *J* = 4.0 Hz, 4H), 7.37 (dd, *J* = 8.5, 2.2 Hz, 4H), 7.32 (d, *J* = 2.1 Hz, 4H), 7.24 (d, *J* = 3.9 Hz, 4H), 6.94 (s, 4H), 6.81 (d, *J* = 8.6 Hz, 4H), 6.67 (s, 4H), 4.39 (d, *J* = 12.4 Hz, 4H), 4.03 (t, 4H), 3.94 (t, 4H), 3.77 (d, *J* = 7.4 Hz, 4H), 3.14 (d, *J* = 12.5 Hz, 4H), 2.32 - 2.20 (m, 4H), 2.05 - 1.90 (m, 8H), 1.27 (s, 18H), 1.21 (s, 18H), 1.01 (t, 6H).

General procedure B for Knoevenagel condensation: Aldehyde precursor (1 equiv.), cyanoacetic acid (5 equiv.), and piperidine (6 equiv.) were dissolved in dry $CHCl_3$ (0.2 M) and warmed to reflux for 8 h. After having the solvent evaporated, an aqueous solution of HCl 10% was added and the mixture was left under magnetic stirring for 5 h at room temperature. The solid that precipitated, was filtered, and washed with water.

Calix-PTZ. Calix-PTZ was synthetized according to general procedure **B** for Knoevenagel condensation using compound **7** (230 mg, 0.19 mmol), cyanoacetic acid (162 mg, 1.9 mmol), piperidine (190 mg, 2.24 mmol) and 15 mL of dry $CHCl_3$. The reaction was quenched with 18 mL of 10% HCl solution. The product was isolated as a dark purple solid (223 mg, 0.16 mmol) with 85% yield. FT-IR υ(cm^{-1}): 2995-2812, 1710 (b), 1574 (s), 1485 (w), 1444-1332 (s), 1320-1132 (s), 1125 (w), 1061 (w), 866 (w), 795 (s). ^1H NMR (400 MHz, DMSO) δ 8.49 (s, 2H), 8.00 (d, *J* = 4.5 Hz, 2H), 7.71 (d, *J* = 4.0 Hz, 2H), 7.64 - 7.58 (m, 4H), 7.19 (d, *J* = 8.4 Hz, 2H), 6.83 (d, *J* = 2.3 Hz, 2H), 6.77 (d, *J* = 2.3 Hz, 2H), 6.67 (s, 2H), 6.64 (s, 2H), 4.24 (dd, *J* = 20.3, 12.3 Hz, 4H), 4.10 - 4.05 (m, 2H), 3.13 - 2.91 (m, 12H), 2.05 (dd, *J* = 18.6, 11.0 Hz, 2H), 1.97 - 1.83 (m, 8H), 1.06 (s, 18H), 0.99 - 0.94 (m, 21H), 0.90 (t, *J* = 7.5 Hz, 6H). HRMS (dual-ESI) *m/z*: calcd for $[M - 2H]^-$ $C_{85}H_{95}N_3O_8S_3$: 689.8067, found 689.8064. ^{13}C NMR spectrum was not recorded due to low solubility of the compound.

Calix-PTZ$_2$. Calix-PTZ$_2$ was synthetized according to general procedure **B** for Knoevenagel condensation using compound **7** (206 mg, 0.12 mmol), cyanoacetic acid (217 mg, 2.4 mmol), piperidine (212 mg, 0.246 mL, 2.49 mmol) and 15 mL of dry $CHCl_3$. The reaction was quenched with 30 mL of 10% HCl solution. The product was isolated as a dark purple solid after crystallization in $CHCl_3$ (203 mg, 0.10 mmol) with 85% yield. FT-IR υ/cm^{-1}): 3048-2830, 1733 (s), 1568 (s), 1444-1320 (s), 1314-1143 (s), 1063 (w), 790 (w). ^{1}H NMR (400 MHz, DMSO) δ 8.35 (s, 4H), 7.90 (d, *J* = 4.5 Hz, 4H), 7.54 (d, *J* = 4.0 Hz, 4H), 7.49 (dd, *J* = 8.5, 2.2 Hz, 4H), 7.43 (d, *J* = 2.2 Hz, 4H), 7.03 (d, *J* = 8.7 Hz, 4H), 6.79 (s, 4H), 6.70 (s, 4H), 4.31 (d, *J* = 12.4 Hz, 4H), 4.03 - 3.88 (m, 8H), 3.72 (t, *J* = 7.4 Hz, 4H), 3.06 (d, *J* = 13.1 Hz, 4H), 2.15 - 2.04 (m, *J* = 14.5, 7.4 Hz, 4H), 1.95 - 1.81 (m, *J* = 14.6, 7.3 Hz, 8H), 1.07 (s, 18H), 1.00 (s, 18H). HRMS (dual-ESI) *m/z*: calcd for $[M - 2H]^-$ $C_{114}H_{110}N_6O_{12}S_6$: 972.3180, found 972.3188. ^{13}C NMR spectrum was not recorded due to low solubility of the compound.

References

1 Li, H., Li, F., Wang, Y., Bai, L., Yu, F. & Sun, L. (**2016**) Visible-Light-Driven Water Oxidation on a Photoanode by Supramolecular Assembly of Photosensitizer and Catalyst. *ChemPlusChem,* **81**, 1056-1059, doi:10.1002/cplu.201500539.

2 Guernelli, S., Laganà, M. F., Spinelli, D., Lo Meo, P., Noto, R. & Riela, S. (**2002**) Host-Guest Interactions between *β*-Cyclodextrin and the (*Z*)-Phenylhydrazone of 3-Benzoyl-5-phenyl-1,2,4-oxadiazole: The First Kinetic Study of a Ring−Ring Interconversion in a "Confined Environment". *J. Org. Chem.,* **67**, 2948-2953, doi:10.1021/jo016214w.

3 Sévery, L., Szczerbiński, J., Taskin, M., Tuncay, I., Brandalise Nunes, F., Cignarella, C., Tocci, G., Blacque, O., Osterwalder, J., Zenobi, R., Iannuzzi, M. & Tilley, S. D. (**2021**) Immobilization of molecular catalysts on electrode surfaces using host–guest interactions. *Nat. Chem.,* **13**, 523-529, doi:10.1038/s41557-021-00652-y.

4 Luo, T., Huang, J. & Liu, J. (**2020**) Application of Novel Calix[4]arene Metal-free Sensitizers in Dye-sensitized Photoelectrochemical Cells for Water Splitting. *Chem. Res. Chin. Univ.,* **36**, 1091-1096, doi:10.1007/s40242-020-0302-0.

5 Tekin, M., Cevik, E., Sayin, S. & Yildiz, H. B. (**2020**) Photocurrent and hydrogen production by overall water splitting based on polymeric composite Calix[n]arene/Cyanin Dye/IrO_2 nanoparticle. *Int. J. Hydrog. Energy,* **45**, 19869-19879, doi:10.1016/j.ijhydene.2020.05.126.

6 Manfredi, N., Boldrini, C. L. & Abbotto, A. (**2018**) Organic Sensitizers for Photoanode Water Splitting in Dye-Sensitized Photoelectrochemical Cells. *ChemElectroChem,* **5**, 2395-2402, doi:10.1002/celc.201800592.

7 Iwamoto, K., Araki, K. & Shinkai, S. (**1991**) Conformations and structures of tetra-O-alkyl-p-tert-butylcalix[4]arenes. How is the conformation of calix[4]arenes immobilized? *J. Org. Chem.,* **56**, 4955-4962, doi:10.1021/jo00016a027.

8 Castillo-Vallés, M., Andrés-Castán, J. M., Garín, J., Orduna, J., Villacampa, B., Franco, S. & Blesa, M. J. (**2015**) Dye-sensitized-solar-cells based on calix[4]arene scaffolds. *RSC Adv.,* **5**, 90667-90670, doi:10.1039/C5RA15184H.

9 Cecconi, B., Manfredi, N., Ruffo, R., Montini, T., Romero-Ocana, I., Fornasiero, P. & Abbotto, A. (**2015**) Tuning Thiophene-Based Phenothiazines for Stable Photocatalytic Hydrogen Production. *ChemSusChem,* **8**, 4216-4228, doi:10.1002/cssc.201501040.

10 Duan, L., Fischer, A., Xu, Y. & Sun, L. (**2009**) Isolated seven-coordinate Ru(IV) dimer complex with $[HOHOH]^-$ bridging ligand as

an intermediate for catalytic water oxidation. *J. Am. Chem. Soc.,* **131**, 10397-10399, doi:10.1021/ja9034686.

11 Li, H., Li, F., Zhang, B., Zhou, X., Yu, F. & Sun, L. (**2015**) Visible Light-Driven Water Oxidation Promoted by Host-Guest Interaction between Photosensitizer and Catalyst with A High Quantum Efficiency. *J. Am. Chem. Soc.,* **137**, 4332-4335, doi:10.1021/jacs.5b01924.

12 Iwamoto, K., Araki, K. & Shinkai, S. (**1991**) Syntheses of all possible conformational isomers of *O*-alkyl-*p-t*-butylcalix[4]arenes. *Tetrahedron,* **47**, 4325-4342, doi:10.1016/S0040-4020(01)87102-7.

13 Manfredi, N., Cecconi, B., Calabrese, V., Minotti, A., Peri, F., Ruffo, R., Monai, M., Romero-Ocana, I., Montini, T., Fornasiero, P. & Abbotto, A. (**2016**) Dye-sensitized photocatalytic hydrogen production: distinct activity in a glucose derivative of a phenothiazine dye. *Chem. Commun.,* **52**, 6977-6980, doi:10.1039/c6cc00390g.

14 Leandri, V., Ruffo, R., Trifiletti, V. & Abbotto, A. (**2013**) Asymmetric Tribranched Dyes: An Intramolecular Cosensitization Approach for Dye-Sensitized Solar Cells. *Eur. J. Org. Chem.,* **2013**, 6793-6801, doi:10.1002/ejoc.201300962.

15 Tauc, J. (**1968**) Optical properties and electronic structure of amorphous Ge and Si. *Mater. Res. Bull.,* **3**, 37-46, doi:10.1016/0025-5408(68)90023-8.

16 Tian, H., Boschloo, G. & Hagfeldt, A. *Molecular Devices for Solar Energy Conversion and Storage*. (Springer: Singapore, Singapore, **2018**)

17 Bockris, J. O. M., Reddy, A. K. N. & Gamboa-Aldeco, M. *Modern Electrochemistry 2A: Fundamentals of Electrodics*. (Springer US: Boston, USA, **2000**)

18 Li, F., Fan, K., Wang, L., Daniel, Q., Duan, L. & Sun, L. (**2015**) Immobilizing Ru(bda) Catalyst on a Photoanode via Electrochemical Polymerization for Light-Driven Water Splitting. *ACS Catal.,* **5**, 3786-3790, doi:10.1021/cs502115f.

19 Kirner, J. T., Stracke, J. J., Gregg, B. A. & Finke, R. G. (**2014**) Visible-light-assisted photoelectrochemical water oxidation by thin films of a phosphonate-functionalized perylene diimide plus CoO_x cocatalyst. *ACS Appl. Mater. Interfaces,* **6**, 13367-13377, doi:10.1021/am405598w.

20 Brouwer, D. H., Alavi, S. & Ripmeester, J. A. (**2008**) NMR crystallography of *p-tert*-butylcalix[4]arene host-guest complexes using ^{1}H complexation-induced chemical shifts. *Phys. Chem. Chem. Phys.,* **10**, 3857-3860, doi:10.1039/B805326J.

21 Brouwer, E. B., Enright, G. D. & Ripmeester, J. A. (**1996**) π-Methyl interactions and p-tert-butylcalix[4]arene-guest stability: NMR and crystallographic studies of cyclohexane and n-pentane inclusion compounds. *Supramol. Chem.,* **7**, 143-145, doi:10.1080/10610279608035189.

22 Lemli, B., Peles, J., Kollar, L., Nagy, G. & Kunsàgi-Màtè, S. (**2006**) The Rate of Host-guest Complex Formation of Some Calixarene Derivatives Towards Neutral Aromatic Guests. *Supramol. Chem.,* **18**, 251-256, doi:10.1080/10610270500450416.

23 Duan, L., Bozoglian, F., Mandal, S., Stewart, B., Privalov, T., Llobet, A. & Sun, L. (**2012**) A molecular ruthenium catalyst with water-oxidation activity comparable to that of photosystem II. *Nat. Chem.,* **4**, 418-423, doi:10.1038/nchem.1301.

24 Boldrini, C. L., Manfredi, N., Montini, T., Baldini, L., Abbotto, A. & Fornasiero, P. (**2021**) Calix[4]arene-based molecular photosensitizers for sustainable hydrogen production and other solar applications. *Curr. Opin. Green Sustain. Chem.,* **32**, 100534, doi:https://doi.org/10.1016/j.cogsc.2021.100534.

25 Sawyer, D. T., Roberts, J. L., Jr. & Sobkowiak, A. *Electrochemistry for chemists*. 2nd edn, (Wiley: New York, USA, **1995**)

26 O'Reilly, J. E. (**1973**) Oxidation-reduction potential of the ferro-ferricyanide system in buffer solutions. *Biochim. Biophys. Acta,* **292**, 509-515, doi:10.1016/0005-2728(73)90001-7.

27 Ito, S., Murakami, T. N., Comte, P., Liska, P., Grätzel, C., Nazeeruddin, M. K. & Grätzel, M. (**2008**) Fabrication of thin film dye sensitized solar cells with solar to electric power conversion efficiency over 10%. *Thin Solid Films,* **516**, 4613-4619, doi:10.1016/j.tsf.2007.05.090.

28 Howard, C. J., Sabine, T. M. & Dickson, F. (**1991**) Structural and thermal parameters for rutile and anatase. *Acta Cryst.,* **47**, 462-468, doi:10.1107/S010876819100335X.

29 Schrödinger Release 2021-3: Maestro, Schrödinger, LLC, New York, NY, **2021**.

30 Banks, J. L., Beard, H. S., Cao, Y., Cho, A. E., Damm, W., Farid, R., Felts, A. K., Halgren, T. A., Mainz, D. T., Maple, J. R., Murphy, R., Philipp, D. M., Repasky, M. P., Zhang, L. Y., Berne, B. J., Friesner, R. A., Gallicchio, E. & Levy, R. M. (**2005**) Integrated Modeling Program, Applied Chemical Theory (IMPACT). *J. Comput. Chem.,* **26**, 1752-1780, doi:10.1002/jcc.20292.

31 Brandt, E. G. & Lyubartsev, A. P. (**2015**) Systematic Optimization of a Force Field for Classical Simulations of TiO_2-Water Interfaces. *J. Phys. Chem. C,* **119**, 18110-18125, doi:10.1021/acs.jpcc.5b02669.

32 Abraham, M. J., Murtola, T., Schulz, R., Páll, S., Smith, J. C., Hess, B. & Lindahl, E. (**2015**) GROMACS: High performance molecular simulations through multi-level parallelism from laptops to supercomputers. *SoftwareX,* **1-2**, 19-25, doi:10.1016/j.softx.2015.06.001.

33 Darden, T., York, D. & Pedersen, L. (**1993**) Particle mesh Ewald: An N·log(N) method for Ewald sums in large systems. *J. Chem. Phys.,* **98**, 10089-10092, doi:10.1063/1.464397.

34 Bussi, G., Donadio, D. & Parrinello, M. (**2007**) Canonical sampling through velocity rescaling. *J. Chem. Phys.,* **126**, 014101, doi:10.1063/1.2408420.

35 Parrinello, M. & Rahman, A. (**1981**) Polymorphic transitions in single crystals: A new molecular dynamics method. *J. Appl. Phys.,* **52**, 7182-7190, doi:10.1063/1.328693.

36 Hess, B., Bekker, H., Berendsen, H. J. C. & Fraaije, J. G. E. M. (**1997**) LINCS: A linear constraint solver for molecular simulations. *J. Comput. Chem.,* **18**, 1463-1472, doi:10.1002/(SICI)1096-987X(199709)18:12‹1463::AID-JCC4›3.0.CO;2-H.

37 Adamo, C. & Barone, V. (**1999**) Toward reliable density functional methods without adjustable parameters: The PBE0 model. *J. Chem. Phys.,* **110**, 6158-6170, doi:10.1063/1.478522.

38 Gaussian 16 Rev. A.03 (Wallingford, CT, **2016**).

39 GaussView Version 6.1 (Semichem Inc., Shawnee Mission, KS, **2016**).

40 Zadmard, R., Taghvaei-Ganjali, S. & Gorji, B. (**2008**) Covalently Linked at the Lower Rim Double-Calix[4]arene as a Precursor for Multicavity Supramolecular Receptor. *Synth. Commun.,* **38**, 1830-1836, doi:10.1080/00397910801982035.

Chapter 6: π-π interaction in DSPEC

Aim of this section

In this section, I present an innovative design for DSPEC, which exploits the π-π stacking interaction between the dye and the WOC. In this case, the dye is functionalized with a graphene layer that should protect the photosensitizer from desorption and, at the same time, be able to interact with a suitable modified WOC *via* π-π interactions. The graphene layer should behave like an electron shuttle between the reduced WOC and the oxidized dye.

This section is short because I started this project late, and every step of the synthetic pathway required an optimization study to increase the yield and some precautions to obtain pure products. Thus, I just present the synthetic pathway and the basic characterizations of the compounds I synthetized. In the end, the obtained **H_2N-TPAThTh** will be converted to the RGO-dye system by the research group of Prof. Menna at the University of Padova.

6.1 Introduction

Carbon nanostructures have recently been explored in energy applications by the scientific community to increase the efficiency and stability of the device. They are known for their superior properties, such as thermal conductivity, metallic or semiconducting electronic behavior, and surface area.[1] Among these materials, graphene is the most common, and it presents different chemical structures, such as graphene, graphene oxide, or reduced graphene oxide (RGO).[2]

These structures differ in the density of the oxygenated groups, the lateral size of sheets, and the number of layers. Moreover, they can be functionalized with organic compounds through either a covalent or supramolecular strategy.[1] The covalent approach allows a more stable linkage, ensures better proximity of the organic compounds to the graphene layer, provides good solubility, and thus enhances the electron-transfer processes. However, a covalent bond causes the introduction of undesirable sp^3 defects in the electronic structure of the graphene. The supramolecular or non-covalent approach highly reduces the complexity of synthetic pathways and purifications involving the graphene suspensions and it avoids the modification of the electron cloud of the graphene. However, this configuration suffers from low stability and requires the dispersion of the organic molecules in the medium.[3]

Graphene has been used for solar applications as quantum dots for sensitizing SCs.[4] However, the first application in dye-sensitized solar cells as a hybrid dyad composed of an organic push-pull dye and an RGO was published in 2017 by the group of Prof. Menna from the University of Padova and Prof. Abbotto from the University of Milano-Bicocca.[5] In this case, an amino-functionalized triphenylamine-based dye was covalently bonded through the Tour reaction to an RGO layer. On the other side, it was functionalized with a carboxylic acid group to anchor the TiO_2. Thus, the D-π-A dye worked as a bridge between the SC and the RGO layer, keeping the latter facing the electrolyte solution. Though this system exhibited a lower photovoltaic performance compared to the DSSC with the reference dye, not including the RGO layer, it showed enhanced stability over time. This stability was attributed to a more stable binding of the dye onto the SC thanks to the presence of the RGO protective layer.

Regarding solar fuels production, graphene-based materials have been used to replace the SC. Many photosensitizers have been covalently or non-covalently bound to it together with platinum nanoparticles or other HECs or WOCs.[6-8] Moreover, some molecular catalysts have been suitably modified with a pendant with a pyrene ring on one extremity in order to immobilize it on particular carbon nanostructures.[9-12]

We aimed to develop a photoanode sensitized with an RGO-combined dye linked to a molecular WOC. The WOC has been properly modified for exploiting non-covalent interactions with the RGO (Figure 41). We chose as WOC a published pyrene-modified $[Ru(bda)(pic)_2]$[13] known for its high efficiency in water oxidation and good stability onto carbon nanostructures thanks to the π-π stacking. To the best of my knowledge, this is the first case where the RGO layer is not used in place of the SC but only as a support between the dye and the WOC. The purposes of this RGO layer are speeding up the charge transfer between dye and WOC and reducing the unwanted interactions between the SC and the WOC acting like a protective layer.

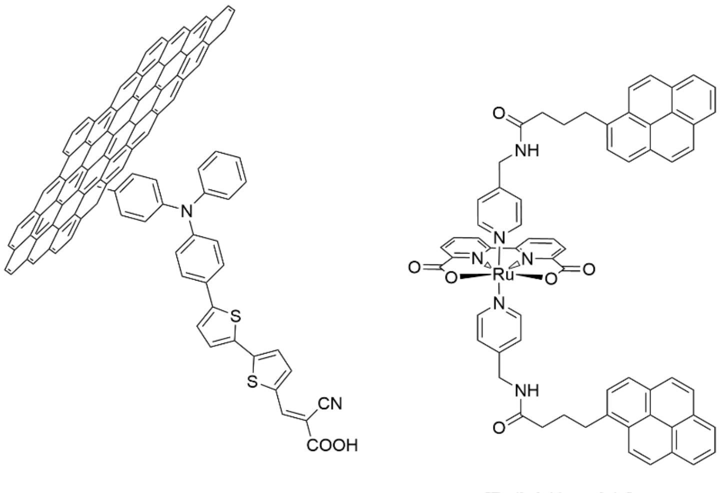

RGO-TPAThTh $[Ru(bda)(pyrpic)_2]$

Figure 41: Structures of the investigated compounds.

6.2 Design and synthesis

The investigated photosensitizer is a triphenylamine-based D-π-A dye characterized by a long π-spacer to collect a large portion of the solar radiation. Its donor moiety is functionalized with an amino group, mandatory to perform the arylation of the RGO layer through Tour reaction. The synthetic pathway for **H_2N-TPAThTh** is depicted in Scheme 6, and the final condensation with the RGO layer to obtain **RGO-TPAThTh** is depicted in Scheme 7.

The synthetic pathway started from the 4-bromo-*N*-(4-nitrophenyl)-*N*-phenylaniline (**1**) synthesized following a literature procedure,[14,15] first nitrating the triphenylamine with sodium nitrate in acetic acid and dichloromethane, and then brominating with *N*-bromosuccinimide in *N*,*N*-dimethylformamide. The obtained product was subjected to a palladium-catalyzed Suzuki-Miyaura cross-coupling performed with 5'-formyl-2,2'-bithiophene-5-boronic acid in a basic environment at 50 °C for 6 h. The next reaction was a Knoevenagel condensation performed with cyanoacetic acid and piperidine, then followed by a zinc-reduction of the nitro group to release the amino group. The last step will be a Tour reaction[5] performed with pristine RGO in the presence of isoamyl nitrite, to finally obtain the dye-sensitized RGO. This last reaction will be performed at the University of Padova, once 200 mg of **H_2N-TPAThTh** will be obtained. All the further optical and electrochemical characterizations of the **H_2N-TPAThTh** are still in progress.

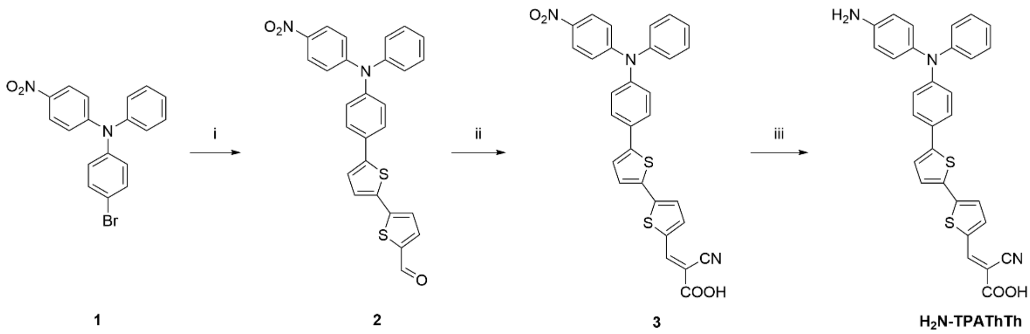

Scheme 6: Synthesis of **H_2N-TPAThTh**. Reagents and conditions. i) 5'-formyl-2,2'-bithiophene-5-boronic acid, $[Pd(dppf)Cl_2]\cdot DCM$, K_2CO_3, Et_3N, Me-THF-MeOH (1:1), 50 °C, 6 h; ii) cyanoacetic acid, piperidine, $CHCl_3$, reflux, 8 h; iii) Zn (powder), HCl 37%, EtOH-H_2O (10:1), reflux, 1 h.

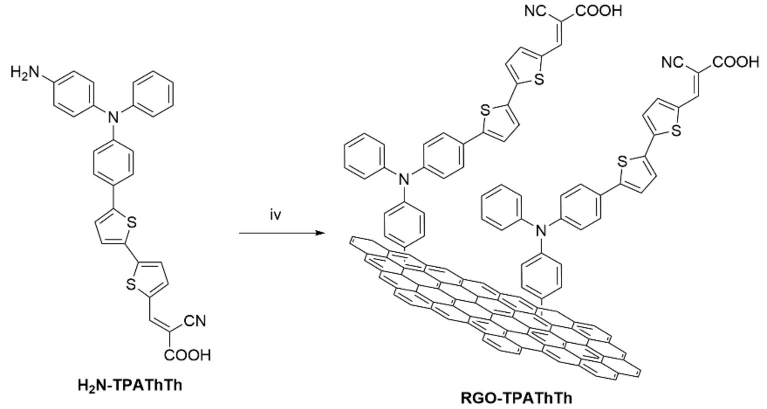

Scheme 7: Synthesis of **RGO-TPAThTh**. Reagents and conditions. iv) pristine RGO, isoamyl nitrite, DMF, 80 °C

In conclusion, this project is still in progress, and for now, just the synthetic pathway to yield the organic dye has been concluded. The following complexation with an RGO layer to obtain the desired **RGO-TPAThTh** will be performed at the University of Padova. Further efforts in this way will prove this innovative design in photoelectrochemical studies.

6.3 Experimental section

6.3.1 General information

NMR spectra were recorded with a Bruker Advance-Neo spectrometer operating at 400 MHz (^{1}H) and 100 MHz (^{13}C). Coupling constants are given in Hz. ATR FT-IR spectra were recorded with a PerkinElmer Spectrum 100. Compounds were purified using flash chromatography with Merck grade 9385 silica gel 230-400 mesh (60 Å). The glassware for water-free reactions was dried in a 130 °C oven for 4 h before use and then attached to the vacuum pump. Inert atmosphere was generated by Schlenk technique using nitrogen flow. Conversion was monitored by thin-layer chromatography (Silica gel on TLC Al foils with fluorescent indicator 254 nm) by using UV light (254 and 365 nm) as a visualizing agent. All reagents were obtained from commercial suppliers at the highest purity grade and used without further purification. Anhydrous solvents were purchased from Acros Organics and used without further purification. Organic phases obtained after extraction were dried with Na_2SO_4 and filtered before removal of the solvent by evaporation. 4-bromo-*N*-(4-nitrophenyl)-*N*-phenylaniline (**1**) was prepared following literature procedures.[14,15]

5'-(4-((4-nitrophenyl)(phenyl)amino)phenyl)-[2,2'-bithiophene]-5-carbaldehyde (2). In oven-dried glassware, **1** (130 mg, 0.35 mmol) was dissolved in 2-methyltetrahydrofuran (10 mL) and methanol (10mL) under nitrogen atmosphere. The solution was degassed with nitrogen flow for 30 min then 5'-formyl-2,2'-bithiophene-5-boronic acid (100 mg, 0.42 mmol), Pd(dppf)Cl_2 (28 mg, 0.035 mmol), K_2CO_3 (483 mg, 3.5 mmol) and triethylamine (4 drops) were added. The reaction mixture was stirred at room temperature and degassed with nitrogen flow for 3 min and then heated at 50 °C for 6 hours. After completion of the reaction as monitored by TLC, the mixture was quenched by pouring into a saturated solution of NH_4Cl (30 mL) and CH_2Cl_2 (30 mL). Filtration on Celite and extractions with organic solvent allowed to isolate the crude product, then purified through column chromatography on silica gel (*n*-heptane/AcOEt, 4:1). The desired product was isolated as a light-yellow solid (78 mg, 0.14 mmol) with 46% yield. ^{1}H NMR (400 MHz, $CDCl_3$) δ 9.87 (s, 1H), 8.07 (d, *J* = 9.3 Hz, 2H), 7.68 (d, *J* = 4.0 Hz, 1H), 7.58 (d, *J* = 8.6 Hz, 2H), 7.40 (t, *J* = 7.8 Hz, 2H), 7.34 (d, *J* = 3.9 Hz, 1H), 7.27 (d, *J* = 4.0 Hz, 1H), 7.25 (d, *J* = 3.9 Hz, 1H), 7.22-7.16 (m, 5H), 7.01 (d, *J* = 9.3 Hz, 2H).

2-cyano-3-(5'-(4-((4-nitrophenyl)(phenyl)amino)phenyl)-[2,2'-bithiophen]-5-yl)acrylic acid (3). Compound **2** (78 mg, 0.16 mmol), cyanoacetic acid (140 mg, 1.60 mmol), and piperidine (0.2 mL, 1,92 mmol) were dissolved in 5 mL of chloroform and warmed to reflux for 5 h. After having the solvent evaporated, an aqueous solution of HCl 10% was added and the mixture was left under magnetic stirring for 1 h at room temperature. The solid that precipitated, was filtered, and washed with water. The desired product was isolated as a red solid (40 mg, 0.07 mmol) with 44% yield. ^{1}H NMR (400 MHz, DMSO) δ 8.45 (s, 1H), 8.11 (d, J = 9.3 Hz, 2H), 7.96 (d, J = 4.0 Hz, 1H), 7.80 (d, J = 8.6 Hz, 2H), 7.65 (d, J = 3.9 Hz, 1H), 7.63 - 7.59 (m, 2H), 7.49 (t, J = 7.8 Hz, 2H), 7.38 - 7.24 (m, 5H), 6.95 (d, J = 9.3 Hz, 2H).

3-(5'-(4-((4-aminophenyl)(phenyl)amino)phenyl)-[2,2'-bithiophen]-5-yl)-2-cyanoacrylic acid (H_2N-TPAThTh). To a room temperature solution of **3** (40 mg, 0.07 mmol) in EtOH (10 mL), zinc powder (7 mg, 0.11 mmol) was added. After stirring for 5 min, HCl 37% (0.1 mL) and H_2O (1 mL) were added. The reaction mixture was refluxed for 1 h and then allowed to cool to room temperature. The reaction mixture was filtered on celite, washed with EtOH and the solvent was evaporated with rotavapor. After addition of a solution of potassium carbonate, an orange solid precipitated and it was filtered. ^{1}H NMR (400 MHz, DMSO) δ 8.11 (d, J = 9.4 Hz, 2H), 7.98 (s, 1H), 7.78 (d, J = 8.7 Hz, 2H), 7.63 (d, J = 4.5 Hz, 1H), 7.56 (d, J = 3.9 Hz, 1H), 7.50 (d, J = 3.8 Hz, 1H), 7.49 - 7.44 (m, 3H), 7.34 - 7.23 (m, 5H), 6.94 (d, J = 9.4 Hz, 2H). FT-IR υ/(cm^{-1}): 2913, 1590, 1490, 1055, 948. ^{13}C NMR spectrum was not recorded due to low solubility of the compound.

References

1 Lazzarin, L., Pasini, M. & Menna, E. (**2021**) Organic Functionalized Carbon Nanostructures for Solar Energy Conversion. *Molecules,* **26**, 5286, doi:10.3390/molecules26175286.

2 Wick, P., Louw-Gaume, A. E., Kucki, M., Krug, H. F., Kostarelos, K., Fadeel, B., Dawson, K. A., Salvati, A., Vázquez, E., Ballerini, L., Tretiach, M., Benfenati, F., Flahaut, E., Gauthier, L., Prato, M. & Bianco, A. (**2014**) Classification Framework for Graphene-Based Materials. *Angew. Chem. Int. Ed.,* **53**, 7714-7718, doi:10.1002/anie.201403335.

3 Gavrel, G., Jousselme, B., Filoramo, A. & Campidelli, S. in *Making and Exploiting Fullerenes, Graphene, and Carbon Nanotubes. Topics in Current Chemistry* Vol. 348 (eds M. Marcaccio & F. Paolucci)(Springer: Berlin, Germany, **2013**).

4 Yan, X., Cui, X., Li, B. & Li, L.-s. (**2010**) Large, Solution-Processable Graphene Quantum Dots as Light Absorbers for Photovoltaics. *Nano Lett.,* **10**, 1869-1873, doi:10.1021/nl101060h.

5 Gatti, T., Manfredi, N., Boldrini, C., Lamberti, F., Abbotto, A. & Menna, E. (**2017**) A D-π-A organic dye - Reduced graphene oxide covalent dyad as a new concept photosensitizer for light harvesting applications. *Carbon,* **115**, 746-753, doi:10.1016/j.carbon.2017.01.081.

6 Du, Y., Dong, N., Zhang, M., Zhu, K., Na, R., Zhang, S., Sun, N., Wang, G. & Wang, J. (**2017**) Covalent functionalization of graphene oxide with porphyrin and porphyrin incorporated polymers for

optical limiting. *Phys. Chem. Chem. Phys.,* **19**, 2252-2260, doi:10.1039/C6CP05920A.

7 Li, R.-X., Liu, X.-F., Liu, T., Yin, Y.-B., Zhou, Y., Mei, S.-K. & Yan, J. (**2017**) Electrocatalytic properties of [FeFe]-hydrogenases models and visible-light-driven hydrogen evolution efficiency promotion with porphyrin functionalized graphene nanocomposite. *Electrochim. Acta,* **237**, 207-216, doi:10.1016/j.electacta.2017.03.216.

8 Li, X., Li, K., Wang, D., Huang, J., Zhang, C., Du, Y. & Yang, P. (**2017**) One-pot synthesis of manganese porphyrin covalently functionalized graphene oxide for enhanced photocatalytic hydrogen evolution. *J. Porphyrins Phthalocyanines,* **21**, 179-188, doi:10.1142/s1088424616501236.

9 Attatsi, I. K., Zhu, W. & Liang, X. (**2020**) Noncovalent immobilization of Co(II) porphyrin through axial coordination as an enhanced electrocatalyst on carbon electrodes for oxygen reduction and evolution. *New J. Chem.,* **44**, 4340-4345, doi:10.1039/C9NJ02408E.

10 Gao, Y., Wei, Y., Lu, Z., Chen, X. & Wang, D. (**2019**) A steady composite molecular anode Ru1/MWCNTsCOOH/GC for robust catalytic water oxidation. *J. Energy Chem.,* **35**, 49-54, doi:10.1016/j.jechem.2018.10.013.

11 Geer, A. M., Liu, C., Musgrave III, C. B., Webber, C., Johnson, G., Zhou, H., Sun, C.-J., Dickie, D. A., Goddard III, W. A., Zhang, S. & Gunnoe, T. B. (**2021**) Noncovalent Immobilization of Pentamethylcyclopentadienyl Iridium Complexes on Ordered Mesoporous Carbon for Electrocatalytic Water Oxidation. *Small Science,* **1**, 2100037, doi:10.1002/smsc.202100037.

12 Gu, T., Kwaku Attatsi, I., Zhu, W., Li, M., Ndur, S. A. & Liang, X. (**2022**) Enhanced electrocatalytic hydrogen evolutions of Co(II) phthalocyanine through axially coordinated pyridine-pyrene. *Inorg. Chim. Acta,* **530**, 120696, doi:10.1016/j.ica.2021.120696.

13 Li, F., Zhang, B., Li, X., Jiang, Y., Chen, L., Li, Y. & Sun, L. (**2011**) Highly efficient oxidation of water by a molecular catalyst immobilized on carbon nanotubes. *Angew. Chem. Int. Ed.,* **50**, 12276-12279, doi:10.1002/anie.201105044.

14 Mangione, M. I., Spanevello, R. A. & Anzardi, M. B. (**2017**) Efficient and straightforward click synthesis of structurally related dendritic triazoles. *RSC Adv.,* **7**, 47681-47688, doi:10.1039/C7RA09558A.

15 Nad, S. & Malik, S. (**2020**) Design, Synthesis, and Electrochromic Behaviors of Donor-Acceptor-Donor type Triphenylamine-iso-Naphthalenediimide Derivatives. *ChemElectroChem,* **7**, 4144-4152, doi:10.1002/celc.202001114.

Chapter 7: Covalent approach in DSPEC

Aim of this section

In this section, I present the first examples of organic dye-based dyads for application in DSPEC photoanodes. The covalent approach favors the formation of a more stable dyad, immobilizing the WOC on the SC surface at a fixed distance, thus avoiding detrimental charge recombination reactions between WOC and SC.

In this case, an axial ligand of the common [Ru(bda)(pic)$_2$] is covalently connected to an organic *push-pull* dibranched dye. I investigated eight different designs changing the donor moiety, the distance between the dye and the WOC, and the different linkage positions on the pyridyl ring of the ligand. The different functionalizations added on the donor moiety of the dye did not influence the optical and electrochemical properties of the molecule. The dyads have been obtained by self-assembly directly on the electrode surface. Their correct formations have been evaluated through electrochemistry and XPS.

The photoelectrochemical studies in a three-electrode DSPEC showed the enhanced photoelectrocatalytic performances of the dyad-sensitized electrodes compared with the dye-sensitized ones. FE have been calculated by means of collector-generator technique. These FE results were elevated and reproducible for the carbazole-based dyes. However, the phenothiazine-based ones presented many out-of-range values indicating a possible degradation of the dyads and a bad charge transfer.

Moreover, IPCE, LHE, and APCE studies have been performed on **CBZ-3Py+Ru** and **CBZ-4Py+Ru**, further demonstrating the formation of the correct dyads and confirming the trend obtained in the collector-generator investigations. Further investigation on the long-chain dyads is in progress to evaluate if the presence of higher mobility between the dye and the WOC portion can increase the efficiencies and speed up the charge transfers.

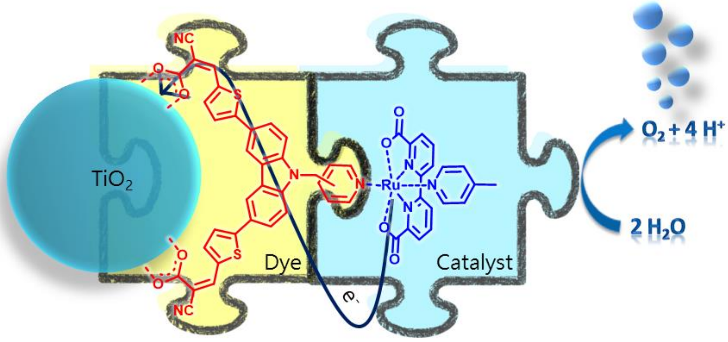

Figure 42: Pictorial representation of the two portions of the dyad connected through a covalent bond between the dye and a ligand of the WOC.

7.1 Introduction

One last approach for DSPEC is the establishment of a covalent bond between the photosensitizer and the WOC. The covalent approach is the most promising because it gives more stability to the system. In fact, with the immobilization of the WOC on the SC surface, it is possible to use pure aqueous media and develop a device, which can work in flow. Moreover, this approach ensures the confinement of the WOC away from the electrode surface. Although this approach is not yet mature in terms of device efficiency, the goal is to improve long-term stability and create a single supramolecular functional system, fully integrated and capable of performing all the necessary functions (light absorption, transfer, and transport of charges, water splitting, and dye regeneration) in an efficient, cooperative and interactive manner.[1] This can be possible thanks to the structural and functional optimization of the single sub-units, their spatial proximity, and the stability of the connections between them.

Many examples exploiting ruthenium photosensitizers have been presented in the literature.[2-6] In these cases, a bidentate ligand complexed two ruthenium centers, with one acting as the dye and the other as the WOC. However, the first example of a dyad employing a [Ru(bda)(L)$_2$]-type WOC was the **Ru-ZnP**, previously mentioned in paragraph 4.4.[7] This was also the first example of the use of abundant and non-precious metals in the photosensitizer portion. Despite this system obtaining a FE of 33% and a maximum IPCE of 18% at 424 nm, it proved the advantages of the integrated systems with respect to the use of the single components. Authors suggested that the low performances could be improved with the use of photosensitizers presenting higher molar extinction coefficients in the visible region and higher oxidation potentials under aqueous environments as well as a more flexible structure to facilitate the radical coupling mechanisms.

When I started this project, no examples of organic dye-based dyads for photoanode applications were present in the literature. The complete absence in the literature of organic-based dyads for photoanodes is surprising, considering the prominent role of metal-free dyes in dye-sensitized solar applications, such as photovoltaics and, more recently, hydrogen generation.[1,8-11] The only two examples employing an organic dye covalently bonded to a catalyst were in the state of the art photocathodes. In both cases, an azide-functionalized cobalt diamine-dioxime was subjected to copper-catalyzed click chemistry with an alkyne-functionalized organic dye.[12,13] However, both designs did not obtain remarkable results in photoelectrochemical hydrogen evolution due to the high degradability of the dyads and the presence of low and highly unstable photocurrents.

More recently, Reisner and coworkers published a diketopyrrolopyrrole dye-based dyad for photoanode applications (Figure 43).[14] In this case, a diketopyrrolopyrrole was functionalized with a cyanoacrylic acceptor and anchor group for binding the TiO_2, and with a pyridyl ring on the other side to coordinate the ruthenium center of the WOC. This dyad obtained a FE for oxygen production of about 44% and a TON for the catalyst of 2.3. These disappointing results were attributed to the strong decrease in current during the water photolysis, which was mainly associated with catalyst detachment or decomposition rather than dyad desorption or chromophore decomposition. Regardless, this work demonstrated the possible application of metal-free organic dyes into molecular dyads for water oxidation.

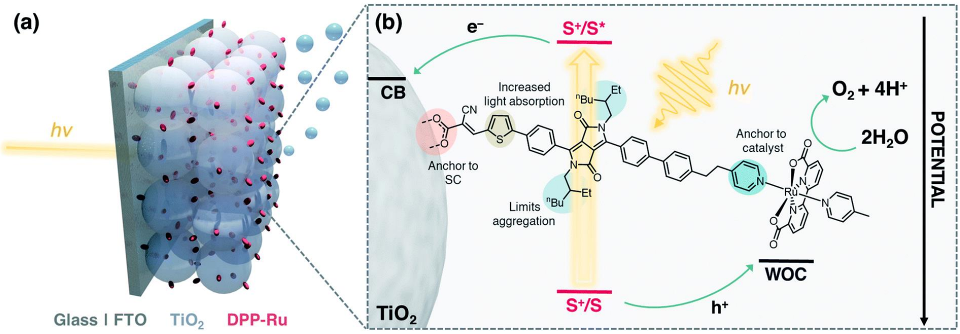

Figure 43: (a) Schematic representation of the water oxidizing dyad-sensitized photoanode. (b) Structure of **DPP-Ru** with design features and electron transfer events. Image from ref 14.

In this project, we investigated organic-based dyads characterized by a metal-free sensitizer covalently bonded to a ruthenium-based benchmark WOC, ([Ru(bda)(L)$_2$]).[15] For metal-free sensitizers, we have considered dibranched D-$(\pi$-$A)_2$ molecules whose classes have been previously investigated in many dye-sensitized photovoltaic and solar fuels production applications.[16-18] The donor moiety has been properly functionalized with a pyridine ligand, which is then used to coordinate the Ru center of the WOC complex. The pyridyl ring has been covalently bound in different modalities, in order to explore the particular properties of each design in the photoelectrochemical oxygen evolution. An alkyl linker between the donor moiety and the pyridyl has been introduced to break the conjugation between the two entities (dye and catalyst), avoiding the perturbation of the optical, electrochemical, and catalytic properties of the two components and circumventing charge recombination processes. The dyads have been obtained directly through self-assembly on the electrode surface and have been characterized optically and electrochemically. Finally, the dyad-sensitized electrodes have been investigated in photoelectrochemical water oxidation by calculating the FE.

7.2 Design and synthesis

The investigated dyes and dyads are depicted in Figure 44 and Figure 45. These compounds are divided in two families depending on the nature of the donor moiety. We considered four phenothiazine-based dyes, four carbazole-based ones, and the corresponding dyads. Phenothiazine and carbazole have been widely studied in the DSSC, DSPC, and DSPEC fields due to the possibility of forming a symmetrical dibranched dye characterized by two π-A branches that increase the light-harvesting capability and the anchoring stability of the system.[1,10,18,19] These compounds differ in geometry (bent for the phenothiazine and planar for the carbazole) due to the sulfur atom present only in the phenothiazine structure that breaks the aromaticity. The central nitrogen atom of both designs can be easily functionalized through a nucleophilic substitution reaction. Despite the nature of the donor moiety, the structure of all investigated dyes is equal but for the functionalization site. The branches are composed of thienyl π-spacers followed by cyanoacrylic acceptor and anchor groups. The pyridyl ring is connected to the donor moiety through a particular alkyl bridge. This alkyl bridge is important because it breaks the conjugation between the WOC and the dye, in order to limit charge recombination. In two cases, a simple methylene group is used as a bridging point while in the other two cases a propyl chain is used. The short-bridge compounds differ for the linkage position on the pyridyl ring; in one case through the *para* position (**PTZ-4Py** and **CBZ-4Py**) and in the other through the *meta* position (**PTZ-3Py** and **CBZ-3Py**). Also, the long-bridge compounds differ for the linkage position: *para* for **PTZ-C3-4Py** and **CBZ-C3-4Py** and *meta* for **PTZ-Py** and **CBZ-Py**. **PTZ-Py** and **CBZ-Py** presented, also, an electron-withdrawing ester group on the pyridyl ring that may affect the electronic properties of the WOC portion.

The synthesis of most investigated dyes is depicted in Scheme 8. The introduction of an electron-withdrawing group on the pyridyl ring required a different synthetic pathway. For this reason, the synthesis of **PTZ-Py** and **CBZ-Py** is depicted in Scheme 9. The general scheme starts with a palladium-catalyzed Suzuki-Miyaura cross-coupling between a 10*H*-3,7-dibromophenothiazine or 9*H*-3,6-dibromocarbazole and the pinacol ester of 5-formyl-2-thienylboronic acid[20] affording the intermediates **2a-b** with protected formyl groups. A following alkylation reaction performed with sodium hydride as base and 4-(bromomethyl)pyridine hydrobromide, 3-(bromomethyl)pyridine hydrobromide, or 3-(pyridin-4-yl)propyl 4-methylbenzenesulfonate as alkylating agent in anhydrous THF or DMF adds the functionalization site on the donor moiety. Subsequent acidic deprotection of the formyl groups and final Knoevenagel condensation with cyanoacetic acid in the presence of piperidine yield the desired sensitizers with the proper pyridine ligand. Acidification with citric acid 1 M aqueous solution allows the protonation of the carboxylic acids leaving the pyridyl ring free.

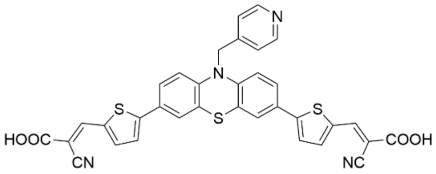

PTZ-4Py

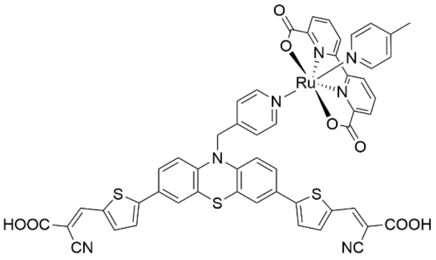

PTZ-4Py+Ru

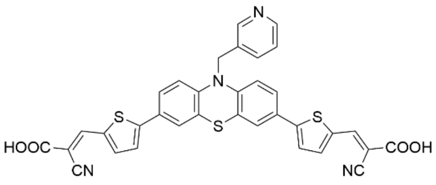

PTZ-3Py

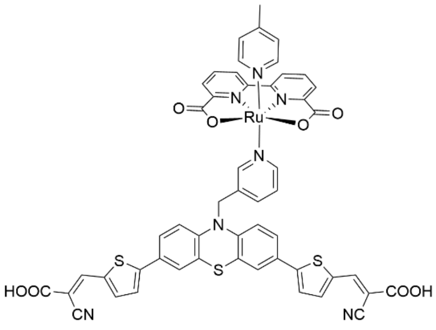

PTZ-3Py+Ru

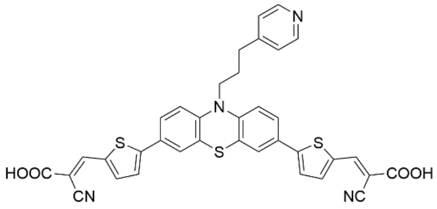

PTZ-C3-4Py

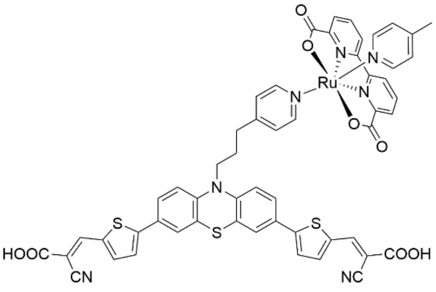

PTZ-C3-4Py+Ru

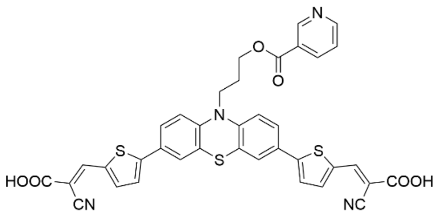

PTZ-Py

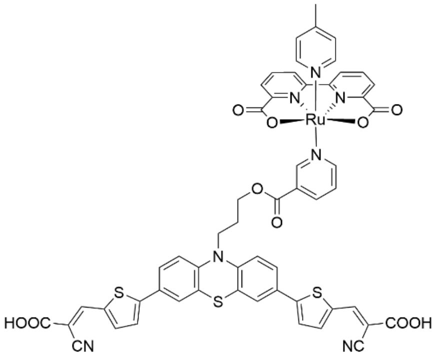

PTZ-Py+Ru

Figure 44: Molecular structures of the investigated phenothiazine-based dyes and dyads.

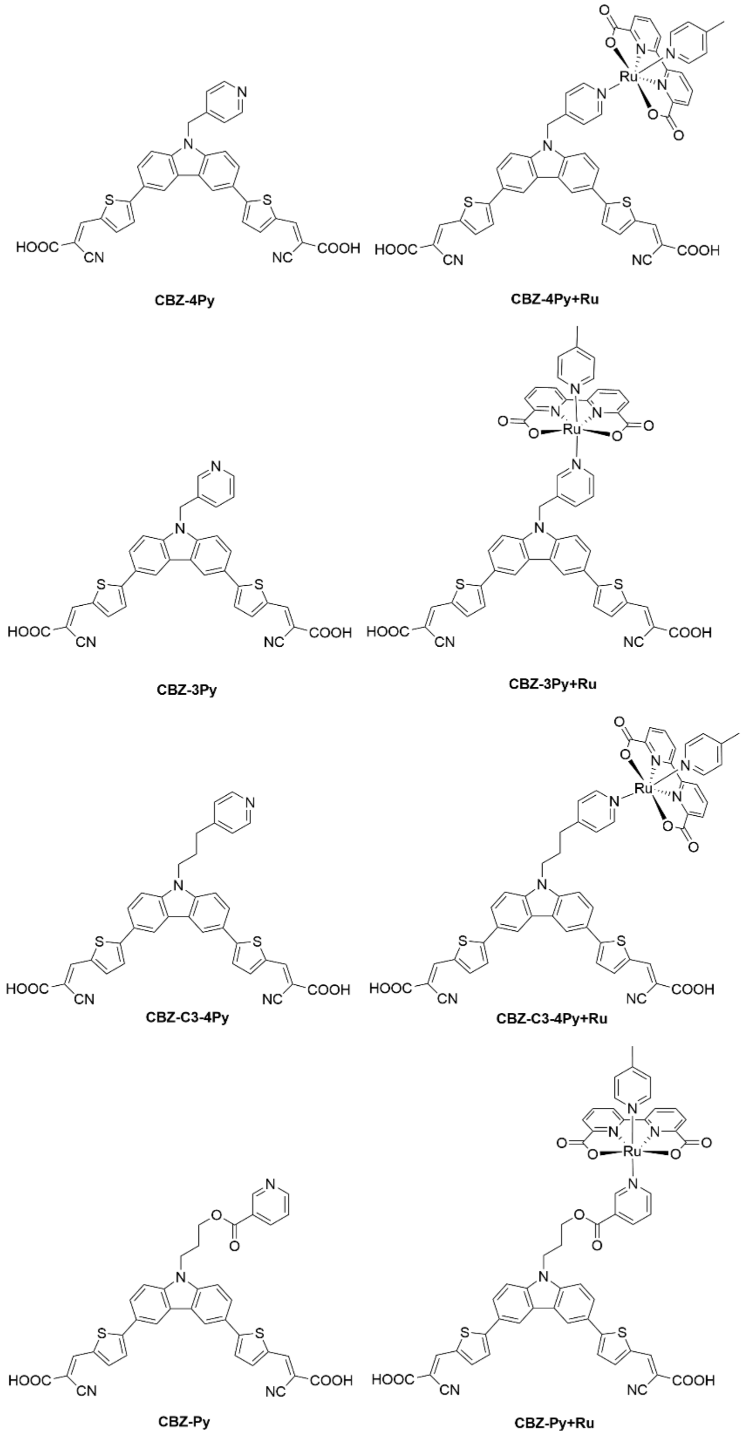

CBZ-4Py **CBZ-4Py+Ru**

CBZ-3Py **CBZ-3Py+Ru**

CBZ-C3-4Py **CBZ-C3-4Py+Ru**

CBZ-Py **CBZ-Py+Ru**

Figure 45: Molecular structures of the investigated carbazole-based dyes and dyads.

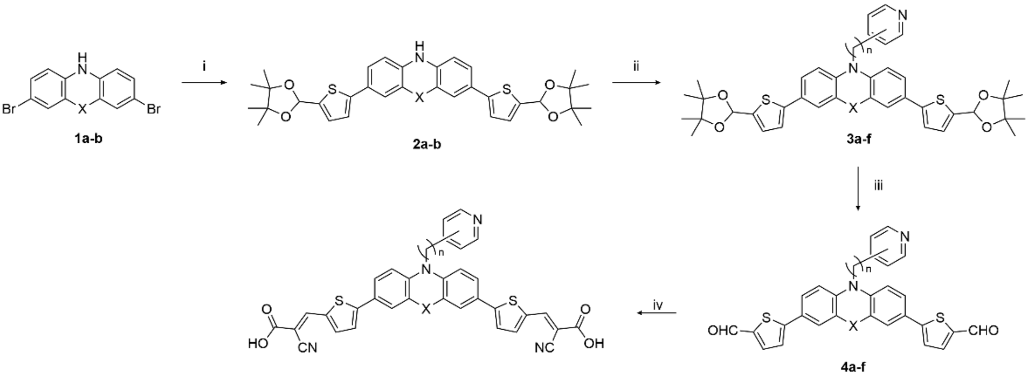

n=1, X = S, linkage in *para*	**PTZ-4Py**
n=1, X = S, linkage in *meta*	**PTZ-3Py**
n=1, X = none, linkage in *para*	**CBZ-4Py**
n=1, X = none, linkage in *meta*	**CBZ-3Py**
n=3, X = S, linkage in *para*	**PTZ-C3-4Py**
n=3, X = none, linkage in *para*	**CBZ-C3-4Py**

Scheme 8: Synthetic pathway for **PTZ-4Py**, **PTZ-3Py**, **CBZ-4Py**, **CBZ-3Py**, **PTZ-C3-4Py**, and **CBZ-C3-4Py**. Reagents and conditions: i) 4,4,5,5-tetramethyl-2-(5-(4,4,5,5-tetramethyl-1,3-dioxolan-2-yl)thiophen-2-yl)-1,3,2-dioxaborolane, Pd(dppf)$Cl_2 \cdot CH_2Cl_2$, K_2CO_3, DME/MeOH (1:1), microwave 100 °C, 70 W, 60 min; ii) 4-(bromomethyl)pyridine hydrobromide or 3-(bromomethyl)pyridine hydrobromide or 3-(pyridin-4-yl)propyl 4-methylbenzenesulfonate, NaH 60%, THF or DMF anhydrous, 0 °C, 30 min and then rt, overnight; iii) HCl 10%/THF (1:2), 50 °C, 2 h; iv) cyanoacetic acid, piperidine, $CHCl_3$ dry, reflux, 8 h.

PTZ-Py and **CBZ-Py** require the introduction of an ester bond in their molecular structure, thus the synthetic pathway is different from the other cases (Scheme 9). The synthesis of **CBZ-Py** has not been concluded before the submission of this thesis. In this case, the synthetic pathway starts with an alkylation reaction with 3-bromopropoxy(*tert*-butyl)dimethylsilane[21] and sodium hydride in anhydrous DMF to afford the intermediates **5a-b**. A following palladium-catalyzed Suzuki-Miyaura cross-coupling performed in similar condition than the other case inserts the π-spacers with the aldehydic functionalizations. The cleavage of the alcoholic protection with tetra-*n*-butylammoniumfluoride in THF and subsequent Steglich esterification with nicotinic acid in dichloromethane release the intermediates **8a**. The synthesis of intermediate **8b** is still in progress. The last Knoevenagel condensation performed with cyanoacetic acid and piperidine in chloroform yields the desired **PTZ-Py** and probably **CBZ-Py** could be obtained with the same conditions. Also in this case, a following acidification with citric acid 1 M aqueous solution allows the protonation of the carboxylic acids leaving the pyridyl ring free.

All the final products have been fully characterized with ^{1}H and ^{13}C NMR, as well as melting point, FT-IR, and HRMS to check the required structures and purities.

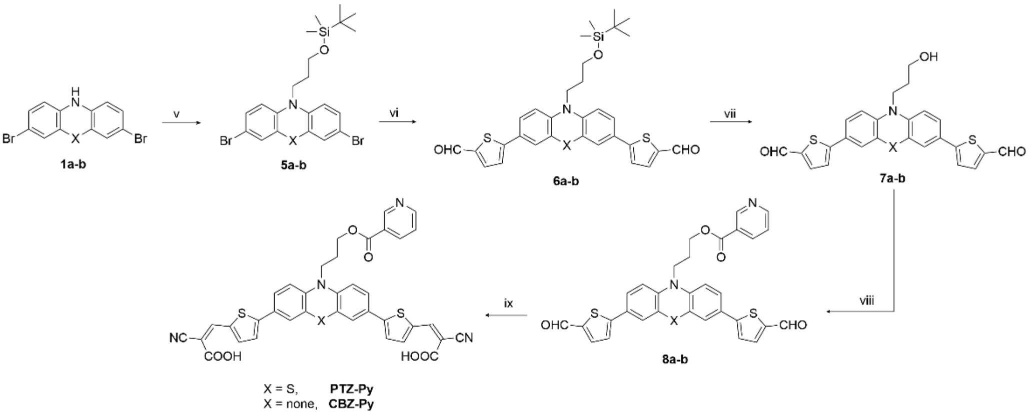

Scheme 9: Synthetic pathway for **PTZ-Py** and **CBZ-Py**. Reagents and conditions: v) (3-bromopropoxy)(tert-butyl)dimethylsilane, NaH 60%, anhydrous DMF, 0 °C, 30 min and then rt, overnight vi) 5-formyl-2-thienylboronic acid, Pd(dppf)Cl$_2$·CH$_2$Cl$_2$, K$_2$CO$_3$, DME/MeOH (1:1), microwave 90 °C, 200 W, 90 min; vii) tetra-*n*-butylammoniumfluoride, THF, 0 °C 5 min, rt, 3 h; viii) nicotinic acid, 4-(dimethylamino)pyridine, *N*,*N'*-dicyclohexylcarbodiimide, CH$_2$Cl$_2$, -10 °C, 2 h, 0 °C, 5 h, ix) cyanoacetic acid, piperidine, CHCl$_3$ dry, reflux, 8 h.

The synthetic attempt to synthetize an organic dye-based dyad is depicted in Scheme 10. Starting from the well-known **[Ru(bda)(DMSO)$_2$]**,[22] **[Ru(bda)(pic)(DMSO)(CH$_3$CN)]** was obtained after reaction in acetonitrile with stoichiometric 4-picoline.[23] A stoichiometric amount of dye dissolved in 1 mL of dimethyl sulfoxide was added to the methanol solution containing the previous intermediate and the mixture was heated at 55 °C under inert atmosphere for one day. However, the product was difficult to purify since it was only soluble in coordinating solvents, which destroy the complex. In fact, the ruthenium portion well dissolves in methanol while the dye portion only dissolves in dimethyl sulfoxide.

To overcome this problem, the dyad was obtained by self-assembly onto the electrode surface. The titanium dioxide electrode was soaked into a 2×10^{-4} M EtOH/DMSO (9:1) solution of the dye together with the precursor of the catalyst **[Ru(bda)(pic)(DMSO)(CH$_3$CN)]** in the same concentration. The films were left sensitizing for 3 h in the dark. Each electrode was rinsed with EtOH to eliminate any residues left on the surface. Since the ruthenium precursor does not carry any anchoring group, this final rinse ensures that the presence of ruthenium in the rinsed electrode can only be due to the formation of the desired complex with the functionalized dye, in turn, anchored to the SC *via* the acceptor-carboxylic functionality.

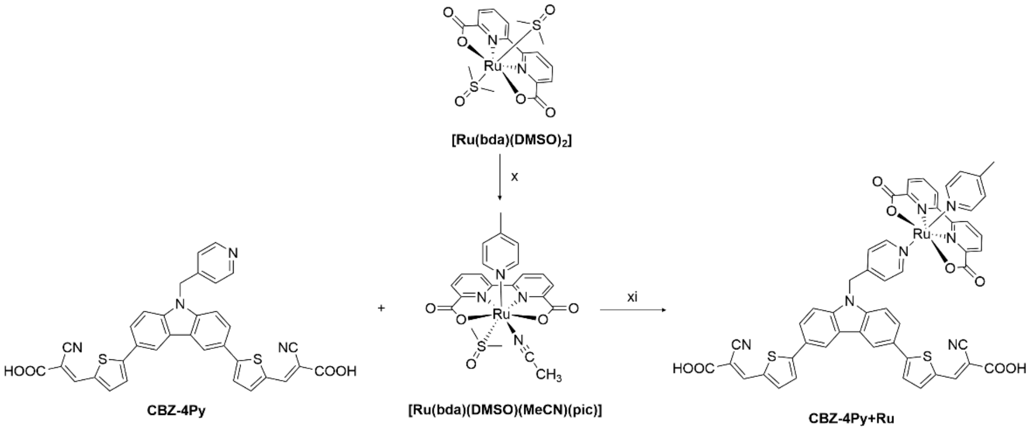

Scheme 10: General procedure for the synthesis of the dyads in solution. Reagents and conditions: x) 4-picoline, acetonitrile, reflux, 1 h; xi) MeOH, DMSO, reflux, 1 day.

7.3 Optical and electrochemical properties

All the final products have been optically characterized both in solution (Figure 46) and adsorbed on 1-μm TiO_2 film (Figure 47). The main relevant optical parameters are collected in Table 5. The phenothiazine derivatives present approximately the same optical properties. The shapes of all the UV-spectra are similar, as are the molar extinction coefficients, confirming the non-influence of the functionalization site on the optical properties. The UV-vis spectra exhibit the typical two bands related to the π–π* absorption in the 300–450 nm range and to the ICT transition in the 400–600 nm range.[24] The absorption maxima for the ICT transition are at ~470 nm for all the dyes, just a little red-shifted for **PTZ-Py**. Th carbazole-based dyes, indeed, present the same ICT transition between 400 and 550 nm, [25] but with two different trends: **CBZ-3Py** and **CBZ-4Py** exhibit a maximum of absorption around 450 nm, while **CBZ-C3-4Py** presents a red-shift of about 15 nm and a higher molar extinction coefficient. We hypothesize that the presence of a longer chain could reduce the aggregation of the molecules due to the planar structure of the carbazole. However, this hypothesis is still under investigation and it could be confirmed or rejected by the behavior of **CBZ-Py** once its synthesis is concluded. Moreover, it was not possible to perform the complete optical and electrochemical characterization of **PTZ-C3-4Py** for question of time. The characterization of **PTZ-C3-4Py** and the synthesis of **CBZ-Py** compounds are currently in progress.

The UV-vis spectra of all the compounds on 1-μm TiO_2 film show similar optical properties to the family they belong to, phenothiazine or carbazole. All the maxima of absorption are blue-shifted of about 20-30 nm due to the formation of an ester bond between the TiO_2 and the dye that reduces the electron-withdrawing strength of the acceptor groups.

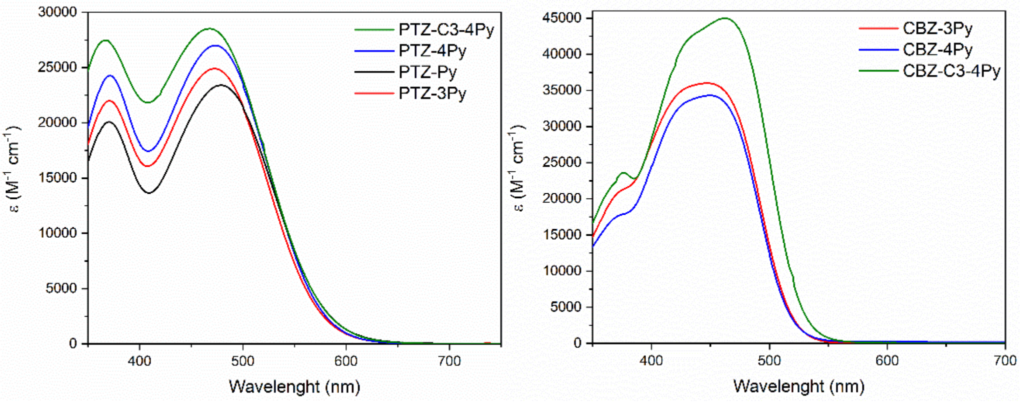

Figure 46: UV-Vis spectra in DMSO solution of the phenothiazine-based dyes (left) and of the carbazole-based dyes (right).

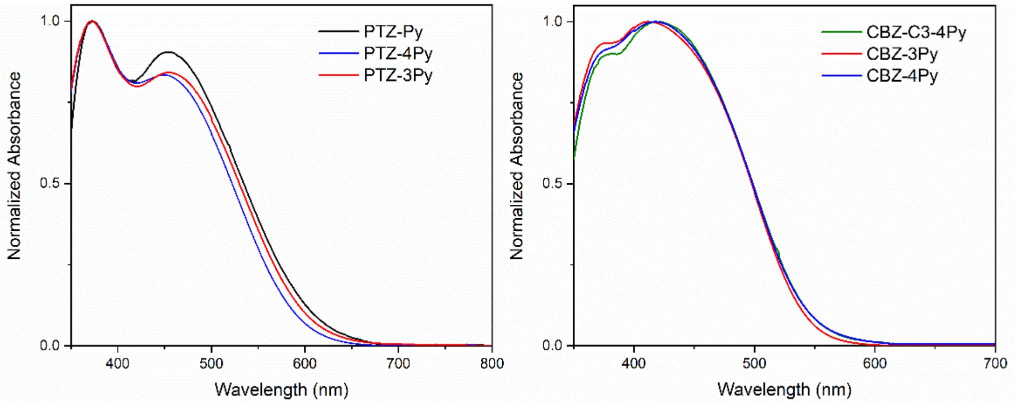

Figure 47: UV-Vis spectra on 1-μm transparent TiO_2 film of the phenothiazine-based dyes (left) and of the carbazole-based dyes (right).

The amount of dye loaded on the film was investigated by soaking the dye-sensitized film into a NaOH 0.1 M in EtOH-H_2O (1:1) until complete desorption of the dye and evaluating the amount of dye present in the solution with UV-vis spectroscopy. Interestingly, the **3Py**-derivatives present a 50%-higher dye-loading than the **4Py**-derivatives. Instead, the long-chain dyes exhibit a dye-loading between the **3Py** and the **4Py** derivatives, around the average values. Optical bandgaps were calculated by means of the Tauc plots[26] and listed in Table 5 as well as λ_{onset}.

Table 5: Optical parameters of investigated sensitizers in solution and on transparent TiO_2 films.

Dye	λ_{max}[a,b] (nm)		λ_{onset}[a,b] (nm)		ε (M^{-1} cm^{-1})	Dye loading[c] (nmol cm^{-2})	E_{gap}^{opt} (eV)	
	soln	film	soln	film			soln	film
PTZ-4Py	370 472	371 450	589	618	27000 ±1000	44.5	2.00	1.91
PTZ-3Py	370 471	371 455	586	624	24900 ±400	65.7	1.96	1.87
PTZ-C3-4Py	367 467	-	601	-	28510 ±30	-	1.93	-
PTZ-Py	370 479	370 455	600	648	23400 ±300	54.0	1.92	1.77
CBZ-4Py	448	417	529	545	34300 ±100	37.1	2.26	2.12
CBZ-3Py	447	413	528	546	36000 ±2000	55.8	2.26	2.14
CBZ-C3-4Py	462	418	540	603	45000 ±600	42.2	2.20	1.95

[a] Dye solution 10^{-5} M in DMSO. [b] 1-µm transparent TiO_2 photoanode. [c] 3.5-µm transparent TiO_2 photoanode

The optical properties of the dyad-sensitized 1-µm TiO_2 films were also investigated (Figure 48). The spectra remained similar to the ones of the bare dye-sensitized films. In some cases, the spectra are wider, perhaps due to a sort of aggregation on the films. The maxima are about in the same position except for **PTZ-3Py+Ru** and **CBZ-C3-4Py+Ru** where the maxima are shifted of about 30 nm.

The electrochemical parameters are listed in Table 6. The oxidation potentials were determined using CV and DPV in solution and adsorbed onto TiO_2. In solution, some compounds presented irreversible oxidation peaks in the CV profile (Figure 49), thus DPV was used to determine the oxidation potentials (Figure 50). The potential of the first oxidation peak for each

DPV curve in solution was considered as the oxidation potential of the dye and reported in Table 6.

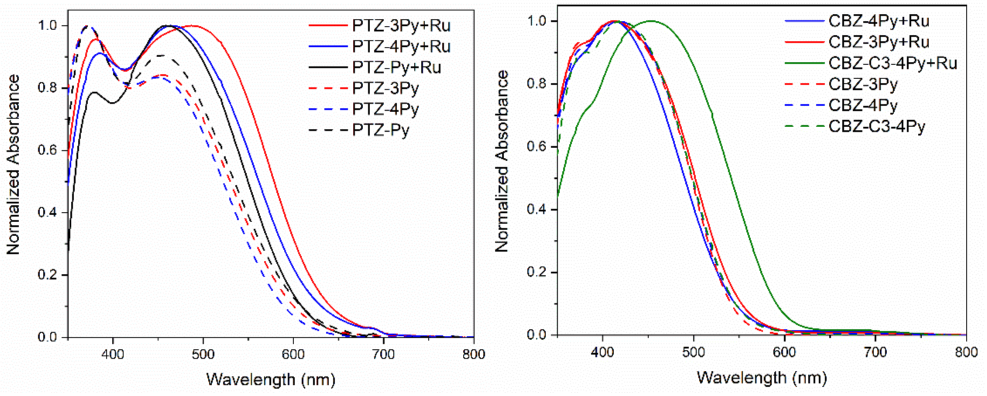

Figure 48: UV-Vis spectra on 1-µm transparent TiO_2 film of the phenothiazine-based dyads (left) and of the carbazole-based dyads (right).

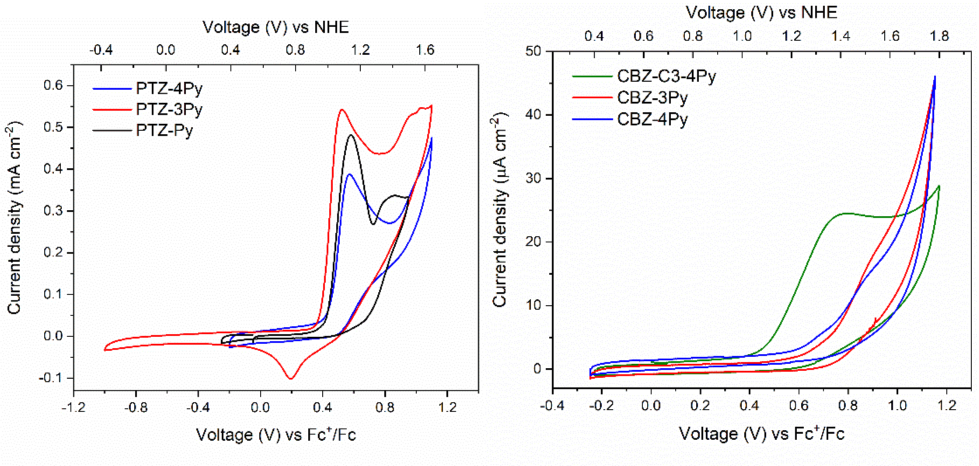

Figure 49: CV of phenothiazine-based dyes (left) and carbazole-based dyes (right) solubilized in 0.1 M $TBAClO_4$ in DMF degassed with nitrogen.

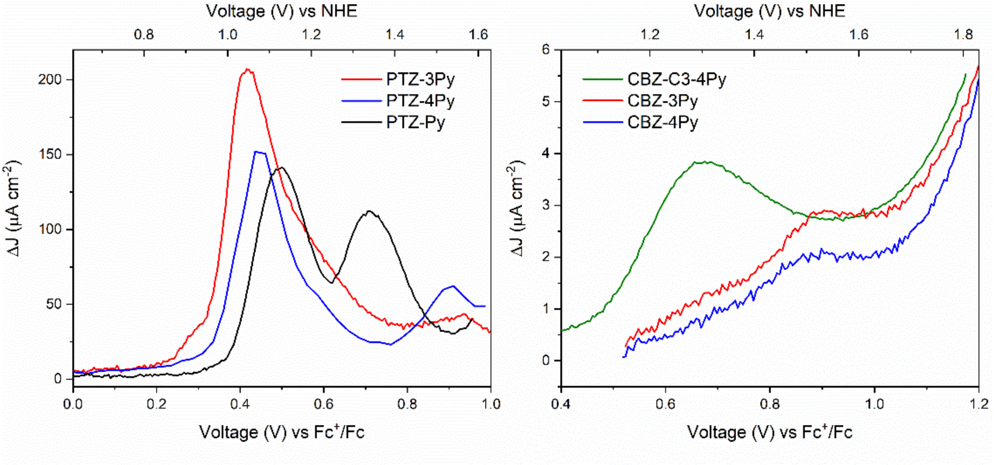

Figure 50: DPV of phenothiazine-based dyes (left) and carbazole-based dyes (right) solubilized in 0.1 M TBAClO$_4$ in DMF degassed with nitrogen.

Table 6: Electrochemical parameters of investigated sensitizers in solution and on 3.5-µm transparent TiO$_2$ film.

Dye	V_{ox}[a,b] (V vs Fc/Fc$^+$) ±10 mV		HOMO[a,b,c] (eV) ±0.05 eV		E_{gap}^{opt} (eV)		LUMO[a,b,d] (eV) ±0.05 eV	
	soln	film	soln	film	soln	film	soln	film
PTZ-4Py	0.45	0.50	-5.68	-5.73	2.00	1.91	-3.68	-3.82
PTZ-3Py	0.42	0.47	-5.65	-5.70	1.96	1.87	-3.69	-3.83
PTZ-Py	0.50	0.41	-5.73	-5.64	1.92	1.77	-3.81	-3.87
CBZ-4Py	0.83	0.59	-6.06	-5.82	2.26	2.12	-3.80	-3.70
CBZ-3Py	0.85	0.78	-6.08	-6.01	2.26	2.14	-3.82	-3.87
CBZ-C3-4Py	0.67	0.54	-5.90	-5.77	2.20	1.95	-3.95	-3.82

[a] in TBAClO$_4$ 0.1 M in DMF. [b] 3.5-µm transparent TiO$_2$ photoanode in TBAClO$_4$ 0.1 M in DMF. [c] Fc$^+$/Fc = 5.23 eV *vs.* vacuum. [d] LUMO = HOMO + E_{gap}^{opt}

The electrochemical characterization of the dye-sensitized photoanodes was performed using CV with 0.1 M TBAClO$_4$ in CH$_3$CN and it is reported in Figure 51. Also, in this case most of the photoanodes present an irreversible oxidation peak, thus also DPV is reported (Figure 52). However, for the carbazole-based dyes the DPV did not present any signal, thus the oxidizing potentials were determined from the onset of oxidation peak in the CV profiles.

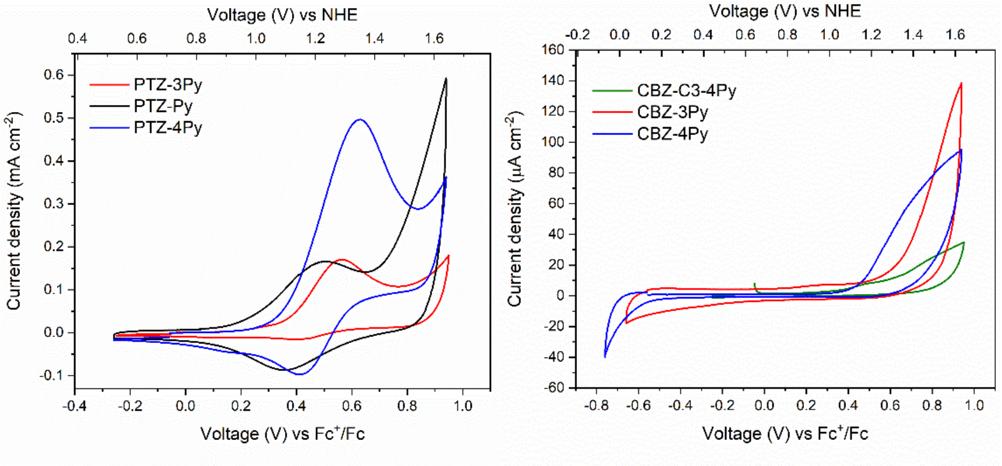

Figure 51: CV on 3.5-µm transparent TiO_2 films of the phenothiazine-based dyes (left) and carbazole-based dyes (right) in 0.1 M $TBAClO_4$ in CH_3CN degassed with nitrogen.

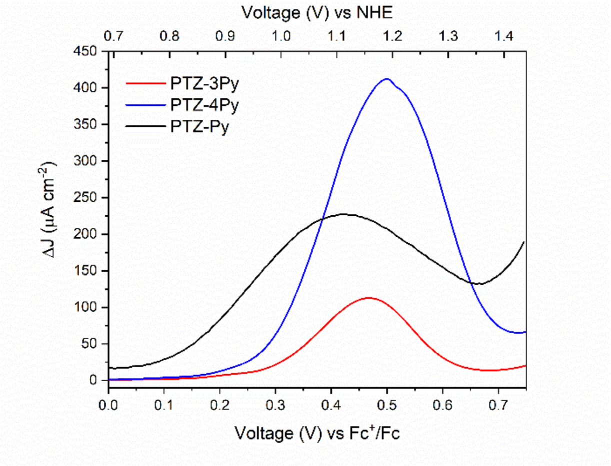

Figure 52: DPV on 3.5-µm transparent TiO_2 films of the phenothiazine-based dyes in 0.1 M $TBAClO_4$ in CH_3CN degassed with nitrogen.

The HOMO of the dyes were obtained by direct conversion of the oxidation potentials, while the LUMO levels were derived by adding the optical bandgaps to the HOMO. The energy levels are schematically depicted in Figure 53. As required, all dyes present a LUMO at higher energy than the CB of TiO_2 (~4.00 eV),[27] thus ensuring the transfer of the excited electrons into the CB of the SC.

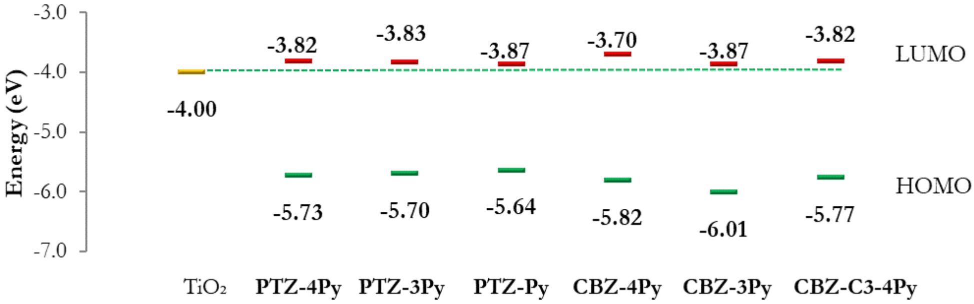

Figure 53: Schematics of calculated energy levels (vs vacuum) of the investigated dyes in comparison with TiO_2 CB.

7.4 Characterization of the photoanodes

The electrochemical properties of the dyad-sensitized anodes have been investigated by CV and compared with those of the dye and the precursor of the catalyst **Ru**, [Ru(bda)(pic)(DMSO)(CH_3CN)] (Figure 54). Dye- and dyad-sensitized electrodes have been prepared as described in paragraph 7.2. In the same way, an electrode was soaked in a **Ru** 2×10^{-4} M DMSO/EtOH (1:9) solution for 3 h and then rinsed with EtOH to remove all unbound compounds. **Ru** does not have any anchor group for TiO_2, thus, as the blue line shows in Figure 54, the electrochemical investigation of the **Ru**-sensitized electrode does not present any signal. In this way, if ruthenium is present on our electrodes, it is because it should be coordinated to our dyes.

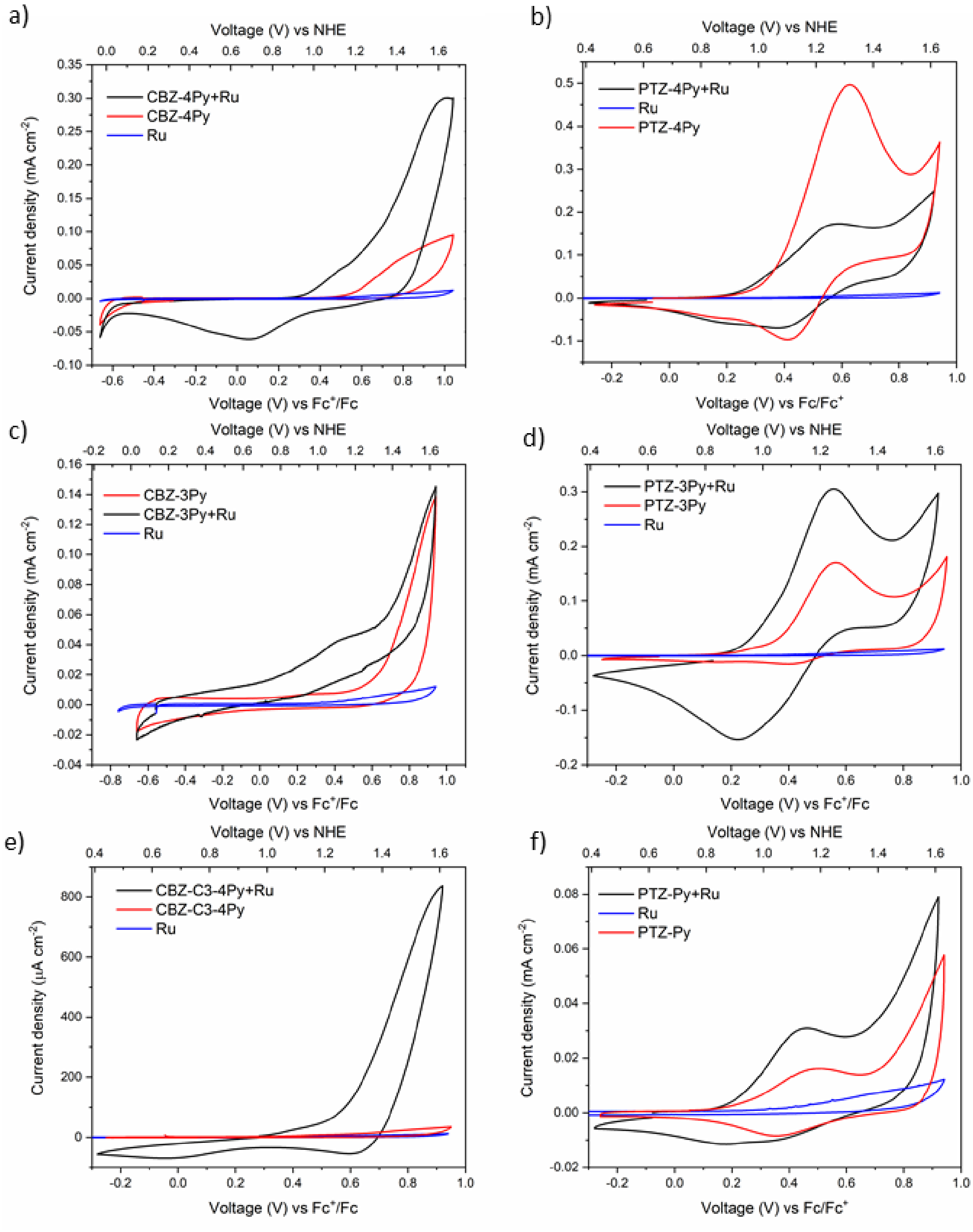

Figure 54: CV of 3.5-µm-TiO_2 films sensitized with **CBZ-4Py+Ru** (a), **PTZ-4Py+Ru** (b), and **CBZ-3Py+Ru** (c), **PTZ-3Py+Ru** (d), **CBZ-C3-4Py** (e), and **PTZ-Py** (f) compared with the corresponding dyes in 0.1 M $TBAClO_4$ in CH_3CN degassed with nitrogen. CE = Pt wire, RE = Ag/Ag$^+$, scan rate 50 mV s^{-1}.

As shown in Figure 54, the dyad-sensitized electrode presents a different behavior than the dye-sensitized films. In the majority of the cases the current density highly increases, especially at ~+1.2 V *vs* NHE that corresponds to the beginning of the water oxidation wave.[28] All carbazole-based dyads exhibit an oxidation bump around +1.1 V *vs* NHE and most dyads a reduction peak in the +0.6-0.9 V *vs* NHE range that is not present in the profile of the dyes. These signals could be ascribed to the ruthenium portion,[14,29] thus indicating the correct formation of the dyads.

Moreover, five dyad-sensitized samples and five dye-sensitized samples were subjected to XPS analysis to confirm the formation of the anchored dyads (**PTZ-4Py**, **PTZ-3Py**, **PTZ-Py**, **CBZ-4Py**, **CBZ-3Py**). **PTZ-C3-4Py** and **CBZ-C3-4Py** have not been synthesized yet when we did this investigation. The research group of Prof. Fenwick at the Queen Mary University of London performed the XPS analysis. The XPS survey spectra on the dye- and dyad-sensitized films show the sulphur and nitrogen peaks on the TiO_2 surface, thus supporting the presence of the dye portion in both spectra (Figure 55). Ruthenium peaks are not resolved in the survey spectra due to the close proximity to the carbon peak. The core-electron binding energy of C 1s and Ru $3d_{5/2}$ are plotted in Figure 56: C 1s peaks of carbon atoms are visible at 285.4 eV (C-C/C-H), 286.9 eV (C-O) and 289.5 eV (O-C=O) (Figure 57).[30] After adsorption of the dyads, the intensity of C-O peak is lowered with respect to C-C/C-H and O-C=O. This can be attributed to the presence of O-C=O groups on the dyads at the binding positions. The XPS spectra of the ruthenium complexes show the peak for Ru $3d_{5/2}$ with a binding energy of 281.7 eV, thus supporting the presence of the Ru complex in the dyad. Meanwhile, Ru $3d_{3/2}$ peaks are hidden by the C 1s peak.[31,32] The presence of the dyads is further supported by the N 1s peak shift to higher binding energy (core-level shown in Figure 58), which is more important in the **PTZ-4Py+Ru** and **CBZ-3Py+Ru** dyad (~ 1 eV). Finally, the valence-band XPS (Figure 59) contains the overlap of the O 2p and Ru 4d peaks. The increase in intensity of the Ru 4d region (<3.5 eV) confirms the presence of the coordination complex.

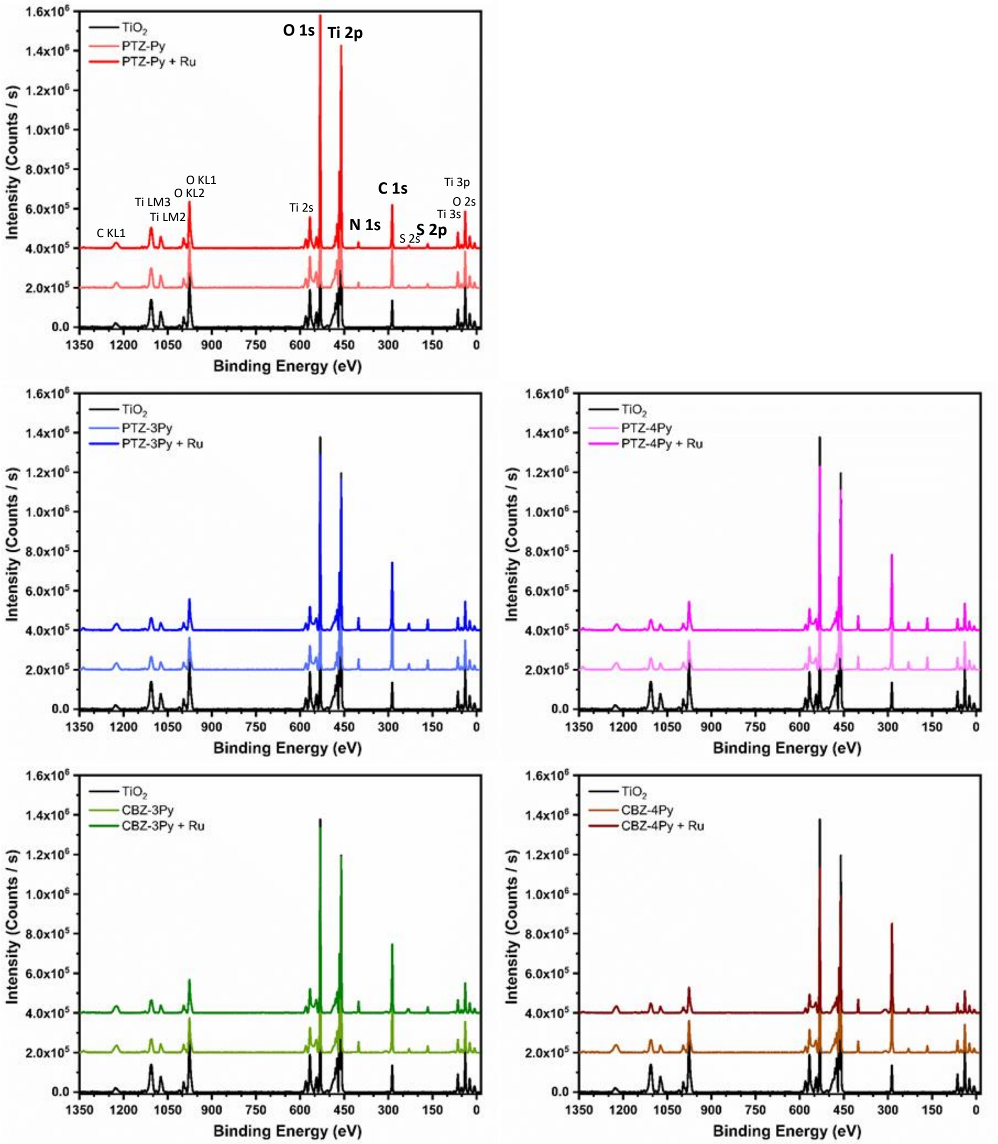

Figure 55: XPS, survey spectra of the analyzed compounds compared to the TiO$_2$ spectrum; core-levels involved in the bonding interaction between TiO$_2$ and the dyes are labelled in bold.

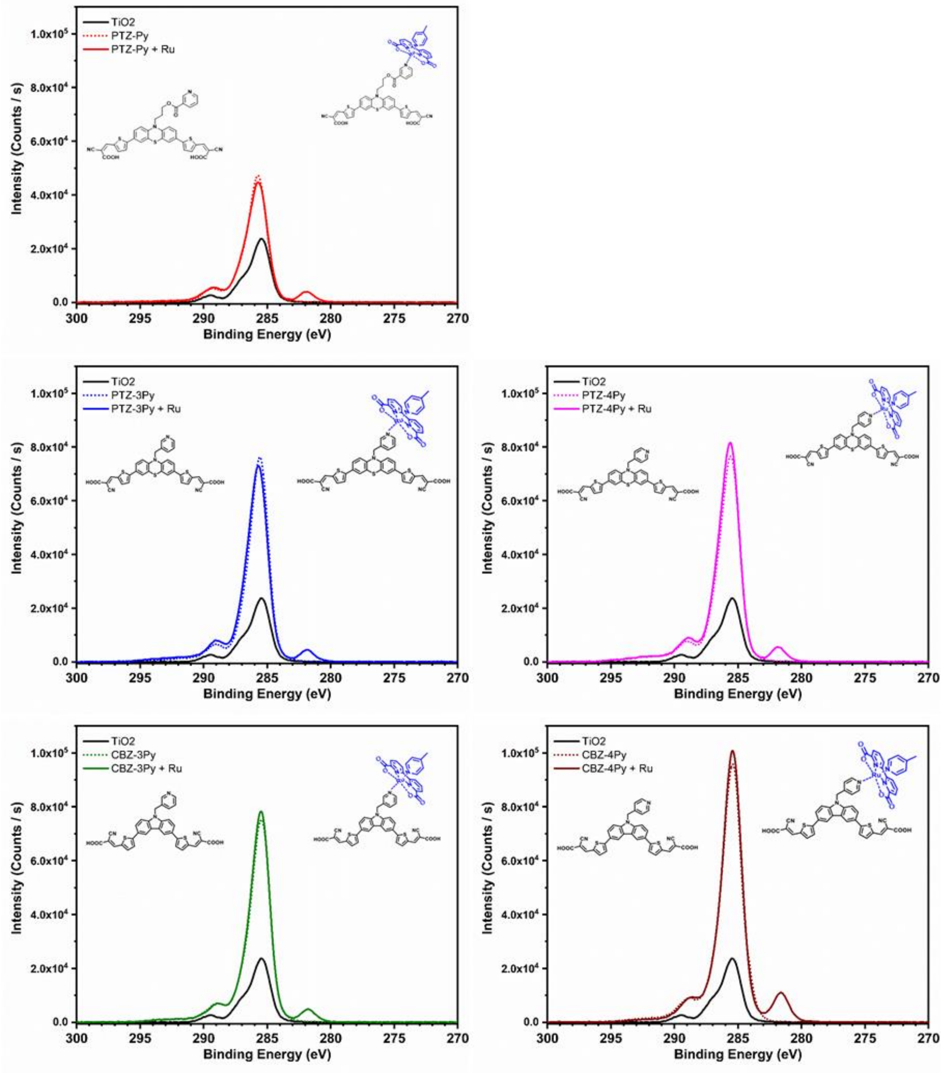

Figure 56: XPS spectra of the high-resolution core level for C 1s and Ru 3d region of the analyzed compounds compared to the bare TiO_2.

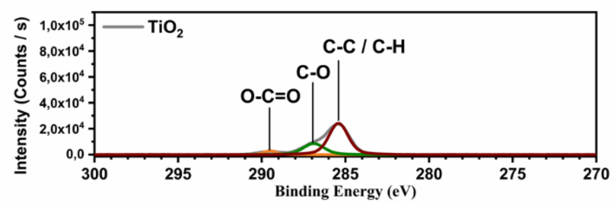

Figure 57: XPS positions of the C 1s peaks of the different carbon atoms.

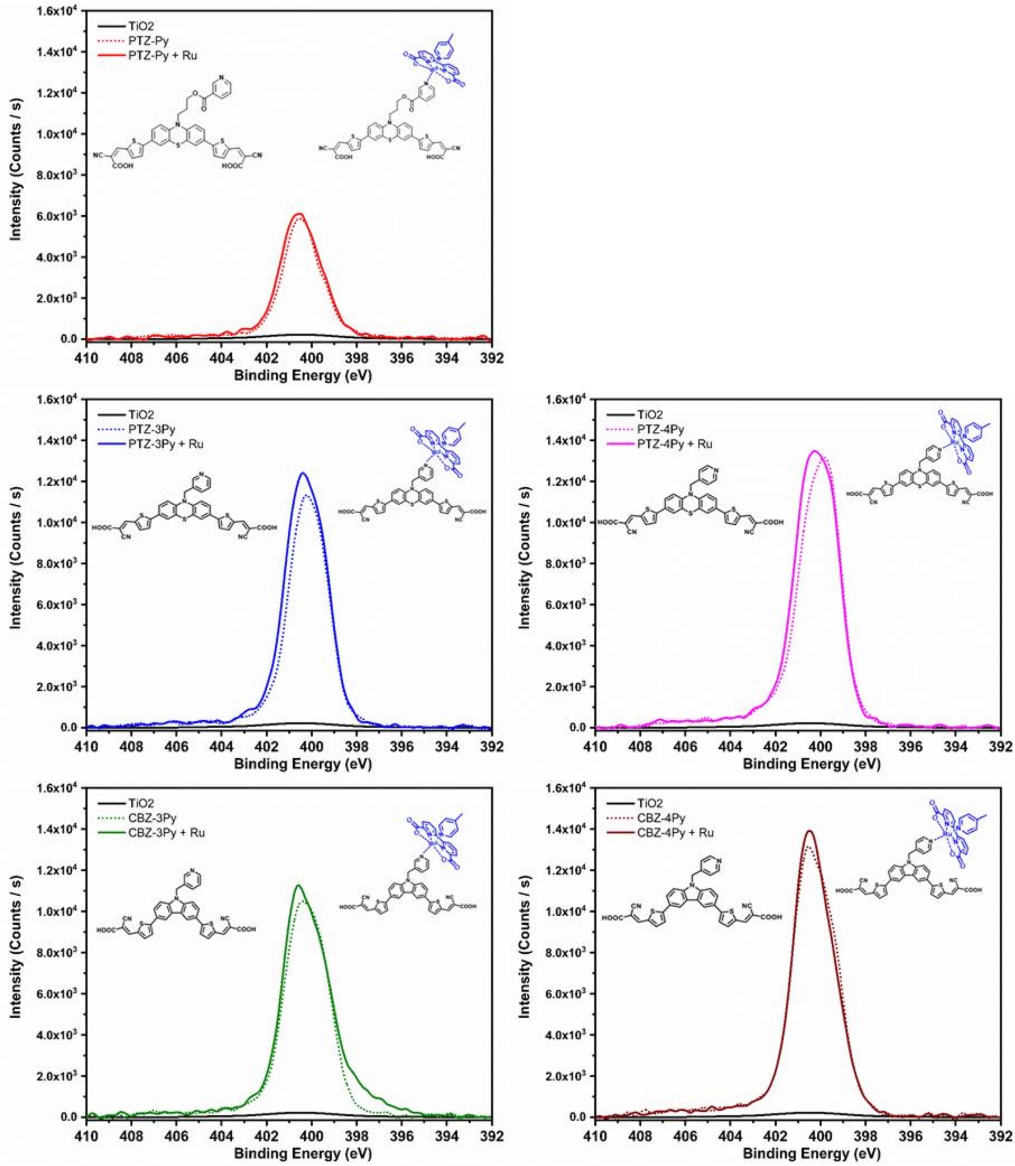

Figure 58: XPS spectra of the high-resolution core level for N 1s region of the analyzed compounds compared to the bare TiO_2.

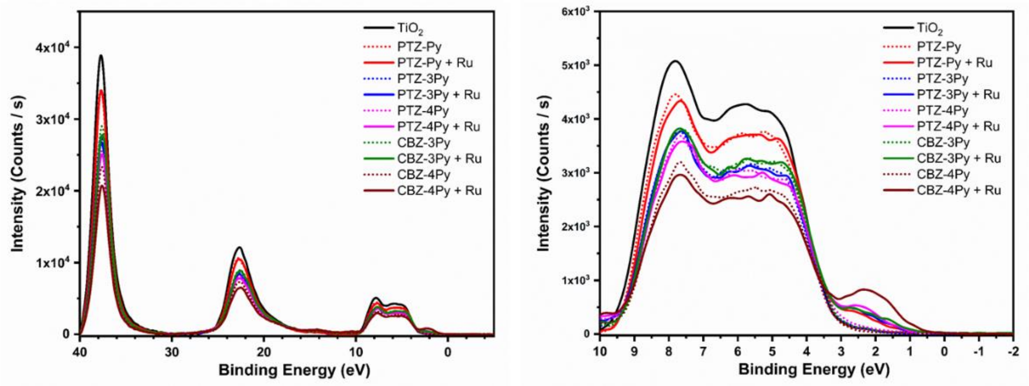

Figure 59: On the left, XPS valence-level spectrum of the analyzed compounds compared to the bare TiO_2, on the right the enlargement of the spectrum in the region where the contribution of ruthenium is clearly visible below 3.5 eV.

7.5 Photoelectrochemistry

The ability of the dyad-sensitized PEC to perform the photoinduced water splitting reaction was measured through photoelectrochemical measurements under white light illumination (200 W Xe lamp, $420<\lambda<800$ nm) in 0.1 M Na_2SO_4 aqueous solution at pH 5.8. The potential at which the best light/dark ratio was recorded in LSV experiments was used as bias in the following CA and oxygen generation experiments (Figure 60). For all samples, a bias of +0.5 V *vs* NHE was chosen. However only the short-chain dyad-sensitized electrodes have been tested in 10-min-CA experiments and compared with the dye-sensitized ones (in the absence of the ruthenium WOC portion). The results obtained are shown in Figure 61. The irradiation was chopped every 60 s for the first 5 min, then the electrodes were illuminated with continuous light for the last five minutes. In all cases, the dye-sensitized electrode was less efficient compared to the dyad-sensitized electrode. The photocurrents recorded at the end of the 10-min-CA experiments for the dyad- and the dye-sensitized electrodes are reported in Table 7, as well as the difference between them.

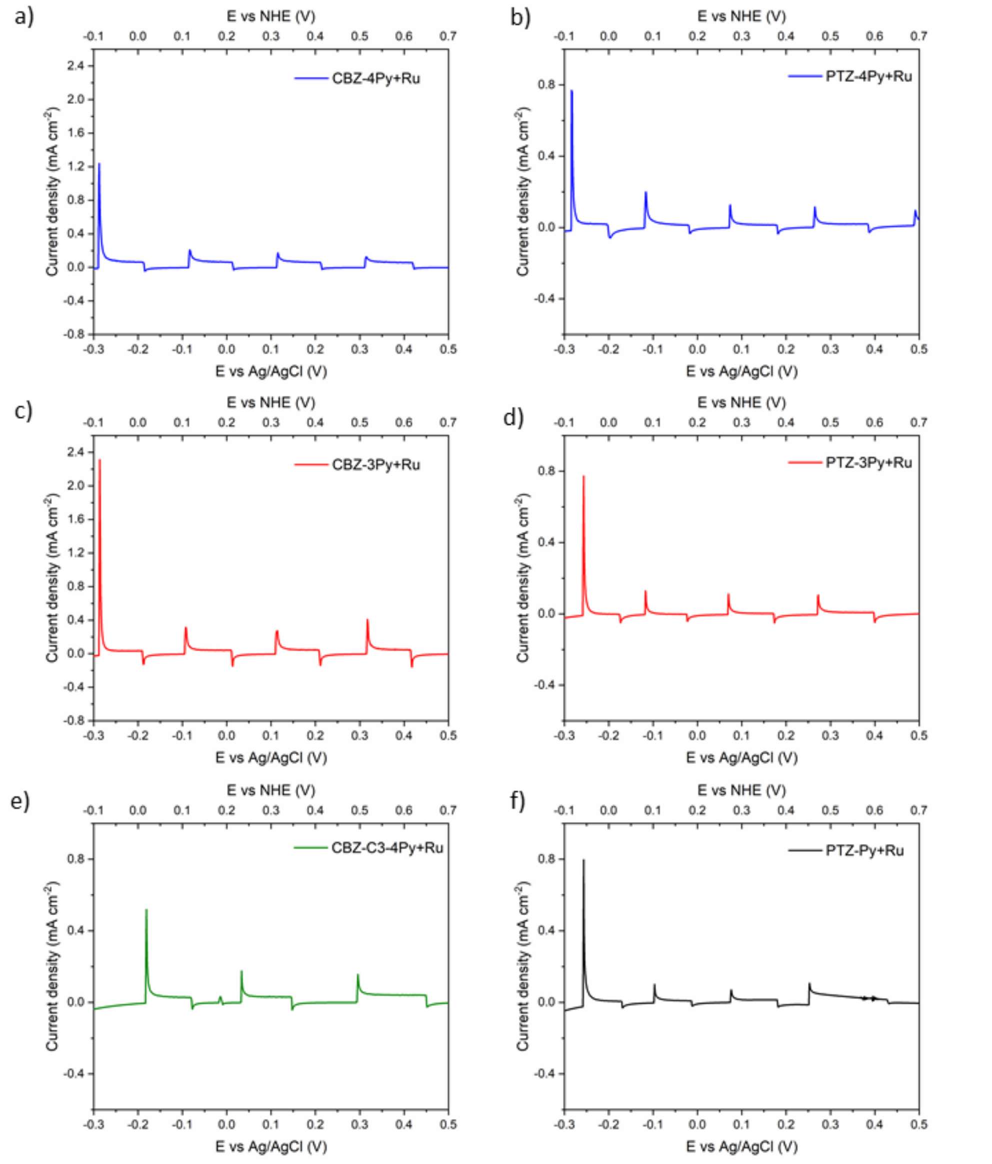

Figure 60: LSV of TiO_2 films sensitized with **CBZ-4Py+Ru** (a), **PTZ-4Py+Ru** (b), **CBZ-3Py+Ru** (c), **PTZ-3Py+Ru** (d), **CBZ-C3-4Py+Ru** (e), and **PTZ-Py+Ru** (f) in 0.1 M $Na_2SO_{4\ (aq)}$ at pH 5.8 under chopped illumination (200 W Xe lamp; $420<\lambda<800$ nm).

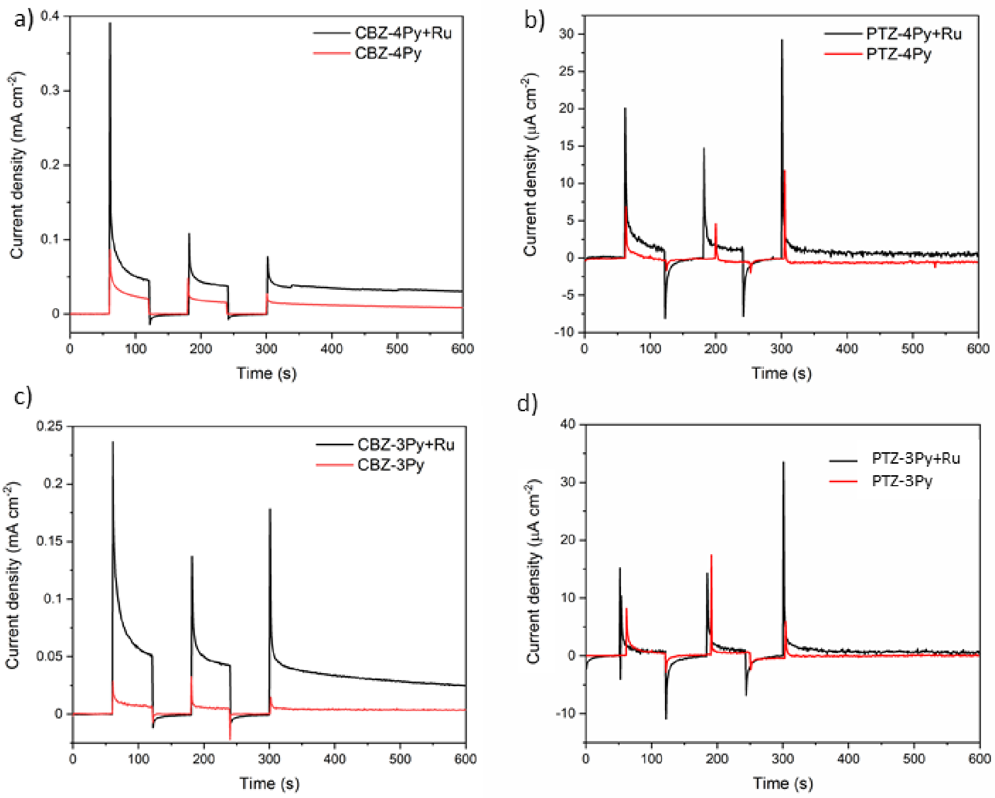

Figure 61: CA of TiO_2 films sensitized with **CBZ-4Py+Ru** (a), **PTZ-4Py+Ru** (b), **CBZ-3Py+Ru** (c), and **PTZ-3Py+Ru** (d) compared with the corresponding dyes in 0.1 M $Na_2SO_{4\,(aq)}$ at pH 5.8 under chopped illumination (200 W Xe lamp; $420<\lambda<800$ nm).

The **CBZ-3Py**-sensitized electrode exhibited a negligible photocurrent of 3.5 μA cm^{-2}, while the corresponding dyad **CBZ-3Py+Ru** presented an 8-times higher photocurrent (25 μA cm^{-2}) at the end of the experiment. Also, in the case of **CBZ-4Py** (8.6 μA cm^{-2}) and the corresponding dyad **CBZ-4Py+Ru** (30 μA cm^{-2}), a performance increase for the latter was observed, but it was less pronounced. These values correspond well to the behavior of other organic sensitizers reported in the literature.[32-34] **PTZ-3Py+Ru** and **PTZ-4Py+Ru** exhibited current densities higher than the corresponding dyes; however, the values obtained were lower than 1 μA cm^{-2}.

Table 7: Photocurrent densities obtained from CA measurements (charge passed over 10 min illumination) in dye- and dyad-sensitized PEC.

Dye	j_{10} (μA cm^{-2})		Δj[c] (μA cm^{-2})
	Dye[a]	**Dye+Ru**[b]	
PTZ-4Py	0	0.6	0.6
PTZ-3Py	0.1	0.7	0.6
CBZ-4Py	8.6	30	21.4
CBZ-3Py	3.5	25	21.5

[a] Current density at the end of the 10-min-CA experiment for the dye-sensitized electrode. [b] Current density at the end of the 10-min-CA experiment for the dyad-sensitized electrode. [c] Variation in current density between the dyad- and the corresponding dye-sensitized electrode after the 10-min-experiement.

CBZ-4Py+Ru- and **CBZ-3Py+Ru**-sensitized electrodes have been also tested in a 2-h-CA experiment to evaluate the long-term stability of these systems

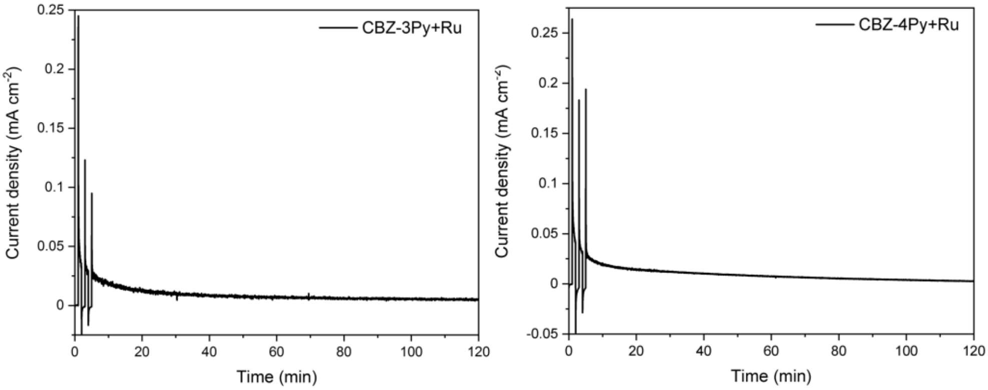

Figure 62: 2-hours-CA of TiO_2 films sensitized with **CBZ-3Py+Ru** (left) and **CBZ-4Py+Ru** (right) in 0.1 M $Na_2SO_{4\ (aq)}$ at pH 5.8 with an applied bias of -0.5 V *vs* NHE under illumination (200 W Xe lamp; $420<\lambda<800$ nm).

The O_2 evolution was measured by means of the collector-generator technique,[35] as recently reported by many studies on DS-PEC water splitting[1,4,35-39] and previously described in paragraph 4.2. The FE obtained in every experiment is reported in Table 8, as well as the average FE on four experiments. Collector-generator experiments were performed only on the short-chain dyads and the obtained graphs are reported in Figure 63.

Table 8: FE and average FE on four collector-generator experiments.

Dyad	FE (%) Experiment n° 1	2	3	4	Average FE[a] (%)
PTZ-4Py+Ru	66	103	110	500	~195[b]
PTZ-3Py+Ru	82	97	120	300	~150[b]
CBZ-4Py+Ru	46	57	63	65	58 ± 12
CBZ-3Py+Ru	77	85	91	95	88 ± 9

[a] FE as average on four experiments. [b] Further comments in the text.

The carbazole-based dyes showed high reproducibility of the data and excellent FE (88% average across all cells, with the best cell efficiency of 95% for **CBZ-3Py+Ru**) higher than most of the ones presented in the literature for similar systems.[1,7,14]

The FE of the phenothiazine-based dyes cannot be considered representative because they present some out-of-range data higher than 300% or 500% together with the evolution of really low photocurrents in the order of 1 nA cm^{-2}. This may be related to the presence of side reduction reactions that happen at the collector. We hypothesize that these dyads may not be stable and degrade while oxidizing water. It could result in the generation of low photocurrents and the detachment of pieces of dye and catalyst from the photoanode that can be reduced by the collector, whose potential is kept at ~-0.6 V *vs* NHE. The presence of UV-vis-active dissolved species in the electrolyte and the discoloration of the photoanode at the end of the experiment could further support this hypothesis.

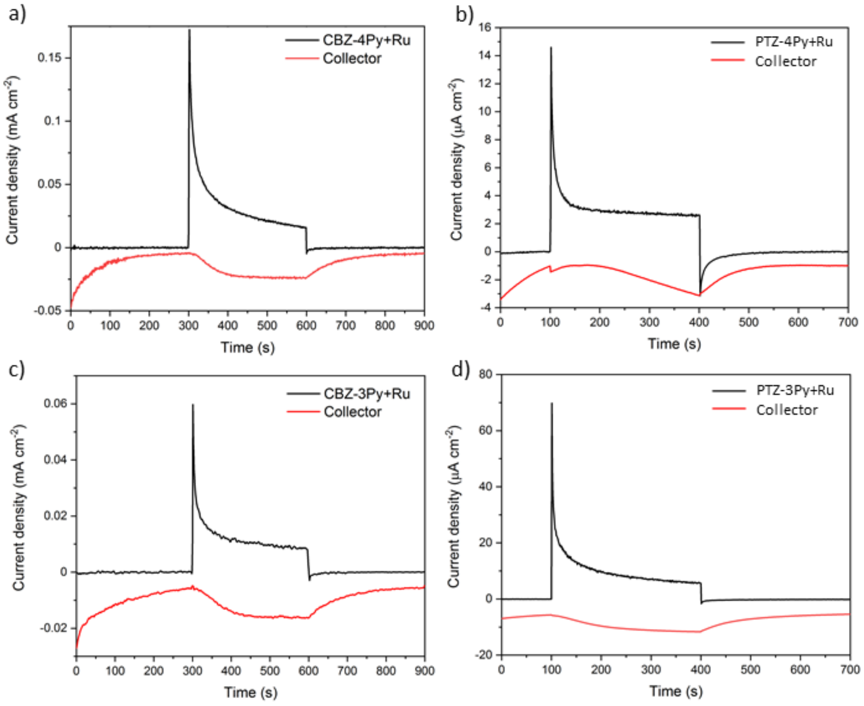

Figure 63: Collector-generator plot of the dyad-sensitized electrodes, **CBZ-4Py+Ru** (a), **PTZ-4Py+Ru** (b), **CBZ-3Py+Ru** (c), and **PTZ-3Py+Ru** (d). Black line: current-time trace at illuminated (200 W Xe lamp; $420 < \lambda < 800$ nm) dyads-sensitized TiO_2 electrode in 0.1 M Na_2SO_4 at pH 5.8 with an applied bias of ~+0.5 V *vs* NHE. Red line: current-time traces at an FTO collector electrode, 400 μm from the photoanode at an applied bias of ~-0.6 V *vs* NHE measured concurrently with the photoelectrochemical-time trace.

A further evaluation of the efficiency of some films was performed with the investigation of the IPCE. IPCE spectra of **CBZ-4Py+Ru**- and **CBZ-3Py+Ru**-sensitized electrodes are shown in Figure 64. In both cases, the IPCE trend corresponds well to the UV-vis spectrum of the compounds presenting an IPCE of 16% and 14% at the λ_{max} of **CBZ-3Py+Ru** and **CBZ-4Py+Ru**, respectively. The higher intensity in the signal of **CBZ-3Py+Ru** agrees with the trend in the FE. Moreover, the IPCE of dyad-sensitized films are compared with the relatives of the corresponding dye-sensitized films, showing a significant difference between them in agreement with the photoelectrochemical experiments. These results further support the formation of the dyads by self-assembly on the electrode surface and present higher or similar IPCE with respect to the most remarkable dyads present in the literature.[7,14]

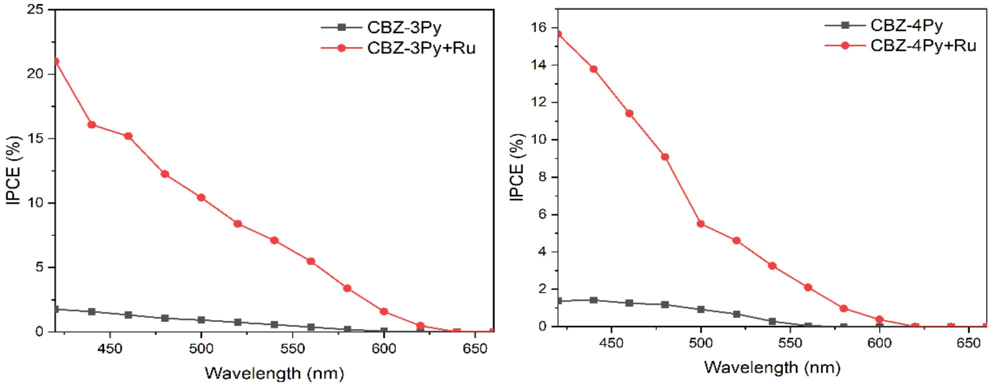

Figure 64: IPCE of dyad-sensitized TiO_2 films of **CBZ-3Py+Ru** (left) and **CBZ-4Py+Ru** (right) compared with the corresponding dye-sensitized film. Experiments performed in 0.1 M Na_2SO_4 at pH 5.8 with an applied bias of +0.5 V vs. NHE under monochromatic illumination.

The LHE of both dyad-sensitized electrodes was also measured to calculate the APCE following Eq. 4.4. LHE and APCE spectra are presented in Figure 65.

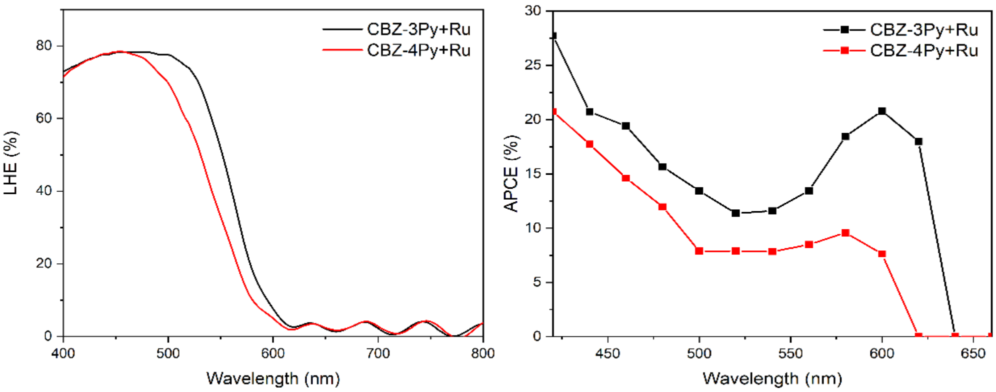

Figure 65: LHE (left) and APCE (right) spectra of **CBZ-3Py+Ru-** and **CBZ-4Py+Ru**-sensitized TiO_2 films.

The notably higher efficiency of **CBZ-3Py+Ru**, compared with **CBZ-4Py+Ru**, could be ascribed to the fact that in the former dyad the rotation around the single bond (between the methylene bridge and the quaternary carbon atom of pyridine) allows the catalyst portion to come closer to the dye. Therefore, a more efficient charge transfer between the dye and the catalyst fragment of the dyad is ensured.

In conclusion, we presented a series of eight dyes and eight corresponding dyads obtained exploiting a covalent bond between the dye and a ligand of the catalyst. The dyads have been obtained by self-assembly of the dye and the WOC portions directly on the electrode surface. The optical and electrochemical properties of both dyes and dyads have been reported. The correct formation of the dyads has been confirmed by XPS and electrochemistry. Most dyads have been tested in PEC and their FE in oxygen evolution has been measured with the collector-generator technique. The phenothiazine-based dyads showed a high liability of the photosystem and low current densities, while the carbazole-based dyads presented a good reproducibility of the data and high FE, as well as IPCE. The **CBZ-3Py+Ru** obtained an average efficiency of nearly 90% and the best cell efficiency of 95% that result in being the highest with the respect to the actual state of the art for similar systems.[7,14] Further investigations in the evaluation of the long-chain dyads in photoelectrochemical water oxidation are in progress. These results trigger new perspectives for the design of efficient covalent molecular dyads based on metal-free dyes for DS-PEC water splitting.

7.6 Experimental section

7.6.1 Spectroscopic and electrochemical investigation of dyes

Absorption spectra were recorded with a V-570 Jasco spectrophotometer. UV-O_3 treatment was performed using Novascan PSD Pro Series – Digital UV Ozone System. The thickness of the layers was measured utilizing a VEECO Dektak 8 Stylus Profiler. CV was carried out at a scan rate of 50 mV s^{-1}, using a Bio-logic SP-240 potentiostat in a three-electrode electrochemical cell under Ar. The working, counter, and the pseudo-reference electrodes were an FTO glass for the carbazole-based dyes and glassy carbon for the phenothiazine-based dyes in solution or a sensitized 3-μm-thick TiO_2 film, a Pt wire, and an Ag/Ag^+ electrode (0.01 M $AgNO_3$ 0.1 M $TBAClO_4$ in ACN). The electrolyte solutions were $TBAClO_4$ 0.1 M in DMF for the characterization in solution, and $TBAClO_4$ 0.1 M in DMF for the characterization on films. The preparation and sensitization of the 3.5 μm thick TiO_2 film are described below. The Pt wire was sonicated for 15 min in deionized water, washed with 2-propanol, and cycled for 5 times in 0.5 M H_2SO_4 before use. The Ag/Ag^+ pseudo-reference electrode was calibrated by adding ferrocene (10^{-3} M) to the test solution after each measurement (potentials measured versus Fc/Fc^+ and converted to NHE by addition of +0.69 V).[40] NHE was converted to vacuum by addition of -4.6 V.[41]

7.6.2 Preparation of photoanodes

The photoanodes have been prepared as described below, adapting a procedure reported in the literature.[42] All the containers used were in glass or Teflon and were treated with EtOH and 10% HCl before use to exclude metal contamination. FTO glass was cleaned in a detergent solution for 15 min using an ultrasonic bath, rinsed with pure water and EtOH. After treatment in a UV-O_3 system for 18 min, a transparent active layer of 0.8 cm^2 was screen-printed using Dyesol 18NR-T active transparent TiO_2 paste. The coated films were thermally treated at 125 °C for 6 min, 325 °C for 10 min, 450 °C for 15 min, and 500 °C for 15 min. The heating ramp rate was 5 - 10 °C/min.

FTO plates coated with 3.5 μm transparent TiO_2 film, prepared as described above, were treated in a UV-O_3 system for 20 min at room temperature, then immersed into a 2×10^{-4} M solution in EtOH/DMSO (9:1) of the dye + catalyst precursor for 3 h at room temperature in the dark. The stained substrates were rinsed with EtOH and dried with a stream of dry nitrogen.

The UV-Vis spectra, CV and LSV were recorded in comparison with a bare 3.5 µm transparent TiO_2 film.

7.6.3 X-ray photoelectron spectroscopy measurements

XPS was performed on Thermo Scientific K-Alpha X-ray photoelectron spectrometer with a monochromatic Al Kα X-ray source under high vacuum (2×10^{-8} mbar), using an electron flood gun to avoid sample charging. The data fitting was performed by Thermo Avantage v5.9911 software, using mixed Gauss-Lorentz functions.

7.6.4 Oxygen evolution quantification by collector-generator technique and Photoelectrochemistry

The dyad-sensitized photoanode was illuminated under an applied bias, thus acting as an O_2 generator. An FTO electrode (previously cleaned via 15 min sonication in EtOH) was sandwiched to the photoanode (with both conducting sides facing inward), in order to be used as the collector, i.e., the electrode at which the reduction of the evolved O_2 takes place. The sandwiched device was held together by 4 layers of unstretched parafilm (ca. 400 μm spacing), sealed by pressing at 65 °C for 60 s. The two lateral sides of the C-G sandwich were left open, allowing for the filling of void space between electrodes with electrolyte solution by capillary forces. Both the photoanode generator and the FTO collector were contacted using Cu tape (also covered by the parafilm layers), and respectively connected to the two working electrodes of a bipotentiostat (Autolab PGSTAT 302 N). An Ag/AgCl electrode and a Pt wire were used as the reference and the counter electrode. The sandwich was then immersed in degassed Na_2SO_4 0.1 M solution (pH 5.8) and illuminated with a 200 W Xenon lamp (using a LOT-Oriel xenon white light source, equipped with a 420 nm cut-off filter to minimize TiO_2 contribution and an IR filter to avoid cell warming). The generator electrode was held at 0.3 V vs Ag/AgCl bias, while the collector at -0.8 V vs Ag/AgCl, identified in literature as the optimal O_2 reduction potential.[35] The collector-generator efficiency of the set-up under our experimental conditions turned out to be 82%, in good agreement with the one reported by the Finke[43] group on a very similar set-up (i.e., with a small gap between the generator and collector).

Photoelectrochemistry has been performed in similar condition. The working, counter, and the pseudo-reference electrodes were a sensitized 3-µm-thick TiO_2 film, a Pt wire and an Ag/AgCl (KCl 3 M) electrode. The electrolyte solutions were Na_2SO_4 0.1 M aqueous solution at pH 5.8. The photoanode generator was contacted using Cu tape and all electrodes were connected to a bipotentiostat (Autolab PGSTAT 302 N). The DSPEC was illuminated with a 200 W Xenon lamp (using a LOT-Oriel xenon white light source, equipped with a 420 nm cut-off filter to minimize TiO_2 contribution and an IR filter to avoid cell warming).

7.6.5 Synthesis

NMR spectra were recorded with a Bruker AMX-500 spectrometer operating at 500.13 MHz (^1H) or Bruker Advance Neo spectrometer operating at 400 MHz (^1H) and 100 MHz (^{13}C). Coupling constants are given in Hz. High resolution mass spectra have been recorded with an Agilent 6230B Time of Flight (TOF) equipped with an electrospray (Dual ESI) source. Flash chromatography was performed with Merck grade 9385 silica gel 230-400 mesh (60 Å). Reactions performed under inert atmosphere were performed in oven-dried glassware, and a nitrogen atmosphere was generated with Schlenk technique. The conversion was monitored by thin-layer chromatography by using UV light (254 and 365 nm) as a visualizing agent. All reagents were obtained from commercial suppliers at the highest purity grade and used without further purification. Anhydrous solvents were purchased from Acros Organics and used without further purification. Extracts were dried with Na_2SO_4 and filtered before removal of the solvent by evaporation. Compounds 10*H*-3,7-dibromophenothiazine (**1a**),[44] 9*H*-3,6-dibromocarbazole (**1b**),[45] 4,4,5,5-tetramethyl-2-[5-(4,4,5,5-tetramethyl-1,3-dioxolan-2-yl)thiophen-2-yl]-1,3,2-dioxaborolane,[20] (3-bromopropoxy)-*tert*-butyldimethylsilane,[21] **[Ru(bda)(DMSO)(MeCN)(pic)]**[23] were prepared according to literature.

3-(pyridin-4-yl)propyl 4-methylbenzenesulfonate. To a solution of4-Pyridinepropanol (150 mg, 1.09 mmol) in DCM (1 mL) benzyltrimethylammonium chloride (10 mg, 0.05 mmol) and 1 mL $NaOH_{aq}$ (30%) are added. *p*-toluenesulfonyl chloride (230 mg, 1.2 mmol) solubilized in 1 mL of DCM is added dropwise. The solution is left stirring at room temperature overnight. The reaction is quenched adding H_2O (20 mL) and extracting with DCM 3 times. The organic phases are washed with water 5 times. The crude product is purified by silica pad (DCM/EtOH, 4:1). The product was isolated as a yellowish oil (240 mg, 0.82 mmol, 75%). ^1H NMR (400 MHz, DMSO) δ 8.41 (dd, J = 4.4, 1.6 Hz, 2H), 7.79 (d, J = 8.3 Hz, 2H), 7.49 (dd, J = 8.6, 0.6 Hz, 2H), 7.13 (d, J = 6.0 Hz, 2H), 4.01 (t, J = 6.3 Hz, 2H), 2.63 - 2.55 (m, 2H), 2.43 (s, 3H), 1.94 - 1.86 (m, 2H).

3,7-bis(5-(4,4,5,5-tetramethyl-1,3-dioxolan-2-yl)thiophen-2-yl)-10*H*-phenothiazine (2a). 10*H*-3,7-dibromophenothiazine (760 mg, 2.11 mmol) and $Pd(dppf)Cl_2{\cdot}CH_2Cl_2$ (172 mg, 0.21 mmol) were dissolved in dimethoxyethane 12.5 mL and stirred for 15 min under nitrogen atmosphere. Then 4,4,5,5-tetramethyl-2-[5-(4,4,5,5-tetramethyl-1,3-dioxolan-2-yl)thiophen-2-yl]-1,3,2-

dioxaborolane (1.50 g, 4.44 mmol) and methanol (12.5 mL) were added, and the solution was stirred for 15 min under nitrogen atmosphere. In the end, K_2CO_3 (2.90 g, 21.1 mmol) was added to the solution and the reaction was performed with microwave irradiation (100 °C, 70 W, 60 min) and then quenched by pouring into a saturated solution of NH_4Cl (70 mL) and CH_2Cl_2 (70 mL). Filtration on Celite and extractions with organic solvent allowed to isolate the crude product, then purified through column chromatography on silica gel (petroleum ether/AcOEt, 3:1). The desired product was isolated as a light-yellow solid (1.10 g, 1.80 mmol) with 84% yield. ^1H NMR (Benzene-d_6, 500 MHz): δ (ppm) = 7.21 (d, J = 1.0 Hz, 2H), 7.09 (dd, J = 7.2, 1.7 Hz, 2H), 6.99 (d, J = 3.5 Hz, 2H), 6.75 (d, J = 3.5 Hz, 2H), 6.24 (s, 2H), 5.76 (d, J = 8.2 Hz, 2H), 4.87 (s, 1H), 1.20 (s, 12H), 1.09 (s, 12H).

3,6-bis(5-(4,4,5,5-tetramethyl-1,3-dioxolan-2-yl)thiophen-2-yl)-9*H*-carabazole (2b). 9*H*-3,6-dibromocarbazole (415 mg, 1.27 mmol) and Pd(dppf)$Cl_2 \cdot CH_2Cl_2$ (106 mg, 0.13 mmol) were dissolved in dimethoxyethane 2.5 mL and stirred for 15 min under nitrogen atmosphere. Then 4,4,5,5-tetramethyl-2-[5-(4,4,5,5-tetramethyl-1,3-dioxolan-2-yl)thiophen-2-yl]-1,3,2-dioxaborolane (950 mg, 2.81 mmol) and methanol (2.5 mL) were added, and the solution was stirred for 15 min under nitrogen atmosphere. In the end, K_2CO_3 (1.75 g, 12.7 mmol) was added to the solution and the reaction was performed under microwave irradiation (100 °C, 70 W, 90 min) and then quenched by pouring into a saturated solution of NH_4Cl (40 mL) and CH_2Cl_2 (40 mL). Filtration on Celite and extractions with organic solvent allowed to isolate the crude product, then purified through column chromatography on silica gel (*n*-heptane/AcOEt, 2:1). The desired product was isolated as a white solid (383 mg, 0.65 mmol) with 51% yield. ^1H NMR (500 MHz, $CDCl_3$): δ (ppm) = 8.30 (s, 2H), 8.09 (s, 1H), 7.68 (dd, J = 8.4, 1.6 Hz, 2H), 7.41 (d, J = 8.4 Hz, 2H), 7.20 (d, J = 3.7 Hz, 2H), 7.14 (d, J = 3.6 Hz, 2H), 6.22 (s, 2H), 1.39 (s, 12H), 1.34 (s, 12H).

10-(pyridin-4-ylmethyl)-3,7-bis(5-(4,4,5,5-tetramethyl-1,3-dioxolan-2-yl)thiophen-2-yl)-10*H*-phenothiazine (3a). Compound **2a** (400 mg, 0.64 mmol) was dissolved in 10 mL of anhydrous THF in a two-necked flask under N_2 atmosphere, then the solution was cooled to 0°C using an ice bath and NaH 60% (39 mg, 0.96 mmol) was added and the solution was stirred at 0 °C for 40 min. Meanwhile in a beaker 4-(bromomethyl)pyridine hydrobromide (143 mg, 0.96 mmol) was dissolved in 25 mL of a saturated aqueous solution of K_2CO_3 and in 25 mL of Et_2O. The mixture was extracted with Et_2O, the organic phase was washed with water, dried on $MgSO_4$. The solution is reduced to 1.5 mL and then slowly introduced in the reaction flask. The resulting solution was stirred at rt overnight. The following day, the reaction mixture was quenched with iced water, then extracted with CH_2Cl_2 and the organic phase was washed with water and dried with $MgSO_4$ and concentrated. The crude was purified using flash column chromatography on silica gel (cyclohexane/AcOEt, 1:1). The desired product was isolated as a light-yellow solid (430 mg 0.60 mmol) with 35% yield. ^{1}H NMR (400 MHz, $CDCl_3$) δ 8.58 (d, *J* = 6.0 Hz, 1H), 7.33 (d, *J* = 2.1 Hz, 1H), 7.26 (d, *J* = 6.0 Hz, 1H), 7.19 (dd, *J* = 8.5, 2.2 Hz, 1H), 7.06 (dd, *J* = 3.7, 0.5 Hz, 1H), 7.02 (d, *J* = 3.7 Hz, 1H), 6.50 (d, *J* = 8.5 Hz, 1H), 6.16 - 6.14 (m, 1H), 5.06 (s, 1H), 1.33 (s, 6H), 1.30 (s, 6H).

10-(pyridin-3-ylmethyl)-3,7-bis(5-(4,4,5,5-tetramethyl-1,3-dioxolan-2-yl)thiophen-2-yl)-10*H*-phenothiazine (3b). Compound **2a** (77 mg, 120 μmol) was dissolved in 4 mL of anhydrous DMF in a two-necked flask under N_2 atmosphere, then the solution was cooled to 0°C using an ice bath and NaH 60% (6 mg, 0.15 mmol) was added. Meantime in another two-necked flask 3-(iodomethyl)pyridine hydroiodide (43 mg, 0.12 mmol) was dissolved in 2 mL of anhydrous DMF under N_2 atmosphere, then the solution was cooled to 0 °C using an ice bath and other NaH 60% (6 mg, 0.15 mmol) was added. After stirring the two solutions at 0 °C for 40 min, they were combined and the resulting solution was stirred at rt for 15 min, when TLC revealed the complete conversion of the starting material. The reaction mixture was quenched with iced water, then extracted with CH_2Cl_2 and the organic phase was washed with water and dried with Na_2SO_4 and concentrated. The crude was purified using flash column chromatography on silica gel (cyclohexane/AcOEt, 1:1). The desired product was isolated as a light-yellow solid (30 mg, 42 μmol) with 34% yield. ^{1}H NMR (DMSO-*d6*, 500 MHz): δ (ppm) = 8.63 (s, 1H), 8.47 (d, *J* = 4.5 Hz, 1H), 7.71 (d, *J* = 8.0 Hz, 1H), 7.47 (d, *J* = 2.2 Hz, 2H), 7.37 (dd, *J* = 8.5, 2.1 Hz, 3H), 7.30 (d, *J* = 3.7 Hz, 2H), 7.14 (d, *J* = 3.7 Hz, 2H), 6.87 (d, *J* = 8.6 Hz, 2H), 6.10 (s, 2H), 5.26 (s, 2H), 1.25 (s, 12H), 1.23 (s, 12H).

9-(pyridin-4-ylmethyl)-3,6-bis(5-(4,4,5,5-tetramethyl-1,3-dioxolan-2-yl)thiophen-2-yl)-9*H*-carbazole (3c). Compound **2b** (270 mg, 0.46 mmol) was dissolved in 12 mL of anhydrous THF in a two-necked flask under N_2 atmosphere, then the solution was cooled to 0 °C using an ice bath, and NaH 60% (36 mg, 0.92 mmol) was added and the solution was stirred at 0 °C for 1 h. Meanwhile in a beaker 4-(bromomethyl)pyridine hydrobromide (177 mg, 0.70 mmol) was dissolved in 25 mL of a saturated aqueous solution of K_2CO_3 and 25 mL of Et_2O. The mixture was extracted with Et_2O; the organic phase was washed with water and dried on $MgSO_4$. The solution is reduced to 1.5 mL and then slowly introduced in the reaction flask. The resulting solution was stirred at rt overnight. The following day, the reaction mixture was concentrated in rotavapor up to 5 mL. Then, 10 mL of Et_2O and 40 mL of iced water were added. The light yellow precipitated solid (285 mg 0.42 mmol) was filtered and washed with Et_2O achieving a

91% yield. ^{1}H NMR (500 MHz, CDCl$_3$): δ (ppm) = 8.52 (d, J = 5.9 Hz, 2H), 8.36 (s, 2H), 7.69 (dd, J = 8.6, 1.6 Hz, 2H), 7.26 (d, J = 8.2 Hz, 2H), 7.21 (d, J = 3.6 Hz, 2H), 7.15 (d, J = 3.6 Hz, 2H), 7.02 (d, J = 5.7 Hz, 2H), 6.21 (s, 2H), 5.51 (s, 2H), 1.39 (s, 12H), 1.33 (s, 12H).

9-(pyridin-3-ylmethyl)-3,6-bis(5-(4,4,5,5-tetramethyl-1,3-dioxolan-2-yl)thiophen-2-yl)-10*H*-carbazole (3d). Compound **2b** (383 mg, 0.65 mmol) was dissolved in 10 mL of anhydrous THF in a two-necked flask under N$_2$ atmosphere, then the solution was cooled to 0 °C using an ice bath and NaH 60% (90 mg, 2.21 mmol) was added. After stirring at 0 °C for 1 h, the 3-(bromomethyl)pyridine hydrobromide (214 mg, 0.85 mmol) was added and the solution was stirred at rt overnight. The following day, the reaction mixture was quenched with iced water, then extracted with CH$_2$Cl$_2$ and the organic phase was washed with water, dried with Na$_2$SO$_4$ and concentrated. The desired product was isolated as a light-yellow solid (420 mg 0.61 mmol) with 95% yield. ^{1}H NMR (400 MHz, CDCl$_3$): δ (ppm) = 8.60 (d, J = 1.8 Hz, 1H), 8.50 (dd, J = 4.8, 1.5 Hz, 1H), 8.32 (d, J = 1.4 Hz, 2H), 7.67 (dd, J = 8.5, 1.8 Hz, 2H), 7.29 (d, J = 8.5 Hz, 3H), 7.19 (d, J = 3.6 Hz, 2H), 7.17 - 7.05 (m, 3H), 6.21 (s, 2H), 5.47 (s, 2H), 1.39 (s, 12H), 1.33 (s, 12H).

10-(3-(pyridin-4-yl)propyl)-3,7-bis(5-(4,4,5,5-tetramethyl-1,3-dioxolan-2-yl)thiophen-2-yl)-10*H*-phenothiazine (3e). Compound **2a** (110 mg, 0.2 mmol) and 3-(pyridin-4-yl)propyl 4-methylbenzenesulfonate (80 mg, 0.3 mmol) was dissolved in 10 mL of anhydrous DMF in a two-necked flask under N$_2$ atmosphere, then the solution was cooled to 0 °C using an ice bath and NaH 60% (40 mg, 1.0 mmol) was added. The resulting solution was stirred at rt for 3 days, when TLC revealed the conversion of the starting material. The reaction mixture was quenched with iced water, then extracted with Et$_2$O and the organic phase was washed with water multiple times and dried with Na$_2$SO$_4$ and concentrated. The crude was purified using a silica pad (first with DCM and then with EtOH). The desired product was isolated as a light-yellow oil (78 mg, 0.1 mmol) with 50% yield. ^{1}H NMR (400 MHz, CDCl$_3$) δ 8.42 (s, 2H), 7.38 (d, J = 2.1 Hz, 2H), 7.34 (dd, J = 8.4, 2.2 Hz, 2H), 7.08 (d, J = 3.7 Hz, 2H), 7.06-7.02 (m, 4H), 6.75 (d, J = 8.5 Hz, 1H), 6.16 (s, 2H), 3.85 (t, J = 6.5 Hz, 2H), 2.74 (t, J = 7.4 Hz, 2H), 2.16 - 2.08 (m, 2H).

9-(3-(pyridin-4-yl)propyl)-3,6-bis(5-(4,4,5,5-tetramethyl-1,3-dioxolan-2-yl)thiophen-2-yl)-9*H*-carbazole (3f). Compound **2b** (200 mg, 0.35 mmol) was dissolved in 10 mL of anhydrous THF in a two-necked flask under N$_2$ atmosphere, then the solution was cooled to 0 °C using an ice bath and NaH 60% (40 mg, 1.02 mmol) was added. After stirring at 0 °C for 1 h, the 3-(pyridin-4-yl)propyl 4-methylbenzenesulfonate (140 mg, 0.48 mmol) was added and the solution was stirred at rt for 3 days. The reaction mixture was quenched with iced water, then extracted with Et_2O and the organic phase was washed with water, dried with Na_2SO_4 and concentrated. The crude was purified using a silica pad (first with DCM and then with EtOH). The desired product was isolated as a light-yellow oil with a quantitative yield. ^1H NMR (400 MHz, $CDCl_3$) δ 8.44 (d, *J* = 4.8 Hz, 2H), 8.28 (d, *J* = 1.5 Hz, 2H), 7.65 (dt, *J* = 8.46, 1.50 Hz, 2H), 7.22 - 7.17 (m, 4H), 7.14 (d, *J* = 3.7 Hz, 2H), 7.02 (d, *J* = 4.6 Hz, 2H), 6.21 (s, 2H), 4.24 - 4.17 (m, 2H), 2.59 (t, *J* = 7.1 Hz, 2H), 2.22 - 2.09 (m, 2H), 1.39 (s, 6H), 1.33 (s, 6H).

General procedure A for the cleavage of the protective group for the aldehydic functionality (iii). Pinacol ester precursor was dissolved in 10% HCl_{aq}/THF (1:2). The mixture was heated at 50 °C for 2 h and then poured into water. K_2CO_3 was slowly added until basic pH was reached, and then THF was removed under reduced pressure. The product precipitated was filtered on Hirsh and washed with water.

5,5'-(10-(pyridin-4-ylmethyl)-10*H*-phenothiazine-3,7-diyl)bis(thiophene-2-carbaldehyde) (4a). Product **4a** was synthetized according to general procedure A for the cleavage of the protective group using product **3a** (270 mg, 0.38 mmol), 30 mL 10% HCl_{aq}/THF (1:2). The desired product was isolated as an orange solid (195 mg) with quantitative yield. ^1H NMR (400 MHz, DMSO): δ (ppm) = 9.88 (s, 2H), 8.55 (dd, *J* = 4.5, 1.4 Hz, 2H), 8.01 (d, *J* = 4.0 Hz, 2H), 7.68 (d, *J* = 4.0 Hz, 2H), 7.65 (d, *J* = 2.2 Hz, 2H), 7.53 (dd, *J* = 8.6, 2.2 Hz, 2H), 7.33 (d, *J* = 5.9 Hz, 2H), 6.80 (d, *J* = 8.7 Hz, 2H).

5,5'-(10-(pyridin-3-ylmethyl)-10*H*-phenothiazine-3,7-diyl)bis(thiophene-2-carbaldehyde) (4b). Product **4b** was synthetized according to general procedure A for the cleavage of the protective group using product **3b** (430 mg, 0.60 mmol), 30 mL 10% HCl_{aq}/THF (1:2). The desired product was isolated after filtration on SiO_2 with CH_2Cl_2 and then with EtOH as an orange solid (230 mg, 0.45 mmol) with 75% yield. 1H NMR (DMSO-*d6*, 500 MHz): δ (ppm) = 9.88 (s, 2H), 8.62 (d, *J* = 1.5 Hz, 1H), 8.48 (d, *J* = 3.6 Hz, 1H), 8.01 (d, *J* = 4.0 Hz, 2H), 7.72 - 7.68 (m, 3H), 7.66 (d, *J* = 2.1 Hz, 2H), 7.54 (dd, *J* = 8.6, 2.1 Hz, 2H), 7.38 (dd, *J* = 7.8, 4.9 Hz, 1H), 6.92 (d, *J* = 8.7 Hz, 2H), 5.32 (s, 2H).

5,5'-(9-(pyridin-4-ylmethyl)-9*H*-carbazole-3,6-diyl)bis(thiophene-2-carbaldehyde) (4c). Product **4c** was synthetized according to general procedure A for the cleavage of the protective group using product **3c** (140 mg, 0.21 mmol), 15 mL 10% HCl_{aq}/THF (1:2). The desired product was isolated as a yellow solid (91 mg, 0.19 mmol) with 91% yield. ^1H NMR (400 MHz, DMSO): δ (ppm) = 9.92 (s, *J* = 0.9 Hz, 2H), 8.91 (dd, *J*

= 1.9, 0.5 Hz, 2H), 8.48 (d, *J* = 6.1 Hz, 2H), 8.09 (d, *J* = 4.0 Hz, 2H), 7.96 (dd, *J* = 8.6, 1.9 Hz, 2H), 7.81 (d, *J* = 4.0 Hz, 2H), 7.74 (d, *J* = 8.6 Hz, 2H), 7.10 (d, *J* = 6.1 Hz, 2H), 5.84 (s, 2H).

5,5'-(9-(pyridin-3-ylmethyl)-9*H*-carbazole-3,6-diyl)bis(thiophene-2-carbaldehyde) (4d). Product **4d** was synthetized according to general procedure A for the cleavage of the protective group using product **3d** (420 mg, 0.61 mmol), 27 mL 10% HCl_{aq}/THF (1:2). The desired product was isolated as a yellow solid (290 mg, 0.60 mmol) with 98% yield. ^1H NMR (400 MHz, DMSO): δ (ppm) = 9.92 (s, 2H), 8.90 (d, *J* = 1.8 Hz, 2H), 8.58 (d, *J* = 1.9 Hz, 1H), 8.46 (dd, *J* = 4.7, 1.5 Hz, 1H), 8.09 (d, *J* = 4.0 Hz, 2H), 7.97 (dd, *J* = 8.6, 1.9 Hz, 2H), 7.85 (d, *J* = 8.7 Hz, 2H), 7.81 (d, *J* = 4.0 Hz, 2H), 7.59 - 7.48 (m, 1H), 7.30 (dd, *J* = 7.8, 4.8 Hz, 1H), 5.83 (s, 2H).

5,5'-(10-(3-(pyridin-4-yl)propyl)-10*H*-phenothiazine-3,7-diyl)bis(thiophene-2-carbaldehyde) (4e) Product **4e** was synthetized according to general procedure A for the cleavage of the protective group using product **3e** (78 mg, 0.10 mmol), 6 mL 10% HCl_{aq}/THF (1:2). The desired product was isolated after a filtration on silica pad (first with DCM, then with DCM/MeOH, 4:1) as a red solid (40 mg, 0.074 mmol) with 74% yield. ^1H NMR (400 MHz, DMSO) δ 9.89 (s, 2H), 8.41 (dd, *J* = 4.5, 1.5 Hz, 2H), 8.02 (d, *J* = 4.0 Hz, 2H), 7.71 (d, *J* = 4.0 Hz, 2H), 7.65 (d, *J* = 2.2 Hz, 2H), 7.62 (dd, *J* = 8.5, 2.2 Hz, 2H), 7.21 (d, *J* = 5.9 Hz, 2H), 7.11 (d, *J* = 8.6 Hz, 2H), 3.97 (t, *J* = 6.8 Hz, 2H), 2.75 (t, *J* = 7.6 Hz, 2H), 2.13 - 2.01 (m, 2H).

5,5'-(9-(3-(pyridin-4-yl)propyl)-9*H*-carbazole-3,6-diyl)bis(thiophene-2-carbaldehyde) (4f) Product **4f** was synthetized according to general procedure A for the cleavage of the protective group using product **3f** (250 mg, 0.35 mmol), 9 mL 10% HCl_{aq}/THF (1:2). The desired product was isolated as a red solid with quantitative yield. ^1H NMR (400 MHz, DMSO) δ 9.92 (s, 2H), 8.86 (d, *J* = 1.6 Hz, 2H), 8.42 (dd, *J* = 4.4, 1.6 Hz, 2H), 8.08 (d, *J* = 4.0 Hz, 2H), 7.96 (dd, *J* = 8.6, 1.9 Hz, 2H), 7.81 (d, *J* = 4.0 Hz, 2H), 7.74 (d, *J* = 8.6 Hz, 2H), 7.21 (dd, *J* = 4.4, 1.6 Hz, 2H), 4.54 (t, *J* = 7.1 Hz, 2H), 2.69 (dd, *J* = 13.1, 4.7 Hz, 2H), 2.19 - 2.08 (m, 2H).

General procedure B for Knoevenagel condensation (iv). Aldehyde precursor (1 equiv.), cyanoacetic acid (5 equiv.), and piperidine (6 equiv.) were dissolved in dry $CHCl_3$ (0.2 M) and warmed to reflux for 8 h. After having the solvent evaporated, a solution of HCl 10% was added, and the mixture was left under magnetic stirring for 5 h at room temperature. The solid that precipitated was filtered and dissolved in a saturated aqueous solution of K_2CO_3. The new solid that precipitated was filtered and dissolved in a solution of citric acid 1 M. Then, the new solid that precipitated was filtered and washed with water.

3,3'-(5,5'-(10-(pyridin-4-ylmethyl)-10*H*-phenothiazine-3,7-diyl)bis(thiophene-5,2-diyl))bis(2-cyanoacrylic acid (PTZ-4Py). PTZ-4Py was synthetized according to general procedure B for Knoevenagel condensation using product **4a** (230 mg, 0.45 mmol), cyanoacetic acid (383 mg, 4.5 mmol), piperidine (460 mg, 5.4 mmol) and 10 mL of dry $CHCl_3$. The reaction was quenched with 10 mL of 10% HCl solution. A dark purple solid (238 mg, 0.37 mmol) was isolated as the product with 82% yield. m.p. › 250 ˚C (dec). ^1H NMR (400 MHz, DMSO): δ (ppm) = 8.55 (d, *J* = 5.8 Hz, 2H), 8.46 (s, 2H), 7.98 (d, *J* = 4.3 Hz, 2H), 7.70 (d, *J* = 4.0 Hz, 2H), 7.62 (d, *J* = 2.2 Hz, 2H), 7.50 (dd, *J* = 8.5, 2.2 Hz, 2H), 7.34 (d, *J* = 5.8 Hz, 2H), 6.83 (d, *J* = 8.7 Hz, 2H), 5.29 (s, 2H). ^{13}C NMR (101 MHz, DMSO) δ 152.08, 151.56, 150.26, 147.01, 146.28, 144.41, 141.92, 134.50, 127.96, 126.48, 125.15, 124.72, 123.22, 122.47, 117.00, 116.83, 98.33, 50.80. FT-IR $\upsilon/(cm^{-1})$: 2908, 1712, 1568 (s), 1426 (s), 1202 (b), 792 (s).

3,3'-(5,5'-(10-(pyridin-3-ylmethyl)-10*H*-phenothiazine-3,7-diyl)bis(thiophene-5,2-diyl))bis(2-cyanoacrylic acid (PTZ-3Py). PTZ-3Py was synthetized according to general procedure B for Knoevenagel condensation using product **4b** (195 mg, 0.38 mmol), cyanoacetic acid (323 mg, 3.8 mmol), piperidine (390 mg, 4.6 mmol) and 25 mL of dry $CHCl_3$. The reaction was quenched with 30 mL of 10% HCl solution. A dark purple solid (208 mg, 0.32 mmol) was isolated as the product with 85% yield. m.p. › 250 ˚C (dec). ^1H NMR (400 MHz, DMSO): δ (ppm) = 8.68 (s, 1H), 8.58 - 8.44 (m, 3H), 8.02 (d, *J* = 4.0 Hz, 2H), 7.78 - 7.72 (m, 3H), 7.67 (d, *J* = 1.9 Hz, 2H), 7.56 (dd, *J* = 8.5, 1.8 Hz, 2H), 7.43 (dd, *J* = 7.7, 4.9 Hz, 1H), 6.99 (d, *J* = 8.7 Hz, 2H), 5.36 (s, 2H). ^{13}C NMR (126 MHz, DMSO) δ 164.03, 151.92, 146.96, 144.18, 143.84, 141.80, 141.69, 136.97, 134.61, 128.24, 127.37, 126.50, 125.27, 124.88, 123.96, 117.10, 116.94, 98.46, 48.77. FT-IR $\upsilon/(cm^{-1})$: 1689 (w), 1584 (s), 1434 (s), 1202 (s), 803 (s).

3,3'-(5,5'-(9-(pyridin-4-ylmethyl)-9*H*-carbazole-3,6-diyl)bis(thiophene-5,2-diyl))bis(2-cyanoacrylic acid) (CBZ-4Py). CBZ-4Py was synthetized according to general procedure B for Knoevenagel condensation using product **4c** (171 mg, 0.35 mmol), cyanoacetic acid (297 mg, 3.5 mmol), piperidine (358 mg, 4.2 mmol) and 10 mL of dry $CHCl_3$. The reaction was quenched with 20 mL of 10% HCl solution. A dark red solid (170 mg, 0.28 mmol) was isolated as the product with 80% yield. Due to low solubility, addition of citric acid (**CA**) was necessary to improve the solubilization of the compound and to record better NMR spectra. m.p. › 250 ˚C (dec). ^1H NMR (400 MHz, DMSO) δ 8.80 (d, *J* = 1.3 Hz, 2H), 8.52 - 8.41 (m, 4H), 8.01 (d, *J* = 4.0 Hz, 2H), 7.87 (dd, *J* = 8.6, 1.4 Hz, 2H), 7.80 (d, *J* = 3.9 Hz, 2H), 7.70 (d, *J* = 8.7 Hz, 2H), 7.10 (d, *J* = 5.4 Hz, 2H), 5.80 (s, 2H), 2.75 (d, *J* = 15.4 Hz, 4H, **CA**), 2.65 (d, *J* = 15.4 Hz, 4H, **CA**). ^{13}C NMR (101 MHz, DMSO) δ 175.32 (**CA**), 171.77 (**CA**),164.32, 154.79, 150.38, 146.77, 146.64, 141.90, 141.77, 134.24, 125.75, 125.18, 124.77, 123.48, 122.12, 119.70, 117.31, 111.22, 98.34, 72.77 (**CA**) 45.41, 43.37 (**CA**). FT-IR *υ*/(cm^{-1}): 2921, 2214 (s), 1702 (s), 1573 (s), 1421 (s), 1199 (s), 793 (s). HRMS (Dual-ESI) *m/z*: calcd. for [M-H]$^-$ $C_{34}H_{20}N_4O_4S_2$: 611.0853, found 611.0845; calcd. for [M-H-CO$_2$]$^-$ 567.0955, found 567.0949; calcd. for [M-H-2CO$_2$]$^-$ 523.1057, found 523.1048

3,3'-(5,5'-(9-(pyridin-3-ylmethyl)-9H-carbazole-3,6-diyl)bis(thiophene-5,2-diyl))bis(2-cyanoacrylic acid) (CBZ-3Py). **CBZ-3Py** was synthetized according to general procedure B for Knoevenagel condensation using product **4d** (290 mg, 0.61 mmol), cyanoacetic acid (690 mg, 8.14 mmol), piperidine (831 mg, 9.77 mmol) and 30 mL of dry $CHCl_3$. The reaction was quenched with 10 mL of 10% HCl solution. A dark red solid (200 mg, 0.33 mmol) was isolated as the product with 60% yield. m.p. › 250 °C (dec). ^{1}H NMR (400 MHz, DMSO): δ (ppm) = 8.83 (d, *J* = 1.4 Hz, 2H), 8.59 (s, 1H), 8.53 - 8.40 (m, 3H), 8.04 (d, *J* = 4.1 Hz, 2H), 7.93 (dd, *J* = 8.6, 1.6 Hz, 2H), 7.87 - 7.82 (m, 4H), 7.54 (d, *J* = 8.0 Hz, 1H), 7.31 (dd, *J* = 7.8, 4.8 Hz, 1H), 5.82 (s, 2H). ^{13}C NMR (101 MHz, DMSO) δ 164.27, 154.90, 149.29, 148.82, 146.90, 142.05, 141.69, 135.05, 134.22, 133.31, 125.77, 125.12, 124.81, 124.29, 123.51, 119.74, 117.26, 111.38, 98.16, 44.06. FT-IR *υ*/(cm^{-1}): 2919, 2213 (s), 1701 (s), 1575 (s), 1423 (s), 1208 (s), 790 (s). HRMS (Dual-ESI) *m/z*: calcd. for [M-H]$^-$ $C_{34}H_{20}N_4O_4S_2$: 611.0853, found 611.0844; calcd. for [M-H-CO$_2$]$^-$ 567.0955, found 567.0947; calcd. for [M-H-2CO$_2$]$^-$ 523.1057, found 523.1046.

3,3'-((10-(3-(pyridin-4-yl)propyl)-10*H*-phenothiazine-3,7-diyl)bis(thiophene-5,2-diyl))bis(2-cyanoacrylic acid) (PTZ-C3-4Py). **PTZ-C3-4Py** was synthetized according to general procedure B for Knoevenagel condensation using product **4e** (40 mg, 0.074 mmol), cyanoacetic acid (63 mg, 0.74 mmol), piperidine (88 µL, 9.77 mmol) and 6 mL of dry $CHCl_3/CH_3CN$ (1:1). The reaction was quenched with 10 mL of 10% HCl solution. A dark red solid (20 mg, 0.030 mmol) was isolated as the product with 40% yield. m.p. › 250 °C (dec). ^{1}H NMR (400 MHz, DMSO) δ 8.41 (d, *J* = 8.0 Hz, 2H), 7.94 (d, *J* = 4.0 Hz, 2H), 7.70 (d, *J* = 3.9 Hz, 2H), 7.61 (d, *J* = 2.0 Hz, 2H), 7.58 (dd, *J* = 8.5, 2.0 Hz, 2H), 7.22 (d, *J* = 5.6 Hz, 2H), 7.12 (d, *J* = 8.6 Hz, 2H), 3.97 (t, *J* = 6.3 Hz, 2H), 2.75 (t, *J* = 7.5 Hz, 2H), 2.13 - 2.00 (m, 2H). ^{13}C NMR (101 MHz, DMSO) δ 164.11, 162.31, 152.24, 147.11, 145.00, 142.16, 134.46, 127.75, 127.24, 126.55, 125.10, 124.97, 124.21, 117.11, 117.01, 98.21, 46.61, 32.70, 26.81. FT-IR *υ*/(cm^{-1}): 2994 (b), 1567 (s), 1451 (s), 1348 (s), 1219 (b), 809 (s).

3,3'-((9-(3-(pyridin-4-yl)propyl)-9*H*-carbazole-3,6-diyl)bis(thiophene-5,2-diyl))bis(2-cyanoacrylic acid) (CBZ-C3-4Py). **CBZ-C3-4Py** was synthetized according to general procedure B for Knoevenagel condensation using product **4f** (280 mg, 0.55 mmol), cyanoacetic acid (470 mg, 5.5 mmol), piperidine (0.65 mL, 6.64 mmol) and 12 mL of dry $CHCl_3/CH_3CN$ (1:1). The reaction was quenched with 5 mL of 10% HCl solution. A dark red solid (60 mg, 0.094 mmol) was isolated as the product with 17% yield. m.p. › 250 °C (dec). ^{1}H NMR (400 MHz, DMSO) δ 8.82 (d, J = 1.6 Hz, 2H), 8.51 (s, 2H), 8.42 (d, J = 6.0 Hz, 2H), 8.06 (d, J = 4.1 Hz, 2H), 7.95 (dd, J = 8.6, 1.8 Hz, 2H), 7.86 (d, J = 4.0 Hz, 2H), 7.77 (d, J = 8.6 Hz, 2H), 7.22 (d, J = 5.9 Hz, 2H), 4.54 (t, J = 6.8 Hz, 3H), 2.82 - 2.63 (m, 3H), 2.22 - 2.10 (m, 3H). ^{13}C NMR (101 MHz, DMSO) δ 164.29, 161.58, 155.29, 147.27, 142.47, 142.18, 141.67, 134.06, 126.83, 125.56, 124.76, 124.74, 123.28, 119.63, 117.15, 111.30, 97.50, 72.89, 32.91, 28.77. FT-IR $\nu/(\mathrm{cm}^{-1})$: 2916, 1554 (s), 1426 (s), 1194 (b), 783 (s).

3,7-dibromo-10-(3-((*tert*-butyldimethylsilyl)oxy)propyl)-10*H*-phenothiazine (5a). Compound **1a** (2.1 g, 5.6 mmol) was dissolved in 50 mL of anhydrous DMF in a two-necked flask under N_2 atmosphere, then the solution was cooled to 0 °C using an ice bath and NaH 60% (1.12 g, 28 mmol) was added and the solution was stirred at 0 °C for 30 min. Then, (3-bromopropoxy)-*tert*-butyldimethylsilane (1.3 g, 5.04 mmol) was added, the ice bath was removed, and the solution was stirred under magnetic agitation overnight at room temperature. The reaction was quenched with ca 600 mL of water and ice. The color of the solution changed from dark red to light green. Then 200 mL of EtO_2 were added, the organic phase was separated, washed with water, and dried over sodium sulfate. The solvent was evaporated under reduce pressure and suspended with petroleum ether. The green solid was filtered over Hirsh and washed with petroleum ether. The filtrate solution was evaporated under reduced pressure and an orange oil was obtained (2.34 g, 4.4 mmol, 87%). ^{1}H NMR (500 MHz, Acetone-d_6) δ 7.35 (dd, J = 8.7, 2.3 Hz, 2H), 7.30 (d, J = 2.3 Hz, 2H), 7.04 (d, J = 8.7 Hz, 2H), 4.06 (t, J = 6.6 Hz, 2H), 3.78 (t, J = 5.7 Hz, 2H), 1.97 (quintet, 2H), 0.87 (s, 9H), 0.01 (s, 6H).

3,6-dibromo-10-(3-((*tert*-butyldimethylsilyl)oxy)propyl)-9*H*-carbazole (5b). Compound **1b** (1.0 g, 3.07 mmol) was dissolved in 34 mL of anhydrous THF in a two-necked flask under N_2 atmosphere, then the solution was cooled to 0 °C using an ice bath and NaH 60% (614 mg, 15 mmol) was added and the solution was stirred at 0 °C for 30 min. Then, (3-bromopropoxy)-*tert*-butyldimethylsilane (700 mg, 2.76 mmol) was added, the ice bath was removed, and the solution was stirred under magnetic agitation for three days at room temperature. The reaction was quenched with ca 600 mL of water and ice. Then 200 mL of EtO_2 were added, the organic phase was separated, washed with water, and dried over sodium sulfate. The solvent was evaporated under reduce pressure and suspended with petroleum ether. The crude product was purified with column chromatography (*n*-heptane 100% and then heptane/Et_2O, 5:0.2). The product was not subjected to further purification, and it was used as it was into the next reaction.

5,5'-(10-(3-((*tert*-butyldimethylsilyl)oxy)propyl)-10*H*-phenothiazine-3,7-diyl)bis(thiophene-2-carbaldehyde) (6a). Compound **5a** (600 mg, 1.13 mmol) and Pd(dppf)$Cl_2 \cdot CH_2Cl_2$ (92 mg, 0.11 mmol) were dissolved in dimethoxyethane 12.5 mL and stirred for 30 min under nitrogen atmosphere. Then (5-formylthiophen-2-yl)boronic acid (424 mg, 2.4 mmol) and methanol (12.5 mL) were added, and the solution was stirred for 30 min under nitrogen atmosphere. In the end, K_2CO_3 (1.6 g, 11.3 mmol) was added to the solution and the reaction was performed with microwave irradiation (90 °C, 70 W, 75 min) and then quenched by pouring into a saturated solution of NH_4Cl (70 mL) and AcOEt (70 mL). Filtration on Celite and extractions with organic solvent allowed to isolate the crude product, then purified through column chromatography on silica gel (petroleum ether/AcOEt, from 7:2 to 5:2). The desired product was isolated as a light-yellow solid (410 g, 0.69 mmol) with 61% yield. ^1H NMR (400 MHz, DMSO) δ 9.89 (s, 2H), 8.01 (d, *J* = 4.0 Hz, 2H), 7.70 (d, *J* = 4.0 Hz, 2H), 7.64 - 7.58 (m, 4H), 7.17 (d, *J* = 9.2 Hz, 2H), 4.05 (dd, *J* = 12.1, 6.9 Hz, 2H), 3.73 (t, *J* = 5.8 Hz, 2H), 1.96 - 1.87 (m, 2H), 0.82 (s, 9H), -0.02 (s, 6H).

5,5'-(9-(3-((*tert*-butyldimethylsilyl)oxy)propyl)-9*H*-carbazole-3,6-diyl)bis(thiophene-2-carbaldehyde) (6b). Crude compound **5b** (740 mg, 1.48 mmol) and Pd(dppf)$Cl_2 \cdot CH_2Cl_2$ (125 mg, 0.15 mmol) were dissolved in dimethoxyethane 2.5 mL and stirred for 15 min under nitrogen atmosphere. Then (5-formylthiophen-2-yl)boronic acid (545 mg, 3.5 mmol) and methanol (2.5 mL) were added and the solution was stirred for 15 min under nitrogen atmosphere. In the end, K_2CO_3 (2.1 g, 14.8 mmol) was added to the solution and the reaction was performed with microwave irradiation (90 °C, 70 W, 90 min) and then quenched by pouring into a saturated solution of NH_4Cl (30 mL) and AcOEt 370 mL). Filtration on Celite and extractions with organic solvent allowed to isolate the crude product, then purified through column chromatography on silica gel (*n*-heptane/AcOEt, 5:3). The desired product was isolated as a light-yellow solid (190 mg, 0.34 mmol) with 23% yield. ^1H NMR (400 MHz, DMSO) δ 9.92 (s, 2H), 8.87 (d, *J* = 1.8 Hz, 2H), 8.08 (d, *J* = 4.0 Hz, 2H), 7.97 (dd, *J* = 8.6, 1.9 Hz, 2H), 7.81 (d, *J* = 4.0 Hz, 2H), 7.72 (d, *J* = 8.5 Hz, 2H), 4.53 (t, *J* = 6.8 Hz, 2H), 3.60 (t, *J* = 5.9 Hz, 2H), 2.00 (t, *J* = 6.3 Hz, 2H), 0.90 (s, 9H), 0.03 (s, 6H).

5,5'-(10-(3-hydroxypropyl)-10*H*-phenothiazine-3,7-diyl)bis(thiophene-2-carbaldehyde) (7a). Compound **7a** was synthesized according to ref. 46, using as reagent compound **6a** (619 mg, 1.04 mmol) and tetra-*n*-butylammoniumfluoride (690 mg, 2.6 mmol) dissolved in 60 mL of THF and stirred at 0 °C for 5 min and then at room temperature for 3 h. The product was obtained as a red solid (310 mg, 0.65 mmol) with 63% yield. ^{1}H NMR (500 MHz, DMSO) δ 9.89 (s, 2H), 8.02 (d, *J* = 3.9 Hz, 2H), 7.70 (d, *J* = 3.9 Hz, 2H), 7.63 (dd, *J* = 8.4, 2.2 Hz, 1H), 7.61 (d, *J* = 2.1 Hz, 1H), 7.16 (d, *J* = 8.5 Hz, 2H), 4.67 (t, *J* = 4.9 Hz, 1H), 4.03 (t, *J* = 7.0 Hz, 2H), 3.56 (td, *J* = 10.9, 5.7 Hz, 2H), 1.88 (q, 2H).

3-(3,7-bis(5-formylthiophen-2-yl)-10*H*-phenothiazin-10-yl)propyl nicotinate (8a). Compound **8a** was synthesized according to ref. 47, using as reagent compound **7a** (300 mg, 0.63 mmol), nicotinic acid (78 mg, 0.63 mmol), dicyclohexylcarbodiimide (196 mg, 0.95 mmol). The crude product was purified with column chromatography using dichloromethane/AcOEt (2:1) as eluent. The product was obtained as a red solid (35 mg, 0.06 mmol, 10%). ^{1}H NMR (500 MHz, DMSO) δ 9.89 (s, 2H), 9.05 (d, *J* = 1.7 Hz, 1H), 8.79 (dd, *J* = 4.8, 1.7 Hz, 1H), 8.22 (dt, *J* = 7.8, 2.0 Hz, 1H), 8.02 (d, *J* = 4.0 Hz, 2H), 7.69 (d, *J* = 4.0 Hz, 2H), 7.63 - 7.59 (m, *J* = 4.3, 2.2 Hz, 4H), 7.51 (dd, *J* = 8.0, 4.8 Hz, 1H), 7.23 (d, *J* = 9.2 Hz, 2H), 4.46 (t, *J* = 6.0 Hz, 2H), 4.22 (t, *J* = 7.0 Hz, 2H), 2.23 - 2.19 (m, 2H).

3,3'-(5,5'-(10-(3-(nicotinoyloxy)propyl)-10*H*-phenothiazine-3,7-diyl)bis(thiophene-5,2-diyl))bis(2-cyanoacrylic acid) (PTZ-Py). **PTZ-Py** was synthetized according to general procedure B for Knoevenagel condensation using product **8a** (35 mg, 0.06 mmol), cyanoacetic acid (51 mg, 0.6 mmol), piperidine (53 mg, 0.62 mmol) and 7 mL of dry $CHCl_3$. The reaction was quenched with 5 mL of 10% HCl aqueous solution. The product was isolated as a dark purple solid (29 mg, 0.04 mmol) with 67% yield. m.p. > 250 °C (dec). ^{1}H NMR (400 MHz, DMSO) δ 9.05 (s, 1H), 8.78 (d, *J* = 3.8 Hz, 1H), 8.32 (s, 2H), 8.21 (d, *J* = 7.9 Hz, 1H), 7.87 (d, *J* = 2.9 Hz, 2H), 7.65 (d, *J* = 3.5 Hz, 2H), 7.59 - 7.46 (m, 6H), 7.22 (d, *J* = 7.9 Hz, 2H), 4.45 (t, *J* = 6.0 Hz, 2H), 4.20 (t, *J* = 6.6 Hz, 2H), 2.21 (dd, *J* = 9.8, 3.3 Hz, 2H). ^{13}C NMR (101 MHz, DMSO) *δ* 165.17, 164.06, 154.07, 150.50, 144.93, 139.91, 137.27, 135.16, 127.94, 126.30, 126.01, 124.80, 124.36, 118.15, 117.07, 63.16, 44.14, 25.79. FT-IR υ/(cm^{-1}): 2931, 1701, 1568 (s), 1357 (s), 1191 (b), 792, 714.

References

1 Decavoli, C., Boldrini, C. L., Manfredi, N. & Abbotto, A. (**2020**) Molecular Organic Sensitizers for Photoelectrochemical Water Splitting. *Eur. J. Inorg. Chem.,* **2020**, 978-999, doi:10.1002/ejic.202000026.

2 Alibabaei, L., Brennaman, M. K., Norris, M. R., Kalanyan, B., Song, W., Losego, M. D., Concepcion, J. J., Binstead, R. A., Parsons, G. N. & Meyer, T. J. (**2013**) Solar water splitting in a molecular photoelectrochemical cell. *Proc. Natl. Acad. Sci. USA,* **110**, 20008-20013, doi:10.1073/pnas.1319628110.

3 Alibabaei, L., Sherman, B. D., Norris, M. R., Brennaman, M. K. & Meyer, T. J. (**2015**) Visible photoelectrochemical water splitting into H_2 and O_2 in a dye-sensitized photoelectrosynthesis cell. *Proc. Natl. Acad. Sci. USA,* **112**, 5899-5902, doi:10.1073/pnas.1506111112.

4 Sherman, B. D., Xie, Y., Sheridan, M. V., Wang, D., Shaffer, D. W., Meyer, T. J. & Concepcion, J. J. (**2017**) Light-Driven Water Splitting by a Covalently Linked Ruthenium-Based Chromophore-Catalyst Assembly. *ACS Energy Lett.,* **2**, 124-128, doi:10.1021/acsenergylett.6b00661.

5 Brennaman, M. K., Gish, M. K., Alibabaei, L., Norris, M. R., Binstead, R. A., Nayak, A., Lapides, A. M., Song, W., Brown, R. J., Concepcion, J. J., Templeton, J. L., Papanikolas, J. M. & Meyer, T. J. (**2018**) Pathways Following Electron Injection: Medium Effects and Cross-Surface Electron Transfer in a Ruthenium-Based, Chromophore-Catalyst Assembly on TiO_2. *J. Phys. Chem. C,* **122**, 13017-13026, doi:10.1021/acs.jpcc.8b04837.

6 Wang, D., Xu, Z., Sheridan, M. V., Concepcion, J. J., Li, F., Lian, T. & Meyer, T. J. (**2021**) Photodriven water oxidation initiated by a surface bound chromophore-donor-catalyst assembly. *Chem. Sci.,* **12**, 14441-14450, doi:10.1039/D1SC03896F.

7 Yamamoto, M., Wang, L., Li, F., Fukushima, T., Tanaka, K., Sun, L. & Imahori, H. (**2016**) Visible light-driven water oxidation using a covalently-linked molecular catalyst-sensitizer dyad assembled on a TiO_2 electrode. *Chemical Science,* **7**, 1430-1439, doi:10.1039/c5sc03669k.

8 Rondán-Gómez, V., Montoya De Los Santos, I., Seuret-Jiménez, D., Ayala-Mató, F., Zamudio-Lara, A., Robles-Bonilla, T. & Courel, M. (**2019**) Recent advances in dye-sensitized solar cells. *Appl. Phys. A,* **125**, 836, doi:10.1007/s00339-019-3116-5.

9 Lee, C.-P., Li, C.-T. & Ho, K.-C. (**2017**) Use of organic materials in dye-sensitized solar cells. *Mater. Today,* **20**, 267-283, doi:10.1016/j.mattod.2017.01.012.

10 Cecconi, B., Manfredi, N., Montini, T., Fornasiero, P. & Abbotto, A. (**2016**) Dye-Sensitized Solar Hydrogen Production: The Emerging Role of Metal-Free Organic Sensitizers. *Eur. J. Org. Chem.,* **2016**, 5194-5215, doi:10.1002/ejoc.201600653.

11 Huang, J. F., Lei, Y., Luo, T. & Liu, J. M. (**2020**) Photocatalytic H_2 Production from Water by Metal-free Dye-sensitized TiO2 Semiconductors: The Role and Development Process of Organic Sensitizers. *ChemSusChem*, doi:10.1002/cssc.202001646.

12 Kaeffer, N., Massin, J., Lebrun, C., Renault, O., Chavarot-Kerlidou, M. & Artero, V. (**2016**) Covalent Design for Dye-Sensitized H_2-Evolving Photocathodes Based on a Cobalt Diimine-Dioxime Catalyst. *J. Am. Chem. Soc.,* **138**, 12308-12311, doi:10.1021/jacs.6b05865.

13 Pati, P. B., Zhang, L., Philippe, B., Fernández-Terán, R., Ahmadi, S., Tian, L., Rensmo, H., Hammarström, L. & Tian, H. (**2017**) Insights into the Mechanism of a Covalently Linked Organic Dye-Cobaloxime Catalyst System for Dye-Sensitized Solar Fuel Devices. *ChemSusChem,* **10**, 2480-2495, doi:10.1002/cssc.201700285.

14 Antón-García, D., Warnan, J. & Reisner, E. (**2020**) A diketopyrrolopyrrole dye-based dyad on a porous TiO_2 photoanode

for solar-driven water oxidation. *Chem. Sci.*, doi:10.1039/D0SC04509H.

15 Duan, L., Fischer, A., Xu, Y. & Sun, L. (**2009**) Isolated seven-coordinate Ru(IV) dimer complex with [HOHOH]$^-$ bridging ligand as an intermediate for catalytic water oxidation. *J. Am. Chem. Soc.,* **131**, 10397-10399, doi:10.1021/ja9034686.

16 Manfredi, N., Monai, M., Montini, T., Salamone, M., Ruffo, R., Fornasiero, P. & Abbotto, A. (**2017**) Enhanced photocatalytic hydrogen generation using carbazole-based sensitizers. *Sustain. Energy Fuels,* **1**, 694-698, doi:10.1039/c7se00075h.

17 Manfredi, N., Boldrini, C. L. & Abbotto, A. (**2018**) Organic Sensitizers for Photoanode Water Splitting in Dye-Sensitized Photoelectrochemical Cells. *ChemElectroChem,* **5**, 2395-2402, doi:10.1002/celc.201800592.

18 Manfredi, N., Cecconi, B. & Abbotto, A. (**2014**) Multi-Branched Multi-Anchoring Metal-Free Dyes for Dye-Sensitized Solar Cells. *Eur. J. Org. Chem.*, 7069-7086, doi:10.1002/ejoc.201402422.

19 Decavoli, C., Boldrini, C. L., Manfredi, N. & Abbotto, A. (**2019**) Dye-sensitized photocatalytic and photoelectrochemical hydrogen production through water splitting. *Rend. Lincei Sc.i Fis. Nat.,* **30**, 469-483, doi:10.1007/s12210-019-00824-6.

20 Leandri, V., Ruffo, R., Trifiletti, V. & Abbotto, A. (**2013**) Asymmetric Tribranched Dyes: An Intramolecular Cosensitization Approach for Dye-Sensitized Solar Cells. *Eur. J. Org. Chem.,* **2013**, 6793-6801, doi:10.1002/ejoc.201300962.

21 Knuhtsen, A., Whiting, R., McWhinnie, F. S., Whitmore, C., Smith, B. O., Green, A. C., Timperley, C. M., Kinnear, K. I. & Jamieson, A. G. (**2021**) μ-Conotoxin KIIIA peptidomimetics that block human voltage-gated sodium channels. *Pept. Sci.,* **113**, e24203, doi:10.1002/pep2.24203.

22 Zhang, B. & Sun, L. (**2019**) Ru-bda: Unique Molecular Water-Oxidation Catalysts with Distortion Induced Open Site and Negatively Charged Ligands. *J. Am. Chem. Soc.,* **141**, 5565-5580, doi:10.1021/jacs.8b12862.

23 Jiang, Y., Li, F., Zhang, B., Li, X., Wang, X., Huang, F. & Sun, L. (**2013**) Promoting the activity of catalysts for the oxidation of water with bridged dinuclear ruthenium complexes. *Angew. Chem. Int. Ed.,* **52**, 3398-3401, doi:10.1002/anie.201209045.

24 Liu, X., Long, J., Wang, G., Pei, Y., Zhao, B. & Tan, S. (**2015**) Effect of structural modification on the performances of phenothiazine-dye sensitized solar cells. *Dyes Pigm.,* **121**, 118-127, doi:10.1016/j.dyepig.2015.05.012.

25 Gupta, K. S. V., Suresh, T., Singh, S. P., Islam, A., Han, L. & Chandrasekharam, M. (**2014**) Carbazole based A-π-D-π-A dyes with double electron acceptor for dye-sensitized solar cell. *Org. Electron.,* **15**, 266-275, doi:10.1016/j.orgel.2013.11.020.

26 Tauc, J. (**1968**) Optical properties and electronic structure of amorphous Ge and Si. *Mater. Res. Bull.,* **3**, 37-46, doi:10.1016/0025-5408(68)90023-8.

27 Tian, H., Boschloo, G. & Hagfeldt, A. *Molecular Devices for Solar Energy Conversion and Storage.* (Springer: Singapore, Singapore, 2018)

28 Gao, Y., Zhang, L., Ding, X. & Sun, L. (**2014**) Artificial photosynthesis--functional devices for light driven water splitting with photoactive anodes based on molecular catalysts. *Phys. Chem. Chem. Phys.,* **16**, 12008-12013, doi:10.1039/c3cp55204g.

29 Duan, L., Bozoglian, F., Mandal, S., Stewart, B., Privalov, T., Llobet, A. & Sun, L. (**2012**) A molecular ruthenium catalyst with water-oxidation activity comparable to that of photosystem II. *Nat. Chem.,* **4**, 418-423, doi:10.1038/nchem.1301.

30 Greczynski, G. & Hultman, L. (**2017**) C 1s Peak of Adventitious Carbon Aligns to the Vacuum Level: Dire Consequences for Material's Bonding Assignment by Photoelectron Spectroscopy. *ChemPhysChem,* **18**, 1507-1512, doi:10.1002/cphc.201700126.

31 Rensmo, H., Westermark, K., Södergren, S., Kohle, O., Persson, P., Lunell, S. & Siegbahn, H. (**1999**) XPS studies of Ru-polypyridine complexes for solar cell applications. *J. Chem. Phys.,* **111**, 2744-2750, doi:10.1063/1.479551.

32 Yamamoto, M., Wang, L., Li, F., Fukushima, T., Tanaka, K., Sun, L. & Imahori, H. (**2016**) Visible light-driven water oxidation using a covalently-linked molecular catalyst-sensitizer dyad assembled on a TiO_2 electrode. *Chem. Sci.,* **7**, 1430-1439, doi:10.1039/c5sc03669k.

33 Yamamoto, M., Nishizawa, Y., Chabera, P., Li, F., Pascher, T., Sundstrom, V., Sun, L. & Imahori, H. (**2016**) Visible light-driven water oxidation with a subporphyrin sensitizer and a water oxidation catalyst. *Chem. Commun.,* **52**, 13702-13705, doi:10.1039/C6CC07877J.

34 Eom, Y. K., Nhon, L., Leem, G., Sherman, B. D., Wang, D., Troian-Gautier, L., Kim, S., Kim, J., Meyer, T. J., Reynolds, J. R. & Schanze, K. S. (**2018**) Visible-Light-Driven Photocatalytic Water Oxidation by a π-Conjugated Donor–Acceptor–Donor Chromophore/Catalyst Assembly. *ACS Energy Lett.,* **3**, 2114-2119, doi:10.1021/acsenergylett.8b01020.

35 Sherman, B. D., Sheridan, M. V., Dares, C. J. & Meyer, T. J. (**2016**) Two Electrode Collector–Generator Method for the Detection of Electrochemically or Photoelectrochemically Produced O_2. *Anal. Chem.,* **88**, 7076-7082, doi:10.1021/acs.analchem.6b00738.

36 Volpato, G. A., Marasi, M., Gobbato, T., Valentini, F., Sabuzi, F., Gagliardi, V., Bonetto, A., Marcomini, A., Berardi, S., Conte, V., Bonchio, M., Caramori, S., Galloni, P. & Sartorel, A. (**2020**) Photoanodes for water oxidation with visible light based on a pentacyclic quinoid organic dye enabling proton-coupled electron transfer. *Chem. Commun.,* **56**, 2248-2251, doi:10.1039/c9cc09805d.

37 Wang, D., Eberhart, M. S., Sheridan, M. V., Hu, K., Sherman, B. D., Nayak, A., Wang, Y., Marquard, S. L., Dares, C. J. & Meyer, T. J. (**2018**) Stabilized photoanodes for water oxidation by integration of organic dyes, water oxidation catalysts, and electron-transfer mediators. *Proc. Natl. Acad. Sci. USA,* **115**, 8523-8528, doi:10.1073/pnas.1802903115.

38 Swierk, J. R., Mendez-Hernandez, D. D., McCool, N. S., Liddell, P., Terazono, Y., Pahk, I., Tomlin, J. J., Oster, N. V., Moore, T. A., Moore, A. L., Gust, D. & Mallouk, T. E. (**2015**) Metal-free organic sensitizers for use in water-splitting dye-sensitized photoelectrochemical cells. *Proc. Natl. Acad. Sci. USA,* **112**, 1681-1686, doi:10.1073/pnas.1414901112.

39 Wee, K.-R., Sherman, B. D., Brennaman, M. K., Sheridan, M. V., Nayak, A., Alibabaei, L. & Meyer, T. J. (**2016**) An aqueous, organic dye derivatized SnO_2/TiO_2 core/shell photoanode. *J. Mater. Chem. A,* **4**, 2969-2975, doi:10.1039/c5ta06678f.

40 Pavlishchuk, V. V. & Addison, A. W. (**2000**) Conversion constants for redox potentials measured versus different reference electrodes in acetonitrile solutions at 25°C. *Inorg. Chim. Acta,* **298**, 97-102, doi:10.1016/S0020-1693(99)00407-7.

41 Bockris, J. O. M., Reddy, A. K. N. & Gamboa-Aldeco, M. *Modern Electrochemistry 2A: Fundamentals of Electrodics.* (Springer US: Boston, USA, **2000**)

42 Ito, S., Murakami, T. N., Comte, P., Liska, P., Grätzel, C., Nazeeruddin, M. K. & Grätzel, M. (**2008**) Fabrication of thin film dye sensitized solar cells with solar to electric power conversion efficiency over 10%. *Thin Solid Films,* **516**, 4613-4619, doi:10.1016/j.tsf.2007.05.090.

43 Kirner, J. T. & Finke, R. G. (**2017**) Sensitization of Nanocrystalline Metal Oxides with a Phosphonate-Functionalized Perylene Diimide for Photoelectrochemical Water Oxidation with a CoO_x Catalyst. *ACS Appl. Mater. Interfaces,* **9**, 27625-27637, doi:10.1021/acsami.7b05874.

44 Zhou, X., Xu, S., Liu, L., Sun, Y., Cheng, J., Duan, X., Zhou, L. & Qu, H. (**2021**) 5,5-Dioxoyphenothiazine-based D-A-D type AIE molecules enabling persistent room temperature phosphorescence,

white light emission and dual-mode mechanochromism. *Dyes Pigm.,* **188**, 109193, doi:10.1016/j.dyepig.2021.109193.

45 Sailer, M., Franz, A. W. & Müller, T. J. J. (**2008**) Synthesis and Electronic Properties of Monodisperse Oligophenothiazines. *Chem. Eur. J.,* **14**, 2602-2614, doi:10.1002/chem.200701341.

46 Corey, E. J. & Venkateswarlu, A. (**1972**) Protection of hydroxyl groups as *tert*-butyldimethylsilyl derivatives. *J. Am. Chem. Soc.,* **94**, 6190-6191, doi:10.1021/ja00772a043.

47 Morishita, S., Saito, T., Hirai, Y., Shoji, M., Mishima, Y. & Kawakami, M. (**1988**) Synthesis and hypolipidemic activity of 2-substituted isobutyric acid derivatives. *J. Med. Chem.,* **31**, 1205-1209, doi:10.1021/jm00401a022.

Chapter 8: WOC in (photo)electrochemical cells

Aim of this section

In this section, I describe the project done at Yale University during my Ph D. period abroad. The group of Prof. Brudvig, who was hosting me, has recently discovered a new way of anchoring molecules onto TiO_2 using BODIPY molecules, which are unfunctionalized at positions 3 and 5. This anchoring is believed to form a B-O bond between the boron atom of the BODIPY molecule and the oxygen atoms of the SC. I joined this project to help with the synthesis of the investigated molecules and to study the anchoring mode of the *meso*-phenylBodipy unfunctionalized at 3 and 5 but with small and large substituents on positions 2 and 6. This study found that the presence of two substituents at positions 2 and 6 greatly reduces the loading of the molecule and even completely prevents it if the substituents are large. A preliminary study on mono-substituted BODIPY molecules in position 2 showed that the molecule could be easily loaded on the surface, no matter how large the substituent was. This behavior could indicate that the binding with the SC may not be perpendicular to the surface, and that the molecule could bend over toward the surface. Based on this first optimization study, I designed and synthesized a new iridium-based WOC, which uses BODIPY as the anchoring group. A ligand of the WOC has been modified by adding a carboxylic group able to form an amide bond with an amino-modified *meso*-phenylBodipy. The **[Ir(3-pyalkBod)(CO)(CH_3CN)]** WOC so obtained was adsorbed first on ITO slides to study its electrochemical activity as a WOC. It was then studied on TiO_2 films to investigate its photoelectrochemical activity since the **3-pyalkBod** ligand absorbs visible light. Despite the new WOC showing high current densities, its application in photoelectrochemical studies as a dyad has completely failed. In fact, it was totally indifferent to the visible irradiation. This could be attributed to poor charge transfer between the WOC and the dye that fails to regenerate the WOC. This problem may be resolved with a deeper study of the energy levels of these compounds and by a modification of the design in order to tune the energy levels of the dye portion. Further studies with XPS, Terahertz spectroscopy, and transmission electron microscopy are ongoing to better characterize the active catalytic species in this research.

8.1 Introduction

Water splitting typically requires additional overpotential to reach appreciable catalytic current densities, resulting in relatively low energy conversion efficiencies.[1-4] To the standard potential for water splitting (1.23 V), the anode and the cathode overpotential (η_a and η_c), and the total voltage drops on other parasitic resistances in the electrochemical cell, including solution resistance, contact resistance, and membrane resistance (η_{other}) must be added. Hence, the potential required for driving the water splitting can be described as Eq. 8.1.[5]

$$E_{op} = 1.23\,V + \eta_a + \eta_c + \eta_{other} \qquad \text{(Eq. 8.1)}$$

η_a and η_c typically result from the unfavorably high energies required for the formation of reaction intermediates on the electrode surface.[6] The E_{op} is one of the most valuable parameters that significantly influences the performance of the electrocatalytic cell. Hence, the most important goal is to reduce the overpotential by adding a suitable catalyst to speed up the water-splitting reaction. The kinetics of the four-electron process of water oxidation is slower than the two-electron process of hydrogen evolution.[7-9] Hence, the addition of a catalyst for water oxidation is almost mandatory to obtain acceptable efficiencies. These electrocatalysts can be used both in DSPEC in combination with a photosensitizer with suitable energy levels and/or in electrochemical cells that obtain the power for driving water oxidation from external solar panels. In most cases, inorganic oxides are used as catalysts in this field. Although the inorganic oxides have high stability, their properties cannot be easily tuned.[10] Thus, molecular catalysts are gaining more interest in the scientific community. Their properties can be easily adjusted, and they present a higher activity than the inorganic oxides and thus require a lower loading either in solution or on a film. Moreover, the loading onto a film leads to even better properties, such as the possibility to develop a device which can work in flow, without contamination of the aqueous medium with the molecular catalysts, and thus make for easier recycling and recovery of the catalysts.[11] The current state-of-the-art electrocatalysts for water splitting are iridium- or ruthenium-based.[12-14] Recently, many examples of first-row transition metal-based WOCs, for example based on copper, iron and, cobalt, have gained favor due to their wide availability of materials, their low cost, and the low risk of depletion, but for now, they still suffer from high lability of the ligands, difficulties in reaching high oxidation states and low efficiencies versus the classical ruthenium or iridium-based ones.[15]

In this section, I present a new iridium-based WOC linked to the electrode surface through an innovative design. It exhibited high current densities with minimal loadings. The group of Prof. Brudvig at Yale University has recently discovered a new way of binding to titanium dioxide by the formation of a B-O bond between the SC and a *N*,*N'*-difluoroboryl-5-

phenyldipyrrin, also known as *meso*-phenylBODIPY (**Bod**). This bond occurs when the 3 and 5 positions of the molecule, typically methylated in most literature examples,[16,17] are unsubstituted in order to avoid a steric conflict with the surface. BODIPY dyes have always seen wide application in different fields, such as bioimaging, ion sensing, light-harvesting, and as a hole- or electron-transfers.[18] Moreover, they have recently been used in homo- or heterogeneous PC and DSPEC with the only purpose of being a light-harvesting material.[19-22] However, these dyes are typically functionalized on the phenyl ring with a carboxylic acid to bind the surface. In other cases, the 3 and 5 positions are functionalized with linkers and anchoring groups for surface attachment.[23] Since the 3 and 5 positions of BODIPY are typically substituted, it is no surprise that prior studies of surface attachment have involved substituted BODIPYs. This substitution is usually preferred because it provides many benefits, including higher extinction coefficients,[24,25] greater fluorescence quantum yields,[26] a redshift of the visible absorption,[17] and good synthetic and commercial availability.[16] However, the steric bulk of these substitutions prevents the boron atom from having any direct interactions with the surface. The present study via XPS and IR on unsubstituted BODIPY confirmed the binding through the boron atom. This new anchor group exhibited better stability in aqueous media than did the carboxylic acid version. Finally, studies with optical pump terahertz probe spectroscopy confirmed the electron injection of the BODIPY even if bonded through the boron atom. This result is convincing evidence that the anchoring chemistry does not inhibit the BODIPY derivatives from injecting excited electrons into the CB of TiO_2.

The first study I did at Yale University regarded the synthesis of a series of 2,6-substituted ***Bod***. I wanted to investigate the orientation of the molecule while binding the TiO_2 and the influence that the functionalizations in the 2 and/or 6 positions could have in the binding mode of this system. These results would be helpful for the design of new BODIPY dyes to couple with a particular WOC for application in DSPEC photoanodes.

8.2 Optimization study

In this optimization study, I synthesized five different BODIPY dyes; four of them have been substituted in the 2 and/or 6 positions with bromine and/or a phenyl group (Figure 66).

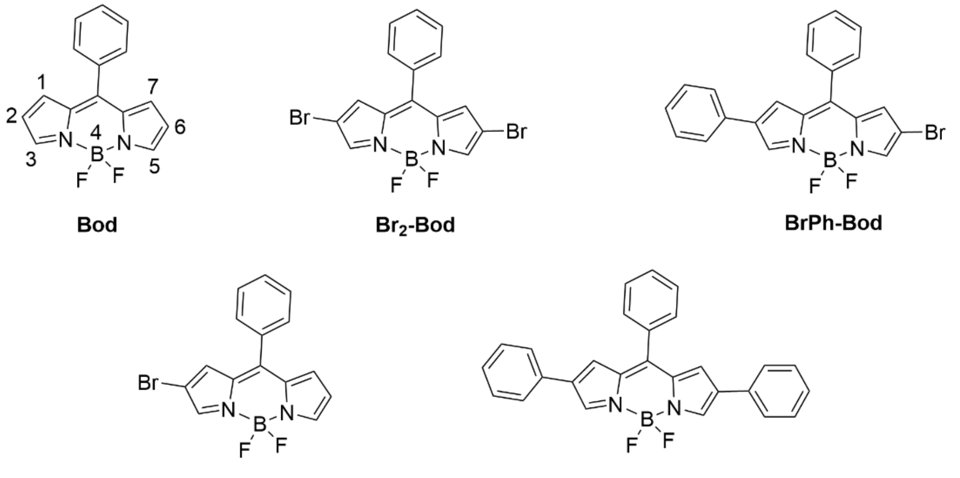

Bod **Br$_2$-Bod** **BrPh-Bod**

Br-Bod **Ph$_2$-Bod**

Figure 66: Molecular structure of investigated 2,6-substituted compounds.

In this study, the bromine is considered a small substituent since its van der Waals radius is comparable to that of a methyl substituent (~2.0 Å).[27] The influence of methyl substituents on the binding was studied previously study for substitution at the 3 and 5 positions, a result that is now in press. In the present work, we decided not to synthesize the 2-phenyl derivative (**Ph-Bod**) because it had the same retention time as **Br-Bod**,[28] hence purification was not possible. The synthesis of these compounds was adapted from literature procedures[28-30] as described in Scheme 11.

Starting from 2,2'-(phenylmethylene)bis(1H-pyrrole),[31] **Bod** was obtained after oxidation with 2,3-dichloro-5,6-dicyano-1,4-benzoquinone (DDQ) in dichloromethane, followed by insertion of the BF_2 group by reaction of the mixture with $BF_3 \cdot Et_2O$ and triethylamine at reflux for 30 min. **Bod** was isolated after purification with column chromatography as an orange solid with green reflections. Bromination with liquid bromine in dry dichloromethane yielded **Br$_2$-Bod** and **Br-Bod** products as fuchsia and orange solids, respectively. A final palladium-catalyzed Suzuki-Miyaura cross-coupling, not pushed to completion, and performed on **Br$_2$-Bod**, gave **Ph$_2$-Bod** and **BrPh-Bod**. All compounds have been characterized *via* NMR (^1H, ^{11}B, ^{19}F) spectroscopy and compared with literature data.

Bod, **Br$_2$-Bod**, and **Ph$_2$-Bod** have been optically characterized in 10^{-5} M acetonitrile solution and their spectra normalized to their molar extinction coefficient as reported in Figure 67. The λ_{max} of all compounds is reported in Table 9, as well as the relative molar extinction coefficients. The λ_{max} of the most intense peak red-shifts of about 30 nm after the introduction of the bromine substituents, and of 80 nm after the insertion of two highly-conjugated donor groups in **Ph$_2$-Bod**. Furthermore, the introduction of two phenyl substituents allows an absorption up to 650 nm.

Table 9: Optical parameters of the investigated compounds in acetonitrile solution

Dye	λ_{max}[a] (nm)	ε (M^{-1} cm^{-1})
Bod	346, 497	58000± 1000
Br$_2$-Bod	372, 530	51000± 1000
Ph$_2$-Bod	390, 580	44000± 1000

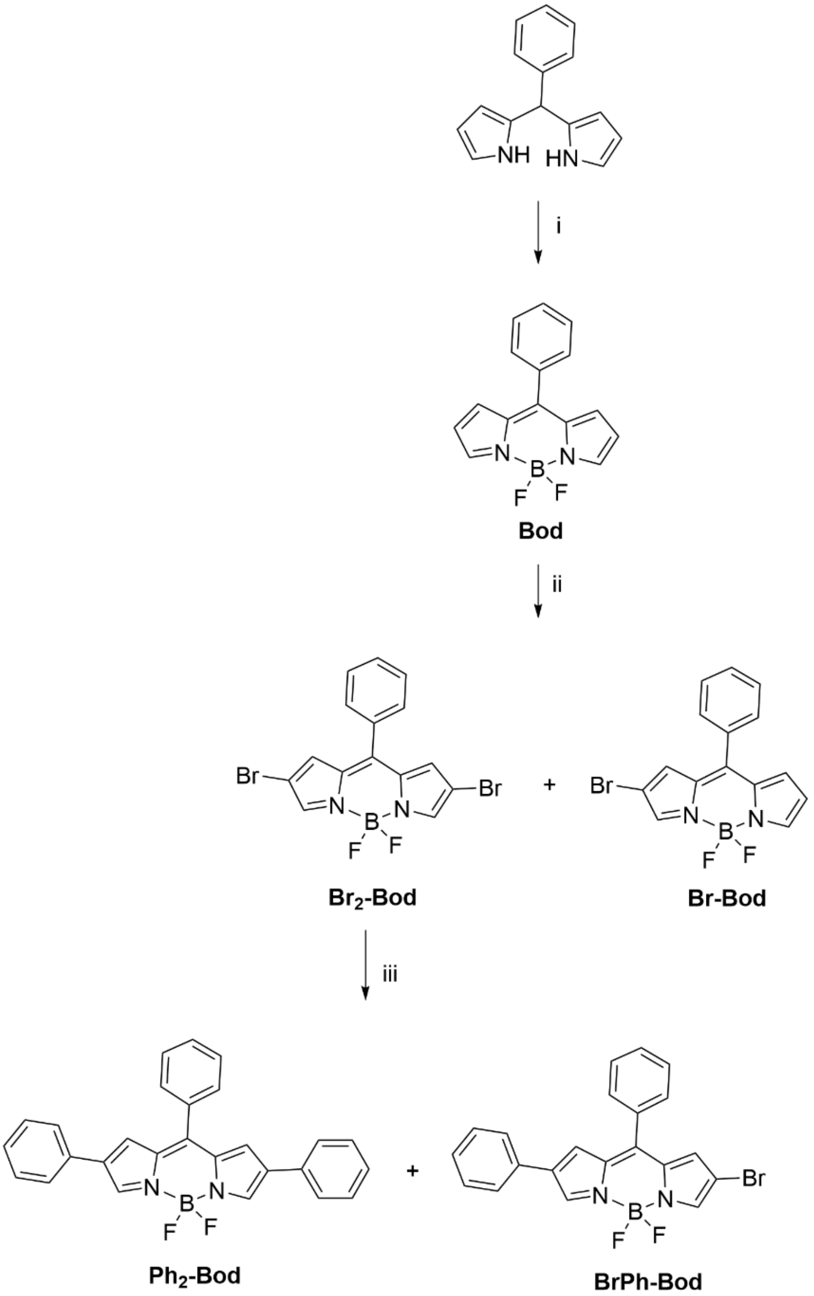

Scheme 11: Synthetic pathway for the investigated compounds. i) 1. DDQ, dry DCM, rt, 10 min, 2. Et_3N, $BF_3 \cdot Et_2O$, reflux, 30 min; ii) Br_2, dry DCM, rt, 2 h; iii) phenylboronic acid, $Pd(dppf)Cl_2 \cdot CH_2Cl_2$, K_2CO_3, Et_3N, Toluene/H_2O (1:1), reflux, 45 min.

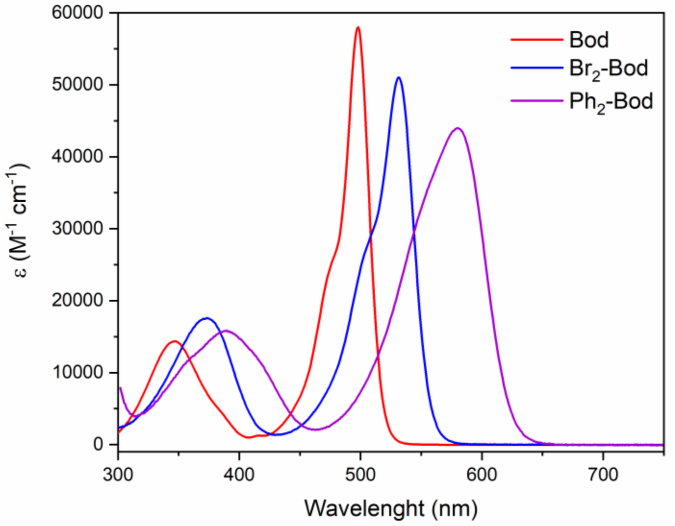

Figure 67: UV-vis spectra in acetonitrile of **Bod**. **Br$_2$-Bod**, **Ph$_2$-Bod**.

The dye-sensitized films were prepared by soaking an oven-dried TiO_2 film on glass in a 5 mM dry acetonitrile/toluene (9:1) solution of the compound and left to sensitize for 20 h at room temperature in the dark. It is mandatory to avoid all contamination from water and humidity to ensure a satisfactory loading. After 20 h, the films were taken out from the sensitization solution and soaked into dry acetonitrile for a few minutes to remove all the unattached compounds. Finally, they were dried under nitrogen flow and kept in the dark until use.

Due to the problems found in the optimization of the sensitization procedure, we managed to obtain the UV-vis analysis of just three dye-sensitized films (**Bod**, **Br$_2$-Bod,** and **Ph$_2$-Bod**), and their spectra are shown in Figure 68 together with an image of the films. The presence of two big substituents, such as phenyl rings in **Ph$_2$-Bod**, on the 2 and 6 positions made the loading on the SC practically impossible. On the other hand, the presence of two small substituents such as bromine atoms in **Br$_2$-Bod**, allowed the loading on the SC but the level was lower than for the unsubstituted **Bod**.

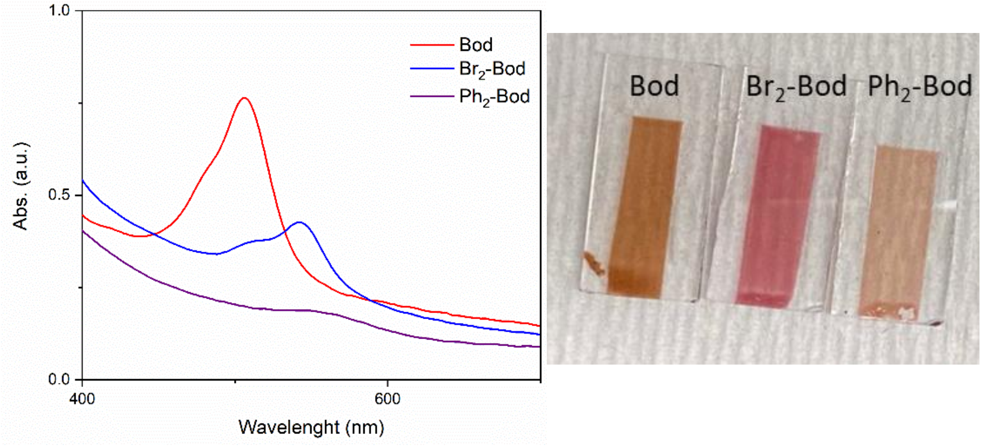

Figure 68: UV-vis spectra on TiO_2 films sensitized with **Bod**, **Br$_2$-Bod** or **Ph$_2$-Bod** (left) and photo of the dye-sensitized films (right).

A preliminary study of **Br-Bod** and **BrPh-Bod** showed a stronger absorption for the **Br-Bod**-sensitized film than the **Br$_2$-Bod**-sensitized one and a similar absorption for the **BrPh-Bod**-sensitized film. These data ideally needed multiple experiments for confirmation that were not possible because of time limitations. However, we hypothesize that the molecules should bind the TiO_2 in an oblique mode with respect to the surface. Hence, the presence of small substituents on the 2 and 6 positions might reduce the binding due to a steric clash. The presence of two large substituents almost completely prevents the binding as is the case for any substituent in the 3 and 5 positions. On the other hand, the presence of just one substituent at the 2 position should allow binding with the TiO_2. Further computational studies in collaboration with the research group of Prof. Batista at Yale University are now in progress to evaluate these hypotheses.

8.3 Synthesis of the electrocatalyst

The research group of Prof. Brudvig works on iridium catalysts for water oxidation. As is the case for their ruthenium counterparts, the iridium catalysts need the proximity of two metal centers to perform water oxidation. They discovered the existence of Ir^{IV}-oxo dimers whose molecular structure is still somewhat uncertain due to the presence of many active isomers.[32,33] Based on these new results on BODIPY molecules, I decided to functionalize a ligand of the iridium WOC [Ir(pyalk)(CO)$_2$][34] (pyalk = 2-(2'pyridyl)-2-propanolate) to anchor this catalyst on the electrode surface by exploiting the anchoring ability of BODIPY dyes. The designs I chose are depicted in Figure 69. I studied a monomeric design **[Ir(3-pyalkBod)(CO)(CH_3CN)]** and a dimeric one **Ir-3pyalkBod dimer**. The dimer should favor the interaction between two iridium centers in proximity and be useful for the identification of the active species in water oxidation. Because of time limitations, I was only able to finish the synthesis and the characterization of the monomer.

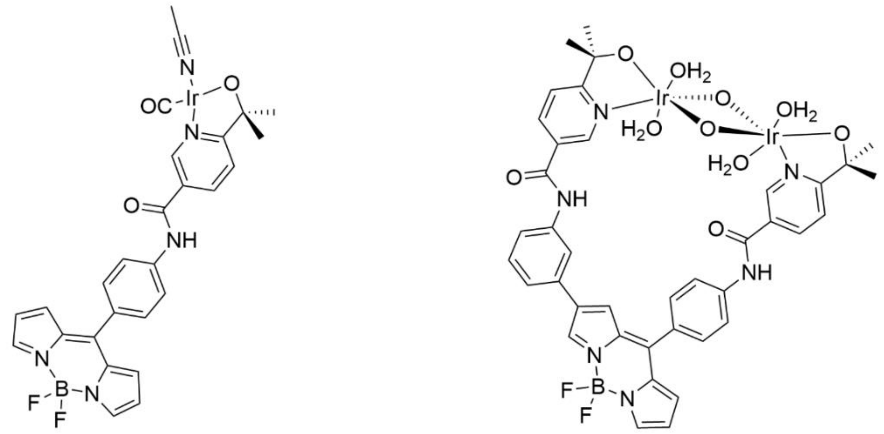

[Ir(3-pyalkBod)(CO)(CH_3CN)]

Ir-3-pyalkBod dimer

Figure 69: Molecular structures of the investigated compounds.

The **[Ir(3-pyalkBod)(CO)(CH_3CN)]** molecule contains two different units connected through an amide bond. The first unit is a *meso*-phenylBodipy functionalized with an amine group on the phenyl ring and without any α-substituents on the pyrrole rings to act as the anchor group. The second one is the catalytic core, resembling [Ir(pyalk)$(CO)_2$]. The addition of a carboxylic group on the *meta* position of the pyridyl ring should connect these two units, breaking the conjugation between them and avoiding detrimental charge recombination reactions between the WOC and the electrode surface.

The synthetic pathway for the molecules of interest is shown in Scheme 12. First, the 2-(2-pyridyl)-2-propanol was properly functionalized for binding to a modified BODIPY molecule. The starting reaction is a *pseudo*-Minisci radical substitution that attached an acetyl group on a 3-cyanopyridine by reaction with metaldehyde, iron sulfate, and *tert*-butyl hydroperoxide in an acid environment. Then, the addition of a methyl group to the carbonyl functionality using methylmagnesium bromide, and a final hydrolysis reaction to convert the nitrile functionality into a carboxylic acid, performed refluxing the previously obtained product in a mixture of ethanol and sodium hydroxide yield intermediate **3**. On the other hand, a BODIPY dye is modified to exploit an amine functionality to form an amide bond with **3**. The amino-functionalized BODIPY portion is prepared by adapting from literature procedures.[35,36] The dipyrrinmethane is prepared by condensing 4-nitrobenzaldehyde and pyrrole using indium trichloride as the catalyst. Then, oxidation with DDQ, subsequent insertion with boron trifluoride diethyl etherate in presence of *N*,*N*-diisopropylethylamine and in the end reduction with iron in acid condition yield the amino-functionalized *N*,*N'*-difluoroboryl-5-phenyldipyrrin **6**. The **3-pyalkBod** ligand is obtained after condensation of compound **3** and compound **6** using oxalyl chloride in benzene to first generate the acyl chloride of **3** and then condense it with the amine functionality of **6** in a basic environment. Finally, the **[Ir(3-pyalkBod)(CO)(CH_3CN)]** WOC is obtained after adding to [Ir(cod)Cl]$_2$ (cod = 1,5-cyclooctadiene) a dichloromethane solution of **3-pyalkBod**, previously deprotonated with an aqueous solution of K_2CO_3. After a short stirring in a nitrogen environment, carbon monoxide is bubbled for 5 minutes to exchange the cod ligand with it and the final addition of acetonitrile releases the desired product.

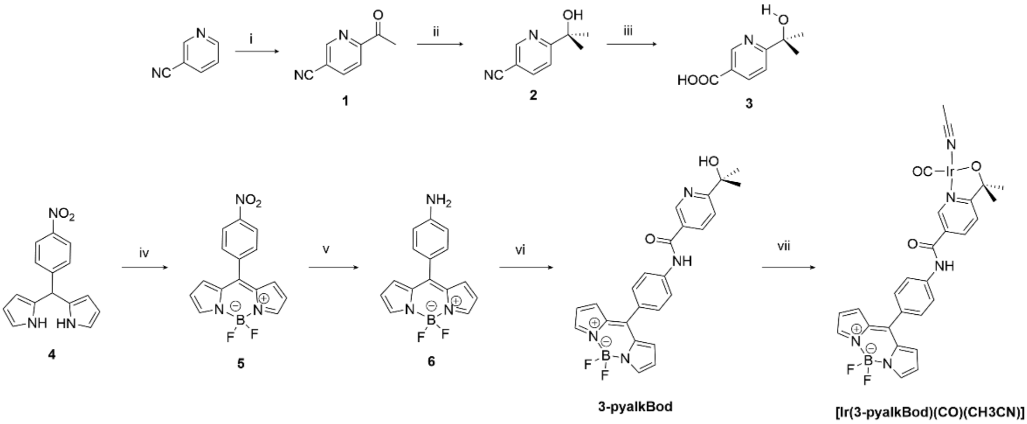

Scheme 12: Synthetic route for **[Ir(3-pyalkBod)(CO)(CH_3CN)]**. i) 1. metaldehyde, acetonitrile, rt, 10 min, 2. $FeSO_4 \cdot H_2O$, trifluoroacetic acid, 70% *tert*-butyl hydroperoxide aqueous solution, reflux, 3.5 h; ii) methyl magnesium bromide, anhydrous THF, 0 °C, 3 h; iii) NaOH, EtOH 70%, reflux, 3 h; iv) 1. DDQ, extra dry DCM, rt, 30 min, 2. *N,N*-diisopropylethylamine, boron trifluoride diethyl etherate, reflux, 1 h; v) iron (powder), HCl 12 M, EtOH/H_2O (6:1), reflux, 90 min; vi) 1. **3**, oxalyl chloride, extra dry DMF, anhydrous benzene, rt, 1.5 h, 2. triethylamine, extra dry DCM, rt, overnight; vii) 1. $K_2CO_{3(aq)}$, DCM, rt, 30 min, 2. $[Ir(cod)Cl]_2$, rt, 30 min, 3. CO bubbling, rt, 5 min, 4. CH_3CN.

The **[Ir(3-pyalkBod)(CO)(CH_3CN)]** has been characterized with FTIR, NMR (^1H, ^{11}B, ^{19}F), and HRMS to check the purity and the correct structure. FTIR confirms the formation of the complex showing the peak at 2024 cm-1 assigned to the CO ligand. The boron triplet and the fluorine doublet of doublets, respectively in ^{11}B and ^{19}F NMR, confirms the retention of the BF_2 core and the addiction of the iridium center in the correct position. The signal of the acetonitrile ligand in ^1H NMR is easily recognizable because it is slightly shifted to lower fields with respect to the signal of the acetonitrile solvent (1.96 ppm in DMSO-d_6). The HRMS spectrum shows the presence of the compound of interest but also the formation of more complex structures with a sort of periodical increase in the mass signals. This behavior is still under investigation.

We studied these compounds both on ITO and FTO+TiO_2 films. With the former, we investigated the electrochemical behavior of the WOC, with the latter the photoelectrochemical behavior of the iridium-bodipy dyad. An ITO or TiO_2 film was soaked in catalyst or ligand 5 mM dry acetonitrile solution and left sensitizing for 20 h at room temperature in the dark. It is crucial to avoid all the contamination from water and humidity to ensure a satisfactory loading. Then, the films were taken out, soaked into dry acetonitrile for a few minutes to remove all the unattached compounds, and dried under nitrogen flow before use.

8.4 Optical properties

The absorption spectra of **3-pyalkBod** and **[Ir(3-pyalkBod)(CO)(CH_3CN)]** in acetonitrile solution are reported in Figure 70 and normalized to the maximum value. BODIPY dyes are characterized by a strong absorption referred to the S_0-S_1 (π-π^*) transition with a λ_{max} of about 500 nm.[29] A weaker transition at higher energy, around 300-400 nm, is solvent dependent and it is attributed to the S_0-S_2 transition related to the electronic configuration of the substituents.[37] Both **3-pyalkBod** and **[Ir(3-pyalkBod)(CO)(CH_3CN)]** present the same absorption contour in the BODIPY portion, and this is another confirmation of the presence of the boron difluoride group in the correct position. Moreover, this confirms that the functionalization of the pyridyl ring in *meta* avoids the conjugation in the complex and thus the displacement of the energy levels of the catalyst and of the dye.

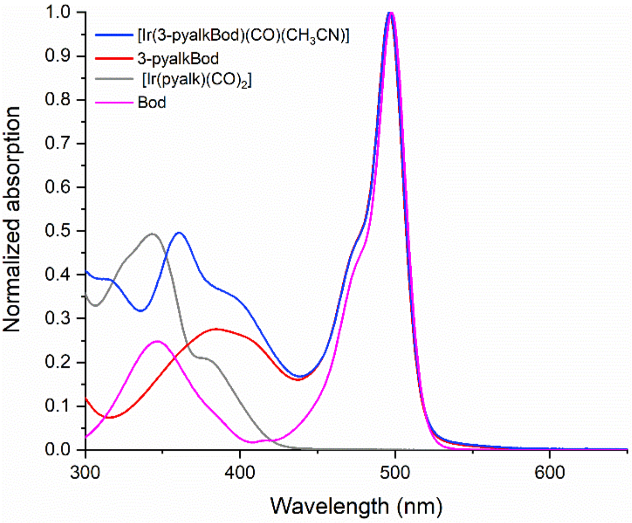

Figure 70: Absorption spectra in acetonitrile solution of the investigated compounds.

With respect to the benchmark **Bod** (Paragraph 8.2), the most significant difference in **3-pyalkBod** is a broadening and red-shifting of about 40 nm of the second transition band due to the presence of a more complex electron-withdrawing substituent on the *meso*-phenyl ring. It is interesting the presence of the peak at 360 nm in the **[Ir(3-pyalkBod)(CO)(CH$_3$CN)]** spectrum whose shape is similar to the **[Ir(pyalk)(CO)$_2$]** spectrum. The difference of about 15 nm in the λ_{max} for that transition may be attributed to the presence of an electron-withdrawing group on the pyridyl ring of 3-pyalkBod in **[Ir(3-pyalkBod)(CO)(CH$_3$CN)]**.

The absorption spectra on ITO or TiO$_2$ films measured using an integrating sphere are reported in Figure 71 and Figure 72, respectively.

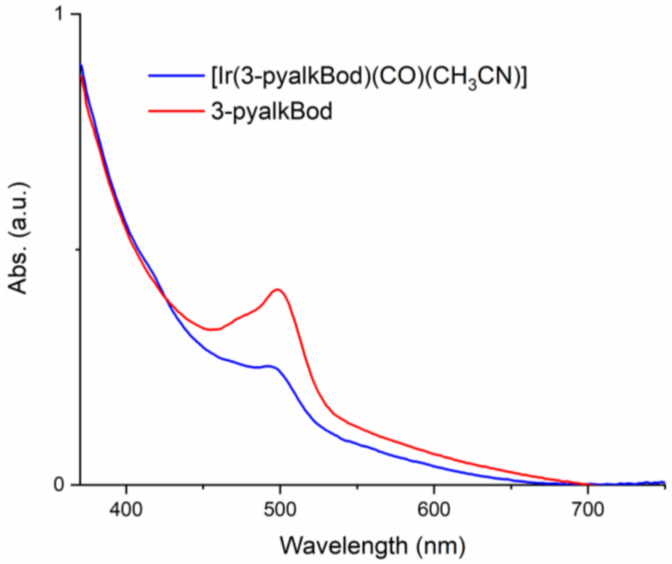

Figure 71: Absorption spectra of the ITO films sensitized with **3-pyalkBod** and **[Ir(3-pyalkBod)(CO)(CH$_3$CN)]**.

On ITO films, the peak of the S_0-S_1 transition is still recognizable and it is slightly redshifted of less than 5 nm. The absorption of the **[Ir(3-pyalkBod)(CO)(CH$_3$CN)]**-sensitized film is lower with respect to the **3-pyalkBod** one. The lower loading may be attributed to a lesser solubility of the compound in the sensitization solution that needs to be highly concentrated (5 mM). On the TiO_2 film, the situation is similar (Figure 72). The strong absorption related to the S_0-S_1 transition of the bodipy portion is still recognizable at 500 nm. However, a secondary peak at 415 nm is present. It could be attributed to the transition related to the iridium portion and the formation of dimeric species. This peak is also present in the ITO spectrum as a small hump at 414 nm. The correct attribution to this peak is still under investigation. In all the spectra, a significant sloping baseline is observed. This increased absorbance could be attributed to the doping of boron from the bodipy-based compounds into the surface of the TiO_2 as the molecules bind to the surface. This increase in absorbance has been reported before for boron doping of TiO_2 and it may also happen in ITO films.[38]

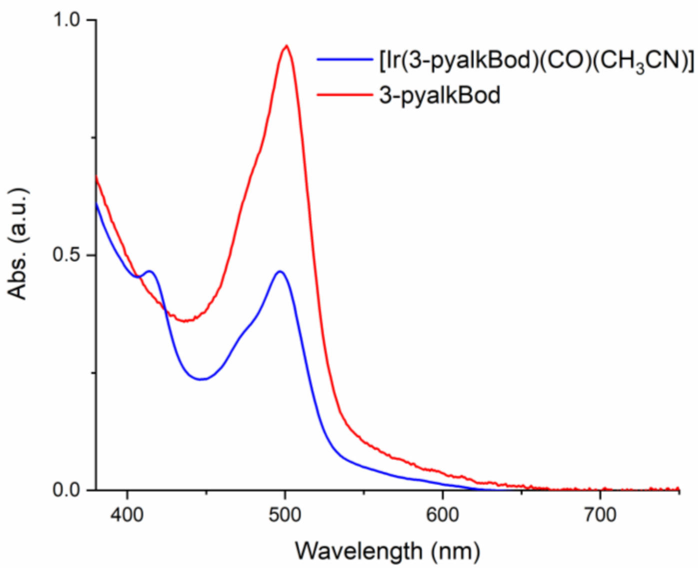

Figure 72: Absorption spectra of the FTO+TiO_2 films sensitized with **3-pyalkBod** and **[Ir(3-pyalkBod)(CO)(CH_3CN)]**.

8.5 Electrochemistry

Electrochemical characterization of the WOC was performed only on films to avoid the generation of complex structures by aggregation or formation of clusters. CV of the sensitized ITO films was performed in 0.1 M Na_2SO_4 aqueous solution at pH 6.7, as shown in Figure 73. The CV of the **3-pyalkBod**-sensitized film presents a similar profile to the blank ITO film. It may mean that the **3-pyalkBod** by itself is not able to generate any current even under an applied potential. **[Ir(3-pyalkBod)(CO)(CH_3CN)]**-sensitized film, instead, shows a high catalytic wave at +1.2 V *vs* NHE that can be assigned to water oxidation catalysis.[39] Then we also see a reversible redox peak at $E_{1/2}$ = +0.74 V *vs* NHE and another irreversible reduction peak at +1.07 V *vs* NHE are present that might be attributed to the Ir(III/IV) couple. However, the potentials seem shifted about 0.1 V with respect to similar systems, thus further studies comparing with other iridium catalysts in the same conditions are needed to test this hypothesis.

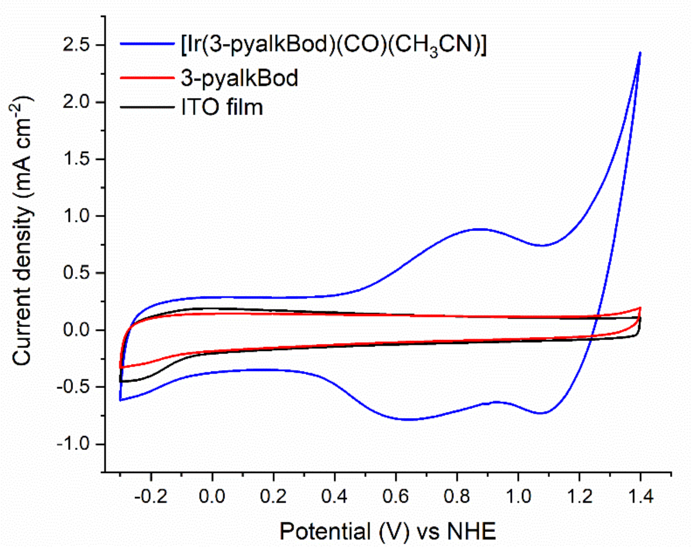

Figure 73: CV of **[Ir(3-pyalkBod)(CO)(CH$_3$CN)]**- and **3-pyalkBod**-sensitized ITO films in Na_2SO_4 0.1 M in H_2O at pH 6.7 degassed with nitrogen.

LSV further confirmed the inability of **3-pyalkBod** in generating currents (Figure 74). In fact, the current evolved by the **3-pyalkBod**-sensitized film is almost negligible compared to the **[Ir(3-pyalkBod)(CO)(CH$_3$CN)]**-sensitized one. At +1.2 V *vs* NHE, the difference in current densities between the two films is about 1.4 mA cm^{-2} and keeps increasing while scanning to higher potentials. Thus, we decided to perform the CA to evaluate the generated current versus time at that potential. As it is shown in Figure 75, the WOC-sensitized film presents a high initial peak with a sharp decrease over time. However, it exhibited a current of 100 µA cm^{-2} after 150 s of experiments, which is more than ten-fold the current generated by **3-pyalkBod**.

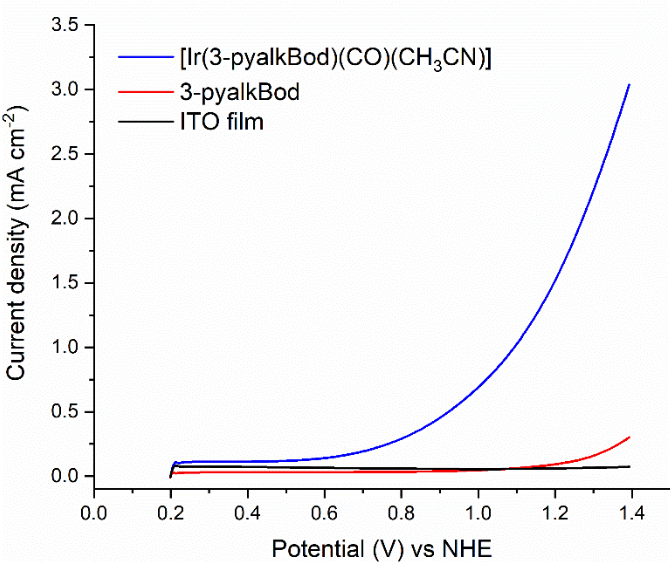

Figure 74: LSV of **[Ir(3-pyalkBod)(CO)(CH$_3$CN)]**- and **3-pyalkBod**-sensitized ITO films in Na_2SO_4 0.1 M in H_2O at pH 6.7 degassed with nitrogen.

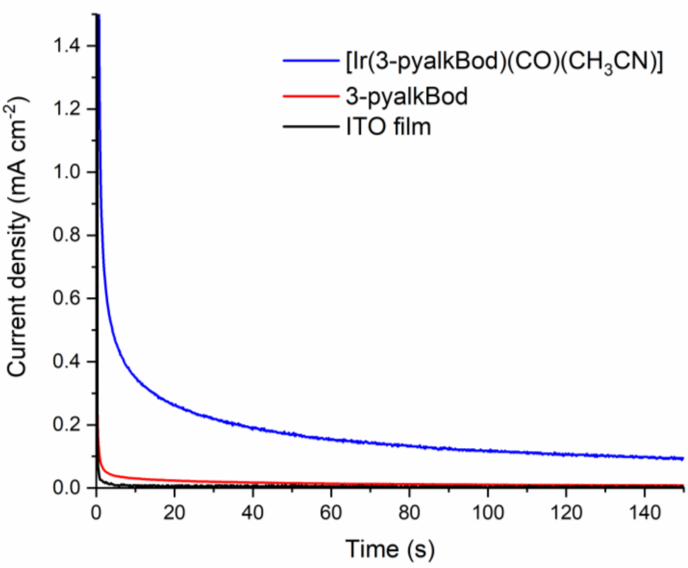

Figure 75: CA of **[Ir(3-pyalkBod)(CO)(CH$_3$CN)]**- and **3-pyalkBod**-sensitized ITO films in Na_2SO_4 0.1 M in H_2O at pH 6.7 degassed with nitrogen with an applied bias of +1.2 V *vs* NHE.

Moreover, the currents obtained by this innovative WOC are higher than the ones generated with a previous published iridium WOC (Figure 76).[40] This could be attributed to a different design in the ligand structure, which incorporates the anchor functionality. Both ligands are characterized by a rigid structure due to the presence of the amide bond. However, the functionalization at position 3 of pyalk, instead of position 4, might favor the formation of more complex structures while reducing the conjugation along the molecule. In fact, the position of the iridium center in the 3-substituted compound is lateral with respect to the axis of the ligand and not on the top of it like in the other case. This conformation might favor the interaction of two iridium centers bound to the electrode surface. This kind of interaction would be completely forbidden in the other case since the iridium center is aligned with the ligand and the contact with another iridium center should be more challenging. More investigations regarding oxygen evolution, XPS, and Terahertz spectroscopy are now ongoing to better evaluate **[Ir(3-pyalkBod)(CO)(CH_3CN)]** and its capabilities in water oxidation.

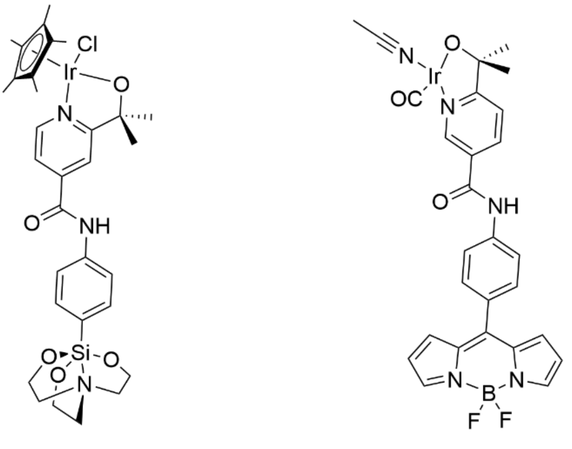

Figure 76: Molecular structures of the previous iridium WOC of ref 40 and **[Ir(3-pyalkBod)(CO)(CH_3CN)]**.

8.6 Photoelectrochemistry

Since **3-pyalkBod** is visible-light active, **[Ir(3-pyalkBod)(CO)(CH_3CN)]** can be considered as a dyad for DSPEC composed of the iridium center as WOC and **3-pyalkBod** as the photosensitizer. Hence, we decided to study its photoelectrochemical water oxidation capability in DSPEC. In this case, the photoanode was composed of an FTO layer covered with a ~4 μm thick layer of TiO_2 obtained by doctor blading. The setup of the cell for the electrochemical study was the same as in the previous study. CV of the sensitized TiO_2 films was performed in 0.1 M Na_2SO_4 aqueous solution at pH 6.7 and it is shown in Figure 77.

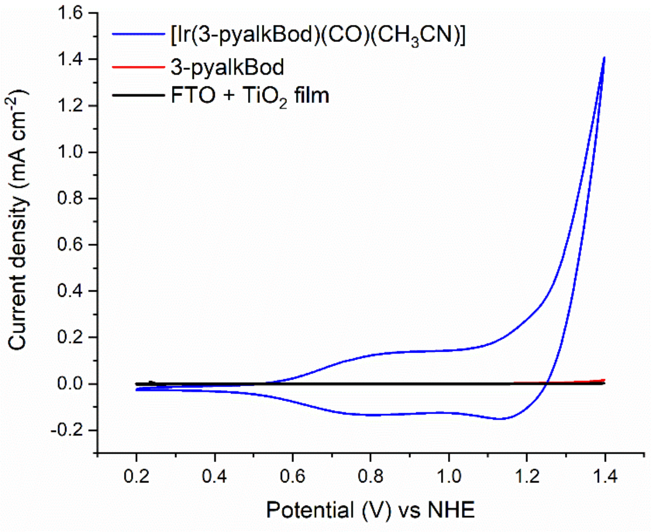

Figure 77: CV of **[Ir(3-pyalkBod)(CO)(CH_3CN)]**- and **3-pyalkBod**-sensitized FTO+TiO_2 films in Na_2SO_4 0.1 M in H_2O at pH 6.7 degassed with nitrogen.

As in the other case, **3-pyalkBod** showed a current density comparable to the blank, and the **Ir(3-pyalkBod)(CO)(CH_3CN)]**-sensitized electrode presented about the same trend showing a redox peak at $E_{1/2}$ = +0.74 V *vs* NHE and the irreversible reduction peak at +1.15 V *vs* NHE. The high catalytic wave that started at +1.1 V *vs* NHE confirmed the capability of this electrode in the oxidation of water.[39] Not surprisingly, the current densities obtained in the ITO case are higher because TiO_2 is less conductive than the ITO.

LSV and CA were performed in a PEC supported with a quartz window in the same three-electrode setup, using Ag/AgCl (KCl 3 M) as RE and a platinum wire as CE. All the experiments are compared to a bare FTO+TiO_2 film. The LSV performed in the dark reflects the same result obtained with the ITO slides (Figure 78). The difference in generated current between the **[Ir(3-pyalkBod)(CO)(CH_3CN)]**- and **3-pyalkBod**-sensitized films was around 200 μA cm^{-2} at 1.2 V *vs* NHE and kept increasing on moving to higher potentials.

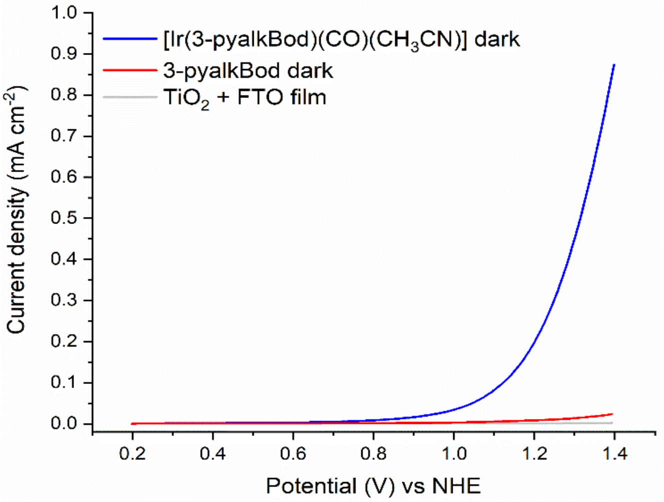

Figure 78: LSV of **[Ir(3-pyalkBod)(CO)(CH_3CN)]**- and **3-pyalkBod**-sensitized FTO+TiO_2 films in Na_2SO_4 0.1 M in H_2O at pH 6.7 degassed with nitrogen in the dark.

LSV characterization was performed also under continuous and chopped irradiation (Figure 79). However, the difference between the current generated in the dark and under irradiation is slight, suggesting that this dyad cannot work by itself in a DSPEC. Also, the 3-pyalkBod-sensitized electrode was tested under continuous and chopped irradiation, but, as we supposed, the current densities did not change (Figure 80).

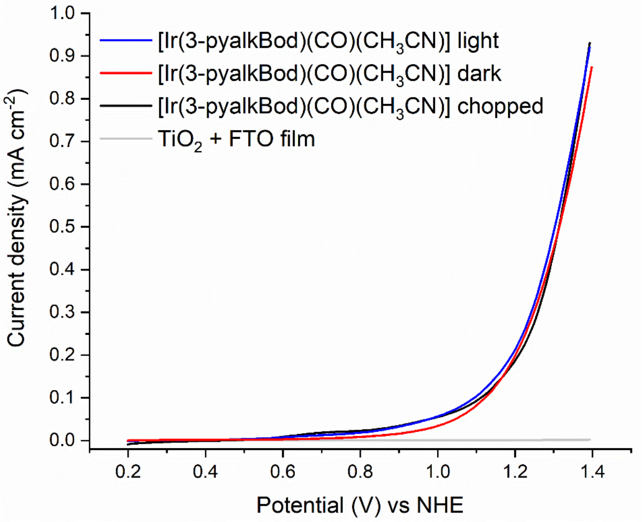

Figure 79: LSV of **[Ir(3-pyalkBod)(CO)(CH$_3$CN)]**-sensitized FTO+TiO$_2$ films in Na$_2$SO$_4$ 0.1 M in H$_2$O at pH 6.7 degassed with nitrogen in the dark, under continuous and 5-s-chopped irradiation.

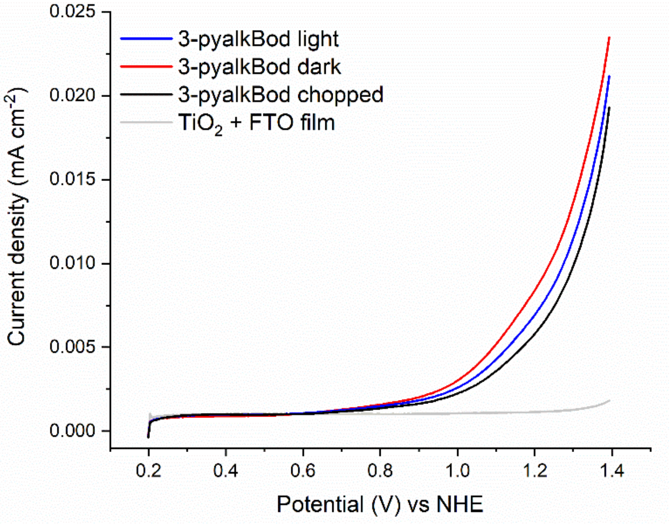

Figure 80: LSV of **3-pyalkBod**-sensitized FTO+TiO$_2$ films in Na$_2$SO$_4$ 0.1 M in H$_2$O at pH 6.7 degassed with nitrogen in the dark, under continuous and 5-sec-chopped irradiation.

The CA experiments gave a further confirmation of the inability of this compound to perform as a dyad in DSPEC photoanodes (Figure 81). The CA was performed under chopped irradiation, and no difference was obtained in the generated currents when the light was turned on. It could mean that the charge transfer in this system does not pass through the dye or that the **3-pyalkBod** does not possess the correct energy levels for driving the iridium WOC in water oxidation.

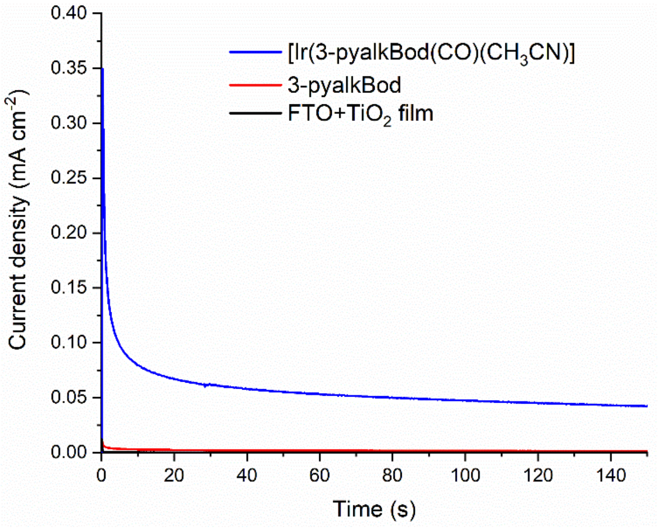

Figure 81: Chronoamperometry of TiO_2+ FTO films sensitized with **[Ir(3-pyalkBod)(CO)(CH_3CN)]** and **3-pyalkBod** in 0.1 M $Na_2SO_{4(aq)}$ at pH 6.7 with an applied bias of +1.0 V versus Ag/AgCl under 30-s chopped illumination (Solar simulator; $420<\lambda<800$ nm).

We know from previous studies with Terahertz spectroscopy that BODIPY dyes anchored to TiO_2 by the boron functionality can inject the electrons in the CB of TiO_2. We still need to understand if the charge transfer between the dye and the WOC portion is possible or not and if this kind of ligand recombines immediately. Moreover, from the CV profiles on both ITO and TiO_2, **3-pyalkBod** did not exhibit any oxidation or reduction peak in that range, suggesting that its energy levels may not match the photoelectrochemical system. These results could also be related to the decrease in the generated currents over time, probably due to an incorrect regeneration of the catalyst.

In conclusion, I investigated the binding mode of a new anchoring group for titanium dioxide that exploits a BODIPY molecule for the formation of a B-O bond with the SC surface. I first functionalized four different BODIPY dyes in positions 2 and 6 with small and large substituents to study the influence of these substitutions on the binding mode. I found that the presence of only one substituent did not influence the binding mode, while the presence of the second substituent reduced it until almost preventing it if the substituent is large. The preliminary results obtained were useful for the design of a new iridium-based WOC that exploited the BODIPY portion as the anchor group. This catalyst exhibited good water oxidation capabilities generating high current density on ITO films. Since one of its ligands, **3-pyalkBod**, is visible light active, we decided to study this compound as dyad in a photoanode for DSPEC. However, solar irradiation did not influence its performance, indicating an incorrect charge transfer from the WOC to the dye. Further studies with XPS, Terahertz spectroscopy, and transmission electron microscopy are ongoing to individuate the water oxidation active species in this research.

8.7 Experimental sections

8.7.1 Preparation of the ITO films

Thin films of nanoparticulate indium tin oxide (ITO) were made on FTO coated glass electrodes. The FTO coated glass was washed by successive sonication in ethanol, water, isopropanol, and acetone. A paste was made by sonicating 0.5 g ITO nanoparticles in 0.5 g glacial acetic acid and 1 g ethanol. Then the paste was deposited onto the cleaned FTO glass using a doctor blading method with one layer of Scotch® Magic™ Tape as the barrier. The films were then annealed in a muffle furnace at 500 ˚C for one hour. Finally, the films were reduced in a tube furnace with an atmosphere of 5% H_2 in N_2 and heated to 300 ˚C for one hour.

8.7.2 Preparation of the TiO_2 films

Mesoporous nanoparticulate TiO_2 thin films were doctor-bladed onto FTO slides, and then annealed for a final thickness of ca. 4 μm, following a literature procedure.[41] The FTO coated glass electrodes were cleaned via sonication to remove any surface contamination that might be present on. Each sonication step took about 15 minutes beginning with water and followed by acetone, isopropanol, and ethanol. After sonication, the slides were then blown dry with air. One layer of TiO_2 was deposited onto the clean substrate by doctor-blade, using commercial TiO_2 paste and one layer of Scotch® Magic™ Tape as the barrier. Ti-Nanoxide T/SP paste was purchased from Solaronix and used as received. The samples were then thermally annealed in a box oven by heating from 25 to 370 ˚C at a rate of 180 ˚C/h, holding at 370 ˚C for 10 min, followed by heating to 480 ˚C at a rate of 180 ˚C/h, holding at 480 ˚C for 30 min, and finally returning to room temperature through ambient cooling. The resulting thickness of the films was ~4 μm as determined by profilometry.

8.7.3 Sensitization of the films

The dye-sensitized films are prepared using a Schlenk technique. Pyrex overnight oven-dried text tubes are cooled under vacuum and then a nitrogen atmosphere is generated. The weighted compound and the film are inserted under nitrogen atmosphere in the sealed test tube. The solvents are dried over molecular sieve for one week before using. The right amount of solvent to achieve 5 mM solution is added to the test tube. The films are left sensitizing in the dark for 20 h. After that time, the films are washed with dry ACN and dried using nitrogen flow. The films are kept in the dark until measurement.

8.7.4 Optical and (photo)electrochemical investigation

The UV-Vis spectra, CV and LSV were recorded in comparison with a bare ITO or TiO_2 film. UV-visible absorption spectra were collected using a Shimadzu UV-2600 spectrophotometer. Cyclic Voltammetry (CV), Linear Sweep Voltammetry (LSV) and Chronoamperometry (CA) were carried out at a scan rate of 100 mV s^{-1}, using a Pine Research Instruments WaveDrive 20 bipotentiostat in a three-electrode electrochemical cell under nitrogen. The working electrodes were sensitized 4-μm-thick TiO_2 films, the counter a Pt wire and the reference an Ag/AgCl (sat.) electrode. The reference electrode was calibrated by adding ferrocene (10^{-3} M) to the test solution after each measurement (potentials measured versus Fc/Fc$^+$ and converted to NHE by addition of +0.40 V).[42] The scan rate is 50 mV/s. The applied bias in CA is +0.8 V vs NHE. Photoelectrochemistry has been performed in a PEC with a quartz window (cut-off ~ 200 nm) in the same three-electrode setup. The irradiation was performed with solar simulator (AM 1.5G, 1 sun, $420<\lambda<800$)

8.7.5 Synthesis

NMR spectra were recorded with Bruker Avance Neo spectrometer operating at 400 MHz (^{1}H), 100 MHz (^{13}C), 128 MHz (^{11}B), and 376 MHz (^{19}F). Coupling constants are given in Hz. High resolution mass spectra have been recorded with a ThermoScientific QExactive Orbitrap FT-MS with a Dionex 3000 UPLC system. Attenuated total reflectance Fourier transform infrared (ATR-FTIR) spectroscopic measurements were performed using an Agilent Technologies Cary 600 series FTIR spectrometer and a PIKE technologies GladiATR. Flash chromatography was performed with Silicycle SiliaFlash P60silica gel 230–400 mesh (60 Å). Reactions performed under inert atmosphere were performed in oven-dried glassware, and a nitrogen atmosphere was generated with Schlenk technique. The conversion was monitored by thin-layer chromatography by using UV light (254 nm) as a visualizing agent. All reagents were obtained from commercial suppliers at the highest purity grade and used without further purification. Anhydrous solvents were purchased over molecular sieves from Acros Organics and used without further purification. Extracts were dried with Na_2SO_4 and filtered before removal of the solvent by evaporation. Compounds (*T*-4)-Difluoro[2-[phenyl(2*H*-pyrrol-2-ylidene-κ*N*)methyl]-1*H*-pyrrolato-κ*N*]boron (**Bod**),[43] (*T*-4)-[4-Bromo-2-[(4-bromo-2*H*-pyrrol-2-ylidene-κ*N*)phenylmethyl]-1*H*-pyrrolato-κ*N*]difluoroboron (**Br$_2$-Bod**),[30] (*T*-4)-[4-Bromo-2-[phenyl(2*H*-pyrrol-2-ylidene-κ*N*)methyl]-1*H*-pyrrolato-κ*N*]difluoroboron (**Br-Bod**),[30] and 2,2'-((4-nitrophenyl)methylene)bis(1*H*-pyrrole) (**4**)[31] were prepared according to literature.

(*T*-4)-[4-Phenyl-2-[(4-phenyl-2*H*-pyrrol-2-ylidene-κ*N*)phenylmethyl]-1*H*-pyrrolato-κ*N*]difluoroboron (Ph$_2$Bod) and (*T*-4)-[4-Bromo-2-[(4-phenyl-2*H*-pyrrol-2-ylidene-κ*N*)phenylmethyl]-1*H*-pyrrolato-κ*N*]difluoroboron (PhBrBod): **Ph$_2$Bod** and **PhBrBod** were obtained from the same Suzuki-Miyaura reaction adapting from the literature[30] and stopping it before complete conversion. In a two-necked round-bottom flask under nitrogen atmosphere, **Br$_2$-Bod** (62 mg, 0.15 mmol) was solubilized in toluene (6 mL), then phenylboronic acid (45 mg, 0.37 mmol) and water (5 mL) were added to the reaction mixture. The solution was inflated with nitrogen for 30 min, then $Pd(dppf)Cl_2 \cdot DCM$ was added, and the solution degassed for other 15 min. In the end K_2CO_3 (207 mg, 1.5 mmol) and two drops of Et_3N were added and the reaction was heated to reflux for 45 min. The reaction is quenched by pouring into a saturated solution of NH_4Cl (30 mL) and DCM (30 mL). After stirring for 30 min, filtration on Celite and separation of the two phases allowed to isolate the crude product. It is then purified through column chromatography on silica gel (Hexanes/AcOEt, 6:1). The desired products were isolated as a deep-blue solid in the case of **Ph_2Bod** (35 mg, 0.083 mmol, 55%) and a purple solid in the case of **PhBrBod** (20 mg, 0.05 mmol 30%). **Ph_2Bod:** ^{1}H NMR (400 MHz, $CDCl_3$) δ 8.30 (s, 2H), 7.66 (t, *J* = 7.5 Hz, 3H), 7.63 - 7.57 (m, 2H), 7.53 (d, *J* = 7.7 Hz, 4H), 7.38 (t, *J* = 7.4 Hz, 4H), 7.29 (d, *J* = 6.9 Hz, 2H), 7.10 (s, 2H). ^{19}F NMR (376 MHz, $CDCl_3$) δ -145.30 (dd, *J* = 57.5, 28.5 Hz). ^{11}B NMR (128 MHz, $CDCl_3$) δ 0.28 (t, *J* = 29.1 Hz). **PhBrBod:** ^{1}H NMR (400 MHz, $CDCl_3$) δ 8.35 (s, 1H), 7.80 (s, 1H), 7.68 - 7.55 (m, 5H), 7.52 (d, *J* = 7.4 Hz, 2H), 7.38 (t, *J* = 7.3 Hz, 2H), 7.31 (d, *J* = 7.3 Hz, 1H), 7.14 (s, 1H), 6.89 (s, 1H). ^{19}F NMR (376 MHz, $CDCl_3$) δ -145.20 (dd, *J* = 56.8, 28.5 Hz). ^{11}B NMR (128 MHz, $CDCl_3$) δ -0.01 (t, *J* = 28.2 Hz).

6-acetylnicotinonitrile (1): Following a reported procedure[40] with modifications, a mixture of nicotinonitrile (1.04 g, 10.0 mmol) and metaldehyde (8.81 g, 50.0 mmol) in acetonitrile (30 mL) was stirred at room temperature under air for 10 min. Iron(II) sulfate heptahydrate (44 mg, 0.16 mmol), trifluoroacetic acid (1.16 g, 10.2 mmol), and a 70% *tert*-butyl hydroperoxide aqueous solution (3.85 mL, 28.0 mmol) were then added in sequence. The mixture was refluxed under air for 17 h. The resulting brown solution was concentrated to afford an oil, which was diluted with ethyl acetate (10 mL) and washed with saturated $NaHCO_3$ aqueous solution (20 mL). The aqueous layer was extracted with ethyl acetate (30 mL × 3). The organic extract was washed with brine, dried with Na_2SO_4, and filtered. The filtrate was concentrated and chromatographed (silica gel, hexanes/ethyl acetate = 5:1 to 3:2). The first band was collected and concentrated to afford a white solid (447 mg, 31%): TLC (silica, hexanes/ethyl acetate = 3:1) R_f = 0.42; ^{1}H NMR ($CDCl_3$, 400 MHz) δ 8.94 (s, 1H), 8.14 (d, *J* = 8.0 Hz, 1H), 8.09 (d, *J* = 8.5 Hz, 1H), 2.74 (s, 3H).

6-(2-hydroxypropan-2-yl)nicotinonitrile (2): Compound **1** (200 mg, 1,37 mmol) is solubilized in anhydrous THF (8 mL) in an oven-dried two-necked round bottom flask under nitrogen atmosphere. The solution is cooled with an ice bath and kept stirring for 15 min. a first portion of methylmagnesium bromide (0.8 mL, 2 mmol, 3 M) is slowly added dropwise. The solution changed from pale yellow to red and the solution is kept stirring at 0 °C for 1 h. Then, the second portion of methylmagnesium bromide (0.5 mL, 1.5 mmol, 3 M) is added and the solution is kept stirring at 0 °C for 1 h and then left coming back to room temperature. The reaction is quenched pouring into an aqueous solution of NH_4Cl and left stirring overnight. The mixture is separated, and the aqueous phase is extracted twice with AcOEt. The organic phases are combined, dried over sodium sulfate, filtered and the solvent is removed through rotary evaporation. The crude product is purified through flash column chromatography (SiO_2, AcOEt/Hex, 1:1). The desired product is isolated as a yellowish oil (135 mg, 0.83 mmol, 60%). ^1H NMR (400 MHz, CD_3CN) δ 8.85 (dd, *J* = 2.1, 0.7 Hz, 1H), 8.11 (dd, *J* = 8.3, 2.2 Hz, 1H), 7.80 (dd, *J* = 8.3, 0.8 Hz, 1H), 3.89 (s, 1H), 1.52 (s, 6H).

6-(2-hydroxypropan-2-yl)nicotinic acid (3): Compound **3** is synthesized adapting from an existing literature procedure.[44] Compound **2** (135 mg, 0.83 mmol) is solubilized in 2 mL EtOH 70% and solid NaOH (133 mg, 3.3 mmol) is added. The solution is stirred for 10 min at rt and became red. The solution is heated at 89 °C for 4 h. The reaction is quenched reducing the solvent and adding 0.2 mL HCl 37% to neutralize the solution. The solid residues were filtered, and the liquid phase is collected, the solvent evaporated, and the product is obtained as a brown solid in a quantitative yield. ^1H NMR (400 MHz, H_2O+D_2O) δ 8.91 (s, 1H), 8.29 (dd, *J* = 8.3, 2.0 Hz, 1H), 7.75 (d, *J* = 8.2 Hz, 1H), 1.95 (d, *J* = 2.8 Hz, 1H), 1.62 (s, 6H).

5,5-difluoro-10-(4-nitrophenyl)-5*H*-4λ⁴,5λ⁴-dipyrrolo[1,2-c:2',1'-*f*][1,3,2]diazaborinine (5): In an oven-dried two-necked round bottom flask, compound **4** (500 mg, 1.87 mmol) is dissolved in extra dry DCM (30 mL) under nitrogen atmosphere. 2,3-dichloro-5,6-dicyano-1,4-benzoquinone (425 mg, 1.87 mmol) is added to the stirring solution in two portion and the solution is left stirring at rt for 30 min. The solution assumed a dark color. Freshly distilled boron trifluoride diethyl etherate (3.7 mL, 30 mmol) is added to the solution and after 10 min, *N,N*-diisopropylethylamine (5 mL, 28 mmol) is slowly added dropwise. The solution is stirred for 30 min at rt and then refluxed for 1 h. The reaction is quenched pouring into a mixture of DCM and water, stirred for 30 min, and then filtrated over celite. The biphasic mixture is separated, the organic phase is washed with water three times and then the aqueous phase is extracted back once with DCM. The organic phases are collected, dried over sodium sulfate, filtrated and the solvent is evaporated through rotary evaporation. The crude product is purified with a filtration over silica (Hex/AcOEt, 2:1) and then is crystallized in hexane to obtain the product as a brown solid with green reflexes (260 mg, 0.83 mmol, 44%). ^1H NMR (400 MHz, $CDCl_3$) δ 8.64 – 8.24 (m, 2H), 8.00 (s, 2H), 7.92 – 7.60 (m, 2H), 6.85 (d, *J* = 4.2 Hz, 2H), 6.59 (d, *J* = 4.2 Hz, 2H). ^{11}B NMR (128 MHz, $CDCl_3$) δ 0.25 (t, *J* = 28.4 Hz). ^{19}F NMR (376 MHz, $CDCl_3$) δ -145.02 (dd, *J* = 57.0, 28.4 Hz).

4-(5,5-difluoro-5*H*-4λ^4,5λ^4-dipyrrolo[1,2-c:2',1'-*f*][1,3,2]diazaborinin-10-yl)aniline (6): Compound **5** (150 mg, 0.48 mmol) is suspended in absolute EtOH (16 mL), subsequently iron powder (200 mg, 3.6 mmol), water (2.7 mL) and HCl 37% (0.06 mL) are added. The reaction is left stirring at 95 °C for 1.5 h. Hot filtration is performed to remove the black precipitate. The solvent is evaporated, and the crude product is purified on a silica pad using DCM as eluent. The pure product is obtained as an orange solid (100 mg, 0.35 mmol, 73%). ^{1}H NMR (400 MHz, $CDCl_3$) δ 7.89 (s, 2H), 7.45 (d, *J* = 8.5 Hz, 2H), 7.02 (d, *J* = 3.9 Hz, 2H), 6.78 (d, *J* = 8.5 Hz, 2H), 6.54 (d, *J* = 2.6 Hz, 2H), 4.10 (s, 2H). ^{11}B NMR (128 MHz, $CDCl_3$) δ 0.30 (t, *J* = 29.0 Hz). ^{19}F NMR (376 MHz, $CDCl_3$) δ -145.21 (dd, *J* = 58.2, 29.1 Hz).

***N*-(4-(5,5-difluoro-5*H*-4λ^4,5λ^4-dipyrrolo[1,2-c:2',1'-*f*][1,3,2]diazaborinin-10-yl)phenyl)-6-(2-hydroxypropan-2-yl)nicotinamide (3-pyalkBod)**: In an oven-dried two-necked round bottom flask, compound **3** (215 mg, 1 mmol) is suspended in dry benzene (12 mL) under nitrogen atmosphere. Oxalyl chloride (0.4 mL, 0.76 mmol, 2M) is added dropwise and the five drops of extra dry DMF are added to solubilize everything and gas bubbles started forming. The solution is left stirring at rt for 1.5 h. The solvent is reduced to 2 mL and extra dry DCM (12 mL), compound **6** (110 mg, 0.38 mmol) and triethylamine (0.1 mL, 0.76 mmol) are added. The solution is left stirring at rt overnight. The reaction is quenched evaporating the solvent, adding water, and filtrating the red precipitate formed. The product is purified through flash column chromatography (SiO_2, AcOEt-Hex-TEA, 1:1:0.05). The product is obtained as a red solid (20 mg, 0.05 mmol, 13%). ^{1}H NMR (400 MHz, $CDCl_3$) δ 9.03 (d, *J* = 1.7 Hz, 1H), 8.45 (s, 1H), 8.19 (dd, *J* = 8.3, 2.3 Hz, 1H), 8.08 (s, 1H), 7.92 (s, 2H), 7.82 (d, *J* = 8.6 Hz, 2H), 7.56 (d, *J* = 8.6 Hz, 2H), 7.51 (d, *J* = 8.3 Hz, 1H), 6.94 (d, *J* = 4.1 Hz, 2H), 6.55 (dd, *J* = 4.2, 1.8 Hz, 2H), 1.84 (s, 6H). ^{11}B NMR (128 MHz, $CDCl_3$) δ 0.29 (t, *J* = 28.9 Hz). ^{19}F NMR (376 MHz, $CDCl_3$) δ -144.68 (dd, *J* = 57.8, 28.8 Hz). ^{13}C NMR (101 MHz, CDCl3) δ 166.81, 164.14, 160.09, 147.28, 144.18, 140.29, 136.25, 134.99, 131.83, 131.53, 130.30, 128.96, 120.03, 119.31, 118.73, 83.23, 27.59. ATR-FTIR $\upsilon/(cm^{-1})$: 3336(b), 2913(b), 1551 (s), 1380(s), 1068(b), 728 (b). HRMS *m/z*: calcd. for $[M+H]^+$ $C_{24}H_{21}BF_2N_4O_2$: 447.1804, found 447.1777.

[Ir(3-pyalkBod)(CO)(CH_3CN)]: In a round bottom flask, **3-pyalkBod** (10 mg, 0.02 mmol) is dissolved in 2 mL DCM and a 1 mL aqueous solution of K_2CO_3 (3 mg, 0.01 mmol) is added. The mixture is stirred and degassed for 30 min with nitrogen. In a second oven-dried two-necked round bottom flask, $[Ir(cod)Cl]_2$ (7 mg, 0.01 mmol) is added while only the DCM solution is transferred from the first flask to the second. The new solution is left stirring till everything is solubilized. Then CO is bubbled for 5 min. Acetonitrile is added and a dark solid formed. The solid is filtered, and the acetonitrile solution is evaporated to obtain a brown solid with a quantitative yield. ^{1}H NMR (400 MHz, CD_3CN) δ 9.07 (d, *J* = 2.3 Hz, 1H), 8.28 (dd, *J* = 8.2, 2.3 Hz, 1H), 8.11 (s, 1H), 8.02 – 7.93 (m, 4H), 7.70 (d, *J* = 8.5 Hz, 2H), 7.62 (d, *J* = 8.4 Hz, 1H), 7.11 (d, *J* = 4.2 Hz, 2H), 6.65 (s, 2H), 1.96 (s, 3H), 1.82 (s, 6H). ^{11}B NMR (128 MHz, CD_3CN) δ 0.22 (t, *J* = 28.3 Hz).^{19}F NMR (376 MHz, CD_3CN) δ -144.86 (dd, *J* = 57.0, 28.5 Hz). ^{13}C NMR was not recorded due to low solubility of the compound. ATR-FTIR υ/(cm^{-1}): 3269(b), 2928 (b), 2024 (s), 1551 (s), 1387 (s), 1254 (s), 1106 (b), 758 (b). HRMS *m/z*: calcd. for $[M+H-F]^+$ $C_{27}H_{23}BF_2IrN_5O_3$: 689.1585, found 689.1572.

References

1 Nocera, D. G. (**2017**) Solar Fuels and Solar Chemicals Industry. *Acc. Chem. Res.,* **50**, 616-619, doi:10.1021/acs.accounts.6b00615.

2 Stamenkovic, V. R., Strmcnik, D., Lopes, P. P. & Markovic, N. M. (**2016**) Energy and fuels from electrochemical interfaces. *Nat. Mater.,* **16**, 57-69, doi:10.1038/nmat4738.

3 You, B. & Sun, Y. (**2016**) Chalcogenide and Phosphide Solid-State Electrocatalysts for Hydrogen Generation. *ChemPlusChem,* **81**, 1045-1055, doi:10.1002/cplu.201600029.

4 Liang, Y., Li, Y., Wang, H. & Dai, H. (**2013**) Strongly Coupled Inorganic/Nanocarbon Hybrid Materials for Advanced Electrocatalysis. *J. Am. Chem. Soc.,* **135**, 2013-2036, doi:10.1021/ja3089923.

5 You, B., Tang, M. T., Tsai, C., Abild-Pedersen, F., Zheng, X. & Li, H. (**2019**) Enhancing Electrocatalytic Water Splitting by Strain Engineering. *Adv. Mater.,* **31**, 1807001, doi:10.1002/adma.201807001.

6 Ding, Q., Song, B., Xu, P. & Jin, S. (**2016**) Efficient Electrocatalytic and Photoelectrochemical Hydrogen Generation Using MoS2 and Related Compounds. *Chem,* **1**, 699-726, doi:10.1016/j.chempr.2016.10.007.

7 You, B. & Sun, Y. (**2018**) Innovative Strategies for Electrocatalytic Water Splitting. *Acc. Chem. Res.,* **51**, 1571-1580, doi:10.1021/acs.accounts.8b00002.

8 You, B., Jiang, N., Sheng, M., Bhushan, M. W. & Sun, Y. (**2016**) Hierarchically Porous Urchin-Like Ni_2P Superstructures Supported on Nickel Foam as Efficient Bifunctional Electrocatalysts for Overall Water Splitting. *ACS Catal.,* **6**, 714-721, doi:10.1021/acscatal.5b02193.

9 You, B., Jiang, N., Sheng, M., Gul, S., Yano, J. & Sun, Y. (**2015**) High-Performance Overall Water Splitting Electrocatalysts Derived from Cobalt-Based Metal-Organic Frameworks. *Chem. Mater.,* **27**, 7636-7642, doi:10.1021/acs.chemmater.5b02877.

10 Shinagawa, T. & Takanabe, K. (**2017**) Towards Versatile and Sustainable Hydrogen Production through Electrocatalytic Water Splitting: Electrolyte Engineering. *ChemSusChem,* **10**, 1318-1336, doi:10.1002/cssc.201601583.

11 Fukuzumi, S. & Hong, D. (**2014**) Homogeneous versus Heterogeneous Catalysts in Water Oxidation. *Eur. J. Inorg. Chem.,* **2014**, 645-659, doi:10.1002/ejic.201300684.

12 van Dijk, B., Rodriguez, G. M., Wu, L., Hofmann, J. P., Macchioni, A. & Hetterscheid, D. G. H. (**2020**) The Influence of the Ligand in

the Iridium Mediated Electrocatalyic Water Oxidation. *ACS Catal.,* **10**, 4398-4410, doi:10.1021/acscatal.0c00531.

13 Ghaderian, A., Kazim, S., Khaja Nazeeruddin, M. & Ahmad, S. (**2022**) Strategic factors to design the next generation of molecular water oxidation catalysts: Lesson learned from ruthenium complexes. *Coord. Chem. Rev.,* **450**, 214256, doi:10.1016/j.ccr.2021.214256.

14 Geer, A. M., Liu, C., Musgrave III, C. B., Webber, C., Johnson, G., Zhou, H., Sun, C.-J., Dickie, D. A., Goddard III, W. A., Zhang, S. & Gunnoe, T. B. (**2021**) Noncovalent Immobilization of Pentamethylcyclopentadienyl Iridium Complexes on Ordered Mesoporous Carbon for Electrocatalytic Water Oxidation. *Small Science,* 2100037, doi:https://doi.org/10.1002/smsc.202100037.

15 Kondo, M., Tatewaki, H. & Masaoka, S. (**2021**) Design of molecular water oxidation catalysts with earth-abundant metal ions. *Chem. Soc. Rev.,* **50**, 6790-6831, doi:10.1039/D0CS01442G.

16 Loudet, A. & Burgess, K. (**2007**) BODIPY Dyes and Their Derivatives: Syntheses and Spectroscopic Properties. *Chem. Rev.,* **107**, 4891-4932, doi:10.1021/cr078381n.

17 Klfout, H., Stewart, A., Elkhalifa, M. & He, H. (**2017**) BODIPYs for Dye-Sensitized Solar Cells. *ACS Appl. Mater. Interfaces,* **9**, 39873-39889, doi:10.1021/acsami.7b07688.

18 Poddar, M. & Misra, R. (**2020**) Recent advances of BODIPY based derivatives for optoelectronic applications. *Coord. Chem. Rev.,* **421**, 213462, doi:10.1016/j.ccr.2020.213462.

19 Badgurjar, D., Shan, B., Nayak, A., Wu, L., Chitta, R. & Meyer, T. J. (**2020**) Electron-Withdrawing Boron Dipyrromethene Dyes As Visible Light Absorber/Sensitizers on Semiconductor Oxide Surfaces. *ACS Appl. Mater. Interfaces,* **12**, 7768-7776, doi:10.1021/acsami.9b20167.

20 Makino, K., I, T. & Kubo, Y. (**2021**) A benzofuran[b]-fused BODIPY as an efficient sensitizer for photocatalytic hydrogen production. *Sustain. Energy Fuels,* **5**, 3676-3686, doi:10.1039/D1SE00387A.

21 Xie, A., Pan, Z.-H., Yu, M., Luo, G.-G. & Sun, D. (**2019**) Photocatalytic hydrogen production from acidic aqueous solution in BODIPY-cobaloxime-ascorbic acid homogeneous system. *Chin. Chem. Lett.,* **30**, 225-228, doi:10.1016/j.cclet.2018.05.003.

22 Shen, X.-F., Watanabe, M., Takagaki, A., Song, J. T. & Ishihara, T. (**2020**) Pyridyl-Anchored Type BODIPY Sensitizer-TiO_2 Photocatalyst for Enhanced Visible Light-Driven Photocatalytic Hydrogen Production. *Catalysts,* **10**, 535, doi:10.3390/catal10050535.

23 Songkhao, J., Banerjee, R., Debnath, S., Narasimhan, S., Wannaprom, N., Vanalabhpatana, P., Seriani, N., Gebauer, R. & Thamyongkit, P. (**2017**) Structure-property relationship of π-extended boron-dipyrromethene derivatives towards optoelectronic applications. *Dyes Pigm.,* **142**, 558-571, doi:10.1016/j.dyepig.2017.03.050.

24 Gubaidullin, R., Nedopekina, D., Tukhbatullin, A., Davletshin, E. & Spivak, A. (**2020**) Design, Synthesis, and Photophysical Properties of BODIPY-Labeled Lupane Triterpenoids. *Chem. Proc.,* **3**, 11, doi:10.3390/ecsoc-24-08102.

25 Chu, G. M., Fernández, I., Guerrero-Martínez, A., Ramírez De Arellano, C. & Sierra, M. A. (**2016**) Fluorescence Quenching in BODIPYs Having Ir- and Rh-Tethered Complexes. *Eur. J. Inorg. Chem.,* **2016**, 844-852, doi:10.1002/ejic.201501283.

26 Zlatić, K., Ayouchia, H. B. E., Anane, H., Mihaljević, B., Basarić, N. & Rohand, T. (**2020**) Spectroscopic and photophysical properties of mono- and dithiosubstituted BODIPY dyes. *J. Photochem. Photobiol., A,* **388**, 112206, doi:10.1016/j.jphotochem.2019.112206.

27 Pauling, L. *The nature of the chemical bond and the structure of molecules and crystals : an introduction to modern structural chemistry.* 3rd edn, (Cornell University Press: Ithaca, USA, **1960**).

28 Liu, Z., Thacker, S. G., Fernandez-Castillejo, S., Neufeld, E. B., Remaley, A. T. & Bittman, R. (**2014**) Synthesis of Cholesterol Analogues Bearing BODIPY Fluorophores by Suzuki or Liebeskind-Srogl Cross-Coupling and Evaluation of Their Potential for

Visualization of Cholesterol Pools. *ChemBioChem,* **15**, 2087-2096, doi:10.1002/cbic.201402042.

29 Farfán-Paredes, M., González-Antonio, O., Tahuilan-Anguiano, D. E., Peón, J., Ariza, A., Lacroix, P. G., Santillan, R. & Farfán, N. (**2020**) Physicochemical and computational insight of 19F NMR and emission properties of *meso*-(*o*-aryl)-BODIPYs. *New J. Chem.,* **44**, 19459-19471, doi:10.1039/D0NJ02576C.

30 Jiao, L., Pang, W., Zhou, J., Wei, Y., Mu, X., Bai, G. & Hao, E. (**2011**) Regioselective Stepwise Bromination of Boron Dipyrromethene (BODIPY) Dyes. *J. Org. Chem.,* **76**, 9988-9996, doi:10.1021/jo201754m.

31 Laha, J. K., Dhanalekshmi, S., Taniguchi, M., Ambroise, A. & Lindsey, J. S. (**2003**) A Scalable Synthesis of Meso-Substituted Dipyrromethanes. *Org. Process Res. Dev.,* **7**, 799-812, doi:10.1021/op034083q.

32 Thomsen, J. M., Huang, D. L., Crabtree, R. H. & Brudvig, G. W. (**2015**) Iridium-based complexes for water oxidation. *Dalton Trans.,* **44**, 12452-12472, doi:10.1039/C5DT00863H.

33 Hintermair, U., Sheehan, S. W., Parent, A. R., Ess, D. H., Richens, D. T., Vaccaro, P. H., Brudvig, G. W. & Crabtree, R. H. (**2013**) Precursor Transformation during Molecular Oxidation Catalysis with Organometallic Iridium Complexes. *J. Am. Chem. Soc.,* **135**, 10837-10851, doi:10.1021/ja4048762.

34 Huang, D. L., Beltrán-Suito, R., Thomsen, J. M., Hashmi, S. M., Materna, K. L., Sheehan, S. W., Mercado, B. Q., Brudvig, G. W. & Crabtree, R. H. (**2016**) New Ir Bis-Carbonyl Precursor for Water Oxidation Catalysis. *Inorg. Chem.,* **55**, 2427-2435, doi:10.1021/acs.inorgchem.5b02809.

35 Frank, F., Alice, L. M., Mauker, P., Alsimaree, A. A., Waddell, P. G., Probert, M. R., Penfold, T. J., Knight, J. G. & Hall, M. J. (**2020**) Synthesis of 3,5-dichloro-4,4-difluoro-4-bora-3a,4a-diaza-s-indacenes (BODIPYs) via Cu(OTf)$_2$ mediated oxidative nucleophilic substitution of hydrogen by chloride. *Tetrahedron,* **76**, 131113, doi:10.1016/j.tet.2020.131113.

36 Paul, N., Sarkar, R., Sarkar, R., Barui, A. & Sarkar, S. (**2020**) Detection of hydrogen sulfide using BODIPY based colorimetric and fluorescent on-off chemosensor. *J. Chem. Sci.,* **132**, 21, doi:10.1007/s12039-019-1724-4.

37 Wei, Z., Sharma, S., Philip, A. M., Sengupta, S. & Grozema, F. C. (**2021**) Excited state dynamics of BODIPY-based acceptor-donor-acceptor systems: a combined experimental and computational study. *Phys. Chem. Chem. Phys.,* **23**, 8900-8907, doi:10.1039/D1CP00453K.

38 Niu, P., Wu, G., Chen, P., Zheng, H., Cao, Q. & Jiang, H. (**2020**) Optimization of Boron Doped TiO$_2$ as an Efficient Visible Light-Driven Photocatalyst for Organic Dye Degradation With High Reusability. *Front. Chem.,* **8**, 172, doi:10.3389/fchem.2020.00172.

39 Materna, K. L., Jiang, J., Regan, K. P., Schmuttenmaer, C. A., Crabtree, R. H. & Brudvig, G. W. (**2017**) Optimization of Photoanodes for Photocatalytic Water Oxidation by Combining a Heterogenized Iridium Water-Oxidation Catalyst with a High-Potential Porphyrin Photosensitizer. *ChemSusChem,* **10**, 4526-4534, doi:10.1002/cssc.201701693.

40 Materna, K. L., Rudshteyn, B., Brennan, B. J., Kane, M. H., Bloomfield, A. J., Huang, D. L., Shopov, D. Y., Batista, V. S., Crabtree, R. H. & Brudvig, G. W. (**2016**) Heterogenized Iridium Water-Oxidation Catalyst from a Silatrane Precursor. *ACS Catal.,* **6**, 5371-5377, doi:10.1021/acscatal.6b01101.

41 Troiano, J. L., Hu, G., Crabtree, R. H. & Brudvig, G. W. (**2020**) Diazo coupling for surface attachment of small molecules to TiO$_2$ nanoparticles. *Chem. Commun.,* **56**, 9340-9343, doi:10.1039/D0CC03631E.

42 Sawyer, D. T., Roberts, J. L., Jr. & Sobkowiak, A. *Electrochemistry for chemists.* 2nd edn, (Wiley: New York, USA, **1995**)

43 Rivera-González, E., Galván-Miranda, E. K., Aguilar-Martínez, M., Farfán, N., Xochitiotzi-Flores, E. & Macías Ruvalcaba, N. A. (**2019**)

Electroreduction of 8-(thiophen-2-yl)- and 8-(phenyl)-dipyrrometheneboron difluorides. A mechanistic study by cyclic voltammetric digital simulation. *Electrochim. Acta,* **317**, 375-383, doi:10.1016/j.electacta.2019.05.127.

44 McElvain, S. M. & Goese, M. A. (**1941**) THE PREPARATION OF NICOTINIC ACID FROM PYRIDINE. *J. Am. Chem. Soc.,* **63**, 2283-2284, doi:10.1021/ja01853a511.

Chapter 9: Conclusions

During my PhD, I have focused on different topics regarding the use of organic dyes as visible light photosensitizers in devices for the production of solar fuels through efficient light harvesting. I investigated two different applications, a photocatalytic and a photoelectrochemical one. For these applications, I considered both covalent and non-covalent approaches.

In the photocatalytic application, we have investigated only a non-covalent approach between the dye and the sacrificial electron donor. We decided not to investigate a covalent interaction, because since the sacrificial electron donor cannot be regenerated by the system, it would have led to the loss of the dye as well. Regardless, the establishment of supramolecular interaction favored the photocatalytic activity confirming the success of the new proposed design.

In the photoelectrochemical application, we investigated both approaches. We presented the first example of calix[4]arene-based dyes employed in photoanodes of DSPEC to exploit their host-guest capabilities. However, the evidence of the establishment of either beneficial or fruitless host-guest interactions between the dyes and the water oxidation catalyst are still under investigation. The second non-covalent approach investigated in DSPEC is the π-π interaction between a graphene-functionalized dye and a suitable modified water oxidation catalyst. All the further characterization and application in DSPEC are ongoing.

On the other hand, the covalent approach should be the most stable and with the immobilization of the water oxidation catalyst at a fixed distance from the SC surface, it is possible to avoid the establishment of detrimental interaction with the

SC. We presented the first example of organic-dye-based dyads for photoanode application. These molecules showed excellent Faradaic efficiency in oxygen evolution being the highest with respect to the actual state of the art for similar systems.[1,2] Further investigations in the evaluation of the long-chain dyads in photoelectrochemical water oxidation are in progress. The other covalent design that is proposed in Chapter 8 failed in the photoelectrochemical application, but this molecule exhibited very good performances as simple water oxidation catalyst in electrochemical cells. This means that this catalyst has the right potential to oxidize water and can be used in combination with an external source of energy, such as solar panels. However further investigation in the dye portion is required to achieve a better charge transfer for the application in DSPEC.

The analysis of the state of the art designs has clearly highlighted that these devices are still in their infancy, not only for the efficiencies, which are in most cases modest, but also especially for the vast horizons of development available. The challenge for research in these fields is very demanding but also highly attractive. The ultimate goal is to develop, from a scientific and technological point of view, a device to produce solar fuels and, by extension to other fields of artificial photosynthesis, of carbon- and nitrogen-based chemicals. These devices should be cheap, easy to prepare, and based on low-cost earth-abundant materials and elements, such as sunlight, water, and carbon-based metal-free compounds. The challenging and ultimate target device is the "fully organic" artificial leaf. For now, the number of papers with organic dyes is very limited, not only when compared with other chemical components of the DSPEC whose development is more mature, such as oxides and organometallic systems, but with the same use of organic dyes in other fields of solar energy, such as photovoltaics (Dye-Sensitized Solar

Cells). However, organic dyes also present many drawbacks like low stability, the presence of charge recombination processes, and low resistance under long-term continuous irradiation. Hence, the research of new electron-rich and electron-poor scaffolds, characterized by an easy synthesis, higher stability, and a low cost is mandatory. The development of integrated systems connected through non-covalent or covalent interaction might increase the robustness and the charge transfer efficiency in these devices. Although this approach is not mature yet in terms of device efficiency for a large-scale application, the goal is to create a single supramolecular functional system, fully integrated and capable of performing all the necessary functions (light absorption, transfer and transport of charges, water splitting, and dye regeneration) in an efficient, cooperative, and interactive manner. This could be possible thanks to the structural and functional optimization of the single sub-units, their spatial proximity, and the stability of the connections between them.

References

1 Yamamoto, M., Wang, L., Li, F., Fukushima, T., Tanaka, K., Sun, L. & Imahori, H. (**2016**) Visible light-driven water oxidation using a covalently-linked molecular catalyst-sensitizer dyad assembled on a TiO2electrode. *Chem. Sci.,* **7**, 1430-1439, doi:10.1039/c5sc03669k.

2 Antón-García, D., Warnan, J. & Reisner, E. (**2020**) A diketopyrrolopyrrole dye-based dyad on a porous TiO2 photoanode for solar-driven water oxidation. *Chem. Sci.*, doi:10.1039/D0SC04509H.